Design, synthesis and characterisation of palladium-based bimetallic electrocatalysts for fuel cells and electrolyzers

UNIVERSITY OF THE
WITWATERSRAND,
JOHANNESBURG

Adewale Kabir Ipadeola (1846796)

A thesis submitted to the Faculty of Science, University of the Witwatersrand, Johannesburg, in the fulfilment for the degree of

Doctor of Philosophy in Chemistry

Supervisor: Prof. Kenneth I. Ozoemena

Johannesburg, October 2020

J

DECLARATION

I solemnly declared that this thesis is self-reliant and independently studied. It is being submitted to the School of Chemistry, Faculty of Science, University of the Witwatersrand, Johannesburg for the award of the degree of Doctor of Philosophy. It has not been submitted previously to any other institution of higher learning for consideration of any degree.

Name: Adewale Kabir Ipadeola (1846796)

Signature: ……  …. Date: …27th October 2020….

DEDICATION

The work is specially dedicated to my late parents, Mr. and Mrs. Ademola and Risikat Ipadeola; my beloved wife, Mariam Oluwatoyin Ipadeola; my siblings, Mr. Mutiu, Toheeb, and Lawal Ipadeola and Mrs. Kabirat Adetoro.

ACKNOWLEDGEMENTS

All praise and might are to almighty Allah for taking me through this journey of life with good health, competence and strength needed to complete this project. Although the journey was extremely challenging, it is quite interesting.

My sincere gratitude goes to my supervisor, Prof. Kenneth Ikechukwu Ozoemena for his immense advice, support, teaching, training and motivation. I am deeply thankful for his inestimable mentoring role throughout this program from the beginning to completion. He is the best mentor and motivator who practically taught me everything I know today on materials chemistry and electrochemistry. He has inculcated confidence in me to carry on to the greatest level in the field of materials for energy storage and conversion applications.

I am most grateful to the Department of Science and Technology, National Research Foundation (DST-NRF) in partnership with The World Academy of Science (TWAS) for the award of prestigious African Renaissance Doctoral Scholarship and the University of the Witwatersrand for Postgraduate Merit Award (PMA), which cover the wherewithal including tuition, accommodation and feeding throughout the program.

There are some individuals and research groups who contributed immensely to the success of this work. I would like to appreciate the assistance, comments, support and advice of all members of the Materials Electrochemistry and Energy Technologies (MEET) group. It is great working with each member of the group and to my Honours' students who allowed me to improve my supervision and mentoring skills. I would also like to recognise the contributions of Catalysis and Materials (CATMAT) group

members. The weekly group meeting is quite educational and helpful to improve my presentation skills. My warm gratitude goes to Prof. Neil Coville for granting me access to LAB 117 for using microwave and furnace for my experiments. He indirectly brought me to Wits University by forwarding the initial communication for Ph.D. supervision with him to Prof. Kenneth I. Ozoemena and then the admission process and scholarship application process began. I highly appreciate Prof. Dave Billings for training and access to the powder XRD instrument used to characterize my materials, Dr. Caren Billing for the use of VMP-300 Potentiostat for some electrochemical measurements, my co-authors: Dr. Hamish A. Miller, Dr. Maria V. Pagliaro, Prof. Francesco Vizza, Veronica Davies and Prof. Qinqying Jia for assistance to use synchrotron at the Brookhaven National Laboratory, Prof. Frank Marken for designing and fabricating the micro-3D printed cell used for proof-of-concept, Prof. Sekar C. Ray for XPS analysis, and Wits microscopy and microanalysis unit (MMU) for training and access to TEM and SEM for my research. To those individuals, I did not mention their names, your contributions to the success of this program are highly recognized and appreciated.

My sincere gratitude goes to my lovely wife, Mrs. Mariam O. Ipadeola for her unwavering supports to make this dream comes true. Her sacrifice to making this a reality is huge, traveling for the program barely 9 months after our marital vow and left her alone in Nigeria. I cannot thank her enough for keying and supporting my dreams. To my late dad, Mr. Ademola K. Ipadeola whom I lost during this journey. I never knew my departure from Nigeria to South Africa at the Muritala Muhammed International Airport would be the last time I would ever see you. The last time I travelled home for a holiday, I could not hold the tears that rolled my cheeks because of the memory of

where I last saw you. May Allah (s.a.w.) forgives you and my lovely mum, Risikat Ipadeola, who passed on 8 years ago, the highest place in heaven (Jannah al Firdaus). I promise to always keep your good legacies. And to my siblings: Mr. Mutiu, Toheeb, and Lawal Ipadeola, as well as Mrs. Kabirat Adetoro for believing and supporting me in prayers.

RESEARCH OUTPUTS

List of Publications

1. K. I. Ozoemena, S. Musa, R. Modise, **A. K. Ipadeola**, L. Gaolatlhe, S. Peteni, G. Kabongo, Fuel cell-based breath-alcohol sensors: Innovation-hungry old electrochemistry, *Current Opinion in Electrochemistry*, **10**(2018): 82 – 87.
2. **A. K. Ipadeola**, B. Rasmita, S. C. Ray, K. I. Ozoemena. Bimetallic Pd/SnO_2 nanoparticles on metal-organic framework (MOF)-derived carbon as electrocatalyst for ethanol oxidation, *Electrocatalysis*, **10**,4(2019): 366 – 380.
3. **A. K. Ipadeola**, K. I. Ozoemena, Alkaline water-splitting reactions over Pd/Co-MOF-derived carbon obtained via microwave-assisted synthesis, *RSC Advances*, **10**,29(2020): 17359 – 17368.
4. T. P. Mofokeng[1], **A. K. Ipadeola[1]**, Z. N. Tetana, K. I. Ozoemena. Defect-engineered nanostructured Ni/MOF-derived carbons for efficient aqueous battery-type energy storage device, *ACS Omega*, **5**,32(2020): 20461 – 20472.
5. **A. K. Ipadeola**, N. Z. L. Mathebula, M. V. Pagliaro, H. A. Miller, F. Vizza, V. Davies, Q. Jia, F. Marken, K. I. Ozoemena. Unmasking the latent passivating roles of $Ni(OH)_2$ on the performance of Pd-Ni electrocatalysts for alkaline ethanol fuel cells, *ACS Applied Energy Materials*, **3**,9(2020): 8786 – 8802.
6. **A. K. Ipadeola**, P. V. Mwonga, S. C. Ray, R. R. Maphanga, K. I. Ozoemena, Palladium-Stannic Oxide Interfacial Chemistry Promotes Hydrogen Oxidation Reactions in Alkaline Medium, *ChemEletroChem* (2020), In press, doi: 10.1002/celc.202000952.

7. **A. K. Ipadeola**, P. V. Mwonga, S. C. Ray, R. R. Maphanga, K. I. Ozoemena. Bifunctional Behavior of Pd/Ni Nanocatalysts on MOF-Derived Carbon for Alkaline Water Electrolysis, *Electroanalysis* (2020), in press, doi:10.1002/elan.202060427.
8. P. V. Mwonga, **A. K. Ipadeola**, S. R. Naidoo, A. Quandt, K. I. Ozoemena. Annealing Boost the Supercapacitive Properties of Molybdenium Disulfide Powder, *Electroanalysis* (2020), in press, doi:10.1002/elan.202060436.

Presentations

1. **A. K. Ipadeola**, K. I. Ozoemena, Bimetallic Pd/SnO_2 nanoparticles on metal-organic frameworks (MOFs)-derived carbon as electrocatalyst for ethanol oxidation. Oral presentation at the 2nd International Workshop on Porous Materials and their Applications (IWPMA–2019) at the Council for Scientific and Industrial Research (CSIR) from 20th – 21st June 2019.
2. O. E Bankole, L. Gaolatlhe, **A. K. Ipadeola**, A. Haruna, K. I. Ozoemena, Co-MOF-derived carbons as promising bifunctional electrocatalysts for oxygen reduction and evolution reactions. Oral presentation at the 2nd International Workshop on Porous Materials and their Applications (IWPMA–2019) at the Council for Scientific and Industrial Research (CSIR) from 20th – 21st June 2019.
3. J. J. Ogada, S. Musa, **A. K. Ipadeola**, H. Miller, F. Vizza, D. Wamwangi, K. I. Ozoemena, Pd/C-CeO_2 as electrocatalyst for alcohol fuel cell. Poster presentation at the Energy Storage and Industry 4.0: Challenges and Prospects at North West, South Africa from 31st July – 2nd August 2019.
4. **A. K. Ipadeola**, K. I. Ozoemena, Bimetallic Pd/SnO_2 nanoparticles on metal-organic frameworks (MOFs)-derived carbon as electrocatalyst for ethanol fuel cell.

Poster presentation at the Energy Storage and Industry 4.0: Challenges and Prospects at North West, South Africa from 31st July – 2nd August 2019.

5. O. E Bankole, L. Gaolatlhe, **A. K. Ipadeola**, A. Haruna, K. I. Ozoemena, Co-MOF-derived carbons as promising cathode electrocatalysts for rechargeable zinc-air batteries, at the Energy Storage and Industry 4.0: Challenges and Prospects at North West, South Africa from 31st July – 2nd August 2019.
6. **A. K. Ipadeola**, K. I. Ozoemena, Bimetallic Pd/SnO_2 nanoparticles on metal-organic frameworks (MOFs)-derived carbon as electrocatalyst for ethanol fuel cell. Poster presentation at the 70th International Society of Electrochemistry, Durban, South Africa from 4th – 9th August 2019.
7. **A. K. Ipadeola**, K. I. Ozoemena, Bimetallic Pd/SnO_2 nanoparticles on metal-organic frameworks (MOFs)-derived carbon as electrocatalyst for ethanol fuel cell. Poster presentation at the 9th Cross faculty Postgraduate Symposium held at the University of the Witwatersrand, Johannesburg, South Africa from 29 – 30th October 2018.
8. **A. K. Ipadeola**, K. I. Ozoemena, Bimetallic Pd/SnO_2 nanoparticles on metal-organic frameworks (MOFs)-derived carbon as electrocatalyst for ethanol fuel cell. Poster presentation at the 30th International Partnership for Hydrogen and Fuel Cells in the Economy (IPHE) Committee Meetings and Related Events held on 4th December 2018.

PROFESSIONAL ASSOCIATIONS

1. Member, South African Chemical Institute.
2. Member, International Society of Electrochemistry.

AWARDS, HONOURS and PRICES

1. Awarded the prestigious NRF-TWAS African Renaissance Doctoral Scholarship, 2018 – 2020.
2. Postgraduate Merit Award at the University of the Witwatersrand, Johannesburg, South Africa, 2018 – 2020.
3. Paper featured on a cover of ChemElectroChem 2020, European Chemical Societies Publishing, Wiley-VCH.

Junior students' supervision

1. I supervised three Honours students and one research assistant program (RAP) student at the University of the Witwatersrand, Johannesburg, South Africa.

ABSTRACT

This thesis describes the study of palladium (Pd)-based bimetallic electrocatalysts for alkaline direct ethanol fuel cell (ADEFC), fuel cell-based breath alcohol sensor (FCBrAS), alkaline water electrolyzer (AWE) and alkaline membrane fuel cell (AMFC). Metal-organic frameworks (MOFs) are synthesized and used as sacrificial templates for making novel MOF-derived carbons (MOFDCs) as supports for Pd-based electrocatalysts using microwave-assisted synthesis. The electrocatalysts are grouped into two: (i) Pd/SnO_2-based nanostructured electrocatalysts (Pd/MOFDC and Pd/SnO_2/MOFDC); and (ii) Pd/Ni-based nanostructured electrocatalysts comprising Pd on Ni-rich and Ni-starved MOFDC (i.e., Pd/Ni/MOFDC and Pd/AT-Ni/MOFDC, respectively). These Pd-based electrocatalysts are thoroughly examined using various state-of-the-art techniques including Raman, Brunauer-Emmett-Teller (BET) surface area analysis, powder x-ray diffraction (PXRD), x-ray photoelectron spectroscopy (XPS), and synchrotron analysis (XANES and EXAFS). For the electrochemical applications, various techniques were used, including cyclic voltammetry, (CV), chronoamperometry, linear sweep voltammetry (LSV), rotating (ring) disc electrode (RDE and RRDE) experiments and electrochemical impedance spectroscopy (EIS). The key reactions of interests for the two renewable energy fields (i.e., fuel cells and electrolyzers) include the ethanol oxidation reaction (EOR), hydrogen evolution (HER), oxygen evolution (OER), hydrogen oxidation (HOR) and oxygen reduction reactions (ORR). Amongst the electrocatalysts, the Pd/AT-Ni/MOFDC exhibits the best EOR activity and micro-ADEFC (peak power density = 24.49 mW cm^{-2} with 68.0 % voltage retention after 24 h) and delivers good sensitivity and limit of detection for FCBrAS. In the AWE, the Pd/MOFDC exhibits better HER kinetics and energies than the Pd/SnO_2/MOFDC while the Pd/SnO_2/MOFDC displays high OER kinetics than the

Pd/MOFDC. The addition of SnO_2 is detrimental for HER but beneficial for OER. The Pd/Ni/MOFDC has high HER and OER activities than the Pd/AT-Ni/MOFDC, due to the presence of $Ni/Ni(OH)_2$ interface advantageous for overall water electrolysis. However, Pd/MOFDC is the most active material for the HER amongst all the electrocatalysts investigated. In another scenario where HOR and ORR were investigated for the electrocatalysts, the Pd/SnO_2/MOFDC shows extremely high HOR kinetics and stability with low energies than the Pd/MOFDC, but lower ORR kinetics. This result shows that the SnO_2 addition suppresses the ORR activity. Interestingly, the Pd/AT-Ni/MOFDC displayed superior HOR and OER activities than the Pd/Ni/MOFDC. The Pd/AT-Ni/MOFDC shows best performance for HOR, while the Pd/MOFDC is best for ORR. The good performance of these novel Pd-based bimetallic nanostructured electrocatalysts bode well for their potential application in renewable energy conversion technologies, alkaline fuel cells and electrolyzers.

TABLE OF CONTENTS

LIST OF FIGURES

LIST OF TABLES

LIST OF SYMBOLS

Å:	Angstrom
α:	Electron transfer coefficient
α_a:	Anodic electron transfer coefficients
α_c:	Cathodic electron transfer coefficients
θ:	Bragg's angle
τ:	Mean crystallite size
η:	Overpotential
ω:	Rotation speeds
υ:	Scan rates
δ:	Standard deviation
λ:	Wavelength
ΔE_{pp}:	Peak-to-peak separation potential
a:	Tafel constant
b:	Tafel slope
b_a:	Tafel slope anode
b_c:	Tafel slope cathode
B_L:	Levich constant
c_o:	Initial concentration
C_{dl}:	Double-layer capacitance
d:	lattice constants
D:	Diffusion coefficient
E:	Potential
$E_{1/2}$:	Half-wave potential
E_A:	Activation energy

E_{ads}: Binding energy

E_{onset}: Onset potential

E_{pa}: Peak anodic potential

E_{pc}: Peak cathodic potential

ErCi: Irreversible chemical reaction

H_{ads}: Adsorbed hydrogen

i: Current

i_{pa}: Peak anodic current

i_{pc}: Peak cathodic current

i-v: Current-voltage

j: Current density

j_a: Current density anodic

j_c: Current density cathodic

j_f: Current density forward

j_{lim}: Diffusion-limited current density

j_K: Kinetic currents

j_m: Mass current densities

$j_{o,s}$: Exchange current density

$j_{o,m}$: Mass activity

j_r: Current density reversed

k^0: Heterogeneous rate constant

K: Dimensionless shape factor with a value

MW: Microwave

n: Number of electrons

O_L: Lattice oxygen

O_V: Oxygen vacancy

O_S: Oxygen surface coverage

P_m: Peak power density

Q: coulombic charge for PdO reduction

R: Universal gas constant

R_b: Bulk resistance

R_{ct}: Charge transfer resistance

R_{int}: Interfacial resistance

R_s: Solution resistance

z: Ionic charge across a membrane

Z: Impedance

Z_w: Warburg impedance

LIST OF ABBREVIATIONS

AC:	Alternative current
ALD:	Atomic layer deposition
An.:	Anode
ADEFC:	Alkaline direct ethanol fuel cell
AEM:	Anion-exchange membrane
AEMFC:	Anion-exchange membrane fuel cell
AMFC:	Alkaline membrane fuel cells
AT:	Acid-treatment (i.e., chemical-etching)
AT-Ni-MOFDC:	Nickel-deficient nanoparticles on metal-organic framework-derived carbon
AWE:	Alkaline water electrolyzer
BAC:	Breath alcohol concentration
BET:	Brunauer-Emmett-Teller
BNL:	Brookhaven National Laboratory
BPDC:	Biphenyl-4,4'-dicarboxylic acid
B-V:	Butler-Volmer
CA:	Chronoamperometry
Cad.:	Cathode
CB:	Carbon black
CE:	Counter electrode
CN:	Coordination number
Co-MOF:	Cobalt-based metal-organic framework
Co/MOFDC:	Cobalt nanoparticles on metal-organic framework-derived carbon
$Co(NO_3)_2.6H_20$:	Cobalt nitrate hexahydrate

CPE:	Constant phase element
CV:	Cyclic voltammetry
DC:	Direct current
µ-DEFC:	Direct ethanol micro-fuel cell
DFT:	Density functional theory
DMF:	Dimethylformamide
ECD:	Electrochemical deposition
ECSA:	Electrochemical active surface area
EDX:	Elemental dispersive X-ray spectroscopy
EEC:	Electrical equivalent circuits
EIS:	Electrochemical impedance spectroscopy
EMS:	Energy management system
EOR:	Ethanol oxidation reaction
EXAFS:	Extended X-ray absorption fine structure
FC:	Fuel cell
FCBrAS:	Fuel cell-based breath alcohol sensor
FCEV:	Fuel cell electric vehicles
FTIR:	Fourier transform infrared spectroscopy
GCE:	Glassy carbon electrode
GHG:	Greenhouse gas
HER:	Hydrogen evolution reaction
HOR:	Hydrogen oxidation reaction
K-L:	Koutecky-Levich
LO:	Longitudinal
LoD:	Limit of detection

LoQ:	Limit of quantification
LSV:	Linear sweep voltammetry
M:	Co-metal catalysts
MCFC:	Molten carbonate fuel cell
MEA:	Membrane electrode assembly
MOF:	Metal-organic framework
MOFDC:	Metal-organic framework-derived carbon
Ni-MOF:	Nickel-based metal-organic framework
Ni-MOFDC:	Nickel-rich nanoparticles on metal-organic framework-derived carbon
NSLS:	National Synchrotron Light Source
OCV:	Open circuit potential
OER:	Oxygen evolution reaction
ORR:	Oxygen reduction reaction
PEMFC:	Proton exchange membrane fuel cell
Pd/M:	Bimetallic palladium
PTFE:	Polytetrafluoroethylene
RDE:	Rotating disk electrode
rds:	Rate-determining step
RE:	Reference electrode
RHE:	Reversible hydrogen electrode
RRDE:	Rotating ring disk electrode
SEM:	Scanning electron microscopy
SOFC:	Solid oxide fuel cell
TEA:	Triethyleneamine

TEM:	Transmission electron microscopy
TGA:	Thermal gravimetry analysis
TMA:	Trimesic acid
VOC:	Volatile organic compound
WE:	Working electrode
XAS:	X-ray absorption spectroscopy
XANES:	X-ray absorption near-edge spectroscopy
XPS:	X-ray photoelectron spectroscopy
XRD:	X-ray diffraction
ZIF:	Zeolitic imidazolate frameworks

CHAPTER 1

Introduction

1.1 Introduction

The motivation, rationale and objectives of this research project, as well as the study layout of the thesis, are summarized in this chapter.

1.2 Motivation and Rationale

Energy management system (EMS) is an imperative method and tool for the generation and consumption of sustainable energy, which are economical and environmentally friendly. Various renewable energy sources are the only way to go about generating energy in large amounts to meeting the enormous demands in recent times [1], as schematically illustrated in **Figure 1.1**. Amongst major components of this system, fuel cell (FC) technology has a unique energy impact and huge investment when constructed and has emerged as one of the most recommended renewable energy for power generation facilities [2]. The FC technologies could be grouped into different classes based on the electrolytes: (i) proton exchange or polymer electrolyte membrane fuel cells (PEMFCs), where acid electrolytes or its polymer membranes are used; (ii) anion-exchange membrane fuel cells (AEMFCs), where alkaline electrolytes or its polymer membranes are used; (iii) molten carbonate fuel cells (MCFCs), where a mixture of molten carbonate salt and porous chemically inert ceramic lithium

aluminium oxide matrix electrolytes are used; and (iv) solid oxide fuel cells (SOFCs), where hard and non-porous ceramic compounds are used as electrolytes.

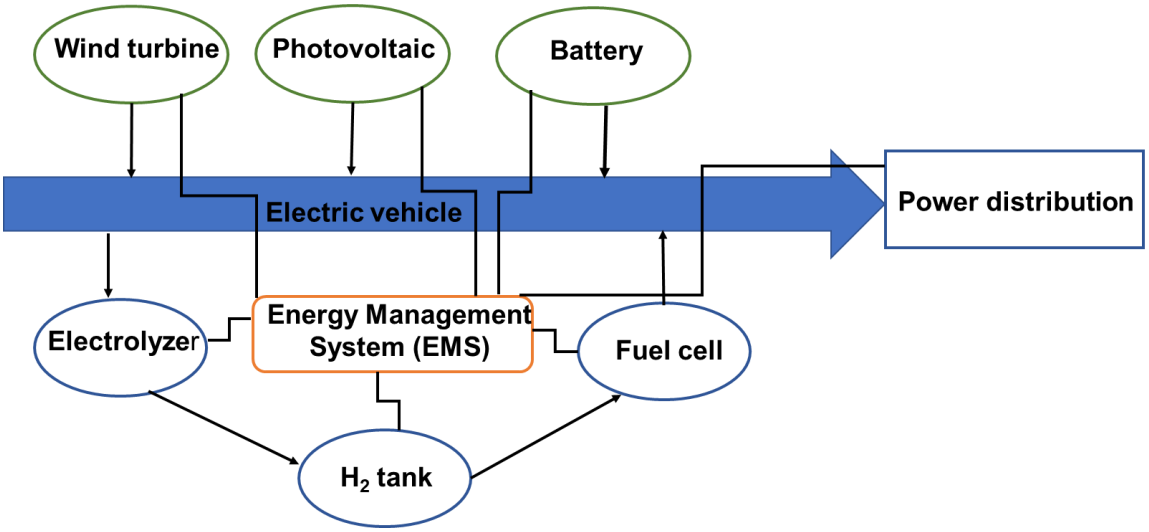

Figure 1.1: Illustration of an energy management system [2]

Amongst these classes, the AEMFC is one of the most advanced FC technologies that have recently attracted excellent attention because of their intriguing features: fast cathodic kinetic, optimum water (H_2O) management mitigating flooding, enhanced electrocatalytic stability and activity, possible use of non-noble metal electrocatalysts for cathodic reaction, to mention but a few. Therefore, this work focuses on the AEMFCs with characteristic improved performances and reduced cost of fabrication. The most used fuels in the FC technologies are hydrogen (H_2) and small molecular weight alcohols like methanol (MeOH), ethanol (EtOH). On this note, the EtOH and H_2 fuels are selectively employed in the fuel cell devices explored in this work because of their low toxicity, and ease of production from abundant resources informed their interest in the following electrochemical devices: alkaline direct ethanol fuel cells (ADEFCs), fuel cell-based breath alcohol sensor (FCBrAS), alkaline water electrolyzer (AWE) and alkaline membrane fuel cells (AMFCs), briefly explained below.

Alkaline direct ethanol fuel cells (ADEFCs) are amongst the most viable, renewable, sustainable and portable electrochemical energy conversion devices developed in recent times because of impressive properties of EtOH fuel such as high theoretical energy density, non-toxic, inexpensive, easy to store and transport, and high-octane rating making them possible to be used in internal combustion engine [3,4]. Also, a large volume of EtOH can be obtained from agricultural and organic municipal wastes. For instance, 90 million litres per year of EtOH are produced globally from agricultural and organic domestic wastes [5]. The ADEFC has proved to be an impressive alternative for fossil fuel technology, as it tends to reduce greenhouse gas (GHG) emission, economical with no negative consequences on climate and health, as well as poses no environmental threat to humanity. The ADEFCs are applicable in portable, stationary, and transportation auxiliary devices.

Fuel cell-based breath alcohol sensor (FCBrAS) is also one of the most promising portable devices for EtOH gas detection from human breath, due to its maximum sensitivity at extremely low EtOH concentration limit, superior selectivity, accuracy, and reproducibility [6,7]. Its major application is found in forensic science such as drunk driving, clinical analysis, environmental science, food and beverage industry [8]. The use of the FCBrAS as an on-site test tool is a good strategy to reduce crime rates, especially drunk driving and other related crimes committed with EtOH intoxication at workplaces. For example, a recent report has it that over 4500 people per annum died on South African roads, due to alcohol impairment while driving [9].

Alkaline water electrolyzer (AWE) is the industrial state-of-the-art technology for producing high purity H_2 fuel, owing to its numerous advantages [10]: (i) relatively cheaper to acid water electrolyzer; (ii) higher durability with facile electrolytes exchangeability and reduced dissolution of electrocatalysts; and (iii) increased H_2 gas purity, as its diffusivity is lower in alkaline condition. In AWE device, high purity hydrogen (H_2) is produced in large quantities, which is the strategy of the hydrogen economy for energy transformation. The H_2 production through the electrochemical water splitting process is a globally effective and efficient approach for clean energy, which mitigates the effect of climate change caused by the GHGs. The H_2 produced is used as fuel for the PEMFCs and AMFCs. Although, oxygen (O_2) gas is equally produced but less important as it is abundant in the air.

Alkaline membrane fuel cells (AMFCs) are emerging power generation technology, which has recently inspired exceptionally good considerations in FC electrocatalysis, due to their unique properties such as [11]: improved cathodic reaction kinetics; diminish corrosion of platinum (Pt) electrocatalyst; (iii) possibility of reduced loading of non-Pt based anode electrocatalysts, and (iv) most favourable H_2O management with reduced flooding. Thus, these properties of the AMFCs make them one of the most important alternative energy to supplement the existing streams of energy supply to meet global energy demands.

Commercialization of the ADEFC, FCBrAS, AWE and AMFC devices have been hindered, as the cost of preparing effective and efficient electrode materials is extremely high and the common electrode material (i.e., Pt) is scarce. Recent strategy to solve this major challenge is the reduced-loading of non-Pt-based electrode

materials for the parameters of concern for a viable development of these devices, which are ethanol oxidation reaction (EOR), hydrogen evolution reaction (HER), oxygen evolution reaction (OER), hydrogen oxidation reaction (HOR) and oxygen reduction reaction (ORR), resulting in reduced cost of fabrication, as the electrocatalysts made up over 40% of the overall cost of FC devices [12]. Most of these parameters: the EOR, HER and HOR are extremely slow, and low utilization of the electrocatalyst due to carbonaceous species poisoning are the major issues for the optimum functioning of these devices because it reduces the active surface area of the electrocatalysts and their overall performances [13,14]. However, nanostructured bimetallic palladium (Pd/M) catalysts deposited on highly conductive porous carbon supports have been amongst the strategies to mitigate these issues and ameliorate the electrocatalysts' activities and cell performances [15,16]. Thus, Pd/M electrocatalysts supported on metal-organic frameworks (MOFs)-derived carbons supports are explored as novel materials for the anodic and/or cathodic reactions of these devices.

The nanostructured Pd electrocatalysts have extensively been studied as a substitute for Pt electrocatalysts with better performance, especially in alkaline environments, involving reduced loading of Pd nanoparticles on different carbon supports such as graphene, carbon black and carbon nanotubes [17,18], but to the best of our knowledge, there are limited reports on the use of novel metal-organic frameworks (MOFs)-derived carbons and/or composite supports. The MOFs are three-dimensional (3D) materials consisting of central metal ions coordinated by a strong bond to the multidentate organic linker and are often used for various catalytic applications because of their unique properties like high internal surface area, tunable structures,

porosity and functionality, as well as strong gas adsorption [19]. The MOFs properties could be tailored for beneficial energy storage and conversion by using them as sacrificial templates via carbonization and/or chemical etching, for the MOFDC production with intriguing characteristics like [20]: low cost of manufacture; inherent high porosity and surface area; good electrical and thermal conductivity; excellent chemical and mechanical stability; ease of heteroatoms functionality to improve electron transports. Moreover, co-metal catalysts (M) like nickel (Ni) and tin (Sn) are expected to improve and stabilize the Pd electrocatalysts by (i) electronic; and (ii) ligand effects [18,21]. Sn and Ni nanomaterials are low-cost and readily abundant materials in the form of cassiterite [22] and garnierite ores [23], respectively. This, therefore, led to the crux of this study, which is to design, synthesize and characterize nanostructured Pd/M (SnO_2, Ni) on MOFDCs and test as novel, reduced-cost and effective electrocatalysts for parameters of concern in the development of the ADEFC, FCBrAS, AWE and AMFC.

In this work, two different MOFs sacrificial templates were systematically synthesized by microwave-assisted methods and then subsequently carbonized and/or chemically etched to produce MOFDCs and/or their composites supports for nanostructured Pd/M (SnO_2 or Ni), which were further used as electrocatalysts for the parameters of concern (EOR, HER, OER, HOR and ORR). Microwave irradiation methods adopted in this study possess characteristics: fast heating rates, saves energy, structural tunability of the MOFs, increased pore size and reduced the nanoparticles to the tune of sub-10 nm [24]. Chemical etching after carbonization of the MOFs helps to fine-tune the physicochemical properties such as improved surface area, electron densities, defects, oxygen vacancies and functionalities of the MOFDCs and composites before

nanostructured Pd deposition toward beneficial electrocatalytic properties [25]. Also, strong oxophilic (co- metal catalysts: Sn, Ni) [26,27] and/or spill-over (co- metal oxide catalysts: SnO_2) [28,29] properties are reported to modulate the electrochemical performances of Pd electrocatalysts, especially for anodic reactions. This led to the objectives of this research work.

1.3 Objectives of the study

The objectives of this research are as follows:

- To synthesize cobalt-based MOF (Co-MOF) and nickel-based MOF (Ni-MOF) sacrificial templates from two distinct organic linkers: biphenyl-4,4'-dicarboxylic acid (BPDC) and 1,3,5-benzenetricarboxylic acid or trimesic acid (TMA), respectively using microwave-assisted synthesis methods. Based on the co-catalysts (M) added to the nanostructured Pd, the electrocatalysts are grouped into two: (i) Pd/SnO_2-based and (ii) Pd/Ni-based electrocatalysts.
- To synthesize cobalt (Co) nanoparticles on MOFDC composites (Co/MOFDC) by carbonization of the as-prepared Co-MOF.
- To synthesize MOFDCs by chemically etching the Co/MOFDC and deposition of SnO_2 nanoparticles to yield SnO_2/MOFDC.
- To synthesize the Pd/SnO_2-based electrocatalysts (Pd/MOFDC and Pd/SnO_2/MOFDC) and those with carbon black (CB) (Pd/CB and Pd/SnO_2/CB) from their precursor materials (MOFDC, SnO_2/MOFDC, CB, SnO_2/CB), using microwave-assisted irradiation.
- To synthesize Ni-rich nanoparticles on MOFDC (Ni/MOFDC) composite by carbonization of the as-prepared Ni-MOF and its chemical etching yield the Ni-deficient nanoparticles on MOFDC (AT-Ni/MOFDC).

- ❖ To synthesize the Pd/Ni-based electrocatalysts (Pd/Ni/MOFDC and Pd/AT-Ni/MOFDC) using microwave-assisted irradiation.
- ❖ To characterize the MOFs' sacrificial templates, MOFDC, composites and electrocatalysts.
- ❖ To test comparative electrochemical activities of the Pd/SnO_2-based electrode materials for the parameters of concern (EOR, HOR, HER, OER, ORR) for the ADEFCs, FCBrAS, AWE and AMFC applications.
- ❖ To test comparative electrochemical activities of the Pd/Ni-based electrode materials for the parameters of concern (EOR, HOR, HER, OER, ORR) for the ADEFCs, FCBrAS, AWE and AMFC applications.

1.4 Outline of the thesis

Chapter 1 (Introduction): This is the introductory chapter of the thesis that explains the motivation, rationale and objectives of this study, as well as illustrates the synopsis of the thesis.

Chapter 2 (Literature review): This chapter reviews recent literature that explains developmental trends for the ADEFC, FCBrAS, AWE and AMFC, their mode of operations and application, electrode materials and their synthetic approaches, and description of electrochemical techniques employed in this study.

Chapter 3 (Experimental methods): This chapter explains, illustrates and demonstrates all the experimental methods for the physical characterization and electrochemical measurements employed in this study.

Chapter 4 (Results and Discussion): This chapter separately reports the microwave-assisted synthesis, physicochemical properties of the Pd/SnO_2- and Pd/Ni-based electrocatalysts and discusses their performance toward the EOR (half-cell reaction)

and alkaline direct ethanol micro-fuel cell (μ-ADEFC, full cell reaction). Then, comparative electrochemical activities of electrocatalysts for the EOR and μ-ADEFC with literature are presented.

Chapter 5 (Results and Discussion): This chapter discusses the electrochemical behavior of the electrocatalysis in Ferri/ferrocyanide ($[Fe(CN)_6]^{4-}$/$[Fe(CN)_6]3^-$) redox probe and the best material is tested for the FCBrAS.

Chapter 6 (Results and Discussion): This chapter separately presents and discusses the results obtained for the Pd/SnO_2- and Pd/Ni-based electrode materials for the AWE. Hence, comparative alkaline HER and OER performances of the Pd/MOFDC, Pd/SnO_2/MOFDC and Pd/CB are reported, as well as those of the Pd/Ni/MOFDC and Pd/AT-Ni/MOFDC electrocatalysts.

Chapter 7 (Results and Discussion): This chapter separately reports and discusses the results obtained from comparative HOR and ORR performances on the Pd/SnO_2- and Pd/Ni-based electrode materials for the AMFCs.

Chapter 8 (General conclusions and future works): This chapter presents the conclusions made from all results obtained in this study with appropriate recommendations for future works.

1.5 References

[1] M. S. H. Nizami, A. Haque, P. H. Nguyen, M. J. Hossain, *Energy*, **188**,1(2019): 116104.

[2] P. J. Hall, E. J. Bain, *Energy Policy*, **36**,12(2008): 4352–4355.

[3] K.I. Ozoemena, *RSC Advance*, **6**(2016): 89523–89550.

[4] R. Othman, A. L. Dicks, Z. Zhu, *International Journal of Hydrogen Energy*,**37**,1(2012): 357–372.

[5] S. P. S. Badwal, S. Giddey, A. Kulkarni, J. Goel, S. Basu, *Applied Energy*, **145**(2015): 80–103.

[6] G. Jiang, M. Goledzinowski, F. J. E. Comeau, H. Zarrin, G. Lui, J. Lenos, A. Veileux, G. Liu, J. Zhang, S. Hemmati, J. Qiao, *Advanced Functional Materials*, **26**,11(2016): 1729–1736.

[7] G. Fine, L. Cavanagh, A. Afonja, R. Binions, *Sensors*, **10**,6(2010): 5469–5502.

[8] K. I. Ozoemena, S. Musa, R. Modise, A. K. Ipadeola, L. Gaolatlhe, S. Peteni, G. Kabongo, *Current Opinions in Electrochemistry*, **10**(2018): 82–87.

[9] E. T. Busayo, A. A. Oyelana, *Ethno Med*, **12**,1(2018): 10–16.

[10] M. Schalenbach, A. R. Zeradjanin, O. Kasian, S. Cherevko, K. J. J. Mayrhofer, *International Journal of Electrochemical Science*, **13**(2018): 1173–1226.

[11] Z. F. Pan, L. An, T. S. Zhao, Z. K. Tang, *Progress in Energy and Combustion Science*, **66**(2018): 141–175.

[12] S. T. Thompson, D. Papageorgopoulos, *Nature Catalysis*, **2**(2019): 558–561.

[13] C. Lamy, S. Rousseau, E. M. Belgsir, C. Coutanceau, J. M. Leger, *Electrochimica Acta*, **49**,22-23(2004): 3901–3908.

[14] Y. Morimoto, E. B. Yeager, *Journal of Electroanalytical Chemistry*, **441**,1-2, (1998): 77–81.

[15] R. M. Antoniassi, A. N. Oliveira, M. Linardi, E. V. Spinace, *International Journal of Hydrogen Energy*, **38**,27(2013): 12069–12077.

[16] H. F. Wang, Z. P. Liu, *Journal of the American Chemical Society*, **130**,33(2008): 10996–11004.

[17] A. E. Fahim, R. M. Abdel-Hameed, N. K. Allam, *New Journal of Chemistry*, **42**,8(2018): 6144–6160.

[18] Y. Zhao, X. Yang, J. Tian, F. Wang, L. Zhan, *International Journal of Hydrogen Energy*, **35**,8(2010): 3249–3257.

[19] K. Leus, I. Muylaert, V. V. Speybroeck, G. B. Marin, P. V. DerVoort, *Studies in Surface Science and Catalysis,* **175**(2010): 329–332.

[20] M. Zhao, S. Ou, C. D. Wu, *Accounts of Chemical Research*, **47**,4(2014): 1199–1207.

[21] R. Awasthi, R. N. Singh, *International Journal of Hydrogen Energy*, **37**,3(2012) 2103–2110.

[22] S. Parimala, S. C. Selin, A. Gnanamani, A. B. Mandal, *Current Research in Chemistry*, 4(3)(2012): 60–67.

[23] S. De, J. Zhang, R. Luque, N. Yan, *Energy and Environment Science*, 9,11(2016): 3314–3347.

[24] O. O. Fashedemi, B. Julies, K. I. Ozoemena, *Chemical Communication*, **49**,20(2013): 2034–2036.

[25] A. K. Ipadeola, K. I. Ozoemena, *RSC Advances*, **10**,29(2020): 17359–17368.

[26] S. A. Park, E. K. Lee, H. Song, Y. T. Kim, *Scientific Reports*, **5**(2015): 13552.

[27] A. K. Ipadeola, R. Barik, S. C. Ray, K. I. Ozoemena, *Electrocatalysis*, **10**,4(2018), 366–380.

[28] P. Y. Lin, M. Meng, J. J. Yuan, S. M. Yu, Y. L. Fu, *Studies in Surface Science and Catalysis*, **112**(1997): 201–210.

[29] R. Sasikala, S. K. Kulshreshtha, *Journal of Thermal Analysis and Calorimetry*, **78**(2004): 723–729.

CHAPTER 2

Literature Review

2.1 Introduction

This chapter discusses the backgrounds, working principles and applications of alkaline direct ethanol fuel cell (ADEFC), fuel cell-based breath alcohol sensor (FCBrAS), alkaline water electrolyzer (AWE) and alkaline membrane fuel cells (AMFCs). The major drawbacks and possible solutions to preparing reduced-cost and effective nano-electrocatalysts with different methods of synthesis, which is the major driving force for the parameters of concern for a viable development of the devices, as reported in the literature. Conclusive reviews on the reduced-cost electrocatalysts without compromise on the performances of the devices are elucidated, as well as electrochemical techniques employed to probe the performance of the nano-electrocatalysts for the applications.

2.2 Alkaline Direct Ethanol Fuel Cell

2.2.1 Background of Alkaline Direct Ethanol Fuel Cell

The ADEFC is a device that converts the chemical energy of EtOH fuel to electrical energy operating in alkaline conditions. The ADEFCs are more attractive amongst the FC technologies, which are viable substitutes to fossil fuel technologies because the production of large volumes and high purity EtOH fuel from organic matters, particularly agricultural and municipal waste products via fermentation process is easy, renewable and environmentally friendly with no negative consequences on the

climate. Hence, the use of this device for power generation is sustainable, as the EtOH fuel is readily available in large quantities for a continuous supply. About two decades ago, ADEFC was first designed, fabricated, and employed to power Schluckspecht vehicle with output voltage ranges of 20 and 45 V [1]. This innovative idea was put forth by a team of researchers from the University of Applied Science, Offenburg. Subsequently, various prototypes of the ADEFCS were built for mobile phone charging and electrical appliances [2,3].

2.2.2 Working Principle of Alkaline Direct Ethanol Fuel Cell

The state-of-the-art ADEFC uses two Pt electrodes (cathode and anode), which are separated by an anion-exchange membrane (AEM), instead of Nafion® membrane electrode assembly (MEA) in the conventional PEMFCs [4,5] for generating electricity, as illustrated in **Figure 2.1** [6]. Besides the membrane substitute, the operation of the FC systems is similar, which ensues simple reaction mechanisms at the electrodes and electrolyte media involving certain volume of EtOH fuel being pumped in through the anode where it undergoes electrocatalytic EOR to generate protons (H^+s), electrons (e^-s) and several by-products (like acetic acid (major), acetate, acetaldehyde and CO_2), as given in **Equations 2.1 – 2.3**. The cleaving of C-C bonds requires so much energy thereby hampering the complete oxidation to CO_2 (**Equation 2.1**), while the production of the acetic acid is the rate-determining step (rds) for the ADEFC (**Equation 2.3**), as there are abundant of OH^- ions in alkaline conditions migrating to the anode to aid the oxidation of EtOH. Then, the H^+s and e^-s generated at the anode compartment migrate through the AEM and external circuit, respectively to the cathode, where O_2 from the air is being reduced (ORR), either directly or serially to produce H_2O, as given in **Equations 2.4 – 2.6**. The reactions occur concurrently as

the generated e-s correlate with electric current for power generation. The overall reaction is governed by the Nernst equation, which helps to deduce the ideal reversible potential and the functioning of the device [7]. In AEMFC, the cathode reaction (ORR) is not a serious problem because it can easily be electrocatalytically driven by transition metals materials like FeCo/C with an excellent performance [8–10]. However, the EOR is the important parameter of concern for the development of the ADEFC, as it is relatively sluggish thereby requires high loading of noble metal electrocatalysts contributing to the huge cost of fabricating the device.

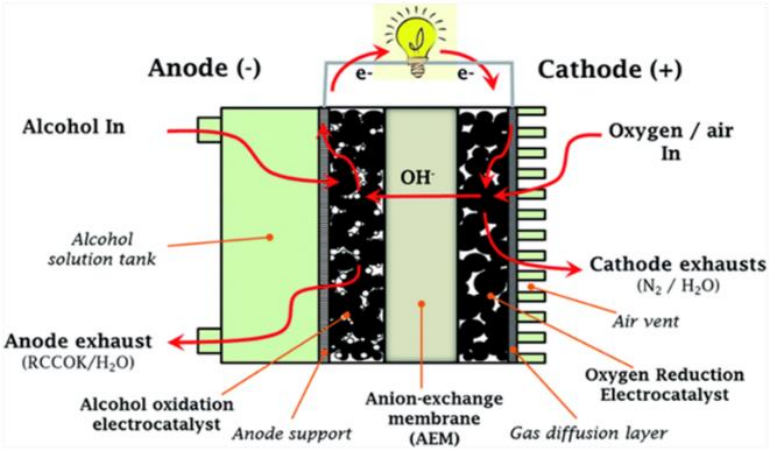

Figure 2.1: Schematic illustration of a typical Alkaline Direct Ethanol Fuel Cell [6]

Anodic reactions

$$CH_3CH_2OH \rightarrow CO_2 + 12e^- + 12H^+ \quad \text{(Total oxidation pathway)} \quad (2.1)$$

$$CH_3CH_2OH \rightarrow CH_3CHO + 2e^- + 12H^+ \quad \text{(Partial oxidation pathways)} \quad (2.2)$$

$$CH_3CH_2OH \rightarrow CH_3COOH + 4e^- + 4H^+ \quad (2.3)$$

Cathodic reactions

$$O_2 + 4e^- + 4H^+ \longrightarrow 2H_2O \quad E^o = 1.230\ V \quad \text{(Direct pathway)} \quad (2.4)$$

$$O_2 + 2e^- + 2H^+ \longrightarrow H_2O_2 \quad E^o = 0.695\ V \quad \text{(Series pathways)} \quad (2.5)$$

$$H_2O_2 + 2e^- + 2H^+ \longrightarrow 2H_2O \quad E^o = 0.695\ V \quad (2.6)$$

2.2.3 Applications of Alkaline Direct Ethanol Fuel Cell

Since the development of the ADEFC, it has been one of the most common FC devices used for various applications: stationary power, portable, backup power generation and transportation, illustrated in **Figure 2.2** and briefly elucidated below.

2.2.3.1 Stationary Power Applications

The ADEFCs are amongst the common FC devices that have been employed as primary power sources if the EtOH fuel is continuously supplied for continuous functioning as supplementary power generation for houses that are not connected to the grid or during an intermittent power outage. The ADEFCs can be connected to the EMS with other energy storage and conversion devices like photovoltaic, batteries, capacitors and wind turbines as either primary or secondary power sources [11], as the standalone systems may need alternative energy during peak periods or unexpected shutdown. Also, when the other energy systems that contribute to the power generation grid is malfunctioning, the ADEFC may serve as an energy generation system. Developed countries like the United States of America, Germany, and Japan have the largest number of stationary fuel cell power stations [12].

2.2.3.2 Portable Power Applications

Portable power FCs are lightweight, durable and miniature energy systems for recharging or powering electronic devices, if the fuel (EtOH) is continuously fed into the system [13]. Unlike energy storage systems (batteries) that are being charged and recharged with either alternative current (AC) or direct current (DC), the ADEFCs do not require charging but continuous supply of EtOH fuel, this put it at advantage for portability [14]. However, rechargeable batteries may not be practicable for certain

portable and military electronic applications due to their heavy nature of not meeting the criteria for portability. Some of the portable devices that can be powered by the FCs are laptops, cellular phones, power tools, military equipment, battery chargers, unattended sensors, and unmanned aerial and underwater vehicles [15].

2.2.3.3 Backup Power Applications

The ADEFC is often used as a power system backup that provides energy when the primary energy source is interrupted. The ADEFC backup devices may be available in different sizes and types with large amounts of the EtOH fuel produced from organic agricultural and municipal wastes, and subsequently supplied continuously, making it viable for commercialization [16]. The backup devices powered by the ADEFC can be used in computer systems, manufacturing facilities, homes and utility substations [17,18].

2.2.3.4 Transportation Applications

The use of the ADEFC for transportation applications is still at developmental infancy because of its relatively high cost of infrastructural requirements but massive efforts are ongoing to reduce its cost to serve as next-generation transportation auxiliary device [19]. Thus, the ADEFC could be used in various transportation applications like automobiles, buses, utility vehicles, scooters and bicycles, as explained subsequently.

2.2.3.4.1 Automobiles

For few decades, many automobile manufacturing companies have been developing and exploring the FC technology for the next-generation FC type of vehicles because the fuel could be produced from local agricultural and municipal wastes in large

quantities, easily be stored and transported, coupled with characteristic CO_2 neutrality [1]. A typical EtOH automobile vehicle operates at temperatures between 60 and 80 ºC and when a polymer membrane is used at an optimum operating temperature of 80 ºC, excellent performance for non-Pt-based electrocatalysts is obtained [20]. Hence, the ADEFC could be connected to automobiles to serve one or more of the followings:

- ❖ As a start-up device that provides all the required power for the automobile engines.
- ❖ Continuously supply a fixed amount of power to the automobile engine for acceleration.
- ❖ As a secondary power source when the primary power source is interrupted or shut down.

As of half a decade ago, very few fuel cell electric vehicles (FCEV) have been commercialized, sold and driven beyond 4,800,000 km (3,000,000 miles) with more than 27,000 EtOH refueling and being refueled at every 314 miles [21]. The United States Department of Energy's fuel cell technology program in 2011 has previously achieved FC and vehicle efficiencies ranges of 53 – 59 and 42 – 53 %, respectively [22] and durability way above 120,000 km (75,000 miles) with less than 10 % degradation [23]. Many recent efforts are directed toward improving the performance and infrastructural requirements of the FCEV, such that as of 2017, more than 6500 FCEVs have been sold globally [24].

2.2.3.4.2 Buses

In the commercial vehicle market, the FCs have been developed successfully to power buses. Although, the buses have more power requirements, space availability,

operating condition and refueling stations, which are the features that make them differ from the vehicles. However, the frequent stops and starts of the buses make them damage faster than expected. An extremely large amount of EtOH fuel needs to be stored onboard in the wide-area available. The FC buses have been considered beneficial relative to the diesel buses because they are environmentally friendly with no emission of GHGs that is needed in most populous and polluted cities [25]. About 100 FC buses are currently available and functioning globally in developed cities like British Columbia, California, Amsterdam, Barcelona, Hamburg, London, Luxembourg, Madrid, Porto, Reykjavik, Stockholm, and Stuttgart [26].

2.2.3.4.3 Utility Vehicles

The state-of-the-art utility vehicles use lead-acid batteries that require frequent maintenance, charging and recharging with lead the major component being extremely poisonous, environmentally and climatic inimical. However, FCs are emerging technology competing for the replacement of lead-acid battery and have been successfully developed and used in utility vehicles in the last decade [27]. Development of the FC utility vehicle has indicated that they have lower operating costs, reduced maintenance, lower downtime and extended range [28] and can be operated indoor, as no emission is involved. Typical utility vehicles that have been powered by FCs are forklifts, golf carts, lawn maintenance, airport movers, wheelchairs and boats.

2.2.3.4.4 Scooters and Bicycles

Scooters and bicycles are amongst the common transportation media in populous countries and have successfully been powered by FCs, perhaps with EtOH fuel being

continuously supplied. The innovative idea of employing FCs to power scooters and bicycles was first initiated and invented in the early 2000s before it was subsequently developed for automobiles and buses [29]. Powering of the scooters and bicycles with the FCs could enable them to run for 4 h and travel 160 km (100 miles) at a speed of 80 km h^{-1} (50 mph) [30].

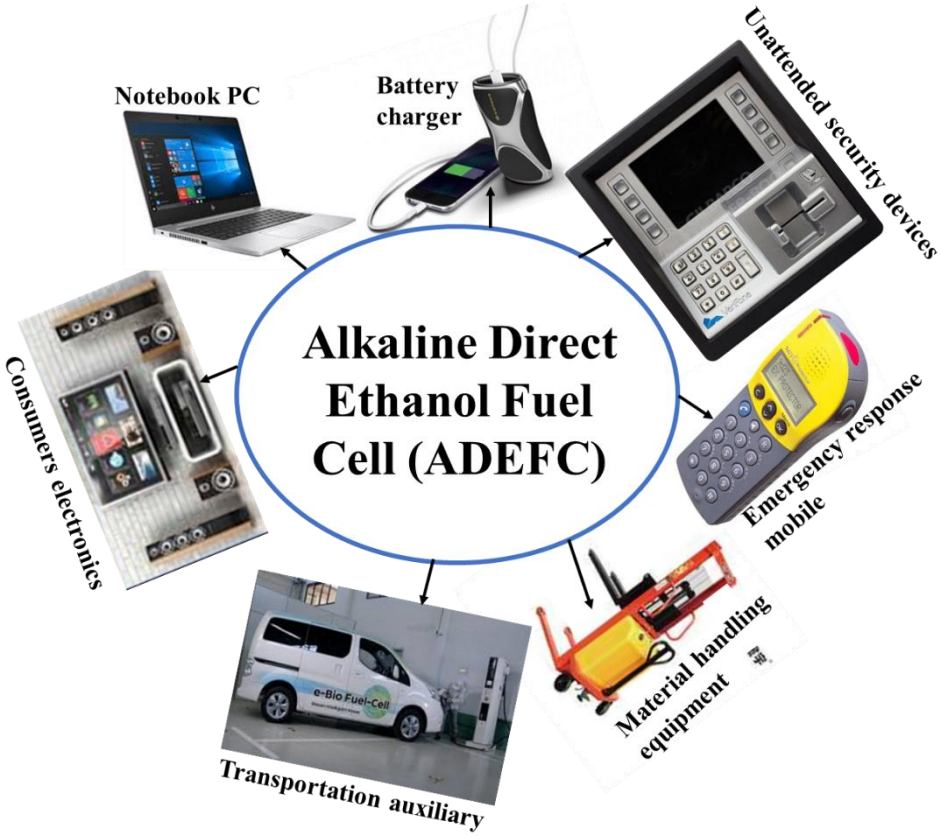

Figure 2.2: Schematic illustration of some devices where the ADEFC is applicable as the power sources

2.3 Fuel Cell-Based Breath Alcohol Sensor

2.3.1 Background of Fuel Cell-Based Breath Alcohol Sensor

The FCBrAS is an electrochemical device that detects EtOH gas from human exhale with impressive characteristics such as portability, fast response, highly accurate, sensitive and selective [31]. F. E. Anstie (1833 – 1874) was the first to possibly observed and detect EtOH in human breath and proposed that a certain amount of

EtOH could be used up daily with no negative consequences to human health [32]. Also in 1831, an American Biochemist, R. N. Harger invented the first practical roadside EtOH breath-detecting device and named it Drunkometer or Breathalyzer. Subsequently in 1979, a Welsh Chemist, Tom Parry Jones invented the first portable FCBrAS (Alcometer), but was approved, manufactured and sold globally by Lion Laboratories. Thereafter, different FCBrAS have been made and sold. In recent years, the FCBrAS has emerged as a replacement for the conventional transdermal testing for an on-spot detection of EtOH because it is convenience, low-cost, rapid and reliable in forensic sciences such as drunk-driving, clinical medicine, environmental science, agriculture, food and beverage industry [33].

2.3.2 Working Principle of Ethanol Gas Fuel Cell Sensor

The FCBrAS imitates the chemistry and operational mode of the ADEFC, comprising of two Pt electrodes (anode and cathode) and separated by a membrane. During the operation of the FCBrAS (**Figure 2.1**), EtOH vapor from the human breath is pumped into the anode compartment rather than the liquid, proceeding with electrocatalytic oxidation, as explained above in **Equations 2.1 – 2.3**. While O_2 from air undergoes complementary ORR to produce H_2O as a by-product, as given in **Equations 2.4 – 2.6**. The e^-s generated from the anodic reaction corresponds to the concentration of EtOH vapor in the breath sample. The state–of–the–art FCBrAS is very expensive, as it operates in an acid electrolyte with extremely high loading of Pt electrodes, the anode and cathode reactions, due to the use of old technology rather than nanotechnology [34]. Also, MEA with a high loading of the Pt has an increased tendency to agglomerate, thereby reducing its electrochemical active surface area

(ECSA) and non-utilization of the Pt catalyst. Another major issue of the FCBrAS is the poisoning of the active sites of the Pt catalyst affecting the cell durability [35].

2.3.3 Applications of Ethanol Gas Fuel Cell Sensor

The FCBrAS is globally applicable in forensic science, as an on-spot testing device for drunk-drivers, clinical testing for alcohol abusers and by employers to keep the employees safe and productive at workplaces. It is also used by law enforcement agencies in agricultural, food and beverages, analytical and environmental industries. In developed countries like the United States of America (USA) and Canada, FCBrAS has been approved as a screening and evidentiary device by parliaments for suspected criminals against established laws. For instance, the USA National Highway Traffic Safety and Administration have been using the FCBrAS as a preliminary screening and evidentiary device to detect if a person is driving with more than 80 mg alcohol per 100 mL of blood by testing only the drivers' breath within the hours of driving [36]. If the alcohol concentration is beyond the above limit, the person can be charged with criminal code [37]. Also, most developed nations, including California and Michigan have logically suggested Consent Laws, where any driver with driver's license would agree to take breathalyzer test if suspected of alcohol abuse by Law enforcement officers.

2.4 Alkaline Water Electrolyzer

2.4.1 Background of Alkaline Water Electrolyzer

The AWE is an old technology that has long been discovered over 200 years ago, with continuous progress [38]. The idea of electrochemical H_2O splitting was first initiated when two gold (Au) wires were dipped into H_2O, leading to gas evolution for electricity

generation, shortly after the discovery of electricity by I. R. Deiman and A. P. van Troostwijk in 1789 [39]. Thereafter, A. Volta invented a voltaic cell that was used for H_2O electrolysis, where H_2 and O_2 gases were evolved [40]. From the inception of the H_2O electrolysis to the present state, tremendous progress has continuously been made, which is necessitated by the high demands of the technology in different industries [41–43]. The discovery of PEM for electricity generation led to the development of the PEM H_2O electrolyzer, although in small–scale level, as the mode of operation of the latter is the reverse of the former [44]. The PEM H_2O electrolyzer has several disadvantages such as [45,46]: (i) extremely costly due to pricey membrane, porous electrode and current collector; and (ii) nondurable. To solve these pitfalls of the PEM H_2O electrolyzer, search for innovative advances birthed the AWE, which is currently used in the industry [47– 49].

The AWE is the state-of-the-art device for producing H_2 and O_2 in the chemical industry with a long history of simplicity, reliability, durability and safety [50]. Owing to recent trends in the hydrogen economy, the AWE is one of the most appropriate methods for its growth without compromise on climate change or posing environmental threats. The AWE operates via two complementary processes, known as the HER and OER, which are the cathodic and anodic reactions, respectively that are driven by the aid electrocatalysts. The electrocatalysts are the most important tools for a viable and effective functioning of the AWE device. Although in alkaline conditions, the OER can be catalysed by non-noble metal catalysts like carbon-based, transition metals because the reaction is relatively more facile, thus reducing the cost of the AWE fabrication. However, HER is extremely sluggish and requires a very active catalyst using Pt electrocatalysts. Thus, the most imperative parameter for AWE is the design and synthesis of efficient and effective electrocatalysts. In recent times, Pd-based

electrocatalysts have drawn so much attention for the AWE because of their superior electrocatalytic performance relative to Pt-based electrocatalysts in alkaline conditions. The fascinating characteristic of Pd-based electrocatalysts informed our choice to explore and discuss its application for the AWE, particularly for the HER with satisfactory performance.

2.4.2 Working Principle of Alkaline Water Electrolyzer

The AWE is characterized by two distinct electrodes separated by a diaphragm that involves the transport of hydroxide (OH^-) ions between the electrodes, as it operates in liquid alkaline electrolyte (i.e., potassium hydroxide (KOH) or sodium hydroxide (NaOH)) [51,52] and splits the gaseous products formed, illustrated in **Figure 2.3**. The operation of the AWE is quite simple where the production and separation of O_2 at anode and H_2 at the cathode from the H_2O when direct current is applied to undergo the OER and HER processes, expressed in **Equations 2.7** and **2.8.** These processes occur with the aid of electrocatalysts, which are non-noble metals like carbon-based or transition metals based-electrocatalysts for the OER and noble metals-based electrocatalysts (like Pt, Pd e.t.c.) for the HER because of its relatively sluggish nature in alkaline environments. These electrodes are separated by the diaphragm, a thin-porous foil (*ca.* 0.50 mm) [53]. The diaphragm creates a little distance between the electrodes, although non-conductive to electrons preventing electric shorts, but allows migration of the OH^- ions produced by the alkaline electrolyte or membrane between the electrodes. The most used diaphragm is Zirfon, which consists of zirconia and polysulfone [54]. Another function of diaphragm is to prevent the mixing of the H_2 and O_2 gases produced at the cathode and anodes, respectively [55].

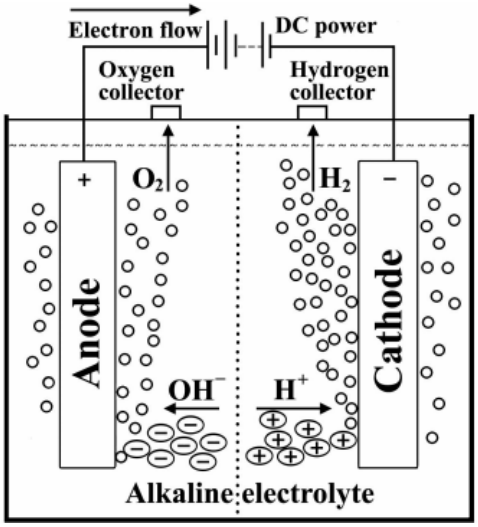

Figure 2.3: Schematic illustration of alkaline water electrolyzer [56]

$$\text{Anodic reaction: } 4OH^- \longrightarrow O_2 + H_2O + 4e^- \quad (2.7)$$

$$\text{Cathodic reaction: } 2H_2O + 2e^- \longrightarrow H_2 + 2OH^- \quad (2.8)$$

2.4.3 Applications of Alkaline Water Electrolyzer

As explained previously, the AWE device is commonly used for H_2 production which serves as a raw material in different industries such as the production of fertilizers for agricultural purpose; precursor material for synthetic fuels, which is an important intermediate chemical for many chemical processes like Fischer-Tropsch synthesis, Haber process and other important fuels (methanol, methane); great innovations in exploring H_2 as important fuel in hydrogen-hybrid vehicles for transportation; heating gas for domestic in cold region worldwide; H_2 is the common fuel use in the gas grid, reducing the evolution of GHGs that could cause global warming and climate change; and also H_2 fuel in the PEMFC and AMFC for electricity generation, which adds up to other renewable energy in the universal electric grid or the EMS [57]. The various applications of the H_2 gas are illustrated in **Figure 2.4**. Although, the most commonly available FC type used for backup power applications is the PEMFC with compressed

H_2 fuel. The AWE is an excellent option for a backup power system, as it produces H_2 gas immediately on demand. Also, the AWE could be employed with electricity generated from solar panels, wind sources or nuclear sources [58]. The AWE is also employed to produce oxygen for the international space station [59].

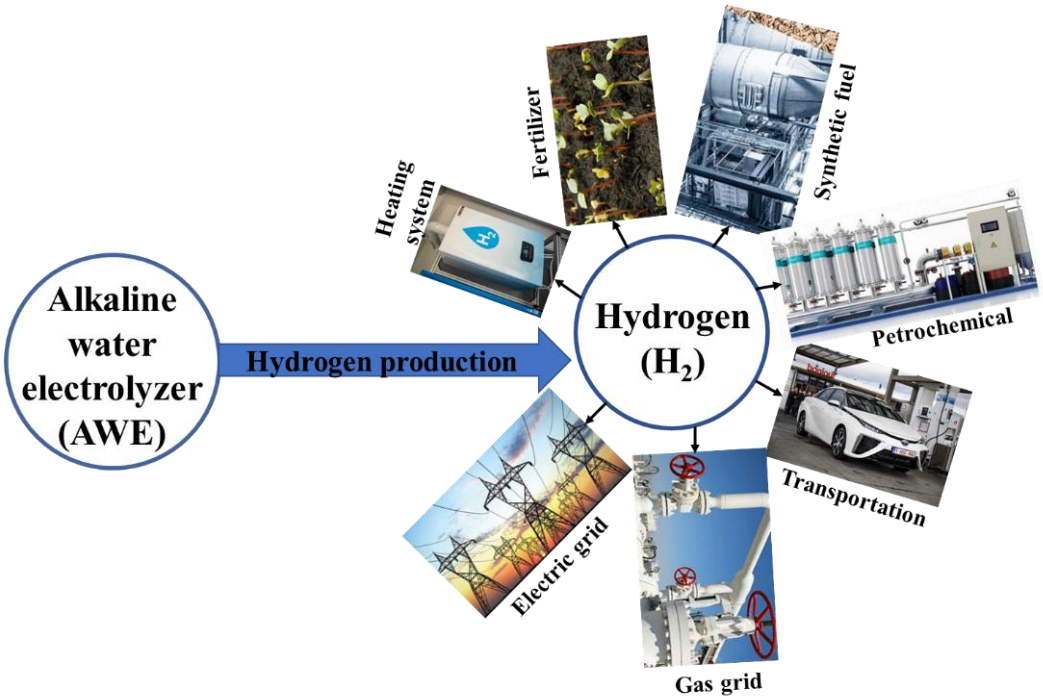

Figure 2.4: Applications of hydrogen produced from alkaline water electrolyzer

2.5 Alkaline Membrane Fuel Cells

2.5.1 Background of Alkaline Membrane Fuel Cells

The most common low-temperature H_2-based FC is the PEMFCs operating in acid conditions, with several challenges such as high loading of highly costly Pt catalysts, making its cost of fabrication extremely high; wearing away of the active sites of the Pt catalysts by leaching, leading to reduced activity and durability; low-utilization of the Pt catalysts caused by poisoning of the intermediate carbonaceous species; the most imperative parameter is the ORR at the cathode with ultralow kinetics. Of the most effective approaches, is to move to the alkaline environments, which birthed the

AMFCs in the early 2000s [60], as it has high tendency to solve several of the challenges with the possibility of non-Pt electrocatalyst, reduced-cost of fabrication and improved activity [61] and above all the ORR activity is relatively facile, which could be effectively catalyzed by transition metals and carbon-based materials. These features make the AMFCs attract so much attention, as it exhibits better performances and cost-effectiveness [62] and are currently the focus in the FC technology [63]. However, the major issues for the viable fabrication of the AMFCs are: (i) the extremely sluggish HOR at the anode, which is a second-order of magnitudes lower than that of the PEMFCs [64]; and (ii) availability of highly conductive AEMs, unlike the highly conductive MEA with Nafion. Although great achievements have been made for highly conductive AEMs in the past decade, as reviewed recently based on quaternary ammonium pendant functional groups [65]. In the advancement of the former, Pd electrocatalysts were explored and have recently proved to exhibit improved HOR performance with comparable and surpassing activities to their Pt counterparts [66,67]. Thus, Pd electrocatalysts were synthesized and explored for the HOR and ORR in this work.

2.5.2 Working Principle of Alkaline Membrane Fuel Cells

The AMFCs are like the PEMFCs, but only differ in the medium of operation. The AMFCs (**Figure 2.5**) consists of two distinct electrodes (i.e., anode and cathode) that are separated by the AEM. The H_2 fuel is pumped in at the anode, while O_2 from the air and H_2O at the cathode, thereby undergo oxidation and reduction reactions via the HOR and ORR, respectively. The ORR at cathode produces hydroxide (OH^-) ions, which migrate through the electrolyte (AEM) to the anode, where it reacts with the H_2 fuel to yield H_2O and e^-s, as expressed in **Equations 2.9 – 2.10**. The e^-s produced

move through the external circuit to generate electric current, while the by-product (H_2O) is passed out [68].

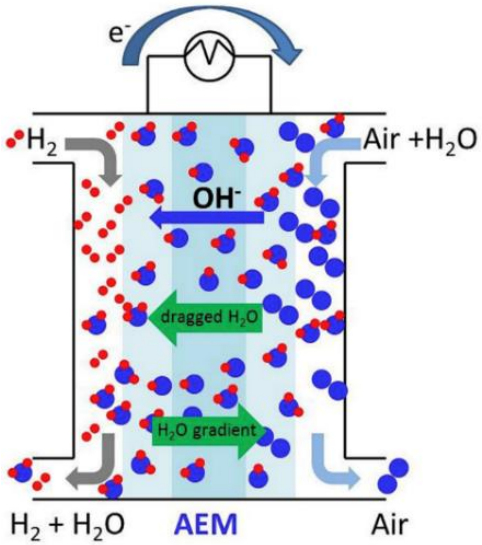

Figure 2.5: Schematic illustration of the alkaline membrane fuel cell [65]

$$\text{Anodic reaction: } H_2 + 2OH^- \longrightarrow 2H_2O + 2e^- \quad (2.9)$$

$$\text{Cathodic reaction: } O_2 + 2H_2O + 4e^- \longrightarrow 4OH^- \quad (2.10)$$

2.5.3 Applications of Alkaline Membrane Fuel Cells

In recent times, the AMFCs have been employed in varieties of applications (**Figure 2.6**) such as power sources for charging some portable devices like laptops, cellular phones, power tools, batteries and stationary devices when connected to the electric grid or EMS as supplementary and emergency power systems for critical areas or used as a grid-independent generator for on-site services; and an automobile is the most interesting application of the AMFCs with tremendous benefits of more power requirements of about 250 kW, although demands operating regimen with frequent starts and stops. Average H_2 fuel for the H_2-vehicle system has been estimated as 15% better than the diesel engine system [45] and are currently being used in

developed cities like Amsterdam, Barcelona, Hamburg, London, Luxembourg, Madrid, Porto, Reykjavik, Stockholm, and Stuttgart [45].

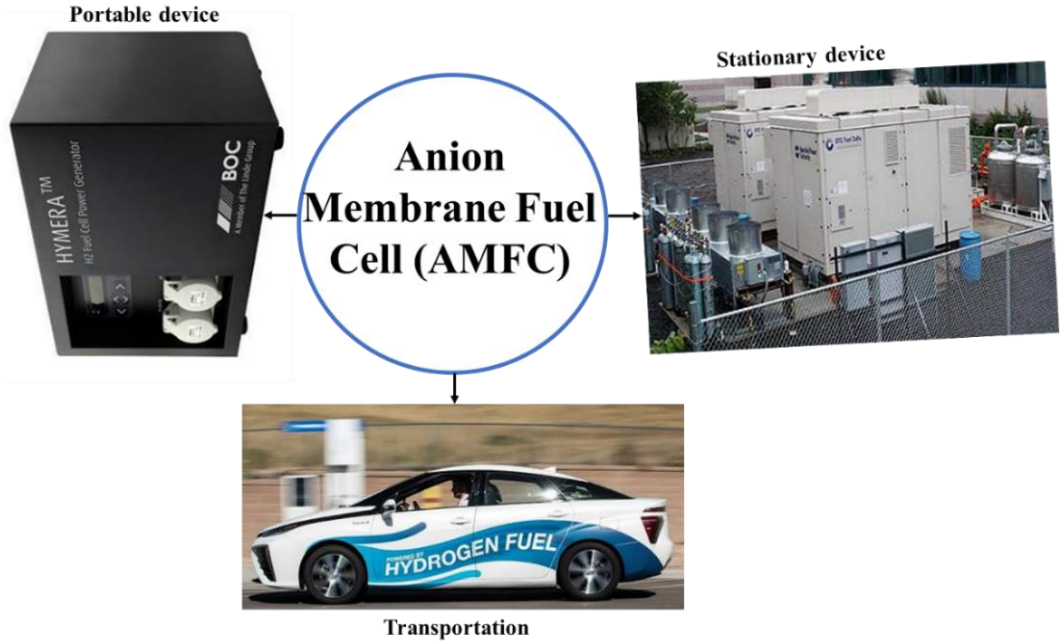

Figure 2.6: Applications of alkaline membrane fuel cell

2.6 Nanostructured Palladium-based Electrocatalysts

The commercially available FC devices are expensive due to the use old technology of bulk Pt electrocatalysts to drive the anodic and cathodic reactions in acidic conditions. The cathodic reaction is the most parameter of concern in these devices, as it is extremely sluggish and necessitated the use of Pt electrocatalysts [69]. Unlike the anodic reaction, which is relatively very fast, about five times more facile than the cathode with very little loading of Pt [70]. Also, the Pt electrocatalyst being very scarce and rarely available are among the challenges of the conventional PEMFCs. The advent of nanotechnology is amongst the strategies employed to reduce the cost of the Pt electrocatalyst and MEA for the fabrication of FC devices [71–73]. The nanotechnology birthed numerous research innovations to reduce the loading of Pt

electrocatalysts (*ca.* 20 %) with various carbon supports that have been reported [74–78]. Although so much improvement in the design and development of reduced-cost Pt electrocatalysts has been made previously and explored with good performances and durability. Tremendous attention is still necessary to make effective and efficient electrocatalysts with reduced costs.

Another alternative strategy employed in FC technologies is a change of media of operation (i.e., from acidic to alkaline media) [50], where the electrocatalysts' performance can be improved. The FC technologies in alkaline media have proved to exhibit impressive characteristics such as [79]: (i) faster reactions kinetics; (ii) possibilities of Pd-based electrocatalysts without compromise on performances; (iii) low anodic and/or cathodic overpotentials; (iv) minimal risks of electrodes corrosion; (v) low risk of carbonaceous species poisoning of the electrocatalyst, which enhances its performances and durability. Also, Pd-based materials have proved to exhibit superior catalytic activities in alkaline environments than Pt-based electrocatalysts [80]. These properties informed the interest of exploring Pd-based materials in alkaline conditions for the electrochemical conversion applications: ADEFC, FCBrAS, AWE and AMFC devices. Thus, Pd-based supported electrocatalysts on novel carbon supports are systematically synthesized and tested for parameters of concern. Although different carbon materials like graphene [81,82], carbon nanotube [83,84], carbon nanofiber [85,86], carbon nitride [87,88], amongst others have been used to support and reduce loading of the Pd electrocatalysts, reports on the use of the carbons derived from MOFs are limited. Moreover, addition of co-metal catalysts (M) such as Co [89,90], Cu [91,92], Ni [93,94], Sn [95,96], Ru [97,98], Ag [99,100], Mn [101,102], Fe [103,104] have been reported to augment the electrocatalytic activities

of the Pd electrocatalysts by ligand and electronic effects with better tolerance to carbonaceous species poisoning in the FC technologies. Interestingly, metal co-catalysts possess oxophilic properties [105,106], while metal oxides co-catalysts have spill-over effects [107,108] in alkaline conditions. The hydroxide promotional properties have been reported to be beneficial for the electrocatalytic performance of noble metals. SnO_2 is a simple, cheap and promising nanosized metal oxide co-metal catalyst that can easily be synthesized in the laboratory from naturally abundant cassiterite ore [109]. While Ni is a modern valuable element largely produced from garnierite ore that is commonly used as catalyst or co-catalyst in energy storage and conversion systems such as hydrogenation, batteries [110–112]. However, there is a tendency for the formation of passive Ni oxides (NiO) or hydroxides during Ni preparation with wet chemistry. The active Ni can easily be cleaned by chemical etching to promote the co-metal catalyst activity of the Ni on the Pd electrocatalyst. The cost-effectiveness and properties of the SnO_2 and Ni informed their choice as co-metal catalysts to Pd electrocatalysts in this work. Hence, novel Pd/M (where M = SnO_2 or Ni) electrocatalysts on MOFDCs were designed, synthesized and explored for the parameters of concern in the FC devices. A systematic approach of first synthesizing novel MOFs and explored as sacrificial templates for making MOFDCs and/or composites. Thereafter, nanostructured Pd was deposited onto the MOFDCs and/or composites.

2.6.1 Metal-Organic Frameworks

The MOFs are structurally constructed from the coordinate covalent bond between metal ions and multidentate organic ligands [113]. A typical example of MOF with Ni

metal and 1,3,5-benzenetricarboxylic acid as an organic linker formed by interchain hydrogen bonds is diagrammatically illustrated in **Figure 2.7**.

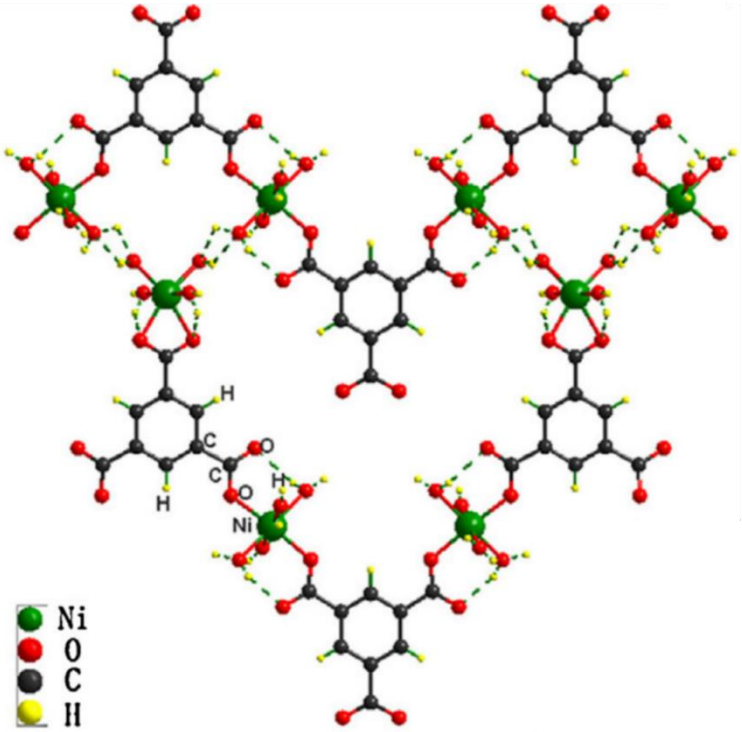

Figure 2.7: A typical 2D sheet motif of Ni-based MOF formed from interchain hydrogen bonds between Ni metal and 1,3,5-benzenetricarboxylic acid [120]

Other common organic linkers or ligands with carboxylates bridging groups are shown in **Figure 2.8**, where the two ligands (BPDC and TMA) used for the preparation of the MOFs in this work are highlighted in red. Amongst the well-known porous materials, MOFs have garnered interesting attention because of their porosity, which makes selectively diffusion of small molecules into the bulk accessible depending on their shapes and sizes [114]. The architectural formation of the MOFs resulted in open frameworks that indicate unique characteristics of porosity, large surface area and pore volume. The porosity is a result of the long organic linkers that afford enormous storage space and adsorption sites within the MOFs, as well as ease of systematically varying and functionalizing their pore structure [115], which makes it easy to tailor the

structure of the MOFs for variety of applications [116]. Despite the impressive properties of the MOFs, they are conspired with low thermal and electrical conductivities that is the frameworks are unstable to high temperature and heat, as well as poor electrons transport [117–119]. These drawbacks of the MOFs limit their use in electrochemical applications. However, carbonization of MOFs helps to enhance their electron transport, electrical conductivity, thermal stability and other properties beneficial for energy storage and conversion applications.

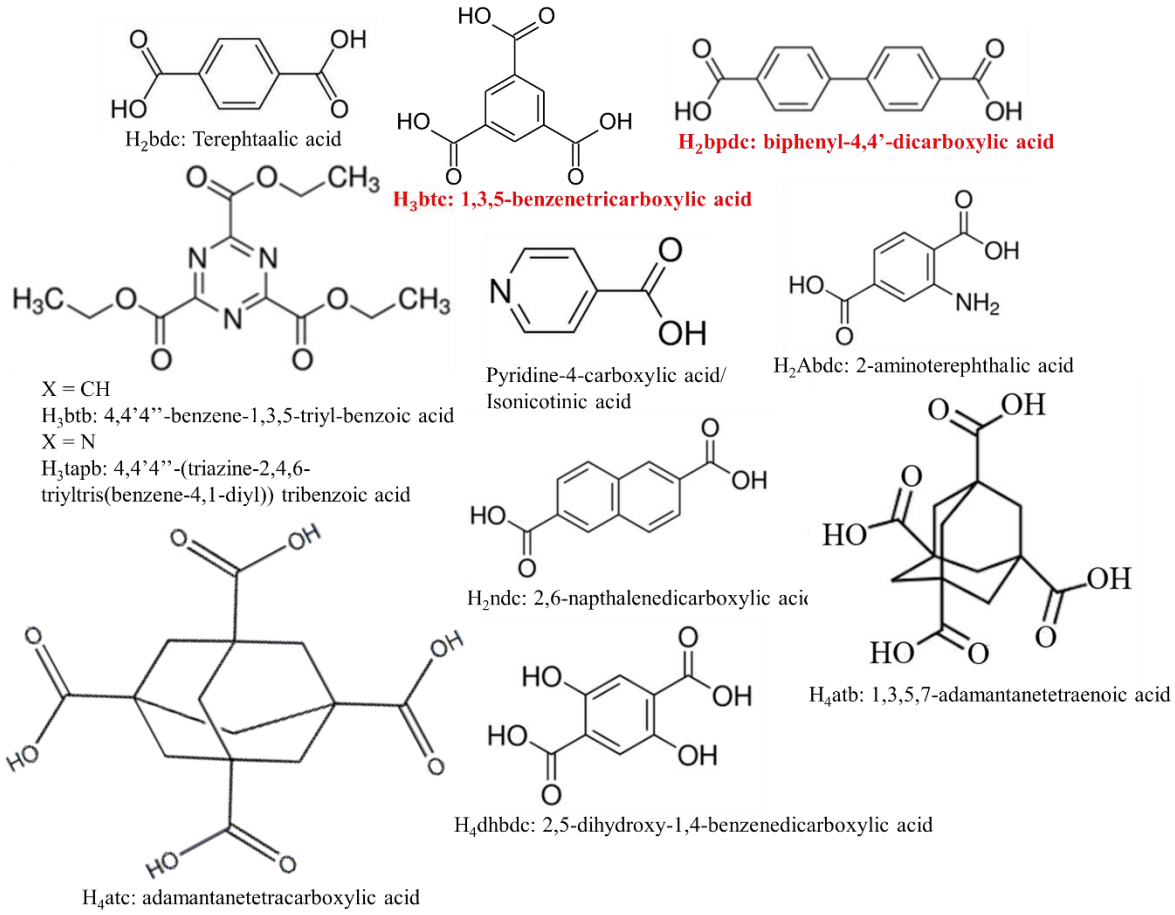

Figure 2.8: Common organic linkers or ligands with carboxylic bridging group

2.6.2 Metal-Organic Frameworks-Derived Carbons and Composites

Addressing these drawbacks, the most effective approach to utilize the intriguing properties of the MOFs and fine-tuning them for electrochemical applications is to

employ the MOFs as sacrificial templates for producing MOFDCs and/or metals supported on MOFDC composites [121,122]. Recently, the MOFs have been used as promising precursor materials for transition metals encapsulated derived carbons in addition to functionalization with heteroatoms [123–125]. The MOFDCs are often made by carbonization or pyrolysis and have proved to exhibit excellent properties such as [126–128]: inherent increased porosity and surface area, good thermal and electrical conductivity, high chemical and mechanical stability and ease of functionalization with hetero-atoms, which were employed for different catalytic applications. For instance, Wang and co-workers [129] adopted a strategy of synthesizing MOFDCs with improved physical properties as high-performance electrodes for an energy storage system. Also, the electrical conductivity of modified ZIF-8-MOFs-derived N-doped porous carbon from the precursor MOFs was improved [130]. These impressive properties are expected in the MOFDCs and/or its composites and informed their choice in this work.

2.6.3 Bimetallic Pd/M Electrocatalysts on Metal-Organic Frameworks-Derived Carbons

As explained previously, Pd electrocatalysts have high potential to completely substitute the Pt electrocatalyst. In recent years, the Pd electrocatalysts have been explored for different electrochemical applications such as FCs, EtOH gas sensing, and H_2O electrolyzers in alkaline conditions with enhanced electrocatalytic performances, stability and durability compared to the Pt electrocatalysts [131]. Thus, Pd/M electrocatalysts are employed for the different parameters of concern (EOR, HOR, HER, OER and ORR) for various applications like ADEFC, FCBrAS, AWE and AMFC, diagrammatically illustrated in **Figure 2.9**. These reasons geared the

numerous attentions to develop more active, efficient and reduced-cost Pd-based electrocatalysts for these reactions. The advent of nanotechnology has made it easy to design and synthesize novel Pd-based electrocatalysts with these befitting characteristics by depositing nanostructured Pd onto the novel MOF-derived carbons (MOFDCs) or composites. Moreover, co-metal catalysts like SnO_2 and Ni have been considered to improve the electrocatalytic performances, mitigate carbonaceous species poisoning and stabilize the Pd electrocatalysts [132–135]. Hence, novel bimetallic Pd/M (where M = SnO_2 or Ni) electrocatalysts anchored MOFDC supports were systematically designed, synthesized, characterized and tested for the EOR, HOR, ORR, HER and OER in ADEFC, FCBrAS, AWE and AMFC applications.

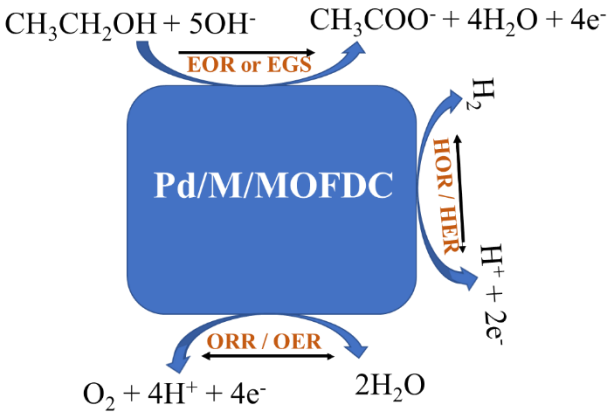

Figure 2.9: Schematic illustration of Pd/M/MOFDC electrocatalysts for parameters of concern in fuel cells and electrolyzers

2.6.4 Synthetic Methods for Preparation and Deposition of Nanostructured Materials

Several synthetic methods have been explored for preparing and depositing nanostructured materials and could be employed for the synthesis of the MOFs and/or nanostructured Pd anchored on MOFDCs or composites. The most common amongst these methods are atomic layer deposition (ALD), electrochemical deposition (ECD),

spray pyrolysis and sol-gel, solvothermal or hydrothermal processes with microwave-assisted, explained below:

2.6.4.1 Atomic Layer Deposition Method

The ALD is the growth of self-imposed film by exposing the chemical species in a layer-by-layer manner. Four major important steps are required in the ALD process, as shown in **Figure 2.10** and explained below:

- ❖ Exposure of metal precursors.
- ❖ The metal precursors, intermediates and by-products are eliminated and purged from the chamber.
- ❖ The exposed metal precursor is then reduced with hetero-atoms like O, N.
- ❖ The precursor materials and by-products molecules are subsequently eliminated or purged from the chamber.

The first stage: self-imposed limitation on the adsorption process of the precursor molecules is the most crucial requirement. This requirement is often satisfied through the linkage of electron-rich hetero-atom species to the metal precursors, which would unavoidably reduce additional adsorption of the metal precursor when the adsorption sites on the monolayer coverage are saturated or passivated. Although the ALD has a couple of benefits for the preparation and deposition of nanostructured materials such as (i) excellent step coverage and conformal deposition on high aspect ratio structure, due to its sequential and self-limiting surface reaction process [136]; (ii) possibility of obtaining high-quality materials at low processing temperature; (iii) ability to reproduce excellently and produce multilayer nanostructured materials in a continuous process; and (iv) possibility of interface modification is allowed because it tends to produce sharp interfaces and superlattices. However, it has the following

limitations: (i) lack of speed leading to only small fraction of the crystal that is deposited in a single cycle, also certain multi-component species could not be grown or deposited by the ALD, as it is not economical; and (ii) size of the reaction chamber confines the chemical residues from the precursors to the chamber.

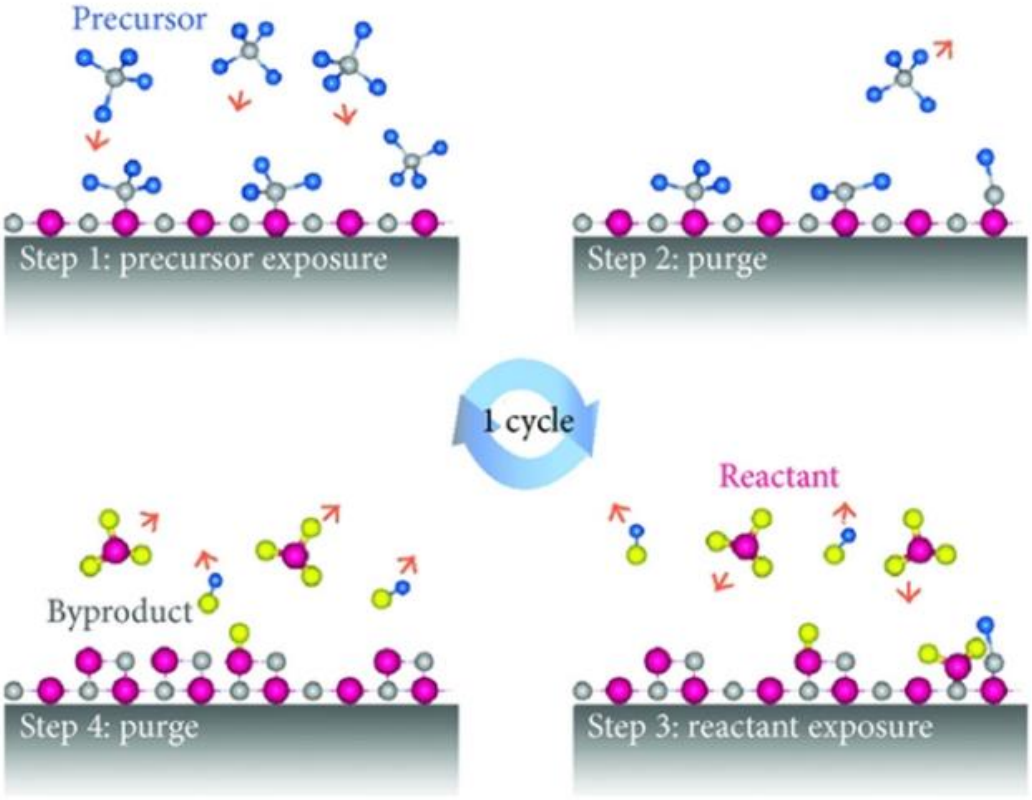

Figure 2.10: Schematic illustration of ALD Method [137]

2.6.4.2 Electrochemical Deposition (ECD) Method

The ECD is a technique of reducing metal precursors or ions from aqueous, organic and fused-salt solutions, as expressed (**Equation 2.11**) and illustrated (**Figure 2.11**).

$$M^{n+}_{solution} + ne^- \longrightarrow M_{lattice} \qquad (2.11)$$

The ECD process could be achieved with two different methods [138]: (i) an electrodeposition method involving external power supply to produce ne^-; and (ii) an electrodeless deposition method involving a reducing agent in solution as e^-s source.

The ECD is among the simplest and most effective strategies for nanostructured fabrication because it tends to customize and control the nanostructured materials' composition and morphology.

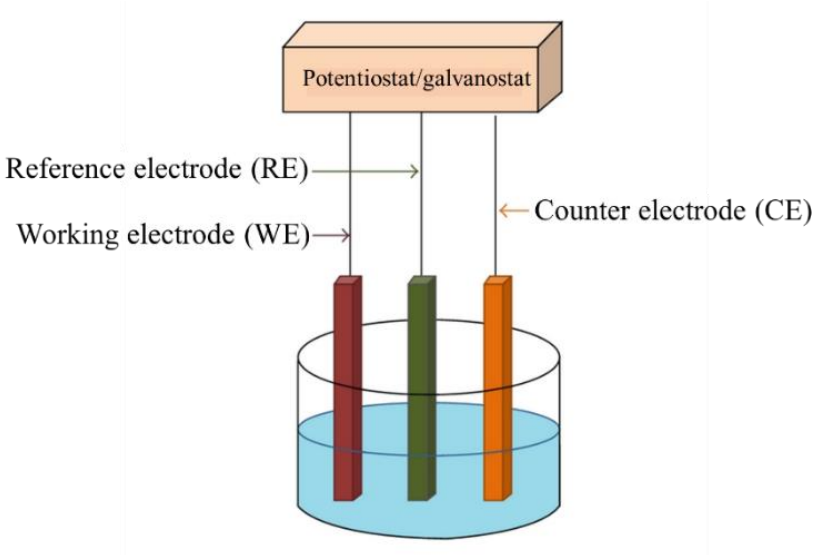

Figure 2.11: Schematic illustration of the ECD system [139]

2.6.4.3 Spray Pyrolysis Method

A spray pyrolysis method is among the most promising film preparation techniques, involving spaying a precursor solution onto a heated glass substrate and deposit a processed film onto it, via a process called pyrosol technique. The mechanism of the spray pyrolysis is that the precursor solution is atomized like little droplets of the solution and then vaporize, and splash/spray on a substrate, leading to the formation of a dried thermally decomposed precipitate [140], as illustrated in **Figure 2.12**. The spray pyrolysis method is based on experience on some variables: solute's concentration, atomization process, temperature, processing time and carrier gases that could influence the expected product. This technique has the following characteristics: high-quality targets thin films on the substrates with no ultra-high vacuum (UHV) system required, low cost, continuously produce the expected product

and the chemical transformation takes place within micron to nano-sized liquid droplets.

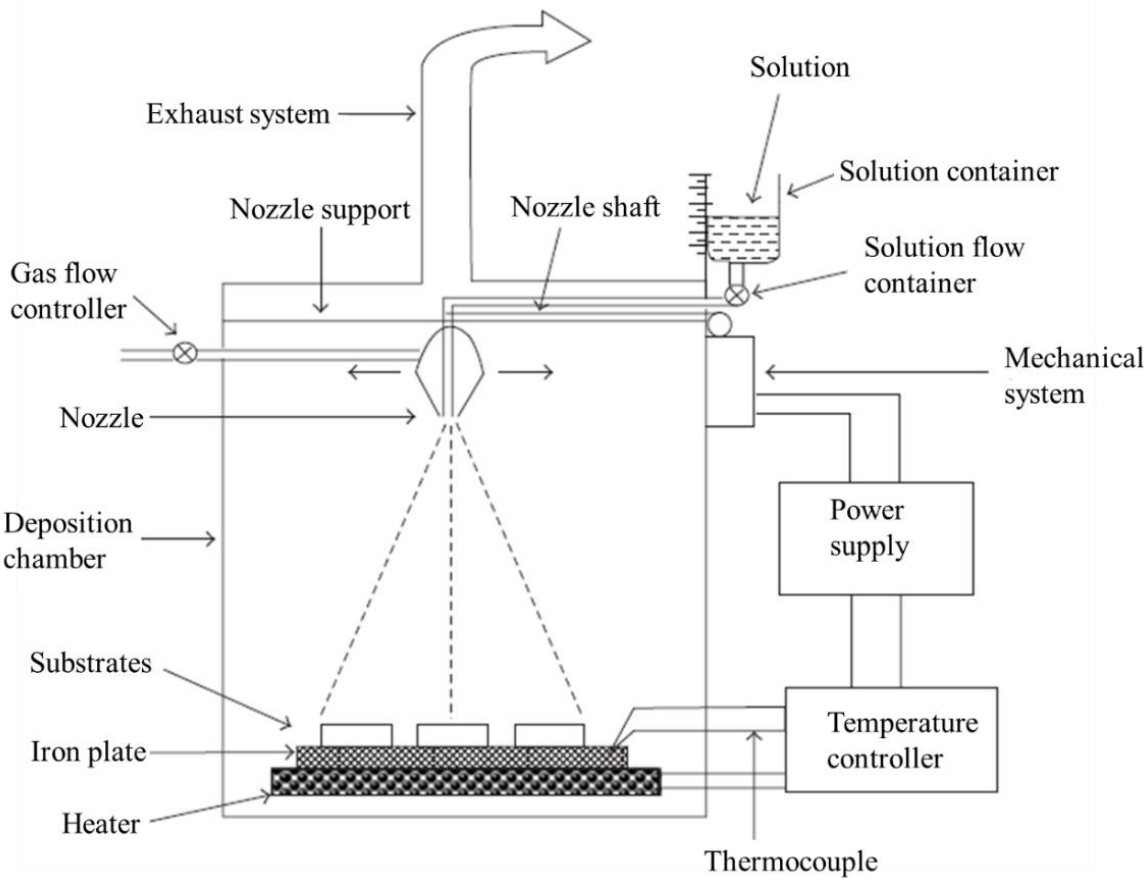

Figure 2.12: Schematic illustration of the spray pyrolysis method [141]

2.6.4.4 Sol-Gel Coating Method

A sol-gel method is a type of wet chemistry employed in the synthesis of nanostructured materials from their chemical solutions with integrated network or gel of precursors for discrete particles or a network of polymers. The most common precursors employed like metal chlorides and alkoxides can easily undergo several hydrolysis and/or polycondensation reactions [142], as the case may be. A typical example of the sol-gel technique is illustrated in **Figure 2.13**. The sol-gel has been considered as a bridge for preparing nanostructured material because the sol

gravitates towards the gel-like diphasic system of liquid and solid, whose morphologies vary from discrete nanoparticles to continuous networks of polymer.

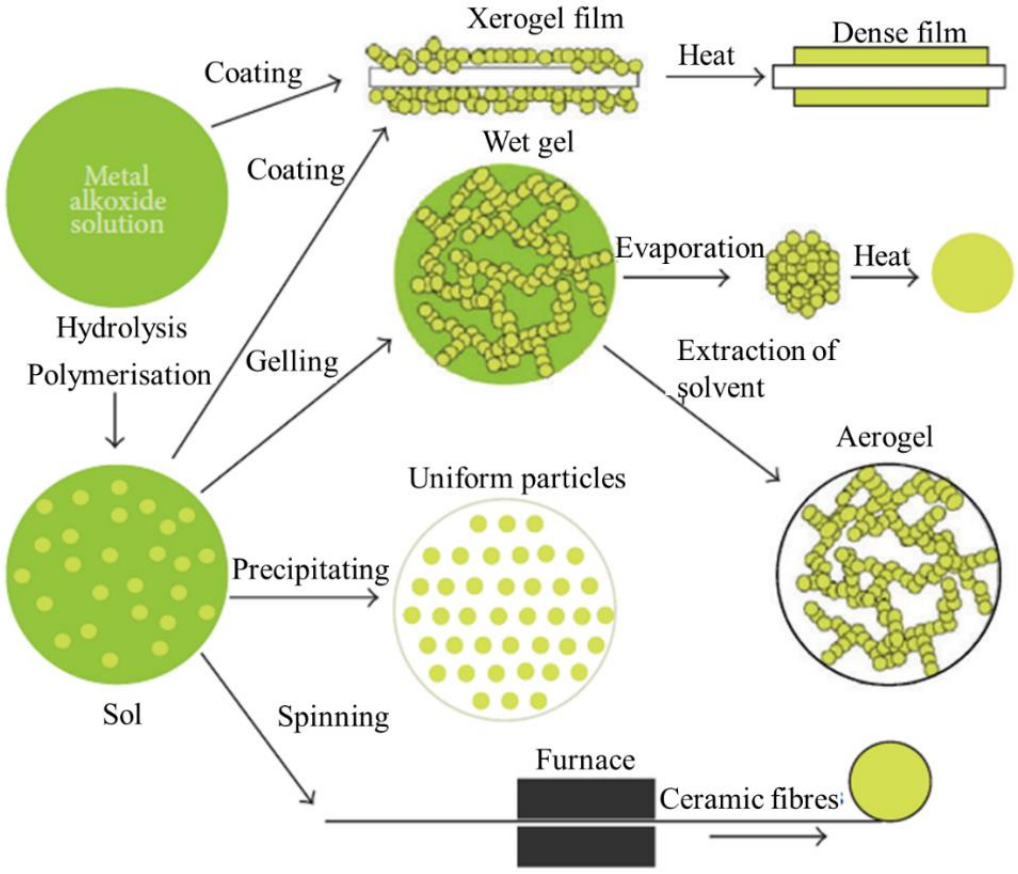

Figure 2.13: Schematic illustration of the sol-gel method [143]

2.6.4.5 Solvothermal or Hydrothermal Synthesis Method

Solvothermal or hydrothermal process is an effective method for the systematic and morphologically controlled preparation of nanostructured materials, which is performed in a tightly sealed Teflon container and heated to a temperature above the boiling point of the solvent (non-aqueous or aqueous) resulting in abrupt increase of the autogenous pressures [144], illustrated in **Figure 2.14**. The process is called solvothermal when the solvent used is non-aqueous, while hydrothermal for aqueous solvent. Increasing temperature and pressure in the solvothermal or hydrothermal process elevates the solubility and reactivity of the reagents, resulting in expected

products [145]. Nuclei formation and growth of the nanostructured are imperative in the process, which could be tuned by changing experimental parameters [146] and thus, influences the properties of the crystals formed. The solvothermal or hydrothermal is commonly employed for controlling the morphology of well-defined nanostructured materials like those of MOFs and nanostructured Pd supported on carbon supports.

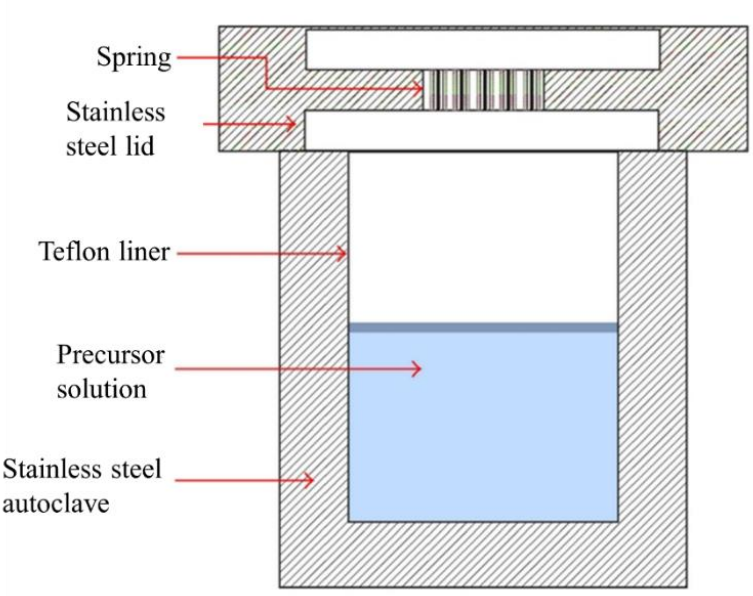

Figure 2.14: Diagrammatic illustration of the solvothermal or hydrothermal process [147]

The three most essential experimental parameters in the solvothermal or hydrothermal process are reaction temperature, solvents properties and capping agents.

- **Reaction Temperature:** The temperature of the reaction has significant role in the properties of expected products during the solvothermal or hydrothermal process. This parameter could vary depending on the nature of the solvent such as viscosity and dielectric constant. A solvent (aqueous) could be more active at high temperatures, while others (organic) are active at low temperatures. Moreover, the solubility of solutes in solvents tend to increase at elevated temperature.

- **Solvents properties:** The solvothermal process could also be influenced by solvents' properties such as polarity, dielectric constant and viscosity. The reaction kinetics, equilibrium and expected products are affected by solvent interaction with precursor reagents, intermediates and final products. Polar solvents such as H_2O, dimethylformamide (DMF) and ethylene glycol (EG) are often used because of their compatibility with most solutes or reagents.
- **Capping Agents:** Facet-specific capping agents are often applied during the preparation of nanostructured materials to aid exposure of their desired facet and thereby enhancing the properties of the expected products during the solvothermal or hydrothermal process. Common examples of capping agents are acids, solvents, surfactants and polymers.

The effectiveness of the solvothermal or hydrothermal process could be traced to: (i) increased solubility of the materials through heating and applied pressure in the set-up to its critical point; (ii) significant improvement to the chemical activities of the precursors with high tendency to replace solid-state synthesis method; (iii) ease to produce novel compounds with characteristic metastable state and specific phase; (iv) simply and precisely control the size, shape distribution and crystallinity of the expected product(s) when appropriate experimental parameters are used; and (v) obtaining substances with low melting point and high vapour pressure. Despite these advantages, there are few drawbacks such as: (i) need of expensive autoclave reactor; (ii) safety issue associated with its usage (high temperature and pressure) during chemical reactions; (iii) very long reaction time, it may take 12 h and above; and (iv) impossible to observe reaction intermediates [148,149]. These drawbacks of the autoclave paves way for the use of microwave, as a viable substitute during

solvothermal or hydrothermal process because the microwave-assisted process is uniform, rapid and volumetric heating [150–152].

2.6.4.5.1 Microwave-Assisted Solvothermal Method

The microwave-assisted synthesis method operates on the underlying condition of aligning dipoles of the precursor samples with an external field through excitation produced by microwave electromagnetic irradiation. Unlike the conventional heating process using autoclave which progresses from outward to inward, microwave-assisted heating progresses from inward to outward uniformly, as illustrated in **Figure 2.15**. The microwave-assisted method is adopted in this work because of its numerous advantages: (i) the synthesis process could be easily tuned to produce desired nanoparticles sizes and shapes with high yields; (ii) orientation alignment of the sample's molecules by electric field leads to internal heat production that aids to fast tract the reaction process and reduces normal energy required; (iii) homogeneous heating of the sample from the center spreading outwards; and (iv) the reaction time is extremely reduced; and (v) magnetic and electric properties of the samples could be controlled through jiggling in experimental measures [153].

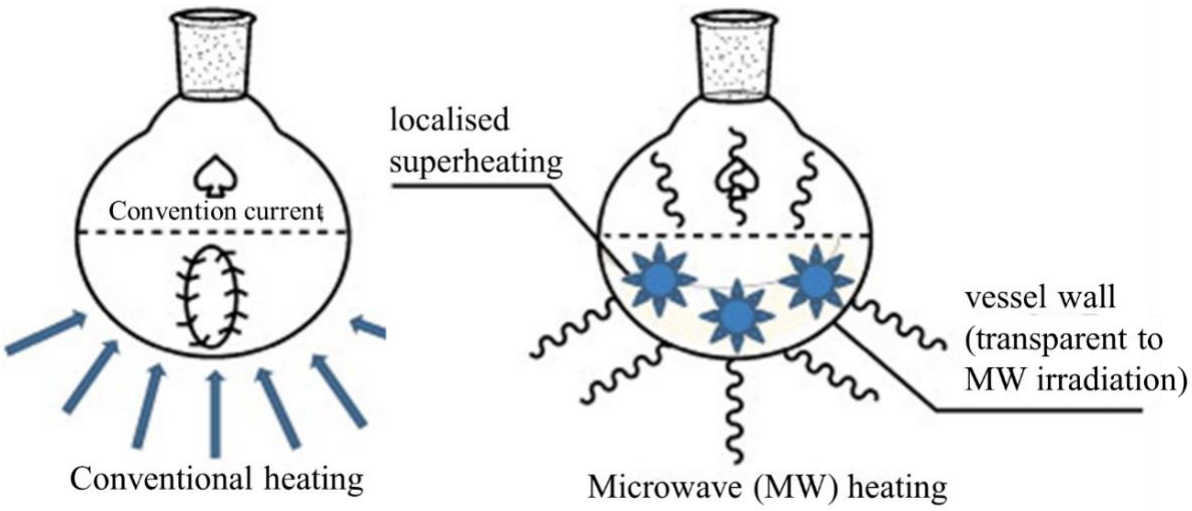

Figure 2.15: Comparing the conventional and microwave-assisted heating [154]

The microwave-assisted method has been effective for preparation of nanostructured materials with a characteristic high degree of crystallinity and mono dispersion [155–157], particularly for top-down of nanostructured Pd electrocatalysts to sub-10 nanosized [147]. Thus, the microwave irradiation is employed to aid the solvothermal process with the polar solvents: DMF and EG because of their good interaction with other reagents, as well as excellent microwave radiation absorption.

2.7 Electrochemical Characterization of the Electrocatalysts

The as-synthesized Pd/M electrocatalysts are tested for the EOR, HOR, HER, ORR and OER using different electrochemical techniques like cyclic voltammetry (CV), linear sweep voltammetry (LSV), chronoamperometry (CA) and electrochemical impedance spectroscopy (EIS).

2.7.1 Cyclic Voltammetry (CV)

The CV is a standard electrochemistry tool and an important potentiodynamic technique employed to determine redox potential windows for an electroactive species in energy storage and conversion devices [159]. The CV technique is performed in an electrolytic cell, which consists of a working electrode (WE), a reference electrode (RE), a counter electrode (CE) and supporting electrolyte. The electrodes connected to potentiostat and signals (current-potential converter) are displayed on the screen on a computer (data acquisition system). The electrochemical signature displayed on the readout is what is happening on the WE/electrolyte interface and its redox potentials range could be electrochemically cycled against time until a desire potential

range is reached. The CE has a much larger surface area than the WE and conducts electric current from the signal source to the WE to avoid polarization of the supporting electrolyte. When the reaction on the WE is anodic, the CE functions as the cathode and vice versa. While the RE retains an accurately fixed electrical potential against the recorded potential on the WE. The supporting electrolytic solution provides an ionic atmosphere to the electrodes during the redox process. The CV technique is often used to study the qualitative information during the electrochemical processes in different conditions such as: (i) presence of intermediates in redox processes and the reaction reversibility; (ii) determine the electron stoichiometry of electrical system; (iii) diffusion coefficient of an analyte and reduction potential to identify the analyte; and (iv) deduce analyte's concentration following the Nernst potential (**Equation 2.12a**), where the concentration of unknown analyte is obtained by generating calibration curve of current against concentration. **Equations 2.12a** and **2.12b** explain the thermodynamics equilibrium of the reaction (i.e., no net flux of ions and the standard reduction potential, $E^0 = 0$).

$$E = \frac{RT}{zF}\ln\frac{[\text{Anode}]}{[\text{Cathode}]} = 2.303\frac{RT}{zF}\log_{10}\frac{[\text{Anode}]}{[\text{Cathode}]} \qquad (2.12a)$$

$$E_{1/2} = \frac{E_{pa} + E_{pc}}{2} \qquad (2.12b)$$

$$\Delta E_{pp} = |E_{pa}| - |E_{pc}| = \frac{60}{\text{n}}\ \text{mV} \qquad (2.13)$$

where E, $E_{1/2}$, ΔE_{pp}, R, T, F, z, E_{pa}, E_{pc} , i_{pa} and i_{pc} are overall potential (V), half-wave potential, peak-to-peak separation (equal 60 mV when n = 1), universal gas constant (8.314 JK^{-1} mol^{-1}), absolute temperature (K), Faraday's constant (96485 C mol^{-1}), number of electrons transferred, peak anodic potential (V), cathodic potential (V), peak anodic current (A) and peak cathodic currents, respectively.

A potentiostat is an electrochemical device that uses direct current (DC) power sources to produce, maintain and accurately determine potential or current, as current or potential passes through the system. Signals of the currents at the WE plotted against the applied potentials, are display as readouts on the computer of the potentiostat, are called the voltammograms. The voltammograms are interpreted to study the electrochemical properties of the analyte of interest in solution or a molecule that is adsorbed onto the WE [160].

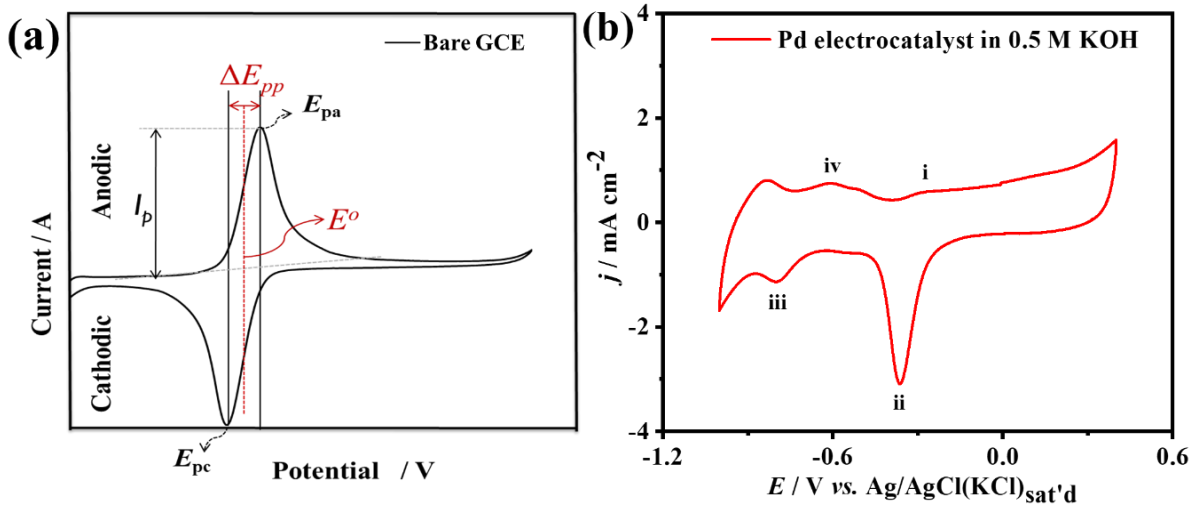

Figure 2.16: Typical CVs (a) bared GCE in Ferri/Ferrocyanide in KCl solutions and (b) Pd electrocatalyst in KOH solution

A typical cyclic voltammogram of bared glassy carbon electrode (GCE) in $Fe(CN)_6^{4-}$ /$Fe(CN)_6^{3-}$ in KCl (standard redox electrolyte) (**Figure 2.16a**), where a reversible redox peak i.e., oxidation and reduction peaks with peak-peak potential separation (ΔE_{pp} of *ca.* 60 mV when n = 1, **Equation 2.13**) and ratio of anodic and cathodic peak currents (i_{pa}/i_{pc} of *ca.* 1). Any variations from these conditions show pseudo-reversible or irreversible redox behavior of the electrode being probed. While **Equation 2.12b** shows the relationship of $E_{1/2}$, which explains the thermodynamics of the reaction. **Figure 2.16b** shows the CV of Pd electrocatalyst in KOH solution, where a well-

resolved voltammogram with four distinct signatures: (i) Pd oxidation; (ii) PdO reduction; (iii) hydrogen adsorption; and (iv) hydrogen desorption. The PdO reduction peak (**ii**) is often integrated to determine the ECSA of electrocatalysts following a formula proposed by Rand and Wood [161], given in **Equation 2.14**.

$$\mathrm{ECSA} = \frac{Q}{S.l} \qquad (2.14)$$

where *Q*, *S*, and *l* are coulombic charge obtained by integrating the PdO reduction charges, coulombic constant (0.424 mC cm^{-2}) for Pd monolayer surface and nanostructured Pd loading (g cm^{-2}) in the electrocatalyst on the surface coverage of the GCE WE.

2.7.2 Linear Sweep Voltammetry (LSV)

The LSV is a voltammetric technique that records current at the WE, as potential window between the WE and RE is ramped linearly with time [162]. The LSV is otherwise known as a polarization curve and the set-up employed is like that of the CV. The potentiostat is connected to the three-electrode configuration (WE, RE and CE). A potential range (ΔE) at the WE are displayed when ramped at a fixed scan rate, which is the slope of the potential to time. The LSV record oxidation or reduction of electroactive species in the form of a peak or trough in the current direction at the potential window, then electroactive species starts to either oxidize or reduce at the WE and the process is monitored or recorded on the readout. Opposite of the process at the WE occurred at the CE and are not monitored or recorded, as the CE helps to balance charges either added or removed by the WE. The potential values at the WE are recorded with respect to the RE with fixed potential.

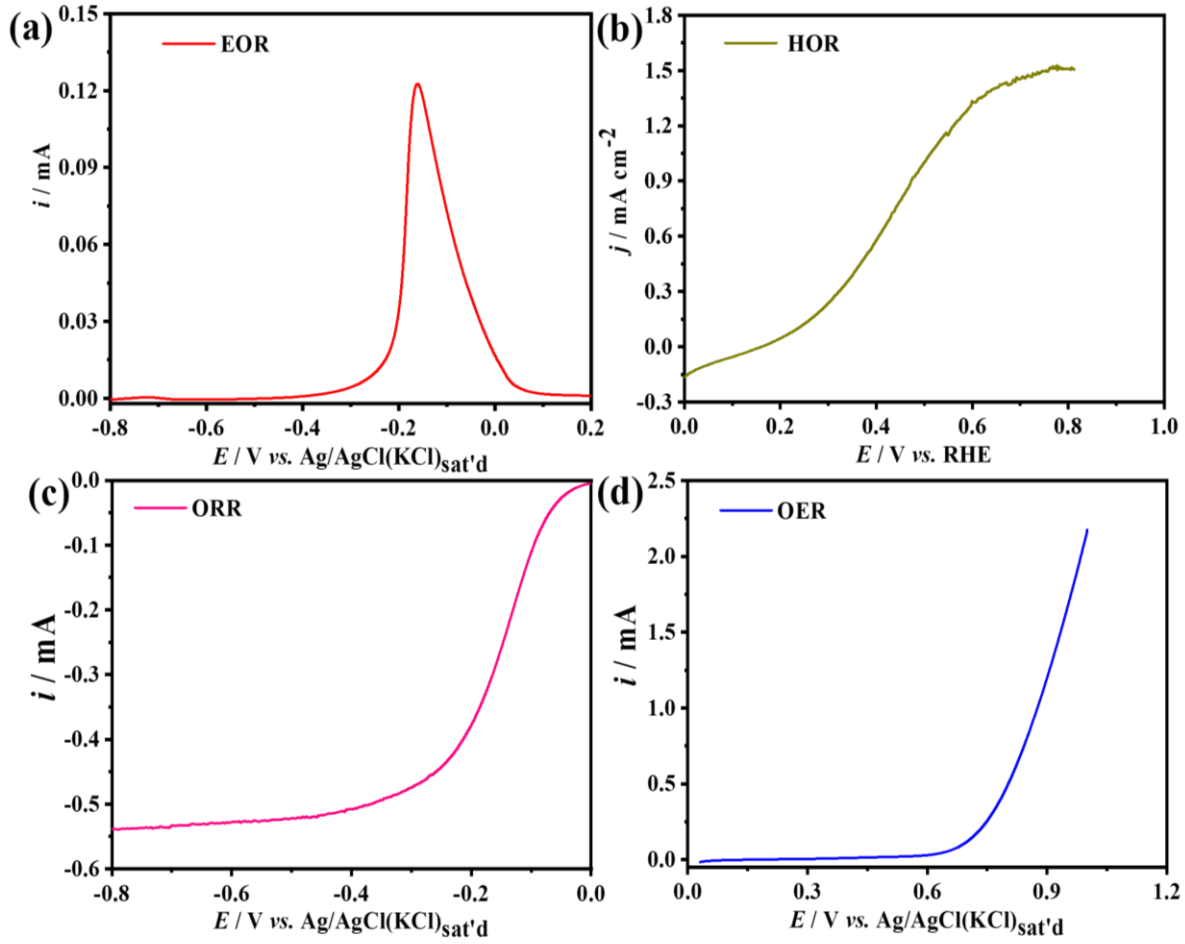

Figure 2.17: Typical examples LSV curves of Pd electrocatalyst for (a) EOR, (b) HOR, (c) ORR and (d) OER at low scan rates

The LSV shows a voltammogram of current against potential. Sensitivity of the current response against the potential could be improved as the scan rate increase because the electrochemical reaction occurs faster at a high scan rate (non-steady-state condition) explains the reaction thermodynamic. Hence, increasing the scan rate results in higher oxidation or reduction signal of the electroactive species at the WE. However, the LSV experimental or polarization curve at a low scan rate (steady-state condition) gives information on the kinetics of either oxidation or reduction of the electroactive species at the WE, especially in cases where the CV is irreversible [163].

The LSV technique could also be used to determine unknown species present and the concentration of a known analyte. **Figure 2.17** shows examples of LSV or polarization curves of Pd electrocatalyst for different reactions of interest (EOR, HOR, ORR, OER) to this work, carried out at different potential ranges and low scan rates (1–10 mV s^{-1}). The kinetic parameter of the electrocatalysts for all the reactions are obtained from the polarization curves using the conventional Tafel formula (**Equations 2.15** and **2.16**), whose values are summarized later.

$$\eta = a + b\log j \tag{2.15}$$

$$b = \frac{2.303RT}{(1-\alpha)nF} \tag{2.16}$$

where η, a, b, α, R, T and F are the overpotential (different between the applied potential and standard reduction potential (E^0)), the Tafel constant, the Tafel slope, the electron transfer coefficient, the universal gas constant, absolute temperature and the Faraday constant, respectively

2.7.3 Chronoamperometry (CV)

The CA is an amperometry electrochemical technique that involves recording current signals from faradaic process at the WE as a function of time after a single or double potential step is applied to the WE during an electrochemical reaction. Information about the nature of the electroactive species can be obtained from the ratio of the peak oxidation against peak reduction current or potential of a maximum peak for a single peak. Nonetheless, the CA produces increased charging currents decaying exponentially with time in resistant-current (*RC*) circuit. The faradaic current is an electron transfer process showing current signal for reaction(s) of interest decaying

and is directly related to the electroactive species' diffusion coefficient following the Cottrell equation (**Equation 2.17**):

$$i = \frac{nFAc^0\sqrt{\mathrm{D}}}{\sqrt{\pi t}} \qquad (2.17)$$

where i, n, F, A, c^0, D and t are current (A), the number of electrons to reduce or oxidize one molecule of an analyte, Faraday constant (96485 C mol^{-1}), initial concentration (mol dm^{-3}) of the reducible sample, diffusion coefficient (cm^2 s^{-1}) for electroactive species and time (s)

The CA experiment could be carried out in the three-electrode and two-electrode configurations with a readout of the current signals over time intervals. The amperometry is classified into two depending on fixed-parameter: (i) controlled-current chronoamperometry and (ii) controlled-potential chronoamperometry. Between the types of amperometry, the latter is the most preferred because it displays an excellent signal to noise ratio [164]. Before the latter experiment, CV and/or LSV would have been carried out to deduce the potential, which could be half-wave potential ($E_{1/2}$, **Equation 2.12b**) or open circuit potential (OCV) or biased potential on the voltammogram and can further be employed to study electrode processes of coupled chemical reactions [165]. A typical CA curve of Pd electrocatalyst is shown in **Figure 2.18**.

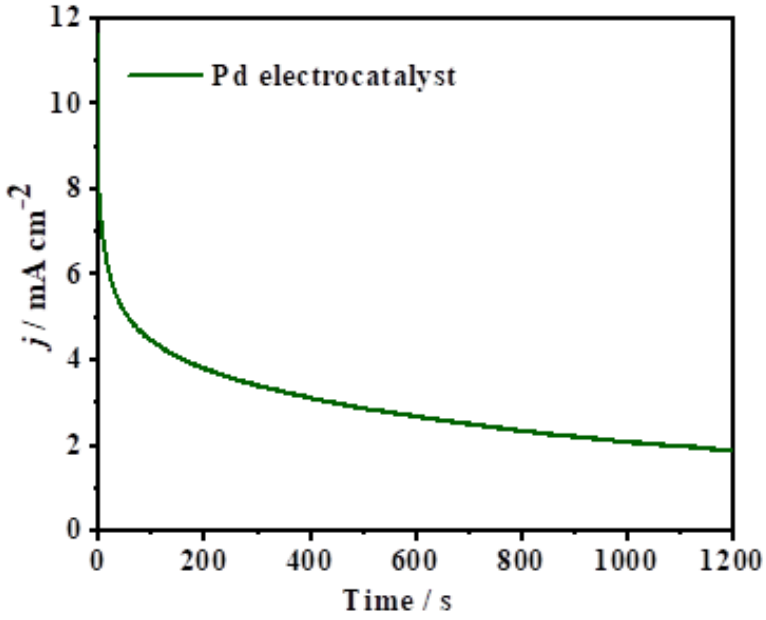

Figure 2.18: A typical CA curve of Pd electrocatalyst at either $E_{1/2}$ or OCV or biased potential for the EOR

2.7.4 Electrochemical Impedance Spectroscopy (EIS)

The EIS is an important electrochemical tool for the characterization of heterogeneous systems. The impedimetric spectra are obtained when a small amplitude sinusoidal electrochemical perturbation with an alternative current (AC) excitation signal (*ca.* 10 mV) is applied over a range of frequencies. The EIS could be carried out at either a fixed potential or current leading to its classification into two: (i) potentiostatic electrochemical impedance spectroscopy (PEIS) where the sinusoidal perturbation is done at a fixed potential (OCV, $E_{1/2}$ or biased potential); (ii) galvanostatic electrochemical impedance spectroscopy (GEIS) where the sinusoidal perturbation is done at fixed current. The two classes of the EIS are imperative tools that allow separation of processes (ionic and electronic) occurring on different timescales, making it easy to probe and study ions diffusion at the electrode-electrolyte interfaces [166]. The former is employed in this study. A series layer of different electrical properties using Voigt electrical equivalent circuits (*EEC*) model to extract the

impedimetric parameters. The EIS parameters such as: resistance (bulk (R_b), interfacial (R_{int}) and charge transfer (R_{ct})); capacitive (dielectric) or constant phase element (*CPE*); inductive; and diffusive (Warburg, Z_w) properties could be determined from the EIS signal when modelled with the appropriate Voigt *EEC* depending on its signature and the information extracted is employed to explain the electrochemical reaction taking place at electrode-electrolyte interfaces [167].

The Nyquist plot is the signal of the impedimetric spectra modelled with the appropriate Voigt *EEC* model to determine the circuit elements depending on the signature of the spectra. Major EIS parameters are: (i) solution resistance (R_s), which is the opposition to the flow of current at the electrodes to the supporting electrolyte during the electrochemical testing, there is ease of ions migration within these components that made up the electrochemical set-up when the R_s value is low and vice versa; (ii) interfacial resistance (R_{int}) is the Voigt resistive element due to ohmic loss from the diffusion of the supporting electrolyte's ions between the anode and cathode, and distance between the electrodes, specific conductance of the electrolytes and area of the WE; (iii) charge transfer resistance (R_{ct}) is an impedance against electrons transfer process between the electrodes and supporting electrolyte, the smaller the value, the better the electrode; (iv) double-layer capacitance (C_{dl}) explains the tendency of the electrocatalyst to homogeneously and regularly store charges and characteristic of the electrical double-layer at the electrode/electrolyte interfaces. If the impedimetric spectra give a perfect semi-circle signature, the C_{dl} is appropriate to define the charge storage system. Otherwise, interfacial capacitance (constant phase element, *CPE*) is the appropriate term when deformed semi-circle is formed from the spectra, which could be traced to inhomogeneity or irregularities of the electrode surfaces and the

impedimetric deviation of the *CPE* (Z_{CPE}) from the C_{dl} is defined according to the power-law relationship (**Equation 2.18**) [168–172]:

$$Z_{CPE} = [Q(j\omega)^{a}]^{-1} \quad (2.18)$$

where Q is the non-ideal capacitance of the electrode/electrolyte interface, ω is the radial frequency and the ideality factor is "*a*" with values range -1 – +1 (i.e., $-1 \leq a \leq 1$): when $a = 0$, the Z_{CPE} equals a pure resistor; $a = 1$, the Z_{CPE} equals a pure capacitor (C_{dl}); $a = -1$, the *CPE* is a pure inductor; while $a = 0.5$, the Z_{CPE} becomes the Warburg impedance (Z_W) ascribed to the diffusion of the supporting electrolyte ions, which is oscillating linearly on the right side or low-frequency region of the semi-circle at 45º [169,171].

A typical Nyquist plot is shown in **Figure 2.19a** with corresponding Voigt *EEC* models and circuit elements (R_s, R_{ct}, C_{dl}, and Z_w) as a result of the impedimetric signature, while Nyquist plot that comprises the other circuit elements (R_{int} and *CPE*) are explained in subsequent chapters where appropriate. Moreover, the impedimetric spectra may further be explained using Bode plots (plots of phase angle or Logarithmic impedance *vs*. Logarithmic frequency, **Figure 2.19b**), giving additional information on the phase angle, adsorption and diffusion properties of the analyte onto the electrode surface.

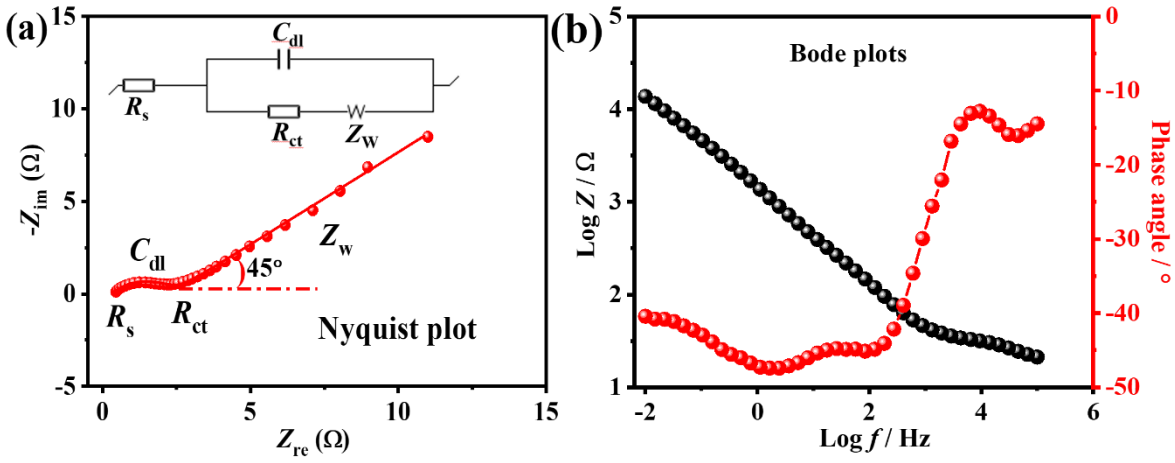

Figure 2.19: (a) A typical Nyquist plot with inset Voigt *EEC* model and circuit elements (R_s, R_{ct}, C_{dl}, and Z_{CPE}) and (b) typical Bode plots

2.7.5 Rotating Disk Electrode (RDE) and Rotating Ring Disk Electrode (RRDE)

In potentiostatic electrochemical measurements, the WE is a modified-GCE without any form of agitation or rotation. While in a few measurements involving potentiodynamic systems, rotating disk electrode (RDE) modified is the WE that rotates during experiments, inducing analyte flowing to the electrode as the electrolyte is agitated [164], thereby reducing the diffusion layer thickness of gaseous analytes. This technique takes advantage of other flow methods like forced convection by either quickly making high rate of steady-state mass transports and reproducibly controlled the convention over mass transfer coefficient [173]. The potentiodynamic technique is often used for the study of gaseous analyte either its production or consumptions (i.e., reactions like ORR, OER, HOR, HER). To further investigate the model or mechanism of the potentiodynamic reaction involving multi-electron processes, kinetic of a slow electron transfer and adsorption-desorption steps, especially for the ORR, rotating ring disk electrode (RRDE) is employed. Like the RDE (**Figure 2.20a**), the RRDE (**Figure 2.20b**) operates on the same principle but has double WE: (i) the disk; and (ii) the ring. The latter forms a ring around the central disk electrode of the WE, which is employed

to probe intermediate species like peroxide formation during the ORR [174]. The two WE of the RRDE are separated by an insulating barrier and connected to the potentiostat through distinct operating conditions to control the electrodes system concurrently. The RDE and RRDE are connected to a rotating motor, where the rotating speed could be set manually or automatically to rotate the electrodes during the potentiodynamic experiments.

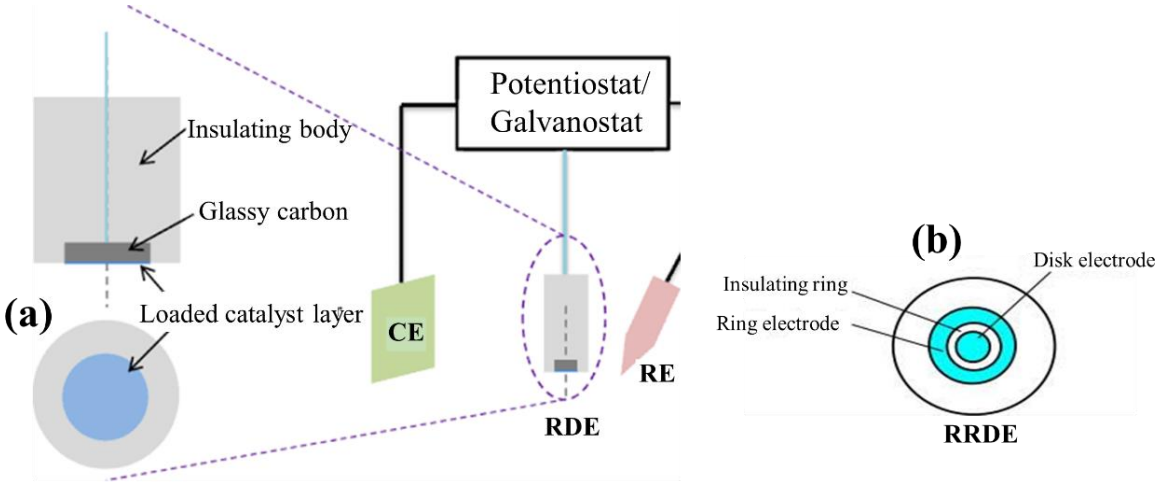

Figure 2.20: Schematic illustration of typical (a) RDE and (b) RRDE

2.7.6 Models used in Potentiodynamic Experiments

Kinetic parameters of potentiodynamic reaction are extracted from models like: Koutecky-Levich and Butler-Volmer formulae.

2.7.6.1 Koutecky-Levich (K-L) Formula

The Koutecky-Levich (K-L) formula is a cogent model for correcting mass transport properties of potentiodynamic reactions that utilize RDE at varied rotation speeds (ω) to deduce kinetic- and diffusion-controlled processes. This model involves a plot inverse of current densities (j^{-1}) against $\omega^{-1/2}$ to give a straight line, as given in **Figure 2.21a**, following **Equation 2.19**. The intercept and slope of the plot correspond to the

diffusion- and kinetic-controlled processes, respectively. In **Equations 2.20** and **2.21** where the diffusion coefficient and kinetic current (j_K, which is directly related to heterogeneous rate constant (k^0)).

$$\frac{1}{j} = \frac{1}{j_K} + \frac{1}{B_L \omega^{1/2}} \quad (2.19)$$

$$B_L = \frac{1}{slope} = 0.62nFc_o D^{2/3} v^{-1/6} \quad (2.20)$$

$$j_K = nFk^0 c_o \quad (2.21)$$

where j and j_K are the mass transfer and kinetic current densities, B_L is the Levich constant and ω is the rotation speed (rad s^{-1}) and bulk concentration (c_o = 1.2 x10^{-6} mol cm^{-3}) of O_2 or H_2 gas in 0.1 M KOH. The B_L is related to the diffusivity or diffusion coefficient of H_2 gas (D), number of electrons (n) transferred and kinematic viscosity of electrolyte (υ = 0.01 cm^2 s^{-1}).

The ω is obtained with revolution per minute (rpm) and converted to radian per second (rad s^{-1}) with the formula given in **Equation 2.22**:

$$\text{rad } s^{-1} = \frac{60}{2\pi} \text{ rpm} \quad (2.22)$$

2.7.6.2 Butler-Volmer (B-V) Formula

Butler-Volmer (B-V) formula (**Equation 2.23)** is a fundamental model employed for mass transport kinetics of potentiodynamic reactions that describes the relationship of electric current of the electrocatalyst or electrode to the voltage difference between the electrocatalyst or electrode and supporting electrolyte, and assumes that both anodic and cathodic reactions occur on the electrocatalyst or electrode. Thus, this model involves a plot of logarithm of current densities (Log j) to the overpotential (η)

to give non-linear curves for the anodic and cathodic contributions, respectively. The intercept of the anodic and cathodic contributions give the corresponding mass transport kinetics like exchange current density ($j_{o,s}$) and Tafel slopes (b_a and b_c) for anodic and cathodic reactions. The Butler-Volmer plot equation has two distinct limiting regions: (i) low overpotential limit, otherwise called polarization resistance (i.e., $E \approx E_{eq}$); and (ii) high overpotential limit, this is when the Butler-Volmer equation collapses to Tafel equation at this condition (i.e., $E \neq E_{eq}$), either as anodic or cathodic is considered in a given linear plot, following **Equations 2.24** and **2.25**, respectively. These equations can be linearized to **Equation 2.15** previously explained.

$$j = -j_o . e^{\left(\frac{-\alpha . z . F}{RT} \cdot \eta\right)} \qquad (2.23)$$

This equation can further be simplified to the anodic and cathodic Tafel formulae, respectively.

$$\text{Anodic Tafel:} \quad \eta = \frac{2.303RT}{(1-\alpha_a).z.F} log\, j_{o,s} - \frac{2.303RT}{(1-\alpha_a).z.F} log\, j_a \qquad (2.24)$$

$$\text{Cathodic Tafel:} \quad \eta = \frac{2.303RT}{\alpha_c.z.F} log\, j_{o,s} - \frac{2.303RT}{\alpha_c.z.F} log\, j_c \qquad (2.25)$$

where overpotential (η = working potential – standard reduction potential (E^0 = 0.0 V for RHE or 0.197V for Ag/AgCl, $(KCl)_{sat'd}$)), cathodic (j_c) and anodic (j_a) current densities (mA cm^{-2}); exchange current density ($j_{o,s}$, mA cm^{-2}), universal gas constant (R), absolute temperature (T (K)), Faraday constant (F), cathodic (α_c) and anodic (α_a) electron transfer coefficients and number of electrons (z) involves in electrode reaction (z = 1).

The Ag/AgCl is referenced to reversible hydrogen electrode (RHE) utilizing a conversion formula given in **Equation 2.26:**

$$RHE = E_{AgIAgCl} + E^{0}_{AgIAgCl} + 0.0591pH \quad (2.26)$$

where $E_{AgIAgCl}$ is the working potential with respect to the AgIAgCl,sat'd KCl reference, $E^{0}_{AgIAgCl}$ is the standard reduction potential of (0.197 V) for the AgIAgCl,sat'd KCl reference and pH of the supporting electrolyte

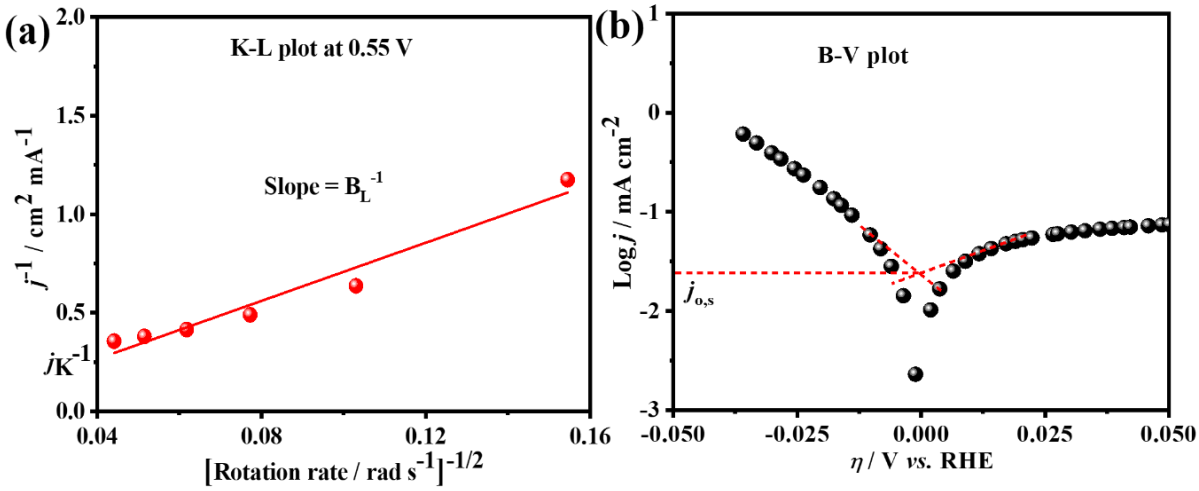

Figure 2.21: Typical (a) Koutecky-Levich plot and (b) Butler-Volmer plot for potentiodynamic system

2.8 References

[1] S. P. S. Badwal, S. Giddey, A. Kulkarni, J. Goel, S. Basu, *Applied Energy*, **145**(2015): 80–103.

[2] R. Szweda, *III-Vs Review*, **19**,4(2006): 48.

[3] S. K. Kamarudin, F. Achmad, W. R. W. Daud, *International Journal of Hydrogen Energy*, **34**,16(2009): 6902–6916.

[4] F. Opekar, K. Stulik, *Analytica Chimica Acta*, **385**,1-3(1999): 151–162.

[5] M. Z. F. Kamarudin, S. K. Kamarudin, M. S. Masdar, W. R. W. Daud, *International Journal of Hydrogen Energy*, **38**,22(2013): 9438–9453.

[6] K. I. Ozoemena, *RSC Advance*, **6**(2016): 89523–89550.

[7] A. Z. Weber, R. L. Borup, R. M. Darling, P. K. Das, T. J. Dursch, W. Gu, D. Harvey, A. Kusoglu, S. Litster, M. M. Mench, R. Mukundan, J. P. Owejan, J. G. Pharoah, M. Secanell, I. V. Zenyuk, *Journal of the Electrochemical Society*, **161**,12(2014): F1254–F1299.

[8] Q. Liu, S. Cao, Y. Qiu, *International Journal of Hydrogen Energy*, **42**,49(2017): 29274–29282.

[9] H. Fang, T. Huang, Y. Sun, B. Kang, D. Liang, S. Yao, J. Yu, M. M. Dinesh, S. Wu, J. Y. Lee, S. Mao, *Journal of Catalysis*, **371**(2019): 185–195.

[10] M. Liu, F. Yu, C. Ma, X. Xue, H. Fu, H. Yuan, S. Yang, G. Wang, X. Guo, L. Zhang, *Nanomaterials*, **9**,9(2019): 1284.

[11] A. Yilanci, H. K. Ozturk, *Progress in Energy and Combustion Science*, **35**,3(2009): 231–244.

[12] X. Zhang, *Clean Energy*, **2**,2(2018): 126–139.

[13] J. P. Pereira, A. M. F. R. Pinto, *Journal of Power Sources*, **256**(2018): 14–19.

[14] K. Schmidt-Rohr, *Journal of Chemical Education*, **95**,10(2018): 1801–1810.

[15] A. Kundu, J. H. Jang, *Encyclopedia of Electrochemical Power Sources, Elsevier, Amsterdam, Netherlands*, (2009): 39–45.

[16] T. Awotwe, A. Alaswad, A. Palumbo, M. Dassisti, A. G. Olabi, *International Journal of Hydrogen Energy*, **41**,37(2016): 16509–16522.

[17] I. Staffell, S. Pfenninger, *Energy*, **145**(2018): 65–78.

[18] S. Collins, P. Deane, B. O. Gallachoir, S. Pfenninger, I. Staffell, *Joule*, **2**(2018): 1–15.

[19] United State Department of Energy, *Technical Reports, U.S. Department of Energy*, (2016).

[20] T. S. Zhao, Y. S. Li, S. Y. Shen, *Frontiers of Energy and Power Engineering in China*, **4**(2010): 443–458.

[21] E. A. Franceschini, H. R. Corti, *Direct Alcohol Fuel Cell, Netherlands, Dordrecht, Springer*, (2014): 321–355.

[22] K. Wipke, S. Sam, K. Jennifer, R. Todd, *National Renewable Energy Laboratory*, (2009).

[23] J. Garbak, *Department of Energy Fuel Cell Technology Program, Annual Progress Report*, (2010).

[24] United States Department of Energy, *Fuel Cell Technology Program*, (2011).

[25] R. Prince, *Global Hydrogen Fuel Cell Vehicles Sales Seeing Progress*, *HybridCars.com*, (2018).

[26] R. V. Lathia, K. S. Dobariya, A. Patel, *Journal of Cleaner Production*, **100**, 141(2017): 462.

[27] National Fuel Cell Program Award, *Calstart*, (2011).

[28] United States Department of Energy, *Argonne National Laboratory, Energy System Division, Economic Impact of Fuel Cell Deployment in Forklifts and for Backup Power under the American Recovery and Reinvestment Act*, (2013).

[29] HyLift–Europe, *Clean Efficient Power for Materials Handling*, www.hylift-projects.eu, (2013).

[30] E. Bryant, *Honda to offer Fuel-Cell Motorcycle*, (2005).

[31] E. N. V. Bike, *Intelligent Energy Archived*, (2008).

[32] T. F. Babor, H. R. Kranzler, R. J. Lauerman, *Recent Developments in Alcoholism*, **5**(1987): 373–397.

[33] K. I. Ozoemena, S. Musa, R. Modise, A. K. Ipadeola, L. Gaolatlhe, S. Peteni, G. Kabongo, *Current Opinion in Electrochemistry*, **10**(2018): 82–87.

[34] J. C. Defant, M. E. Hamerly, D. S. Segal, S. Cohen, *US Patent Application US*, 2018/0049668A1, (2018).

[35] S. Litster, G. McLean, *Journal of Power Sources*, **130**,1-2(2004): 61–76.

[36] M. R. Rahman, J. T. S. Allan, M. Z. Ghavidel, L. E. Prest, F. S. Saleh, E. B. Easton, *Sensor Actuators B*, **228**(2016): 448–457.

[37] The United State of America Federal Register, *Highway Safety Programs*, **77**,115(2012): 35748–35750.

[38] The Government of Canada*, Criminal Code Section 254 R.S.C.*, (1985): C–46.

[39] K. Zeng, D. Zhang, *Progress in Energy Combustion Science*, **36**(2010): 307–326.

[40] R. De Levie, *Journal of Electroanalytical Chemistry*, **476**,1**(**1999): 1–94.

[41] W. Kreuter, H. Hofmann, *International Journal of Hydrogen Energy*, **23**, 8(1998): 661–666.

[42] C. T. Bowen, H. J. Davis, B. F. Henshaw, R. Lachance, R. L. Leroy, R. Renaud, *International Journal of Hydrogen Energy*, **9**,1-2(1984): 59–66.

[43] H. Wendt, G. Kreysa, *Electrochemical Engineering, Springer–Verlag: Berlin, Heidelberg*, 1st Edition, (1999).

[44] D. Pletcther, F. C. Walsh, *Industrial Electrochemistry, Blackie Academic & Professional: London*, 2nd Edition, (1990).

[45] P. W. T. Lu, S. Srinivasan, *Journal of Applied Electrochemistry*, **9**(1979): 269.

[46] F. Barbir, *PEM Fuel Cells, Theory and Practice, Academic Press*, Chapter 10 (2005): 337–397.

[47] C. A. C. Sequeira, D. M. F. Santos, *Polymer Electrolytes: Fundamentals and Applications; Woodhead Publishing Limited: Cambridge*, (2010).

[48] S. A. Grigoriev, V. I. Porembsky, V. N. Fateev, *International Journal of Hydrogen Energy*, **31**,2(2006): 171–175.

[49] A. K. Ipadeola, K. I. Ozomena, *RSC Advances*, **10**(2020): 17359–17368.

[50] A. Marshall, B. Borresen, G. Hagen, M. Tsypkin, R. Tunoid, *Energy*, **32**,4(2007): 431–436.

[51] M. Carmo, D. Fritz, J. Mergel, D. Stolten, *International Journal of Hydrogen Energy*, **38**,35(2013): 14921–15856.

[52] A. N. Colli, H. H. Girault, A. Battistel, *Materials*, **12**,8(2019): 1336.

[53] M. Schalenbach, A. R. Zeradjanin, O. Kasian, S. Cherevko, K. J. J. Mayrhofer, *International Journal of Electrochemical Science*, **13**(2018): 1173–1226.

[54] M. Schalenbach, W. Lueke, D. Stolten, *Journal of the Electrochemical Society*, **163**,14(2016): F1480–F1488.

[55] P. Haug, M. Koj, T. Turek, *International Journal of Hydrogen Energy*, **42**,15(2017): 9406–9418.

[56] H. Dotan, A. Landman, S. W. Sheehan, K. D. Malviya, G. E. Shter, D. Grave, D. Grave, Z. Arzi, N. Yehudai, M. Halabi, N. Gal, N. Hadari, C. Cohen, A. Rothschild, G. S. Grader, Nature Energy, **4**,9(2019): 786–795.

[57] F. M. Mulder, B. M. H. Weninger, J. Middelkoop, F. G. B. Ooms, H. Schreuders, *Energy and Environmental Science*, **10**,3(2017): 756–764.

[58] M. Rezaei, A. Mostafaeipour, M. Qolipour, M. Momeni, *Frontiers in Energy*, **13**(2019): 539–550.

[59] S. S. Kumar, V. Himabindu, *Materials Science for Energy Technologies*, **2**,3(2019): 442–454.

[60] J. R. Varcoe, R. C. T. Slade, *Fuel Cells*, **5**,2(2005): 187–200.

[61] R. C. T. Slade, J. P. Kizewski, S. D. Poynton, R. Zeng, J. R. Varcoe, *Encyclopedia of Sustainability Science and Technology, Springer, New York, NY, In: R. A. Meyers* (2012).

[62] R. Zeng, J. R. Varcoe, *Recent Patents on Chemical Engineering*, **4**,2(2011): 93–115.

[63] J. R. Varcoe, P. Atanassov, D. R. Dekel, A. M. Herring, M. A. Hickner, P. A. Kohl, A. R. Kucernak, W. E. Mustain, K. Nijmeijer, K. Scott, T. Xu, L. Zhuang, *Energy and Environmental Science*, 7,10(2014): 3135–3191.

[64] J. Zheng, W. Sheng, Z. Zhuang, B. Xu, Y. Yan, *Science Advances*, **2**,3(2016): e1501602.

[65] D. R. Dekel, *Journal of Power Sources*, **375**,31(2018):158–169.

[66] H. A. Miller, A. Lavacchi, F. Vizza, M, Marelli, F. D. Benedetto, F. D'Acapito, Y. Paska, M. Page, D. R. Dekel, *Angewandte Chemie International Edition*, **55**,20(2016): 6004–6007.

[67] H. Yu, E. S. Davydova, U. Ash, H. A. Miller, L. Bonville, D. R. Dekel, R. Maric, *Nano Energy*, **57**(2019): 820–826.

[68] M. Winter, R. J. Brodd, *Chemical Reviews*, **104**,10(2004): 4245–4269.

[69] H. A. Gasteiger, F. T. Wagner, *Applied Catalysis B: Environmental*, **56**,1–2(2005): 9–35.

[70] A. Mahata, A. S. Nair, B. Pathak, *Catalysis Science and Technology*, **9**,18(2019): 4835–4863.

[71] S. Lister, G. McLean, *Journal of Power Sources*, **130**,1–2(2004): 61–76.

[72] M. S. Wilson, J. A. Valerio, S. Gottesfeld, *Electrochimica Acta*, **40**,3(1995): 355–363.

[73] Z. Qi, A. Kaufman, *Journal of Power Sources*, **113**,1(2003): 37–43.

[74] R. P. Ramasamy, *Encyclopedia of Electrochemical Power Sources*, *Chapter 227,* **2** (2009): 787–805.

[75] I. Firtina, S. Guner, A. Albostan, *International Journal of Energy Research*, **35**,2(2011): 146–152.

[76] E. Slavcheva, G. Topalov, G. Ganske, I. Radev, E. Lefterova, U. Schnakenberg, *Electrochimica Acta*, **55**,28(2010): 8992–8997.

[77] M. Kim, J. N. Park, H. Kim, S. Song, W. H. Lee, *Journal of Power Sources*, **163**,1(2006): 93–97.

[78] K. L. Huang, Y. C. Lai, C. H. Tsai, *Journal of Power Sources*, **156**,2(2006): 224–231.

[79] A. V. Tripkovi'c, K. DjPopovi'c, B. N. Grgur, B. Blizanac, P. N. Ross, N. M. Markovic, *Electrochemical Acta*, **47**,22-23(2002): 3707–3714.

[80] V. Baglio, V. Antonucci, A. S. Aric'o, *Advances in Nanotechnology, Materials and Devices, Wiley-VCH GmbH and Co*, (2009): 1–78.

[81] C. S. Sharma, R. Awasthi, R. N. Singh, A. S. K. Sinha*, Physical Chemistry Chemical Physics*, **15**,46(2013): 20333–20344.

[82] M. H. Seo, S. M. Choi, H. J. Kim, W. B. Kim, *Electrochemistry Communications*, **13**,2(2011): 182–185.

[83] Z. Zhuang, W. Chen, *Journal of Colloid Interface Science*, **538**(2019): 699–708.

[84] S. Takenaka, T. Tsukamoto, H. Matsune, M. Kishida, *Catalysis Science and Technology*, **3**,10(2013): 2723–2731.

[85] C. H. Lee, H. I. Joh, *Electrochemical Communications*, **106**(2019): 106516.

[86] M. D. Mobarakeh, *Fibers Polymers*, **18**(2017): 95–101.

[87] F. He, K. Li, C. Yin, Y. Wang, H. Tang, Z. Wu, *Carbon*, **114**(2017): 619–627.

[88] T. Bhowmik, M. K. Kundu, S, Barman, *International Journal of Hydrogen* Energy, **41**,33(2016): 14768–14777.

[89] E. Antolini, *Energy and Environmental Science*, **2**,9(2009): 915–931.

[90] S. Tominaga, T. Osaka, *Advances in Electrocatalysis*, **2011**(2011): 13.

[91] E. Lopex-Chavez, F. D. L. Castillo-Alvarado, *International Journal of Hydrogen Energy*, **41**,48(2016): 23281–23286.

[92] O. Muneeb, E. Do, D. Boyd, J. Perez, J. L. Haan, *Applied Energy*, **235**(2019): 473–479.

[93] S. Y. Shen, Y. S. Li, *Journal of Power Sources*, **195**,4(2010): 1001–1006.

[94] J. Zhao, A. Sarkar, A. Manthiram, *Electrochimica Acta*, **55**,5(2010): 1756–1765.

[95] J. Kim, T. Momma, T. Osaka, *Journal of Power Sources*, **189**,2(2009): 999–1002.

[96] Q. Qin, J. Xie, Q. Dong, G. Yu, H. Chen, *New Journal of Chemistry*, **43**,48(2019): 19242–19252.

[97] J. M. Fisher, N. Cabello-Moreno, E. Christian, D. Thompsett, *Electrochemistry Solid-State Letters*, **12**,5(2009): B71–B81.

[98] X. Qin, L. Zhang, G. L. Xu, S. Zhu, Q. Wang, M. Gu, X. Zhang, C. Sun, P. B. Balbuena, K. Amine, M. Shao, *ACS Catalysis*, **9**,10(2019): 9614–9621.

[99] K. Park, S. Takenaka, *International Journal of Hydrogen Energy*, **42**,30(2017): 18951–18958.

[100] P. Hasler, T. Allmendinger, *Journal of Power Sources*, **45**,1(1993): 93–103.

[101] H. U. Park, Y. U. Kwon, *Ultrasonics Sonochemistry*, **58**(2019): 104673.

[102] H. D. Dong, Y. Y. Chen, M. Han, S. L. Li, J. Zhang, J. S. Li, Y. Q. Lan, Z. H. Dai, J. C. Bao, *Journal of Materials Chemistry A*, **2**,5(2014): 1272–1276.

[103] M. Neergat, G. Varadarajan, R. Ramesh, *Journal of Electroanalytical Chemistry*, 658,1–2(2011): 25–32.

[104] Y. Tang, S. Cao, Y. Chen, T. Lu, Y. Zhou, L. Lu, J. Bao, *Applied Surface Science*, **256**,13(2010): 4196–4200.

[105] P. M. de Souza, L. Nie, L. E. P. Borges, F. B. Noronha, D. E. Resasco, *Catalalyis Letters*, **144**(2014): 2005–2011.

[106] S. A. Park, E. K. Lee, H. Song, Y. T, Kim, *Scientific Reports*, **5**(2015): 13552.

[107] W. Curtis, Conner, J. L. Falconer, *Chemical Review*, **95**(1995): 759–788.

[108] A. Gotti, R. Prins, *Journal of Catalysis*,**175**,2(1998): 302–311.

[109] S. Parimala, S. C. Selin, A. Gnanamani, A. B. Mandal, *Current Research in Chemistry*, 4(3)(2012): 60–67.

[110] S. De, J. Zhang, R. Luque, N. Yan, *Energy and Environment Science*, 9,11(2016): 3314–3347.

[111] A. Quindimil, U. De-la-Torre, B. Pereda-Ayo, J. A. Gonzalez-Marcos, *Applied Catalysis B: Environmental*, 238(2018): 393–403.

[112] F. Wu, G. Yushin, *Energy and Environment Science*, 10(2)(2017): 435–459.

[113] S. L. James, *Chemical Society Review*, **32**,5(2003): 276–288.

[114] Y. Kim, S. Huh, *CrystEngComm*, **18**,20(2016): 3524–3550.

[115] H. Furukawa, K. E. Cordova, M. O'Keeffe, O. M. Yaghi, *Science*, **341**,6149(2013): 1230444.

[116] W. Lu, Z. Wei, Z. Y. Gu, T. F. Liu, J. Park, J. Park, J. Tian, M. Zhang, Q. Zhang, T. Gentle III, M. Botch, H. C. Zhou, *Chemical Society Review*, **43**,16(2014): 5561–5593.

[117] L. Sun, B. Liao, D. Sheberla, D. Kraemer, J. Zhou, E. A. Stach, D. Zakharov, V. Stavila, A. A. Talin, Y. Ge, M. D. Allendorf, G. Chen, F. Leonard, M. Dinca, *Joule*, **1**,1(2017): 168–177.

[118] L. Sun, M. G. Campbell, M. Dinca, *Angewandte Chemie International Edition*, **55**,11(2016): 3566–3579.

[119] C. H. Hendon, D. Tiana, A. Walsh, *Physical Chemistry Chemical Physics*, **14**,38(2012): 13120–13132.

[120] L. Kang, S. X. Sun, L. B. Kong, J. W. Lang, Y. C. Luo, *Chinese Chemical Letters*, **25**(2014): 957–961.

[121] J. Tang, R. R. Salunkhe, J. Liu, N. Torad, M. Imura, S. Fukukawa, Y. Yamauchi, *Journal of American Chemical Society*, **137**,4(2015): 1572–1580.

[122] X. Xu, W. Shi, W. Liu, S. Ye, R. Yin, L. Zhang, *Journal of Material Chemistry A*, **6**,47(2018): 24086–24091.

[123] D. Wang, L. Xiao, P. Yang, Z. Xu, X. Lu, L. Du, O. Levin, L. Ge, X. Pan, J. Zhang, M. An, *Journal of Material Chemistry A*, **7**,23(2019): 11007–11015.

[124] L. Yang J. Shui, L. Du, Y. Shao, J. Liu, L. Dai, Z. Hu, *Advanced Materials*, **31**,13(2019): e1804799.

[125] C. Hu, Y. Xiao, Y. Zou, L. Dai, *Electrochemical Energy Review*, **1**(2018): 84–112.

[126] A. Serov, K. Artyushkova, P. Atanassov, *Advanced Energy Materials*, **4**,10(2014): 1301735.

[127] X. Lu, L. Du, D. Wang, P. Yang, L. Liu, J. Zhang, M. An, O. Levin, J. Wang, L. Ge, *ChemElectroChem*, **5**,21(2018): 3323–3329.

[128] W. Liu, J. Huang, Q. Yang, S. Wang, X. Sun, W. Zhang, J. Liu, F. Huo, *Angewandte Chemie International Edition*, **56**,20(2017): 5512–5516.

[129] M. Wang, X. Xu, Y. Liu, Y. Li, T. Lu, L. Pan, *Carbon*, **108**(2016): 433–439.

[130] Y. Li, J. Kim, J. Wang, N. L. Liu, Y. Bando, A. A. Alshehri, Y. Yamauchi, C. H. Hou, K. C. Wu, *Nanoscale*, **10**,31(2018): 14852–14859.

[131] L. Zhang, Q. Chang, H. Chen, M. Shao, *Nano Energy*, **29**(2016): 198–219.

[132] A. K. Ipadeola, R. Barik, S. C. Ray, K. I. Ozoemena, *Electrocatalysis*, **10**,4(2019): 366–380.

[133] C. Wen, Y. Wei, D. Tang, B. Sa, T. Zhang, C. Chen, *Scientific Reports*, **7**(2017): 4907.

[134] E. S. Davydova, S. Mukerjee, F. JAouen, D. R. Dekel, *ACS Catalysis*, **8**,7(2018): 6665–6690.

[135] H. Meng, D. Zeng, F. Xie, *Catalysis*, **5**,3(2015): 1221–1274.

[136] S. M. George, *Chemical Reviews*, **110**,1(2010): 111–131.

[137] H. Kim, H. B. R. Lee, W. J. Maeng, *Thin Solid Films*, **517**,8(2009): 2563–2580.

[138] A. M. Fernandez, M. E. Calixto, P. J. Sebastian, S. A. Gamboa, A. M. Hermann, R. N. Noufi, *Solar Energy Materials and Solar Cells*, **52**,3–4(1998): 426–431.

[139] M. Paunovic, M. Schlesinger, *Wiley–Interscience, Hoboken, NJ, USA*, (2006).

[140] P. S. Patil, *Material Chemistry and Physics*, **59**,3(1999): 185–198.

[141] C. D. Lokhande, A. M. More, J. L. Gunjakar, *Journal of Alloys and Compounds*, **486**,1–2(2009): 570–580.

[142] W. H. Yen, C. C. Hsieh, H. W. Wang, C. Y. Hung, M. C. Tsui*, Journal of Chinese Chemical Society*, **57**,5(2010): 1162–1166.

[143] A. Cannavale, F. Fiorito, M. Manca, G. Tortorici, R. Cingolani, G. Gigli*, Building and Environment*, **45**,5(2010): 1233–1243.

[144] A. Rabenau, *Angewandte Chemie International Edition*, **24**,12(1985): 1026–1040.

[145] W. Ouyang, R. Alain, P. Santiago K. Cerdan-Gomez, R. Luque, *Photoactive Inorganic Nanoparticles: Surface Composition and Nanosystem Functionality Micro and Nano Technologies*, Chapter 5, (2019): 109–138.

[146] G. Zou, H. Li, Y. Zhang, K. Xiong, Y. Qian, *Nanotechnology*, **17**,11(2006): S313–S320.

[147] N. Asim, S. Ahmadi, M. A. Alghoul, F. Y. Hammadi, K. Saeedfar, K. Sopian, *International Journal of Photoenergy*, **2014**(2014): 21.

[148] S. Ito, T. N. Murakami, P. Comte et al., *Thin Solid Films*, **516**,14(2008): 4613–4619.

[149] C. H. Huang, Y. T. Yang, R. A. Doong, *Microporous and Mesoporous Materials*, **142**,2–3(2011): 473–480.

[150] R. Roy, D. Agrawal, J. Cheng, S. Gedevanishvili, *Nature*, **399**,1(1999): 668–670.

[151] S. G. Deng, Y. S. Lin, *Journal of Materials Science Letters*, **16**,15(1997): 1291–1294.

[152] K. J. rao, P. A. Ramakrishnan, R. Gadagkar, *Journal of Solid-State Chemistry*, **148**,1(1999): 100–107.

[153] A. S. Grewal, K. Kumar, S. Redhu, S. Bhardwaj, *International Research Journal of Pharmaceutical and Applied Science*, **3**,5(2013): 278–285.

[154] A. K. Rathi, M. B. Gawande, R. Zboril, R. S. Varma, *Coordination Chemistry Reviews*, **291**(2015): 68–94.

[155] S. Uchida, M. Tomiha, N. Masaki, A. Miyazawa, H. Takizawa*, Solar Energy Materials and Solar Cells*, **81**,1(2004): 135–139.

[156] C. Feldmann, H. O. Jungk, *Angewandte Chemie International Edition*, **40**,2(2001): 359–362.

[157] T. Yamamoto, Y. Wada, H. Yin, T. Sakata, H. Mori, S. Yanagida, *Chemistry Letters*, **31**,10(2002): 964–965.

[158] O. O. Fashedemi, B. Julies, K. I. Ozoemena, *Chemical Communications*, **49**,20(2013): 2034–2036.

[159] Y. Li, T. Zhang, *Progress and Recent Trends in Microbial Fuel Cells*, (2018): 143–165.

[160] N. Elgrishi, K. J. Rountree, B. D. McCarthy, E. S. Rountree, T. T. Elsenhart, J. L. Dempsey, *Journal of Chemical Education*, **95**,2(2017): 197.

[161] D. A. J. Rand, R. Woods, *Journal of Electroanalytical Chemistry*, **31**,1(1971): 29–38.

[162] T. M. Nahir, R. A. Clark, E. F. Bowden, *Analytical Chemistry*, **66**,15(2002): 2595–2598.

[163] S. Cheng, D. Xing, D. F. Call, B. E. Bruce, *Environmental Science Technology*, **43**,10(2009): 3953–3958.

[164] A. J. Bard, R. F. Larry, *Wiley*, 2nd Edition (2000).

[165] M. P. Foley, P. Du, K. J. Griffith, J. A. Karty, M. S. Mubarak, K. Raghavachari, D. G. Peters, *Journal of Electroanalytical Chemistry*, **647**,2(2010): 194–203.

[166] C. L. C. Ellis, E. Smith, H. Javaid, G. Berns, D. Venkataraman, *Perovskite Photovoltaic, Basic to Advanced Concepts and Implementation, Academic Press*, Chapter 6, (2018): 163–196.

[167] T. Mavric, M. Bencina, R. Imani, I. Junkar, M. Valant, V. Kralj-Iglic, A. Iglic, *Advances in Biomembranes and Lipid Self-Assembly*, **27**(2018): 63–105.

[168] A. S. Adekunle, K. I. Ozoemena*, Electrochimica Acta*, **53**,19(2008): 5774–5782.

[169] J. Pillay, K. I. Ozoemena, *Electrochimica Acta*, **54**,22(**2009)**: 5053 – 5059.

[170] B. O. Agboola, K. I. Ozoemena, *Physical Chemistry Chemical Physics*, **10**,17(2008): 2399–2408.

[171] K. I. Ozoemena, N. S. Mathebula, J. Pillay, G. Toschi, J. A. Verschoor, *Physical Chemistry Chemical Physics*, **12**,2(2010): 345–357.

[172] A. T. Chidembo, K. I. Ozoemena, B. O. Agboola, V. Gupta, G. G. Wildgoose, R. G. Compton, *Energy and Environmental Science,* **3**,2(2010): 228–236.

[173] G. Denuault, M. Sosna, K. J. Williams, *Handbook of Electrochemistry*, (2007): 431–469.

[174] T. J. Schmidt, U. A. Paulus, H. A. Gasteiger, R. J. Behm*, Journal of Electroanalytical Chemistry*, **508(**2001): 41–47.

CHAPTER 3

Experimental Methods

3.1 Introduction

Experimental and characterization techniques employed in this work are discussed in this chapter. This chapter listed the chemicals and materials used for the preparation of precursor materials and Pd-based electrocatalysts, and explains the methodology, physical characterization and the electrochemical set-ups: (i) three-electrode system for half-cell reaction (anode or cathode); (ii) micro-3D printed cell for μ-ADEFC, and (iii) EtOH gas sensing set-up for FCBrAS, as a proof-of-concept, as well as the electrochemical techniques: CV, LSV, CA and EIS.

3.2 Materials and Chemicals

All the materials and chemicals used in this work are listed in **Table 3.1**. All the chemicals were used as received without additional purification.

Table 3.1: All materials and chemical reagents used in this work

Materials and chemicals	Purity and specifications	Supplier
Absolute ethanol	ACS reagent, 99 %	MK Chemical
Nafion perfluorinated ion-exchange resin	5 wt % mixture in lower aliphatic alcohols	Sigma Aldrich

Potassium hydroxide pellets (KOH)	ACS reagent, 85 %	Association of Chemical Entrepreneur (ACE)
Sodium hydroxide pellets (NaOH)	ACS reagent, 85 %	Association of Chemical Entrepreneur (ACE)
Tin(ii)chloride.dihydrate ($SnCl_2.2H_2O$)	> 94 %	Chem-supply
Carbon black	Timical Super C45	
Cobalt nitrate hexahydrate ($Co(NO_3)_2.6H_20$)	98 %	Sigma Aldrich
Nickel nitrate hexahydrate ($Ni(NO_3)_2.6H_2O$)	98 %	Sigma Aldrich
Biphenyl,4,4'–dicarboxylic acid (BPDC)	97 %	Sigma Aldrich
1,3,5-benzenetricarboxylic acid or trimesic (TMA)	99.9 %	Sigma Aldrich
Triethyleneamine (TEA)	≥ 99.5 %	Sigma Aldrich
Dimethylformamide (DMF)	99.8 %	Sigma Aldrich
Ethylene glycol (EG)	99.8 %	Sigma Aldrich
Potassium tetrachloropalladate (VI) (K_2PdCl_4)	99.99 %	Sigma Aldrich
Pure Nitrogen (N_2)	>99.8 %	AFROX
Pure Argon (Ar)	99.998 %	AFROX

Hydrochloric acid (HCl)	32 %	Association of Chemical Entrepreneur (ACE)
2-propanol	HPLC-grade	Sigma-Aldrich
purity deionized water (Millipore)	Resistivity 18.2 MΩ	Direct-Q 3 system
Zoltek® carbon cloth	99 %	ZOLTEK
Copper (Cu) grid	200 meshes	Spi
Alumina powder	50 nm	Sympatec GmbH
polytetrafluoroethylene (PTFE) binder	60 wt % dispersion in water	Sigma-Aldrich

3.3 Methodology

Two different MOFs were prepared in this work with different metals (Co and Ni) cores and the organic linkers highlighted in **Figure 2.8**. The as-prepared MOFs were made by microwave-assisted solvothermal methods and employed as sacrificial templates to prepare metals nanoparticle supported on MOF-derived carbons (Co/MOFDC and Ni/MOFDC) with additional modifications of chemical etching and/or deposition of co-catalyst (SnO_2) nanoparticles before nanostructured Pd deposition by microwave-assisted solvothermal method. The MOFs sacrificial templates were made from two distinct organic linkers: (i) biphenyl-4,4'-dicarboxylic acid (BPDC); and (ii) trimesic acid (TMA) or 1,3,5-benzenetricarboxylic acid. While the Pd/M-based electrocatalysts synthesized were demonstrated for the applications herein are grouped into two: (i) Pd/SnO_2-based electrocatalysts (i.e., Pd/MOFDC and Pd/SnO_2/MOFDC), whose EOR performances are compared with Pd/carbon black (CB) and Pd/SnO_2/CB; and (ii)

Pd/Ni-based electrocatalysts (i.e., Pd/Ni/MOFDC and Pd/AT-Ni/MOFDC). The experimental procedures employed for the synthesis of all the precursors, composites and electrocatalysts are extensively explained in chapter 4.

3.4 Materials Characterization

The following physical characterization techniques such as Fourier transform infrared spectroscopy (FTIR), Raman spectroscopy, powder X-ray diffraction (PXRD), transmission electron microscopy (TEM), scanning electron microscopy (SEM), elemental dispersive X-ray spectroscopy (EDX), X-ray photoelectron spectroscopy (XPS), X-ray absorption spectroscopy (XAS) consisting of X-ray absorption near-edge spectroscopy (XANES) and Fourier-transform of the extended X-ray absorption fine structure (FT-EXAFS), Brunauer-Emmett-Teller (BET) and thermogravimetric analysis (TGA) are employed to probe the physicochemical properties of the samples including the as-prepared MOFs sacrificial templates, composites and electrocatalysts.

3.4.1 Fourier-Transform Infrared Spectroscopy (FTIR)

The FTIR is an analytical technique used to determine functional groups present in organic and/or inorganic samples. It measures the infrared radiation absorption of the samples against wavelength. This technique helps to recognize molecular constituents and composition of the samples. In this work, all experiments were carried out with the use of the BRUKER TENSOR 27 FTIR spectrometer with OPUS software. The method employed for data collection: few mg of each dried and ground sample was loaded on the sample plate of the instrument to fill it, then data-sheet was prepared to save the sample IDs and location, thereafter the instrument was switched on and log onto the OPUS software as the operating instruction was followed.

3.4.2 Raman Spectroscopy

The Raman spectroscopy is a surface analytical technique that uses inelastic photons scattering or Raman scattering with monochromatic light sources in the visible, near infrared or near ultraviolet range to interact with vibration modes of the sample's molecules. This interaction determines the structural fingerprints of the vibrational modes of the molecule in the samples. This technique is mainly important for characterizing carbon materials. In this work, experiments were conducted with the BRUKER SENTERRA Raman Spectrometer with excitation wavelength (514.5 nm), Beam power (0.4 mW), spectra resolution (3 cm^{-1}) and scanned in a range of 250 – 2500 cm^{-1}. The method employed for data collection: few mg of each dried and ground sample was loaded on the sample plate of the instrument to fill it, then data-sheet was prepared to save the sample IDs and location, thereafter the instrument was switched on and log onto the OPUS software as the operating instruction was followed.

3.4.3 Power X-ray Diffraction (PXRD)

The PXRD is a rapid non-destructive analytical technique with the operation of constructive interference of monochromatic X-ray. It is employed basically to determine phases and structures of crystalline samples and gives information on the dimension of unit cell. The sample to be analyzed must be uniform and finely ground, as the average composition of the bulk is ascertained. The PXRD was done using Bruker D2 XRD with Cu$K\alpha$ radiation (λ = 1.5046 Å, 45 kV, 40 mA, step size = 0.02º). The diffractograms were scanned from doubled Bragg's angle (2θ) of 5 to 100º to determine crystal information of the sample. The method employed for data collection: uniformly and finely ground samples were properly packed into the powder specimen sample holder and the surfaces were smoothened and inserted into the instrument

and scanned from double Bragg's angle (2θ) of 8 to 110º to reveal the crystal information of the samples. The lattice parameters of the diffractograms were calculated using Scherrer's formula, given in **Equation 3.1**.

$$\tau = \frac{K\lambda}{\beta\, cos\theta} \qquad (3.1)$$

Where τ, K, λ, β and θ are the mean crystallite size, a dimensionless shape factor with a value (0.9), the wavelength of Cu $K\alpha$ radiation (1.5406 Å), the full-width half maximum of the peak in consideration after baseline subtraction in radians and the Bragg angle (º), respectively.

3.4.4 X-ray Photoelectron Spectroscopy (XPS)

The XPS is a surface-sensitive technique that can measure the qualitative and quantitative elemental composition and chemical state of the elemental constituents of samples. The XPS spectra were obtained using the AXIS SUPRA XPS instrument with monochromatic AlKα radiation (1486.7 eV), X-ray power 300 W, and X-ray spot size 900 µm and the constituent elements are calibrated at their respective binding energies. The method employed for data collection: powder of each sample was dispersed in EtOH and sonicated for uniformity to obtain a paste, then the paste was casted onto surface of a cleaned silicon wafer, smoothen the surface and allowed to dry in the air and a survey spectrum was obtained by scanning over a wide range of binding energies, as well as each elemental composition was scanned at its respective binding energies ranges.

3.4.5 X-ray Absorption Spectroscopy (XAS)

The XAS is a sophisticated technique performed at synchrotron radiation facilities with intense and tunable X-ray beams and utilized to determine the local geometric and/or electronic structure of the samples. The XAS measurements were conducted by calibrating the photon energy (0.1 – 100 eV) using a crystalline monochromator in the range where core electrons could be excited at the K-edge for each element (Pd and Ni) in consideration. The XAS generates two main spectra regions as follows:

3.4.5.1 Absorption Threshold

The transition to the lowest unoccupied states is used to determine the absorption threshold, which could be classified into two:

- States at the Fermi level in an element that gives edge rise with an arctangent shape.
- Bound core electrons in insulating material with Lorentzian line shape occurring in a pre-edge region at lower energies than the transitions to the unoccupied level.

3.4.5.1.1 X-ray Absorption Near-Edge Structure (XANES)

The XANES is an XAS that is controlled by transitions from the core to quasi-bound electronic states and involves multiple scattering resonances for photoelectrons with low kinetic energy range (10 – 150 eV) beyond the chemical potential or shape resonances in molecular spectra because final states of short life-time have multiple domains with the continuum fano line-shape. The XANES helps to deduce final oxidation states of constituent elements in samples.

3.4.5.1.2 Fourier-Transform of the Extended X-ray Absorption Fine Structure (FT-EXAFS)

The FT-EXAFS predominates when the scattering cross-section with neighboring elements is weak in high kinetic range of the photoelectron. Thus, XAS experimental analysis is centred on the two regions of the XANES and FT-EXAFS.

The method employed for the XAS data: electrode inks were prepared by mixing 8.2 MΩ purity deionized water (Millipore), 2-propanol (HPLC-grade, Aldrich), 5 wt% Nafion solution and the catalyst powder. The sticky paste (ink) was hand-painted on a Zoltek® carbon cloth and dried for 15 min in a vacuum oven at 65 ºC. The determining Pd geometric loadings were chosen to offer 0.3 transmission mode at the Ni and Pd K-edges. The data at the Ni and Pd K-edge of the samples were acquired in the transmission mode at the beamline 7-BM of the National Synchrotron Light Source (NSLS) II, Brookhaven National Laboratory (BNL). The experimental methods employed in this work were detailed in previous report [1]. All the XAS data were collected with respect to the appropriate reference foil to support energy alignment and normalization. The data were further processed and fitted utilizing the Ifeffit-based Athena [2] and Artemis [3] programs, while the scans were calibrated, aligned and normalized with the background being removed utilizing the IFEFFIT suite [4]. The χ(R) were modelled with FEFF6 to calculate the single scattering paths [5]. The Δμ-XANES analysis was performed following methods previously described [6] and the spectra difference was calculated using **Equation 3.2**.

$$\Delta\mu = \mu(V) - \mu(0.54V) \qquad (3.2)$$

Where Δμ, μ(V) and μ(0.54V) are the spectra difference, the absorption coefficient of the sample at a potential of interest and is the reference signal at 0.54 V, respectively.

3.4.6 Brunauer-Emmett-Teller (BET) Surface Area

The BET surface area is a technique that adopts N_2 adsorption/desorption at -195 ºC and thereafter the sample was outgassed at 150 ºC for 4 h under a N_2 gas. This technique is basically employed to determine specific surface area, porosity and pore volume of samples. The BET analysis was done using the BET Micromeritics TriStar 3000 with relative pressure ranges of 0.05 to 0.30 from the absorption data for the surface area measurements. The method employed for BET data: before the BET measurement, the sample was first pre-treated at elevated temperature (80 ºC) in inert high purity N_2 flow to remove any contaminants, as the contaminants could seriously affect the BET surface in subsequent analysis and the operating instruction of the instrument was strictly followed to obtain the BET data.

3.4.7 Thermogravimetric Analysis (TGA)

The TGA is a quantitative analytical method employed to keep track of the mass of the constituent elements of samples as the temperature increase under a stable gas flow. The TGA profile gives information like phase transformations, adsorption, desorption, chemisorption, thermal decomposition, oxidation and reduction of the samples. This analysis was carried out using the PerkinElmer TGA 4000 analyzer. The method employed for TGA profile: each sample was loaded from the top of the sample pan with a thermocouple, a protective tube isolates both heating elements and cooling coils from the sample pan, then ambient air was flown through the sample at a flow rate (20 mL min^{-1}) and heating rate (10 ºC min^{-1}).

3.4.8 Transmission Electron Microscopy (TEM)

The TEM is a kind of microscopic technique that can image nanosized (< 100 nm) components of the sample. The TEM micrographs are obtained when beams of electrons are transmitted to interact with the sample. This technique is employed to determine morphology and mean particle size of the nanostructured samples. The TEM micrograph was carried out with the FEI Tecnai T12 Sprint TEM, while the nanoparticles size distribution was carried out using ImageJ. The method employed for TEM imaging: samples were first prepared by dispersion of very little amount of sample in EtOH to obtain a very dilute solution, then coated a drop of the diluted solution on the Cu grid and allowed to dry at room temperature before the analysis. The dried coated Cu grid was then inserted into the instrument and the operating instruction was strictly followed.

3.4.9 Scanning Electron Microscope (SEM) and Energy Dispersive X-ray Spectroscopy (EDXS)

The SEM is another microscopic technique that gives images of samples' surface when beams of electrons are focussed on the surface of the sample. Interaction of the beams of electrons on the surface of the sample gives the image of the sample's surface morphology and topography. The SEM images were acquired utilizing the FEI Nova Nanolab 600 SEM with an acceleration voltage of 2.00 kV, coupled with EDX which is used to identify the elemental composition of the samples. Samples preparation was performed by coating very little amount of powder sample on carbon tape and may be further coated with Au to prevent the samples from charging. The carbon tapes containing the samples were inserted into the instrument and the operating instruction was strictly followed.

3.5 Experimental details for Electrochemical Measurements

Two distinct cells were fabricated for the electrochemical measurements: (i) three-electrode configuration using a beaker modified cell; and (ii) Full cell testing using a micro-3D printed cell (shown and explained in the next chapter).

3.5.1 Three-Electrode Configuration

In the three-electrode configuration (**Figure 3.1**) for half-cell reactions, working (electrocatalysts ink modified with glassy carbon electrodes (GCE, 3.0 mm, 0.071 cm^2 and 5.0 mm, 0.196 cm^2)), counter (Pt wire) and reference (AglAgCl, saturated KCl) electrodes were used for hydrostatic reactions, but RDE and/or RRDE are used for hydrodynamic reactions. The modified electrocatalysts inks on the GCEs performed by dispersion of 2.0 mg of each electrocatalyst in 1.0 mL of EtOH and 50 µL of Nafion and then sonicated for 30 min to ensure uniform mixing. The GCE was well polished with a slurry made with 1.0 µm of alumina powder. Then, the prepared electrocatalyst ink (5.0 µL) was drop-casted onto the well-polished GCE and allowed to dry in air at room temperature before further use, to afford each electrocatalyst's loading of 0.00097 mg_{Pd}. All electrochemical measurements were investigated in freshly prepared KOH solution (0.5 or 0.1 M) and some of the parameters of interest are referred to a reversible hydrogen electrode (RHE) utilizing the formula previously explained in **Equation 2.26**.

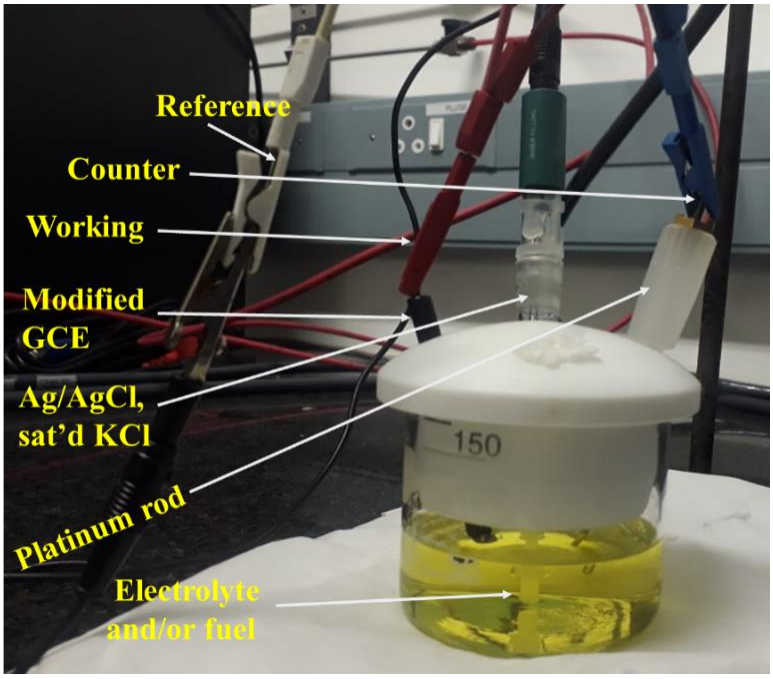

Figure 3.1: Three-electrode configuration set-up

3.6 Electrochemical Techniques

All electrochemical measurement of the half-cell reactions and full cell, as well as gas sensing were performed with at least two of the following techniques: CV, LSV, current-voltage (i-v) curves, galvanostatic discharge test, CA and EIS at different experimental conditions depending on the reaction of interest, as elucidated in subsequent chapters.

3.7 Reference

[1] Q. Jia, W. Liang, M. K. Bates, P. Mani, W. Lee, S. Mukerjee*, ACS Nano*, **9**(2015): 387–400.

[2] M. Newville, *Journal of Synchrotron Radiation*, **8**(2001): 322–324.

[3] B. Ravel, K. Gallagher, *Physica Scripta*, **2005**(2005): 606.

[4] M. Newville, P. Limacrvincedilscaron, Y. Yacoby, J. J. Rehr, E. A. Stern, *Physical Review*, **47**(1993): 14126.

[5] A. L. Ankudinov, B. Ravel, J. J. Rehr, S. D. Conradson, *Physical Review B*, **58**(1998): 7565–7576.

[6] Q. Jia, D. E. Ramaker, J. M. Ziegelbauer, N. Ramaswamy, A. Halder, S. Mukerjee, *Journal of Physical Chemistry C*, **117**(2013): 4585–4596.

CHAPTER 4

Study of Nanostructured Pd/M Electrocatalysts MOF-Derived Carbons for Direct Ethanol Micro-Fuel Cell

4.1 Introduction

In the last decade, the alkaline DEFCs have emerged as one of the most promising renewable energy conversion devices to replace the commonly used fossil fuel technology because of their well-known advantages stemming from: less toxicity of the fuel (EtOH) used, making the device environmentally benign; gross availability of the fuel from agricultural waste, helping to channel useless material to useful resources; and above all a close range of theoretical energy density to fossil fuel [1–5]. For viable commercialization of the alkaline DEFCs, amongst the many efforts to realize this was the development of efficient and effective non-Pt electrocatalysts which are currently explored to drive the sluggish anodic reaction (EOR), as the complementary cathodic reaction (ORR) could easily be driven by non-noble metal catalysts like FeCo/C, thereby reducing the overall cost of fabricating the alkaline DEFC devices [6–8]. Pd-based electrocatalysts involving deposition of nanostructured Pd/M anchored on carbon supports, where the co-metal catalysts (M = Sn, Ni, Fe, Ru, Mg, e.t.c.) to mitigate the major challenges stemming from poor utilization of the catalyst to carbonaceous species poisoning have displayed intrinsic excellent electrocatalytic properties superior to those of Pt materials, especially in alkaline

conditions [9–11]. However, little or no reports have been made for the used carbon supports derived from the MOFs. The choice of the MOF-derived carbons supports could be traced to their inherent properties, previously explained in Chapter 2 sub-section 2.6.1 and 2.6.2.

Thus, in this Chapter, systematic design and synthesis of novel Pd-based electrocatalysts classified into two different batches: (i) the Pd/SnO_2-based electrocatalysts (i.e., Pd/MOFDC and Pd/SnO_2/MOFDC) and their electrocatalytic activities toward EOR and µ-DEFC compared to Pd/CB and Pd/SnO_2/CB (where CB = carbon black); and (ii) the Pd/Ni-based electrocatalysts (i.e., Pd/Ni/MOFDC and Pd/AT-Ni/MOFDC) and their comparative electrocatalytic properties toward EOR and µ-DEFC are demonstrated.

4.2 Results and Discussion

Based on the ligands (BPDC and TMA) precursors used for the preparation of the MOFs sacrificial templates and co-metal catalysts led to the classification of the as-prepared electrocatalysts into two: (i) Pd/SnO_2-based electrocatalysts (Pd/MOFDC and Pd/SnO_2/MOFDC), whose EOR activities were compared to Pd/CB and Pd/SnO_2/CB; and (ii) Pd/Ni-based electrocatalysts (Pd/Ni/MOFDC and Pd/AT-Ni/MOFDC). Thus, the synthesis methods, results and discussion are explained within each class of the electrocatalysts demonstrated for EOR and µ-DEFC separately and then compared their overall performances.

4.2.1 Microwave-Assisted Solvothermal Synthesis of Pd/SnO_2-based electrocatalysts

Co-MOF was first made with the BPDC organic linkers and triethyleneamine (TEA) to functionalize with nitrogen, followed by carbonization and chemical etching (MOFDC), then the addition of SnO_2 nanoparticles to yield SnO_2/MOFDC and subsequent nanostructured Pd deposition to afford Pd/SnO_2-based electrocatalysts, as diagrammatically illustrated in **Figure 4.1** and briefly explained: The microwave-assisted solvothermal synthesis of the Co-MOF is as follows: 0.4366 g of $Co(NO_3)_2.6H_20$ was mixed with 0.3634 g of BPDC and 1.5 mL of TEA, and dissolved in 50 mL of DMF. The mixture was stirred for 30 min and sonicated for 15 min to ensure uniform mixing of the components. Then, the homogenized mixture was subjected to microwave (MW, Anton Paar Multiwave 3000 system, λ = 0.122236 m) irradiation at 600 W for 30 min and cooled to room temperature. Dark purple precipitates were obtained, collected and washed with ethanol several times with the aid of centrifuge. The as-prepared Co-MOF was dried in a vacuum oven at 60 ºC overnight.

The as-prepared Co-MOF (prepared above) was placed in a quartz boat and heated in a tube furnace from 25 to 600 ºC under an inert environment of Ar flow at 5 K min^{-1}, subsequently ramped the heating to 800 ºC at 3 K min^{-1} and maintained for 3 h to produce Co nanoparticles anchored on MOFDC (Co/MOFDC). The prepared Co/MOFDC was chemically etched with 2.0 M HCl (10 mL) to remove the Co nanoparticles and afford the MOF-derived carbon (MOFDC), which was washed severally with distilled H_2O and dried in a vacuum oven at 80 ºC overnight before use for the preparation of SnO_2/MOFDC, Pd/MOFDC and Pd/SnO_2/MOFDC.

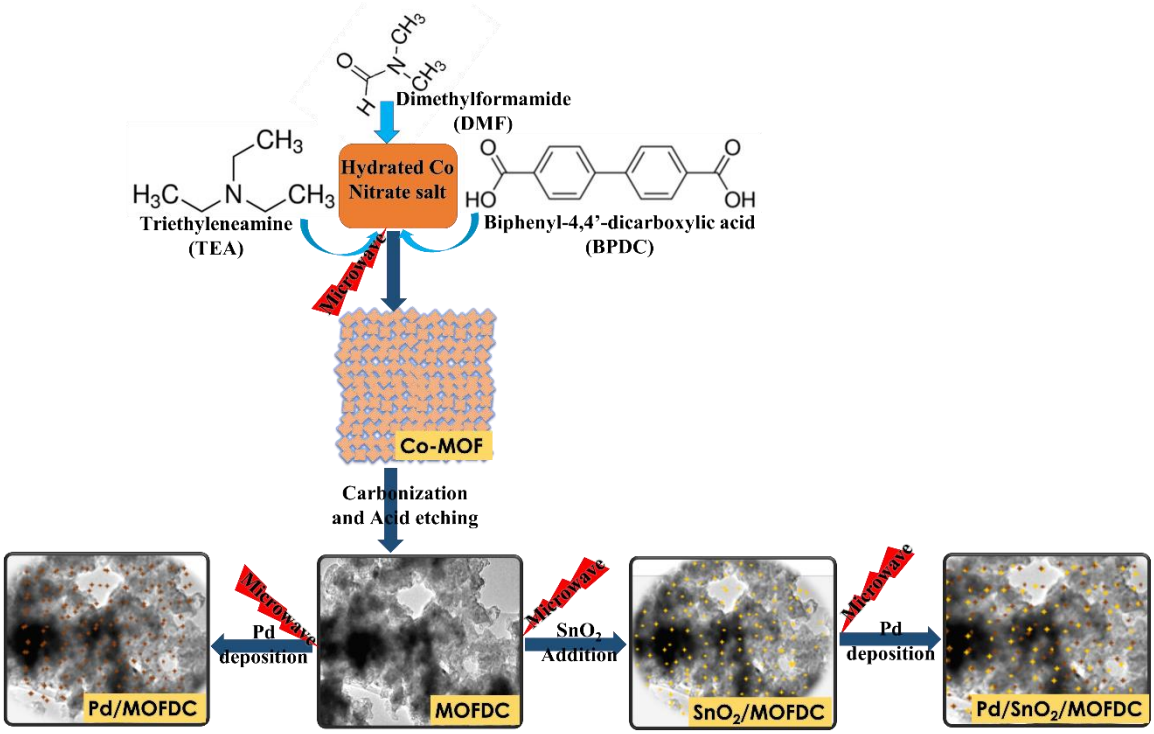

Figure 4.1: Diagrammatic illustration of the Pd/SnO_2-based electrocatalysts (Pd/MOFDC and Pd/SnO_2/MOFDC)

SnO_2 nanoparticles were deposited on the prepared MOFDC using microwave-assisted solvothermal synthesis: Briefly, 47.8 mg of $SnCl_2.2H_2O$ and 80 mg of the MOFDC were added to 50 mL of a mixture of EG and H_2O (4:1 by volume). The mixture was stirred for 2 h and sonicated for 1 h until uniformity is attained. Then, subjected to MW irradiation at 600 W for 1 h. The as-prepared SnO_2/MOFDC was washed severally with H_2O and collected using centrifugation and further dried in a vacuum oven at 80 ºC for 4 h. This procedure was repeated for the preparation of SnO_2/CB, where carbon black (CB) was used rather than the MOFDC.

The Pd/SnO_2-based electrocatalysts (Pd/MOFDC and Pd/SnO_2/MOFDC) were made by dissolving 61.35 mg of K_2PdCl_4 in 50 mL of EG in two separate flasks and stirred for 30 min, as the solutions' pH is adjusted to 12 with 1.0 M NaOH solution. Then, 80

mg each of the as-prepared MOFDC and SnO_2/MOFDC were added separately to the two flasks containing the solutions and stirred for additional 30 min. The two separate solutions were subjected to MW irradiation at 600 W for 1 h to deposit nanostructured Pd on the respective supports. Thereafter, the pH of the resulting solutions containing Pd/MOFDC and Pd/SnO_2/MOFDC were reduced to 3 with 0.1 M HNO_3, as Pd nanoparticles optimally precipitate in acidic condition. The Pd/SnO_2-based electrocatalysts were further washed with ethanol with the aid of centrifuge and dried in a vacuum oven at 80 ºC for 4 h. This procedure was repeated for the preparation of Pd/CB and Pd/SnO_2/CB using CB and SnO_2/CB as supports.

4.2.2 Pd/SnO_2-based Electrocatalysts for Direct Ethanol Micro-Fuel Cell

The physical properties of the Co-MOF precursor, intermediate composites and Pd/SnO_2-based electrocatalysts are thoroughly investigated using Raman, powder XRD, XPS, EDX, TEM and BET, and tested for EOR (half-cell reaction, **Figure 3.1**) and µ-DEFC (full cell, **Figure 4.14**).

4.2.2.1 Raman Spectroscopy

Figure 4.2 shows the Raman spectra of the as-prepared Co-MOF sacrificial template, Co_3O_4/MOFDC and MOFDC. The following vibrational modes: longitudinal (LO) mode, Co-O, C-N aliphatic, C-O-C, (C-O-C) asymmetric, (C-C) aliphatic, (C-O-C)ring + CH and (C-C) ring at 130, 404, 631, 850, 1139, 1199, 1266 and 1440 cm^{-1}, respectively are present in the as-prepared Co-MOF sacrificial template, confirming its synthesis. Then, the carbonization of the Co-MOF sacrificial template at high temperature (800 ºC) decomposes the frameworks and resulted in the formation of Co_3O_4 nanoparticles supported MOF-derived carbon (Co_3O_4/MOFDC). Hence, the Raman spectrum of the

Co_3O_4/MOFDC reveals cobalt oxides vibration modes: E_g, F_{2g} and A_{1g} at 481, 524 and 691 cm^{-1}, as well as the first-order D- and G-bands of carbon at 1349 and 1586 cm^{-1}, respectively, confirming the breakdown of the Co-MOF frameworks.

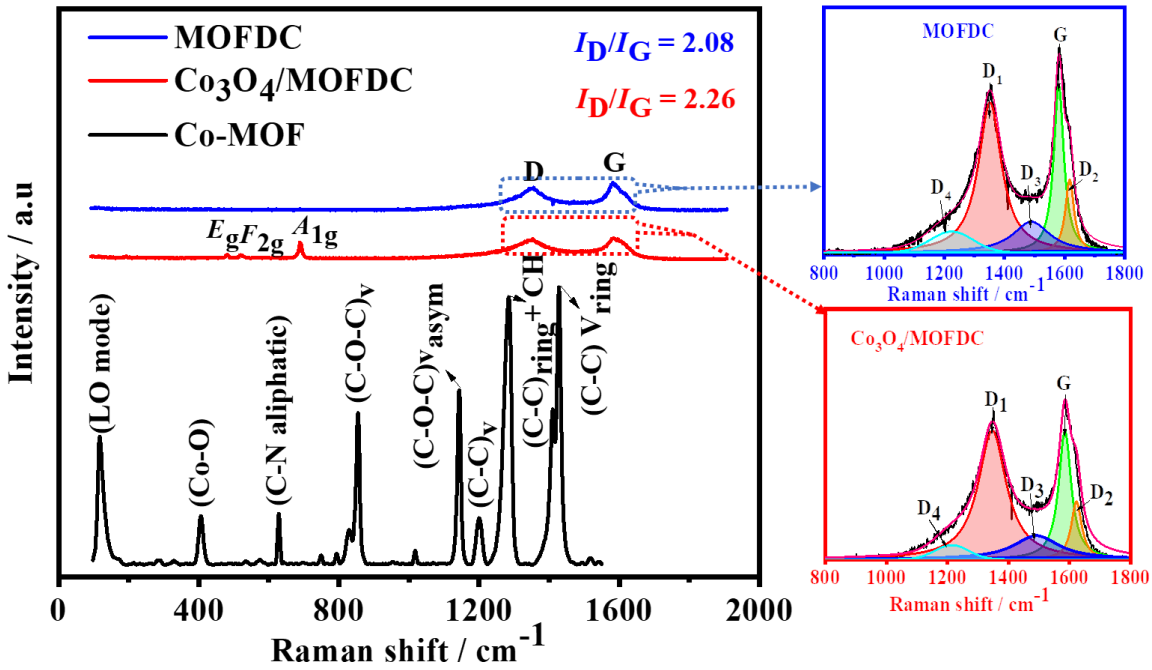

Figure 4.2: Raman spectra of the as-prepared Co-MOF, Co_3O_4/MOFDC and MOFDC

Thereafter, the as-prepared Co_3O_4/MOFDC was chemically etched, removing the Co_3O_4 nanoparticles to yield the MOFDC. Only the D- and G-bands are present in the Raman spectrum of the MOFDC with shifts to higher and lower frequencies of the D-(1352 cm^{-1}) and G-(1582 cm^{-1}) bands, respectively. The shifts of these bands may be ascribed to the removal of metallic Co and inducing disorders, resulting in lattice defect, distortion and finite particle size [12]. The D- and G-bands are further split into five distinct spectra: D_4 (1229 cm^{-1}), D_1(1343 cm^{-1}), D_3 (1489 cm^{-1}), G (1575 cm^{-1}) and D_2 (1610 cm^{-1}), where the values of I_{D1}/I_G are calculated. The I_{D1}/I_G values of 1.76 and 1.95 were evaluated for the MOFDC and Co_3O_4/MOFDC, respectively according to previously established method [13,14]. The reduced I_{D1}/I_G value of the MOFDC shows that it is more graphitic than the composite [15,16].

4.2.2.2 Powder X-ray Diffraction (PXRD)

The PXRD (**Figure 4.3**) was employed to reveal the crystallinity and structure of the as-prepared Co-MOF, Co_3O_4/MOFDC, MOFDC and electrocatalysts. In **Figure 4.3a**, the multiple diffractions of the Co-MOF reveal that it is crystalline. This is consistent with the diffraction peaks obtained previously for Co-MOF using 1,3,5-tricarboxylic acid chelating agent [17]. The differences in these diffraction peaks are traced to the different chelating agents. The following diffraction peaks: 25.8, 36.5, 42.6, 44.0, 51.7 and 61.6º correspond to the C(002), Co_3O_4(311), Co_3O_4(100), Co(111), Co(200) and Co_3O_4(440), respectively. These results show that there is a mixture of Co and Co_3O_4 nanoparticles on the carbon support and agree with the previous report [18]. The graphitic carbon (MOFDC) diffraction is most pronounced at 25.8º with little diffraction peaks for the Co/Co_3O_4 nanoparticles, indicating removal of most of the metal/metal oxide nanoparticle after acid treatment.

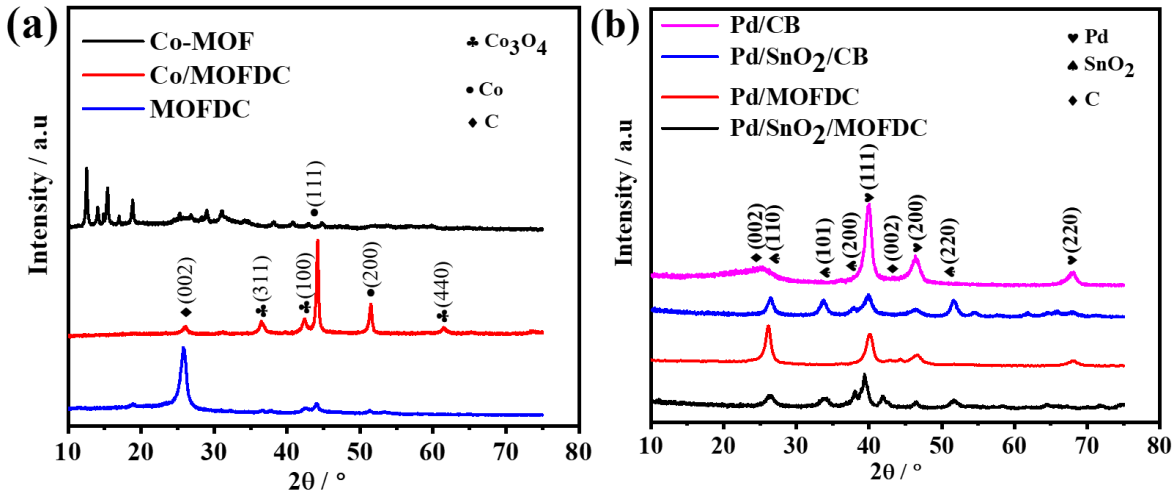

Figure 4.3: PXRD of (a) the as-prepared Co-MOF, Co_3O_4/MOFDC and MOFDC, and (b) Pd/CB, Pd/SnO_2/CB, Pd/MOFDC and Pd/SnO_2/MOFDC

Table 4.1: Lattice parameters of the Pd/SnO_2-based electrocatalysts at 2θ of *ca.* 40º

Lattice parameters	Pd/SnO_2-based Electrocatalysts			
	Pd/MOFDC	Pd/SnO_2/MOFDC	Pd/CB	Pd/SnO_2/CB
2θ / º	40.069	39.296	40.091	39.873
d / Å	2.2476	2.2900	2.2465	2.2626
τ / nm	7.60	6.80	9.76	7.84

Figure 4.3b shows the diffraction peaks of the Pd/CB, Pd/SnO_2/CB, Pd/MOFDC and Pd/SnO_2/MOFDC electrocatalysts. All the electrocatalysts have diffraction peaks: 25.6, 40.0, 46.5 and 68.0º ascribable to the C(002), face-centred cubic lattices Pd(111), Pd(200) and Pd(220), respectively. The SnO_2 containing electrocatalysts have additional diffraction peaks at 26.4, 33.7, 37.9 and 51.6º attributable to SnO_2(110), SnO_2(101), SnO_2(200) and SnO_2(220), respectively. These results agree with previously reported XRD patterns for Pd/SnO_2-based electrocatalysts [11]. The lattice parameters: lattice constants (*d* / Å) and crystallite sizes (*τ* / nm) of the electrocatalysts at double Bragg's angle (2θ of *ca.* 40º) are calculated following Scherrer's formula (**Equation 3.1**) and summarized in **Table 4.1**. It was observed that the crystallite of the electrocatalysts containing SnO_2 reduced with increase Pd interatomic distance relative to the ones without SnO_2. These results may be due to the strong interaction of the SnO_2 and nanostructured Pd, leading to alloying properties of the metals nanoparticles [19].

4.2.2.3 X-ray Photoelectron Spectroscopy (XPS)

Chemical states of the constituent elements of the SnO_2 containing electrocatalysts were probed qualitatively and quantitatively using the XPS analysis (**Figure 4.4**). A

wide survey of the Pd/SnO_2/CB (**Figure 4.4a**) and Pd/SnO_2/MOFDC (**Figure 4.4b**) reveal the following constituent elements: Pd, Sn, O, N and C. Further understanding of the chemical environments of the constituent elements, spectrum corresponding to each element is deconvoluted into two or more spectra. **Figures 4.4c** and **4.4d** show the deconvoluted Pd 3*d* into doublet of $3d_{5/2}$ and $3d_{3/2}$ at binding energies of 335.6 and 341.0 eV for the electrocatalysts, ascribable to the mixed formation of Pd and PdO_x, respectively [20]. The formation of the PdO may be traced to the stabilization of the metallic Pd by the SnO_2 interaction [21]. **Figure 4.4e** shows the doublet deconvoluted Sn(IV) $3d_{5/2}$ and $3d_{3/2}$ at binding energies of 487.3 and 495.5 eV, respectively for the Pd/SnO_2/CB, revealing the presence of only the SnO_2. While the Pd/SnO_2/MOFDC (**Figure 4.4f**) has quartet deconvoluted spectra with additional spectra at 484.9 and 493.4 eV attributed to metallic Sn $3d_{5/2}$ and Sn $3d_{3/2}$ of metallic Sn, respectively, indicating that the Pd/SnO_2/MOFDC has a mixture of SnO_2 and metallic Sn. These observations revealed that increased electron density of the MOFDC due to doping with heteroatoms reduced some of the SnO_2 to metallic Sn. The chemical environments of the carbon support for the electrocatalysts were confirmed from the C 1*s* deconvolution (**Figure 4.4g**) for the Pd/SnO_2/CB at binding energies of 280.1, 284.8 and 286.8 eV, corresponding to metallic carbide, C-C (sp^3 only), and O=C-O bonds, whereas the Pd/SnO_2/MOFDC (**Figure 4.4h**) has metallic carbide, C-C (sp^3), C=C (sp^2) and C-N at binding energies of 280.9, 281.9, 282.5 and 284.6 eV, respectively.

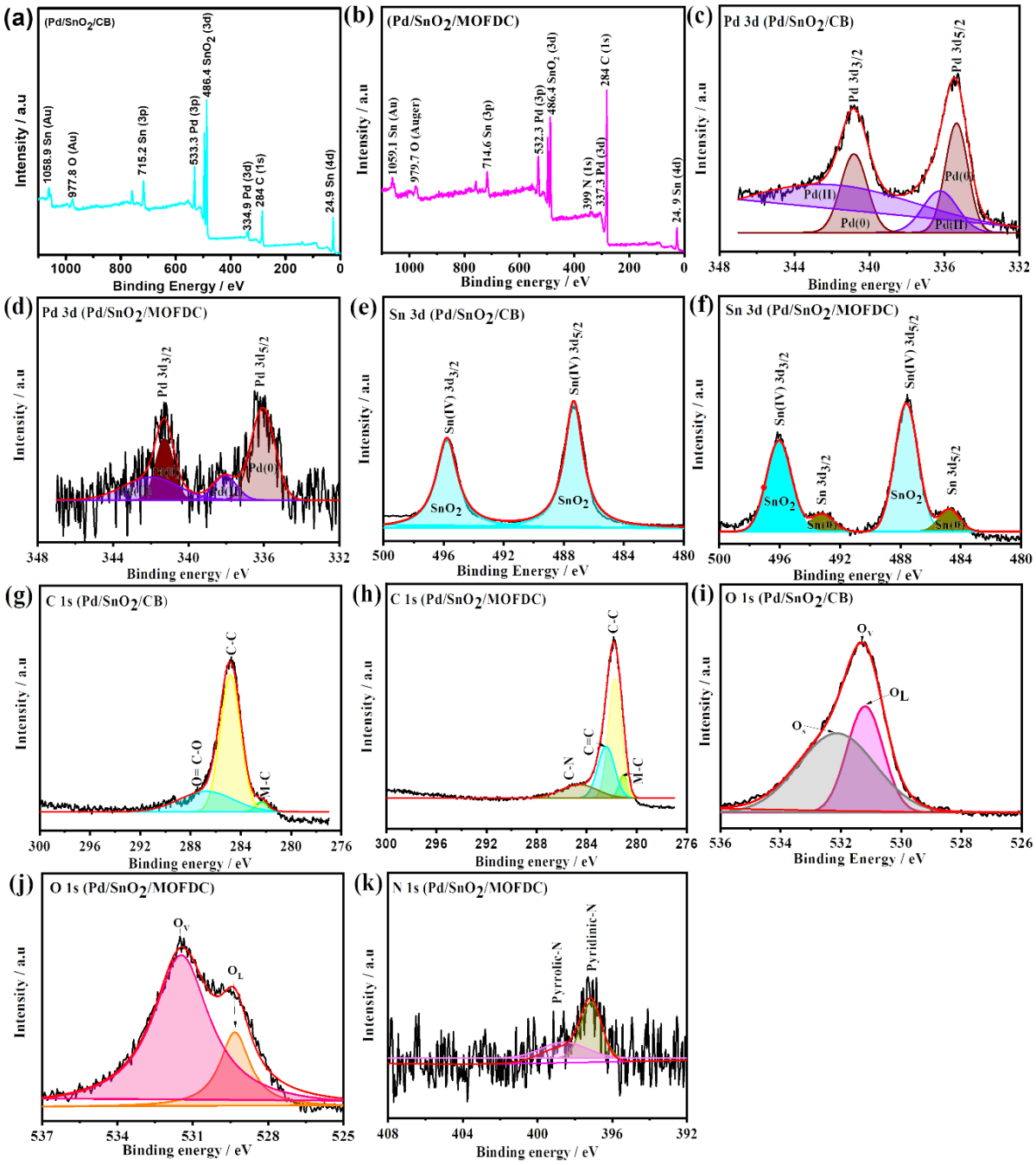

Figure 4.4: XPS of (a) Pd/SnO_2/CB, (b) Pd/SnO_2/MOFDC, deconvolved peaks (c,d) Pd 3*d*, (e,f) SnO_2 3*d*, (g,h) C 1*s*, (i,j) O 1*s* and (k) N 1*s*

The presence of the C-N in the Pd/SnO_2/MOFDC could be traced to the use of TEA, among the precursor materials for the synthesis of the Co-MOF sacrificial template for the MOFDC. Deconvolution of O 1*s* of the Pd/SnO_2/CB (**Figure 4.4i**) gives three broad distinct peaks at binding energies at 531.0 (lattice oxygen, O_L)), 531.3 (oxygen

vacancy, O_V) and 532.4 eV (oxygen surface coverage, O_S) attributed to the metal-oxygen bond, oxygen deficiency and surface coverage of OH, respectively. Whereas the O 1*s* deconvolution of the Pd/SnO_2/MOFDC (**Figure 4.4j**) shows two broad distinct spectra at 529.5 and 531.5 eV attributed to the O_L and O_V, respectively. These results confirmed the deficiency of oxygen and metals-O bonds in the electrocatalyst with MOFDC support corroborate with a reduced amount of O in the XPS quantitative analysis (**Table 4.2**) and strong alloying of the Pd and Sn metallic oxides. This observation may be traced to the reducing properties of the MOFDC because of its increased electron density. **Figure 4.4k** shows N 1*s* deconvoluted peaks for only Pd/SnO_2/MOFDC, containing pyridinic-N and pyrrolic-N at 397.2 and 398.9 eV, respectively. The presence of N only in the Pd/SnO_2/MOFDC is traced to the use of TEA for the synthesis of the sacrificial template. The qualitative elemental analysis of the electrocatalysts is summarized in **Table 4.2**.

Table 4.2: XPS Percentage by the mass elemental composition of the Pd/SnO_2-based electrocatalysts

XPS	Pd/SnO_2-based Electrocatalysts	
Elemental compositions	Pd/SnO_2/MOFDC	Pd/SnO_2/CB
Pd / wt %	16.16 ± 0.59	15.46 ± 0.37
Sn / wt %	21.09 ± 0.66	21.77 ± 1.11
C / wt %	51.01 ± 0.92	51.36 ± 0.93
O / wt %	10.35 ± 0.62	11.41 ± 0.69
N / wt %	1.38 ± 0.65	0.00

4.2.2.4 Transmission Electron Microscopy (TEM)

The TEM (**Figure 4.5**) was used to view the morphology of the MOFDC, SnO_2/MOFDC and Pd/SnO_2/MOFDC. The MOFDC (**Figure 4.5a)** shows a flake-like morphology without nanoparticles supported on it, whereas the deposition of SnO_2, Pd and Pd/SnO_2 on the MOFDC reveals some nanoparticles with mixed morphologies from spherical and pseudo-spherical, as shown in **Figures 4.5b** – **4.5d**.

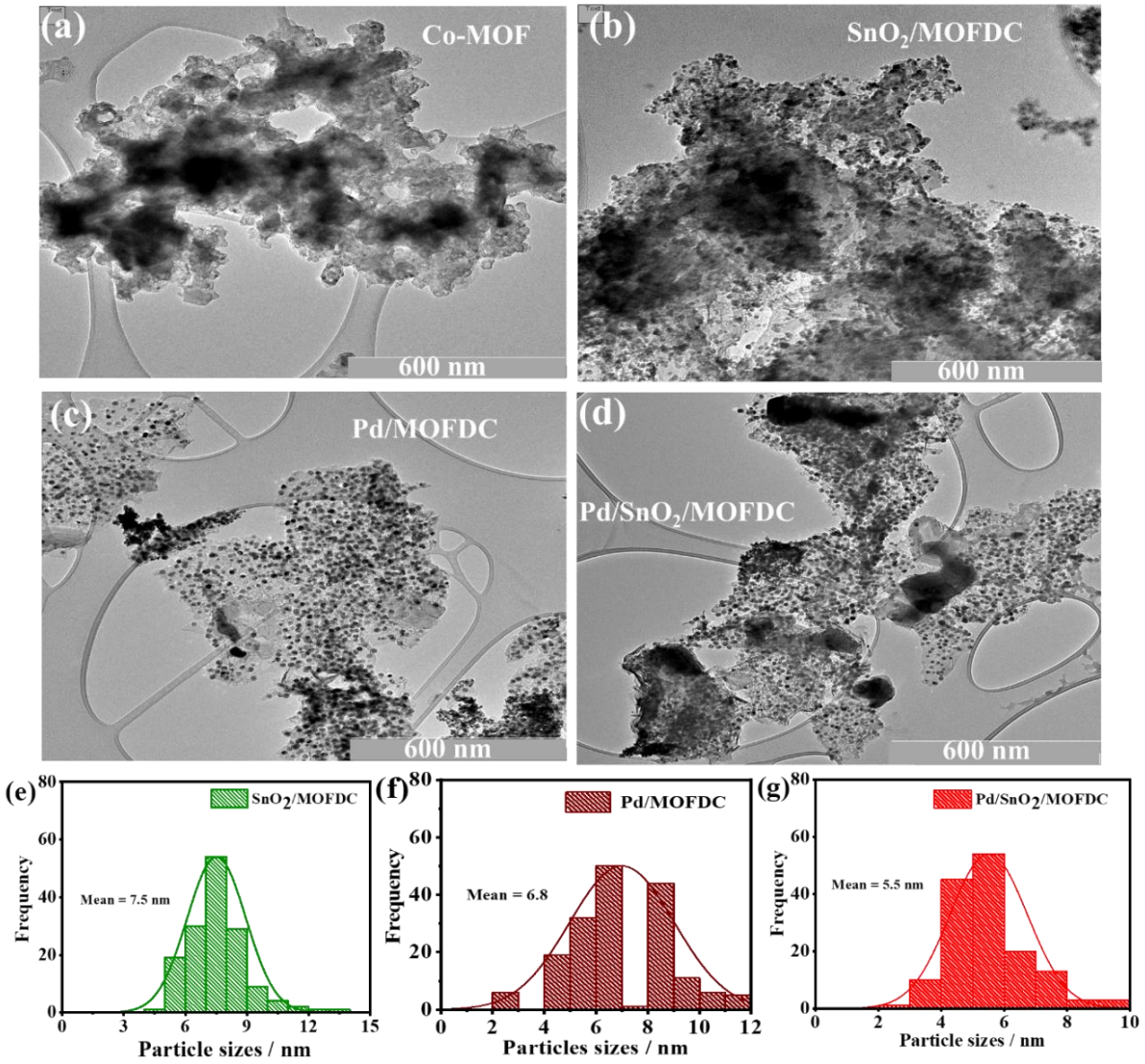

Figure 4.5: TEM images of (a) MOFDC (b) SnO_2/MOFDC, (c) Pd/MOFDC and (d) Pd/SnO_2/MOFDC, particle size distribution of (e) SnO_2/MOFDC, (f) Pd/MOFDC and (g) Pd/SnO_2/MOFDC

The mean particle size of the SnO_2 was 7.5 ± 0.8 nm (**Figure 4.5e**), while the Pd and Pd/SnO_2 alloy have mean particle sizes of 6.8 ± 0.6 (**Figure 4.5f**) and 5.5 ± 0.5 nm (**Figure 4.5g**), respectively. The reduced mean particle size of the Pd/SnO_2 alloy may be due to the longer exposure to MW irradiation.

4.2.2.5 Energy Dispersive X-ray Spectroscopy (EDXS)

The qualitative elemental composition of the electrocatalysts was further tested for using the EDX (**Figure 4.6**), revealing the following elements: Pd, Sn, C, O and Co. The presence of Co in the Pd/SnO_2/MOFDC is traced to the Co-MOF sacrificial template, which agrees with the PXRD result that Co residue was left after chemical etching. This composition is expected in the Pd/MOFDC, except for the absence of Sn.

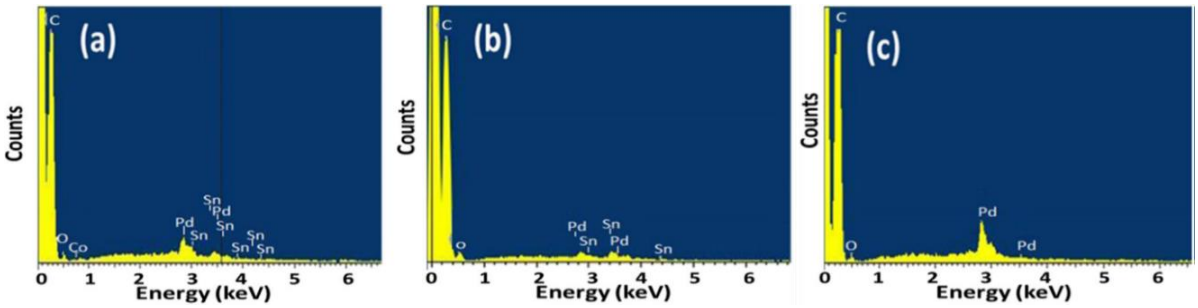

Figure 4.6: EDXS of (a) Pd/SnO_2/MOFDC, (b) Pd/SnO_2/CB and (c) Pd/CB

4.2.2.6 Thermogravimetric Analysis (TGA)

Figure 4.7 shows the TGA micrographs of the as-prepared Co-MOF, Co_3O_4/MOFDC, MOFDC, SnO_2/MOFDC and Pd/SnO_2/MOFDC, which is carried out in the air. The as-prepared Co-MOF shows two thermal decomposition steps: (i) loss of water molecules around 100 ºC because it tends to adsorb water; and (ii) complete decomposition of its frameworks at 372 ºC down to 541 ºC with residue of Co oxide nodes, proving that

the Co-MOF is thermally unstable at 400 ºC and above. This result agrees with Co-MOF using 2,5-dihydroterephtalic acid chelating agent [18].

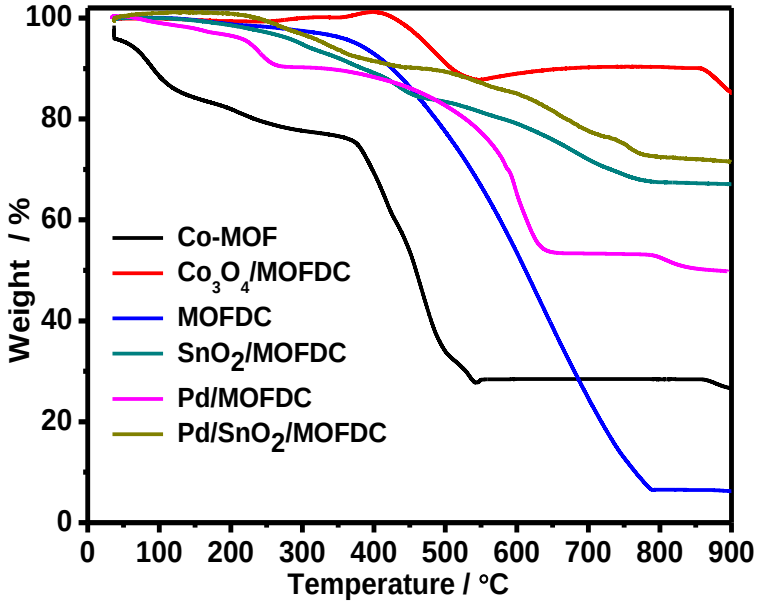

Figure 4.7: TGA profiles of Co-MOF, Co/MOFDC, MOFDC, SnO_2/MOFDC, Pd/MOFDC and Pd/SnO_2/MOFDC

The Co_3O_4/MOFDC seems to be more thermally stable than the precursor sacrificial template with a single thermal decomposition. Before the decomposition, remaining metallic Co became oxidized to Co_3O_4 between 400 to 541 ºC and became thermally stable afterward. The MOFDC begins decomposition at 420 to 790 ºC with 6.7 wt % residue of Co oxide. The SnO_2/MOFDC displays a single stretched decomposition step from 234 to 762 ºC with 67.3 % residue, which could be a mixture of SnO_2 and little Co oxide. Two steps thermal decomposition was observed in the Pd/MOFDC and Pd/SnO_2/MOFDC: (i) detachment of the carbon support from the Pd and Pd/SnO_2 between 239.5 to 401.3 ºC; and (ii) decomposition of the metal and alloy from 531.0 to 772.0 ºC with residues of 53.6 and 70.8 % for the Pd/MOFDC and Pd/SnO_2/MOFDC, respectively.

4.2.2.7 Brunauer-Emmett-Teller (BET)

Physical properties such as surface area, pore volumes and pore sizes of the Co-MOF sacrificial template, MOFDC, Pd/MOFDC and Pd/SnO_2/MOFDC are investigated using the BET analysis, summarized in **Table 4.3**. The as-prepared Co-MOF has the highest pore size, but the lowest pore volume and surface area. The MOFDC has increased surface area and pore volume, due to the carbonization and chemical etching of the sacrificial template but its pore size decreased. Deposition of the Pd and Pd/SnO_2 on the MOFDC change these properties for the Pd/MOFDC (150.20 m^2 g^{-1}, 0.085 cm^3 g^{-1}, 4.18 nm), and Pd/SnO_2/MOFDC (76.54 m^2 g^{-1}, 0.068 cm^3 g^{-1}, 6.43 nm).

Table 4.3: BET analysis of the Pd/SnO_2-based materials

Samples	BET parameters		
	Pore size / nm	Pore volume / cm^3 g^{-1}	S_{BET} area / m^2 g^{-1}
Co-MOF	15.74	0.055	24.41
MOFDC	3.98	0.104	143.67
Pd/MOFDC	4.18	0.085	150.20
Pd/SnO_2/MOFDC	6.43	0.068	76.54

4.2.2.8 Three-Electrode Configuration Measurements

Half-cell ethanol oxidation reaction (EOR) for the Pd/SnO_2-based electrocatalysts was tested with CV, LSV, CA and EIS.

4.2.2.8.1 Cyclic Voltammetry (CV)

Figure 4.8a shows the CV of the Pd/SnO_2-based electrocatalysts modified on the GCE, which was run in an N_2-purged 0.5 M KOH solution. All the electrocatalysts display well-resolved voltammograms with hydrogen adsorption/desorption peaks around -0.65 and -1.00 V (*vs.* AglAgCl, $(KCl)_{sat'd}$). The most important peak is the PdO reduction in the range -0.29 – -0.43 V (*vs.* AglAgCl, $(KCl)_{sat'd}$) because it is significant for the determination of the ECSA. It was observed that this peak shifted to a more negative potential for the Pd/SnO_2/MOFDC than the Pd/MOFDC, indicating less energy is required. Then, the ECSA of the electrocatalysts are calculated following **Equation 2.11** and are recorded as 962.0 ± 2.3, 806.6 ± 1.9, 263.4 ± 0.4 and 235.3 ± 0.4 cm^2 mg^{-1} for the Pd/SnO_2/MOFDC, Pd/SnO_2/CB, Pd/MOFDC and Pd/CB, respectively. Then, electrocatalytic performances of the electrocatalysts were tested in a mixture of 0.25 M EtOH and 0.25 M KOH solution at a scan rate of 50 mV s^{-1}, shown in **Figure 4.8b**. Two distinct well-resolved voltammograms are shown with forwarding and reversed signatures: the forward signature indicates progressive Pd electrocatalyst oxidation, while the reversed is the subsequent PdO reduction [22].

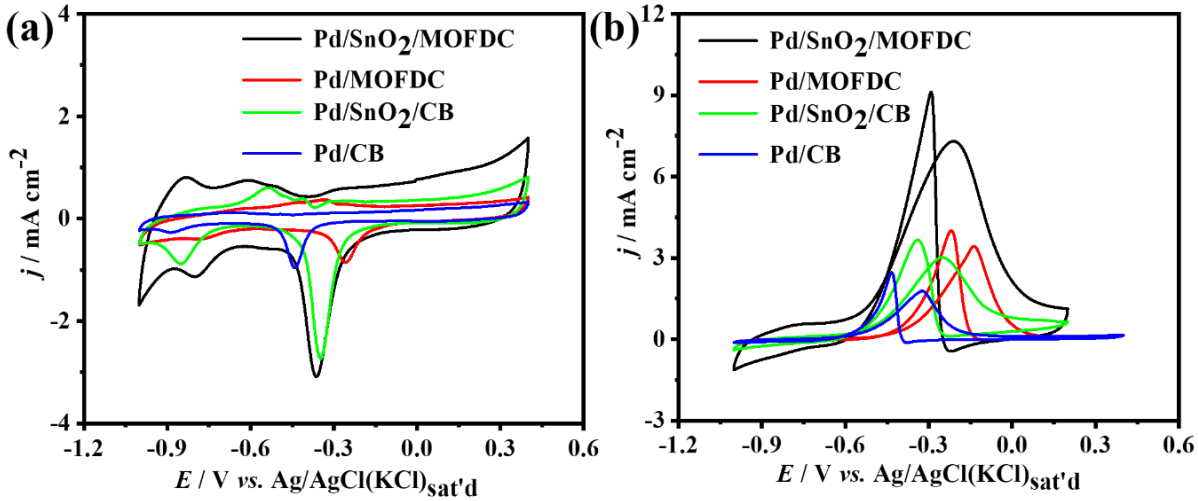

Figure 4.8: CV of the Pd/SnO_2-electrocatalysts in (a) 0.5 M KOH only and (b) mixture of 0.25 M EtOH and 0.25 M KOH at scan rate 50 mV s^{-1}

Significant parameters: onset potential (E_{onset}), peak potential separation (ΔE), current density (j) and the ratio of forward to reversed scans (j_f/j_r) of the electrocatalysts, elucidating the energy, activity toward and tolerance to CO poisoning during the EOR. The E_{onset} values (at j = 0.5 mA cm^{-2}) of -0.595, -0.570, -0.621, and –0.650 V (*vs.* AgIAgCl, $(KCl)_{sat'd}$) were recorded for the Pd/CB, Pd/MOFDC, Pd/SnO_2/CB and Pd/SnO_2/MOFDC, with ΔE values of 0.12, 0.89, 0.94 and 0.80 V, respectively. The least E_{onset} value of the Pd/SnO_2/MOFDC shows that it requires the lowest energy to catalyze the EOR, revealing fast kinetics amongst the electrocatalysts investigated. This observation may be attributed to the synergy between the Pd, Sn and SnO_2 for facile electro-oxidation of the EtOH [23]. When the EOR activities of the electrocatalysts are verified with the j values. The j value of the Pd/SnO_2/MOFDC increased relatively by factors of 2.4, 2.3, and 4.3 times to those of Pd/SnO_2/CB, Pd/MOFDC and Pd/CB, respectively. This result shows that the Pd/SnO_2/MOFDC does not only require the lowest energy toward EOR, but also has high electrocatalytic performance, amongst other electrocatalysts. Also, tolerance of these electrocatalysts were probed with j_f/j_r values, which are recorded as 0.80, 0.82, 0.7, and 0.70 for the Pd/SnO_2/MOFDC, Pd/SnO_2/CB, Pd/MOFDC and Pd/CB, respectively. This result shows that the addition of the SnO_2 improves tolerance of the electrocatalysts to carbonaceous species poisoning [23].

To further understand the interaction of the electrode in the electrolyte, CV at different scan rates (υ = 25 – 800 mV s^{-1}) are studied. As the υ values increase, the j values of the forward scans increase concurrently for all the electrocatalysts, shown in **Figures 4.9a – 4.9d**. Then, plots of the increased j values were made against $\upsilon^{1/2}$ (**Figure 4.9e**), gave straight-line plots where the R^2 values (0.979 – 0.995) obtained are close to unity,

showing that the interaction between the electrodes and electrolyte is diffusion-controlled process. However, the non-zero intercepts indicate that reaction at modified working electrode−electrolyte interfaces could be at least in part diffusion controlled, although localized resistivity phenomena could also contribute. Also, non-linear plots are obtained when the j values were normalized with the $\upsilon^{1/2}$ values and plotted against the υ values (**Figure 4.9f**), indicating that the mechanism of the EOR on the Pd/SnO_2-based electrocatalysts follows a coupled chemical reaction of reversible redox chemistry and then irreversible chemical reaction (*ErCi*) [24]. Non-linear plots were also obtained when the j_r/j_f values were plotted against the υ values (**Figure 4.9g**), further explaining tolerance of the electrocatalysts to CO poisoning. The result confirms that the anti-poisoning properties of the electrocatalysts are improved on the addition of SnO_2.

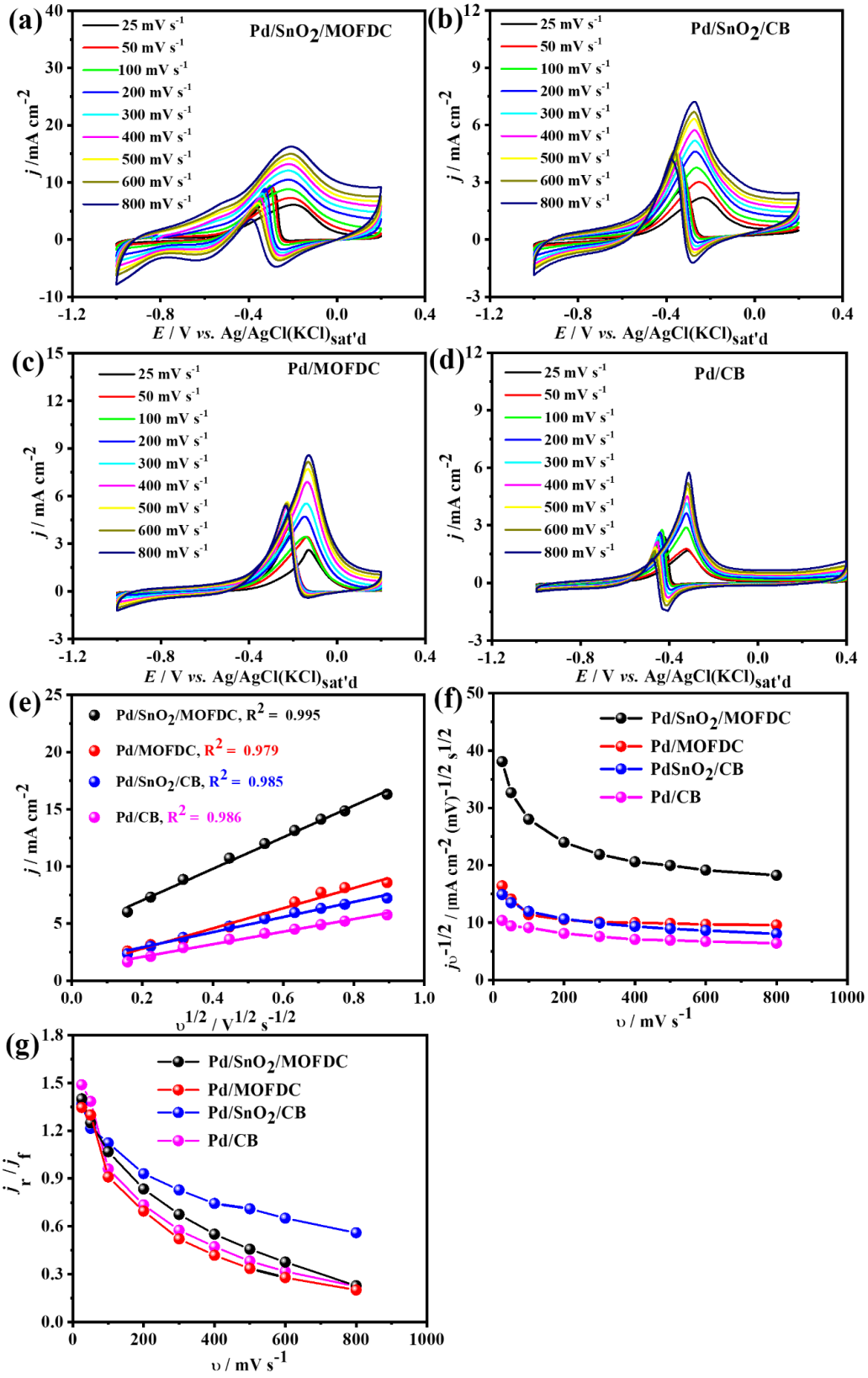

Figure 4.9: (a–d) CV at different scan rates, (e) plots of j_f *vs.* $\upsilon^{-1/2}$, (f) plots of $j\upsilon^{-1/2}$ *vs.* υ and (g) plots of $1/j_f/j_r$ *vs.* υ of the Pd/SnO_2-based electrocatalysts in a mixture of 0.25 M EtOH and 0.25 M KOH.

4.2.2.8.2 Linear Sweep Voltammetry (LSV)

The effect of EtOH concentrations changes to the EOR activities of the Pd/SnO_2-based electrocatalysts was demonstrated using the LSV (**Figures 4.10a – 4.10d**). It was observed that increasing EtOH concentrations up to 0.875 M, increase the *j* values of the Pd/SnO_2-based electrocatalysts for EOR and additional increase in EtOH concentration resulted in slight increase *j* values of the electrocatalysts containing SnO_2, but a sudden decrease in the *j* values of the electrocatalysts without SnO_2, shown in **Figure 4.10e**. The slight increase in the *j* values was further understood by plotting the logarithm of the *j* values against logarithm [EtOH] for only the Pd/SnO_2/MOFDC (**Figure 4.10f**), which revealed a significant increase of the logarithm values. These observations may be ascribed to an insufficient amount of OH^- ions present at elevated concentrations (> 0.875 M), as the EOR is a function of both concentrations of OH^- ions and EtOH. However, the OH^- spill-over and oxophilic properties of the SnO_2 and Sn respectively are beneficial to increasing the current response slightly rather than losing their activities in the case of the electrocatalysts without the SnO_2.

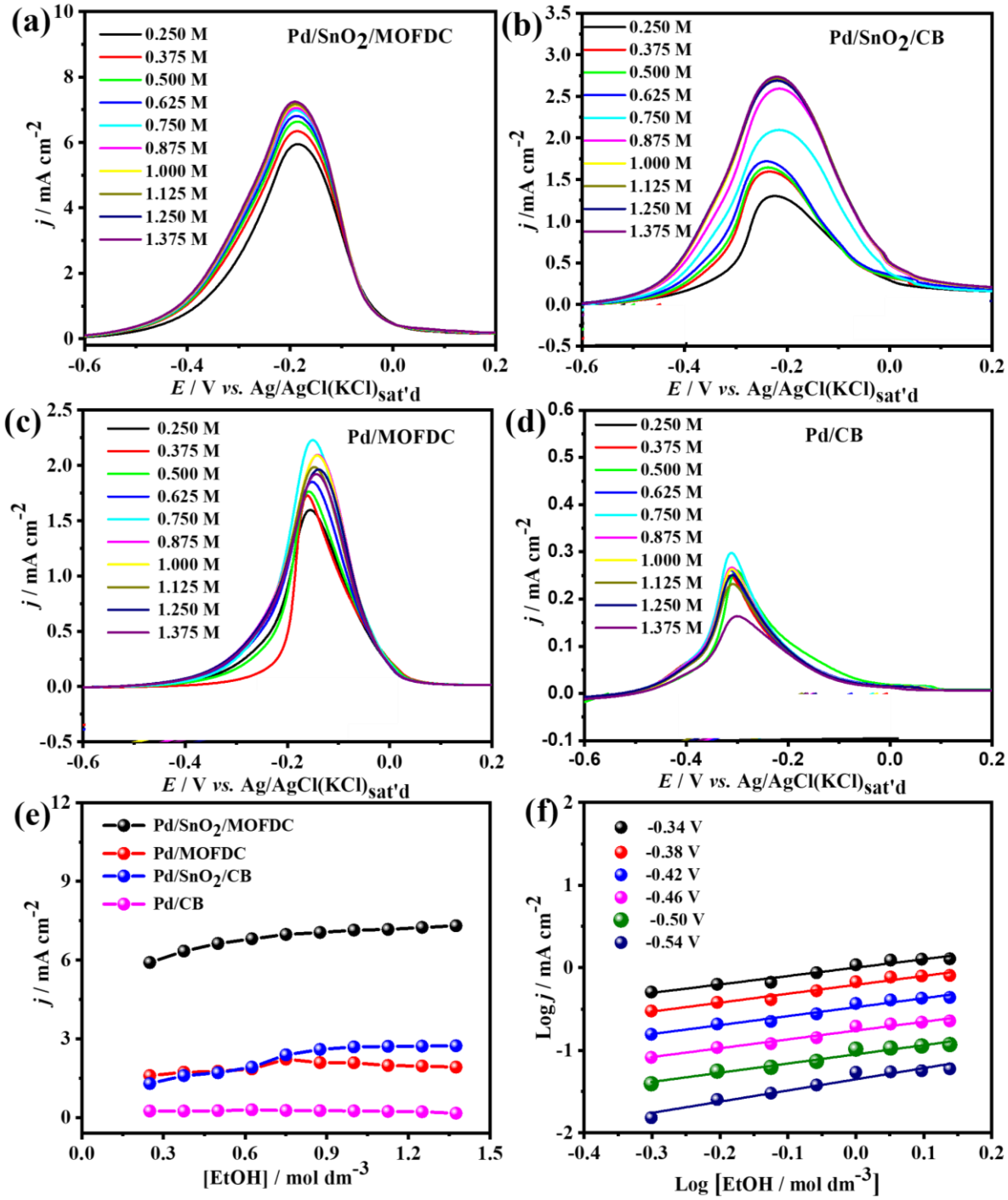

Figure 4.10: (a–d) LSV of the Pd/SnO_2-based electrocatalysts in 0.25 M KOH and different [EtOH] at scan rate 1.0 mV s^{-1}, (e) plots of *j vs.* [EtOH] and (f) plots Log *j vs.* Log [EtOH] for the Pd/SnO_2/MOFDC only.

These LSV curves were further explored to study kinetic parameters of the Pd/SnO_2-based electrocatalysts, as the experiment was investigated at a slow scan rate (1.0

mV s^{-1}), where the kinetics of EOR could easily be measured using **Equations 2.12** and **2.13**. Tafel plots (**Figures 4.11a – 4.11d**) of the electrocatalysts were made, where η is plotted against logarithm j values, and extrapolated Tafel slopes (b) of 216.1 ± 8.0, 179.1 ± 8.0, 151.8 ± 3.0 and 125.7 ± 4.0 mV dec^{-1}, with electron transfer coefficient (α) values of 0.73, 0.67, 0.61 and 0.53 for the Pd/SnO_2/MOFDC, Pd/SnO_2/CB, Pd/MOFDC and Pd/CB, respectively. These results show the rate determining step of the EOR is when carbonyl group (CH_3CO) and OH^- ions combined to form CH_3COOH as by-product.

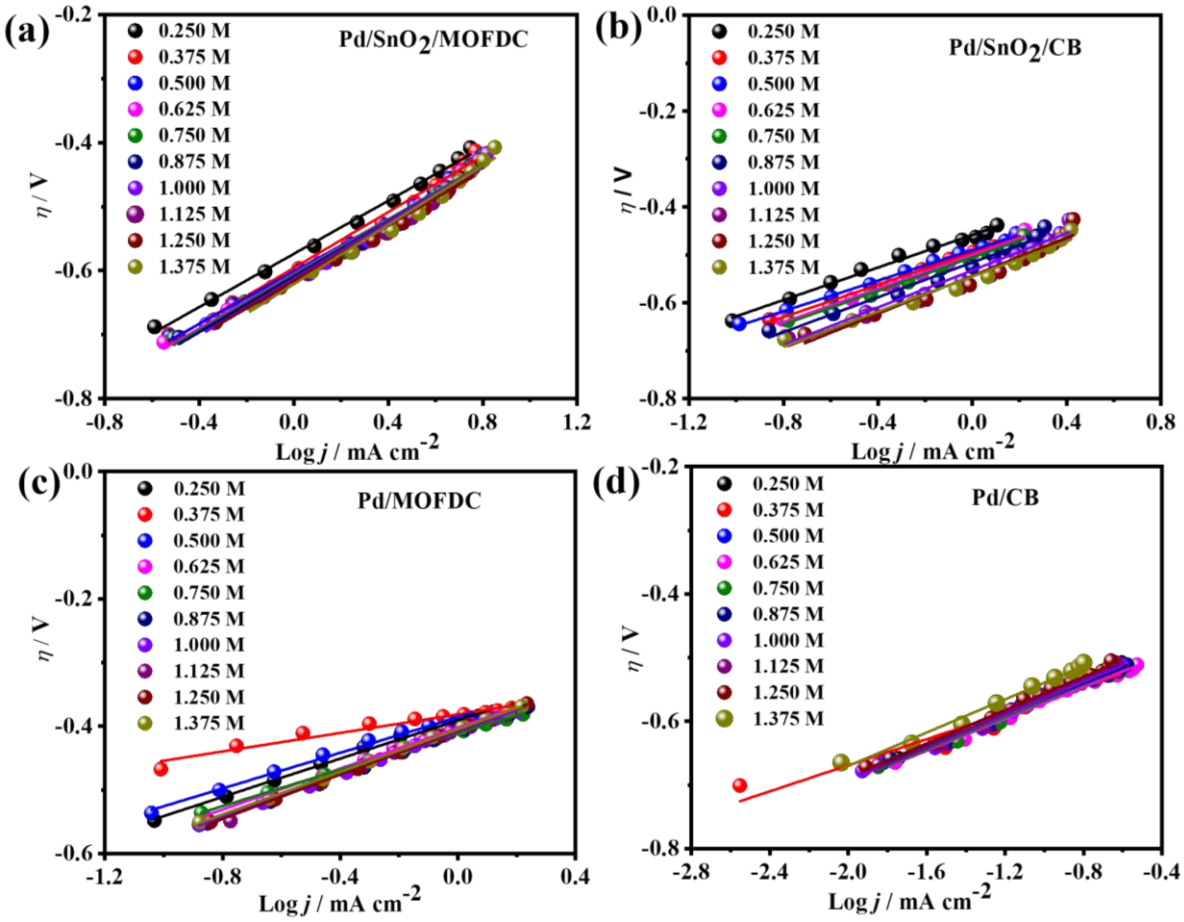

Figure 4.11: Tafel plots of the Pd/SnO_2-based electrocatalysts in 0.25 M KOH and different EtOH concentrations at scan rate 1.0 mV s^{-1}

4.2.2.8.3 Electrochemical Impedance Spectroscopy (EIS)

The EIS was further employed to elucidate the interaction between the Pd/SnO_2-based electrocatalysts and electrolytes in terms of fast electron transports. Nyquist plots (**Figures 4.12a** and **4.12c**) of the electrocatalysts with a Voigt *EEC* model (**Figure 4.12b**) to deduce the EIS parameters (summarized in **Table 4.4**): R_s is the solution resistance which explains the ohmic property of the electrocatalysts to the electrolytes; R_{ct} is the charge transfer resistance that indicates electron transport properties of the electrocatalysts in the electrolyte during the EOR; and constant phase element (*CPE*) is a deformed double-layer capacitor (C_{dl}) and its standard deviation ($0.5 < a < 1$) show the pseudo-capacitive behavior of the electrocatalysts, according to the power-law relationship (**Equation 2.18**). The (R_s + R_{ct}) value explains the holistic facile properties of the electrocatalysts towards the EOR. The smaller the (R_s + R_{ct}) value, the better the electrocatalysts. The Pd/SnO_2/MOFDC with the lowest (R_s + R_{ct}) further confirms its superior electrocatalytic performance for the EOR, amongst other electrocatalysts investigated in the same condition.

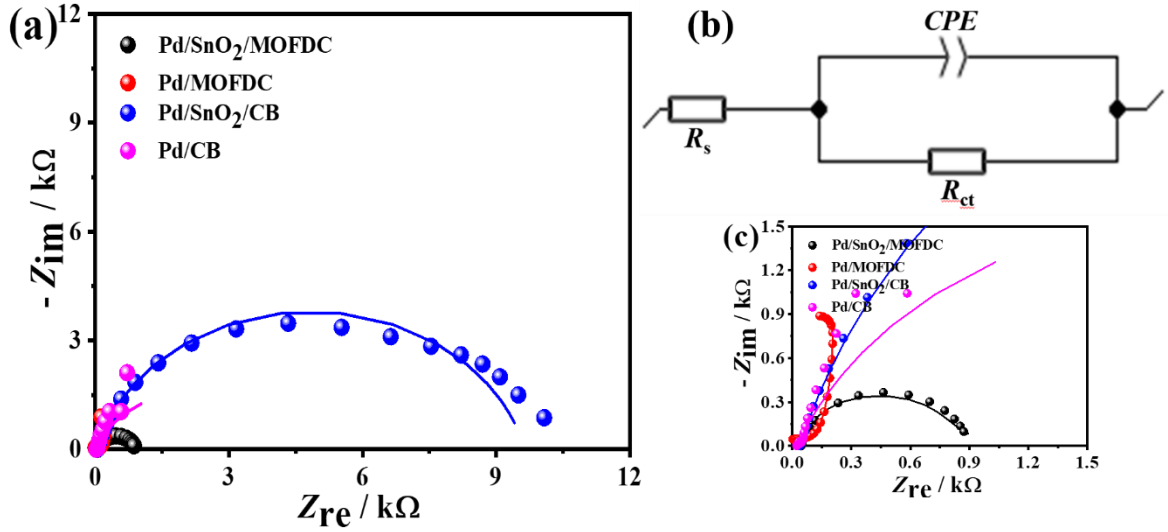

Figure 4.12: (a) Nyquist plots, (b) Voigt *EEC* and (c) expanded area of the Pd/SnO_2-based electrocatalyst at potential -0.33 V (*vs.* AgIAgCl, $(KCl)_{sat'd}$) in a mixture of 0.25 M EtOH and 0.25 M KOH

Table 4.4: EIS parameters of the Pd/SnO_2-based electrocatalysts toward EOR deduced from the Nyquist plots and the modelled Voigt *EEC* at -0.33 V *vs.* AglAgCl, $(KCl)_{sat'd}$

EIS parameters	Pd/SnO_2-based Electrocatalysts			
	Pd/SnO_2/MOFDC	Pd/MOFDC	Pd/SnO_2/CB	Pd/CB
R_s / Ω	45.27 ± 0.26	33.77 ± 0.36	38.11 ± 0.21	25.02 ± 0.24
R_{ct} / kΩ	0.90 ± 0.43	0.92 ± 0.12	9.61 ± 0.17	4.42 ± 1.52
CPE / µF.s^(a-1)	106.80 ± 0.67	271.70 ± 1.7	12.56 ± 6.42	32.54 ± 0.18
a	0.90	0.54	0.85	0.79

4.2.2.8.4 Chronoamperometry (CA)

The CA was used to study the long-term durability of the Pd/SnO_2-based electrocatalysts during the EOR. The CA (**Figure 4.13**) of the electrocatalysts were carried out at potential -0.33 V *vs.* AglAgCl, $(KCl)_{sat'd}$ for 1200 s. It was observed that the *j* values begin to decline rapidly for all the electrocatalysts because of the accumulation of CO species passivating their active sites during the EOR [25,26]. The Pd/SnO_2/MOFDC still has *j* values after the 1200 s stability test with the least overall reduction in the *j* value compared to the other electrocatalysts, whose *j* values are closed to zero. The result confirms the tolerance of the Pd/SnO_2/MOFDC toward the EOR, amongst the electrocatalysts.

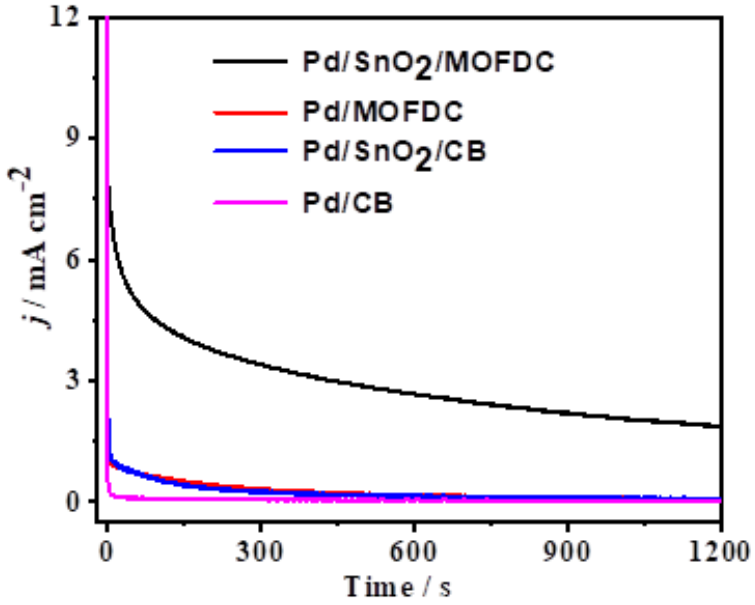

Figure 4.13: CA of the Pd/SnO_2-based electrocatalysts at potential -0.33 V (*vs.* AgIAgCl, $(KCl)_{sat'd}$) in a mixture of 0.25 M EtOH and 0.25 M KOH for 1200 s

4.2.2.9 Two-electrode Configuration (Full Cell)

The experimental set-up and electrochemical measurements for the two-electrode configuration are elucidated in the sub-section below:

4.2.2.9.1 Micro-3D printed Cell

Alkaline µ-DEFC analysis was explored as proof-of-concept with the aid of a micro-3D printed cell (**Figure 4.14**). The micro-3D printed cell set-up was fabricated with two-electrode configuration: the WE and CE (reference connected to the counter), which are connected to the cathode and anode of the cell, respectively with aid of Cu foil as a current collector. For the µ-DEFC, the cathode and anode are made by making slurries of 10.0 mg of FeCo/C (3.0 wt % metal) and 10.0 mg of the electrocatalysts that were mixed separately in a mixture of 200 µL of EtOH and 20 µL of PTFE binder. Then, the FeCo/C and electrocatalysts slurries were coated on double carbon papers and nickel foam, and the coated electrocatalysts of the double carbon papers and

nickel foam are sandwiched in laminated sheets and fabricated into anode and cathode compartments, respectively.

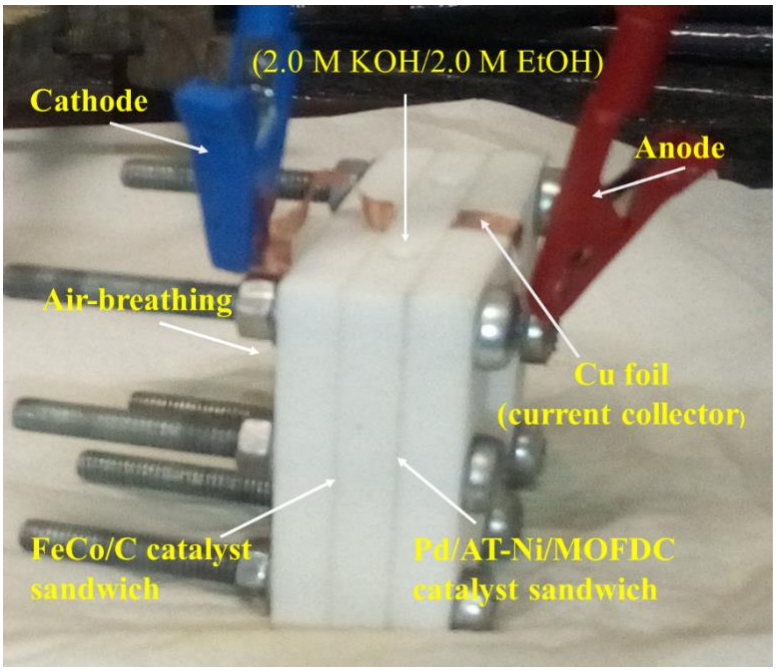

Figure 4.14: Membraneless µ-DEFC set-up with the aid of micro 3D-printed cell

4.2.2.9.2 Direct Ethanol Micro-Fuel Cell (µ-DEFC) Measurements

Because the Pd/SnO_2/MOFDC and Pd/MOFDC have the lowest series resistance (R_s + R_{ct}) values in the half-cell reaction, the two electrocatalysts are considered and employed in the proof-of-concept, investigated for the µ-DEFC using the micro-3D printed cell (**Figure 4.14**). **Figure 4.15a** shows the potential and power curves of the electrocatalysts, where the Pd/MOFDC and Pd/SnO_2/MOFDC have peak power density (P_m) values of 11.06 and 19.73 mW cm^{-2}, respectively. Then, the electrocatalysts were subjected to a galvanostatic discharge test at 40 mA cm^{-2} for 24 h, shown in **Figure 4.15b**. The Pd/SnO_2/MOFDC has a voltage drop from 0.94 to 0.58 V, corresponding to 62.0 % energy retention, while the potential drop of the Pd/MOFDC was from 0.84 to 0.44 V, amounting to 52.0 % energy retention. The

addition of SnO_2 to the electrocatalyst does not only improve the electrocatalytic performance, but also retain more energy. These results were further probed using EIS at initial and after 24 h discharge test, shown **Figure 4.15c** at open circuit potential (*OCV*) of 0.72 V with the Voigt *EEC* model (**Figure 4.15d**) and the EIS parameters summarized in **Table 4.5**.

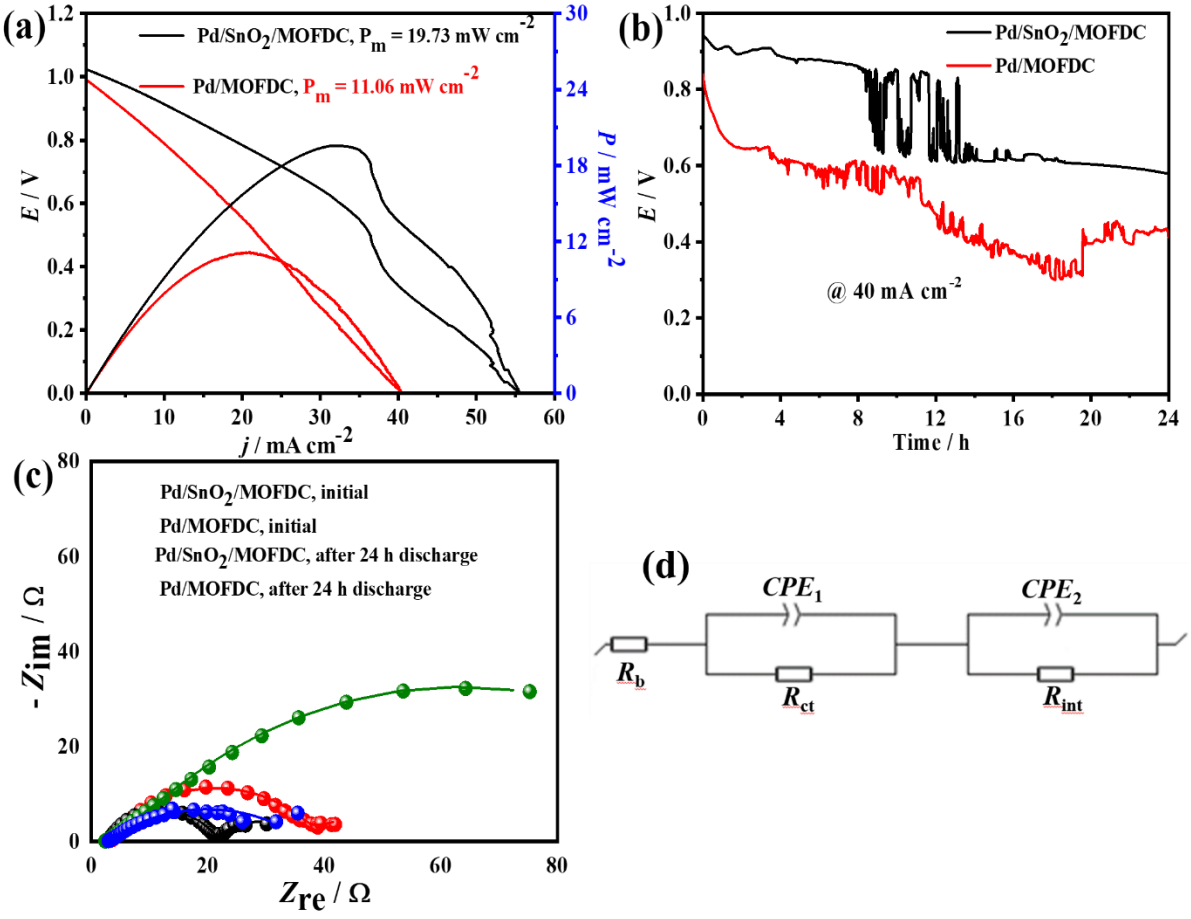

Figure 4.15: (a) potential and power curves, (b) galvanostatic discharge test at 40 mA cm^{-2} and (c) Nyquist plots at initial and after 24 h discharge test of the Pd/SnO_2/MOFDC and Pd/MOFDC using the micro-3D printed cell

The Voigt *EEC* model consists of the following: (i) bulk resistance (R_b) which is the resistance to the current collector, EtOH/KOH electrolyte, electrodes and electrical connections employed for the µ-DEFC testing; (ii) the Voigt element at the high-frequency regions (R_{int}/CPE_1) correlates to the interfacial resistance due to ohmic drop

of the diffusion of the electrolyte ions between the electrodes, the distance between the electrodes, specific conductance of the electrolytes and the area of the working electrode, and interfacial capacitance (*CPE* from the inhomogeneity or irregularity of the electrode surfaces); and (iii) the Voigt element at the low-frequency regions (R_{ct}/CPE_2) correlates to the electron transfer resistance at the materials and the related non-ideal double-layer capacitance. Following the power-law formula previously explained (**Equation 2.18**), the impedance of the *CPE* (Z_{CPE}) is well known to be connected with the ideality factor "*a*" which ranges between -1 and +1 (i.e., $-1 \leq a \leq 1$): when $a = 0$, the Z_{CPE} equals a pure resistor; $a = 1$, the Z_{CPE} equals Z_{Cdl} (i.e., a pure capacitor); $a = -1$ the Z_{CPE} is a pure inductor; while $a = 0.5$ the CPE becomes the same as the Warburg impedance (Z_w) due to the electrolyte ion diffusion [27,28]. The $0.5 < a < 1.0$ values obtained confirmed the inhomogeneous charge storage elements used in the Voigt *EEC*. Series resistance ($R_b + R_{int} + R_{ct}$) values of *ca.* 26.0 and 50.0 Ω are recorded for the Pd/SnO_2/MOFDC and Pd/MOFDC, which increased to *ca.* 38.0 and 123 Ω, respectively after 24 h discharge test. The increased ($R_b + R_{int} + R_{ct}$) values of 5.0 and 146.0 % for the Pd/SnO_2/MOFDC and Pd/MOFDC may be ascribed to the accumulation of the CO species on their active sites during the EOR, which poisons the Pd/MOFDC after the discharge test. However, a little increase of the ($R_b + R_{int} + R_{ct}$) value for the Pd/SnO_2/MOFDC confirms its tolerance to the poisoning effect.

Table 4.5: EIS parameters from the Nyquist plots of Pd/SnO_2-based electrocatalysts for the µ-DEFC at *OCV* 0.72 V with the Voigt *EEC* model

EIS parameters	Pd/SnO_2-based electrocatalysts			
	Pd/SnO_2/MOFDC		Pd/MOFDC	
	Initial	After 24 h discharge	initial	After 24 h discharge
R_b / Ω	2.89 ± 0.50	2.82 ± 0.33	3.63 ± 0.46	2.27 ± 0.81
R_{int} / Ω	14.89 ± 1.58	33.70 ± 3.54	34.97 ± 4.27	36.23 ± 1.36
CPE_1 / mF. s^(1-*a*)	66.52 ± 5.76	10.31 ± 0.00	0.20 ± 0.14	25.92 ± 0.05
a_1	0.66	0.49	0.72	0.40
R_{ct} / Ω	8.51 ± 2.45	1.72 ± 0.26	11.25 ± 8.53	84.41 ± 8.79
CPE_2 / mF. s^(1-*a*)	0.07 ± 0.01	34.34 ± 0.06	51.03 ± 8.73	12.85 ± 0.99
a_2	0.78	0.80	0.78	0.66

4.2.3 Pd/Ni-based Electrocatalysts for Ethanol Oxidation Reaction and Direct Ethanol Micro-Fuel Cell

Synthesis of the Pd/Ni-based electrocatalysts was thoroughly explained and characterized with FTIR, Raman, powder XRD, XPS, XAS, SEM and EDX, TEM, BET and tested for EOR (half-cell reaction, **Figure 3.1**) and µ-DEFC (full cell, **Figure 4.14**).

4.2.3.1 Microwave-Assisted Solvothermal Synthesis of Pd/Ni-Based Electrocatalysts

Ni-MOF was first prepared with the TMA and TEA, followed by carbonization and/or chemical etching and then nanostructured Pd deposition to afford the Pd/Ni-based electrocatalysts, as diagrammatically illustrated in **Figure 4.16** and briefly explained:

1.1632 g of $Ni(NO_3)_2.6H_2O$ was mixed with 1.6811 g of TMA and 1.5 mL of TEA, and dissolved in 50 mL of EG. The mixture was stirred and sonicated for 30 min until it was homogeneous and thereafter MW irradiated at 600 W for 30 min and cooled to room temperature. A deep green crystal was obtained after being severally washed with ethanol with the aid of centrifuge and further dried in a vacuum oven at 80 ºC for 4 h.

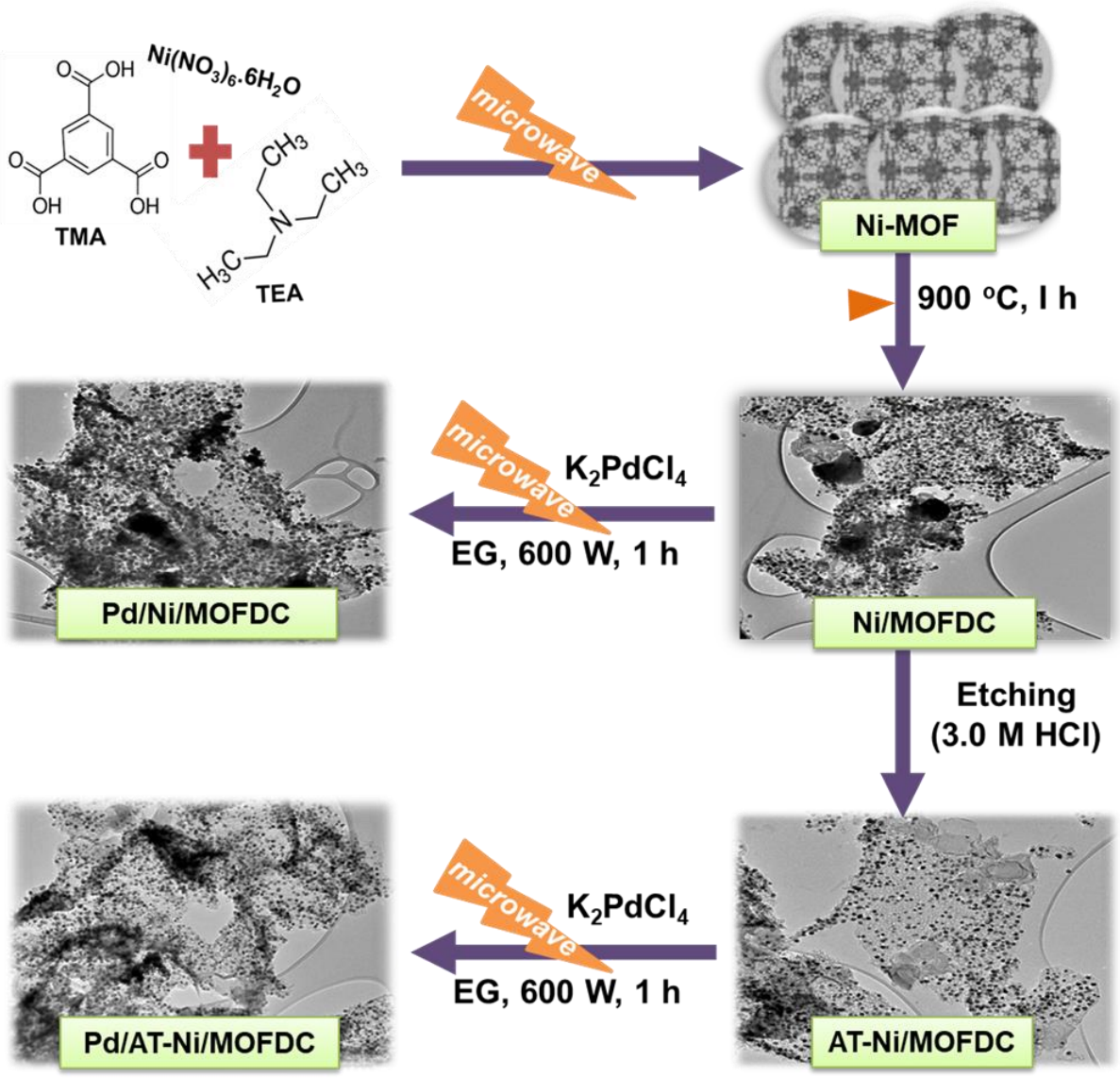

Figure 4.16: Diagrammatic illustration of the Pd/Ni-based electrocatalysts (Pd/Ni/MOFDC and Pd/AT-Ni/MOFDC)

The Ni-MOF made above was placed in a quartz boat and heated in a furnace from room temperature to 900 ºC in an inert atmosphere of N_2 flow of 5 K min^{-1} for 3 h and

further maintained for 1 h at the same temperature to produce the NI/MOFDC. Half a portion of the as-prepared Ni/MOFDC was chemically etched with 3.0 M HCl acid (10 mL) for 48 h, then washed severally with distilled water to produce acid-treated Ni/MOFDC, abbreviated as AT-Ni/MOFDC. Thus, there are two distinct products (Ni/MOFDC and AT-Ni/MOFDC) obtained here.

The preparation of the Pd/Ni/MOFDC and Pd/AT-Ni/MOFDC follows similar procedures as in sub-section 4.2.1. Although, 76.68 mg of K_2PdCl_4 and 100 mg each of the Ni/MOFDC and AT-Ni/MOFDC composites (prepared above) were used instead.

4.2.3.2 Physical Characterization of the Pd/Ni-Based Electrocatalysts

The Pd/Ni-based electrocatalysts were thoroughly characterized with FTIR, Raman, powder XRD, XPS, XANES, FT-EXAFS, SEM, EDX, TEM and BET, explained below:

4.2.3.2.1 Fourier Transform Infrared spectroscopy (FTIR)

Figure 4.17a shows the FTIR spectrum of the as-prepared Ni-MOF. The following peaks: 3320, 2925, 2865, 869, 1047,1427, 1568, 1365, 704, 548 and 1726 cm^{-1} correspond to -OH stretching (str), C-H str, C-H bending (b), C-H in-plane (ip), C-H out-of-plane (oop), C-C str of aromatic, COO^- symmetric (sym), COO^- asymmetric (asy), CO in-plane bending, NiO coordination and CO str vibration, respectively. Significant of the vibration bonds are: present of broad -OH is traced to the uncoordinated COOH of the 1,3,5-benzenetricarboxylic acid or absorption of moist air; the C-H_{str}, C-H_b, C-H_{ip}, C-H_{oop}, C-C_{str} are due to aromatic ring [29], the symmetric and asymmetric of COO^- explain bidentate nature of the chelating agent (TMA); the CO_b,

CO_{str} and NiO coordination suggest incorporation of the metal core in the ligand's framework for the formation of the Ni-MOF [30,31]. After carbonization and/or chemical etching, the FTIR spectra (**Figure 417b)** show the same functional groups in the Ni/MOFDC and AT-Ni/MOFDC, which are Ni-O (548 cm^{-1}), C=C (2025.5 cm^{-1}), C≡N (2168.8 cm^{-1}), carboxylic acid O-H (2363.4 – 2680.0 cm^{-1}), C-H bending (2946.2 cm^{-1}) and C-H stretching (3100.0 cm^{-1}). These results show that the frameworks of the MOF were broken down at high temperature.

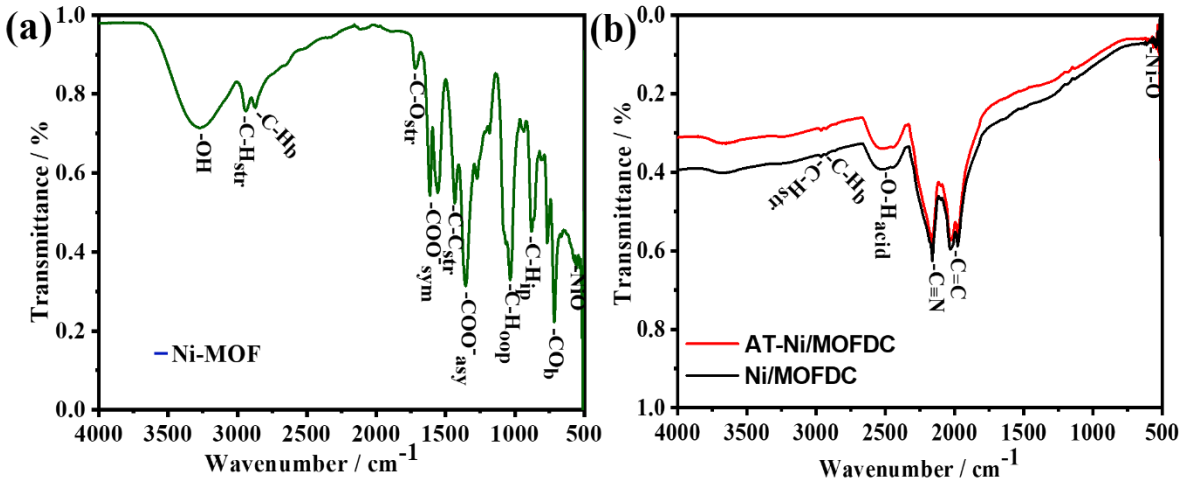

Figure 4.17: FTIR spectrum of the (a) as-prepared Ni-MOF and (b) Ni-based composites

4.2.3.2.2 Raman Spectroscopy

Figure 4.18 shows the Raman spectra of the Ni/MOFDC and AT-Ni/MOFDC. The Ni-based composites were obtained by subjecting the as-prepared Ni-MOF sacrificial template to carbonization and subsequent chemical etching of half a portion of the carbonized form. The immediate product (Ni/MOFDC) gives the following vibration modes: Ni-OH, first disorder (D-band), graphitic (G-band) and second order-disorder (2D) band at 487,1350, 1599 and 2436 cm^{-1}, while the chemically etched product (AT-Ni/MOFDC) gives the D-, G- and 2D-bands at 1345, 1581 and 2436 cm^{-1}, respectively.

The disappearance of the Ni-OH the AT-Ni/MOFDC is due to the chemical etching to remove the passive layer of the metal hydroxide. Whereas slight shift the D- and G-band of the AT-Ni/MOFDC is ascribed to defect created by chemical etching. The defect induced by acid treatment of the composite was affirmed by further deconvoluting the D- and G-bands into five distinct D_4, D_1, D_3, G and D_2 spectra at corresponding Raman shifts of 1229, 1343, 1489, 1575 and 1610 cm^{-1}, respectively. Then, I_{D1}/I_G values of 1.8 and 2.1 were evaluated for the Ni/MOFDC and AT-Ni/MOFDC, respectively according to the previously established method [13,14]. The AT-Ni/MOFDC exhibits increased I_{D1}/I_G value implies noticeable defects in its crystal arrays.

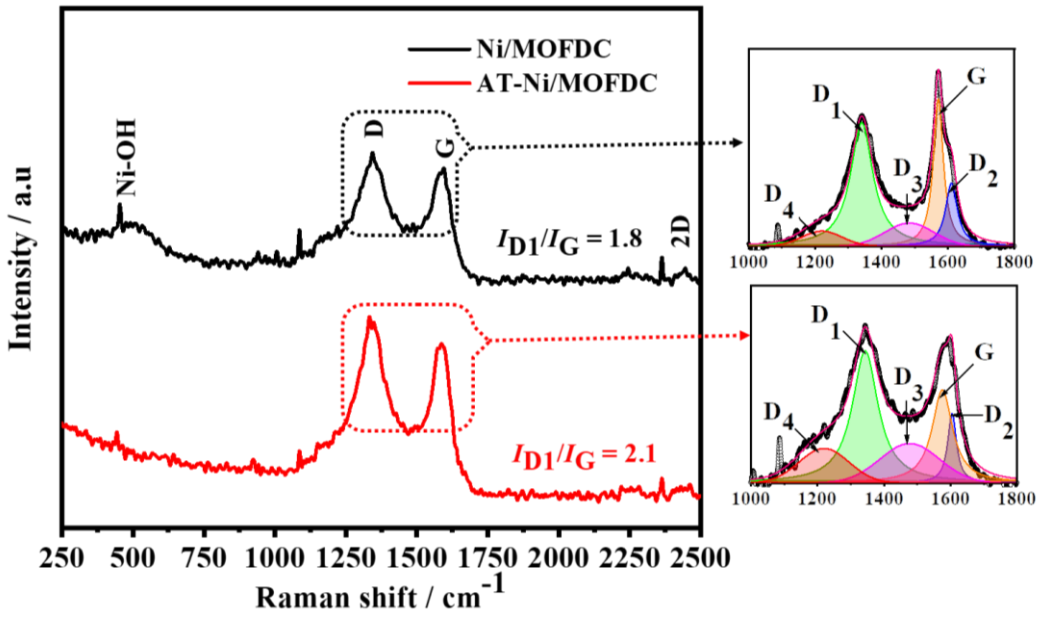

Figure 4.18: Raman spectra of the Ni/MOFDC and AT-Ni/MOFDC

4.2.3.2.3 Powder X-Ray Diffraction (PXRD)

Figure 4.19 shows the PXRD of the Ni-MOF template, composites and Pd/Ni-based electrocatalysts. The as-prepared Ni-MOF gives diffraction peaks at 10.0 and 22.7º, corresponding to miller indices of Ni-MOF(100) and Ni-MOF(101), respectively as shown in **Figure 4.19a**. This result agrees with the previous diffraction peaks

previously reported for Ni-MOF [20]. The composites display similar diffraction peaks at 26.3, 44.9, 52.1, 76.7, 93.1 and 98.4º, ascribed to C(002), Ni(111), Ni(200), Ni(220), Ni(311) and Ni(222), respectively. However, the diffraction peaks are broader in the AT-Ni/MOFDC confirming the defects and strain produced after being chemically etched [21,22] and agree with the Raman spectra (**Figure 4.18**). The electrocatalysts (**Figure 4.19b**) have additional diffraction peaks at 40.3, 46.8, 68.1, 82.2 and 87.0º, assigned to Pd(111), Pd(200), Pd(220), Pd(311) and Pd(222), respectively, which are face-centred cubic lattice of palladium. Crystallite sizes (τ) and lattice distances (d) of the electrocatalysts were calculated considering only the Pd(111) index, being the most pronounced diffraction pattern, using Scherrer's equation (**Equation 3.1**) and the values are summarized in **Table 4.6**.

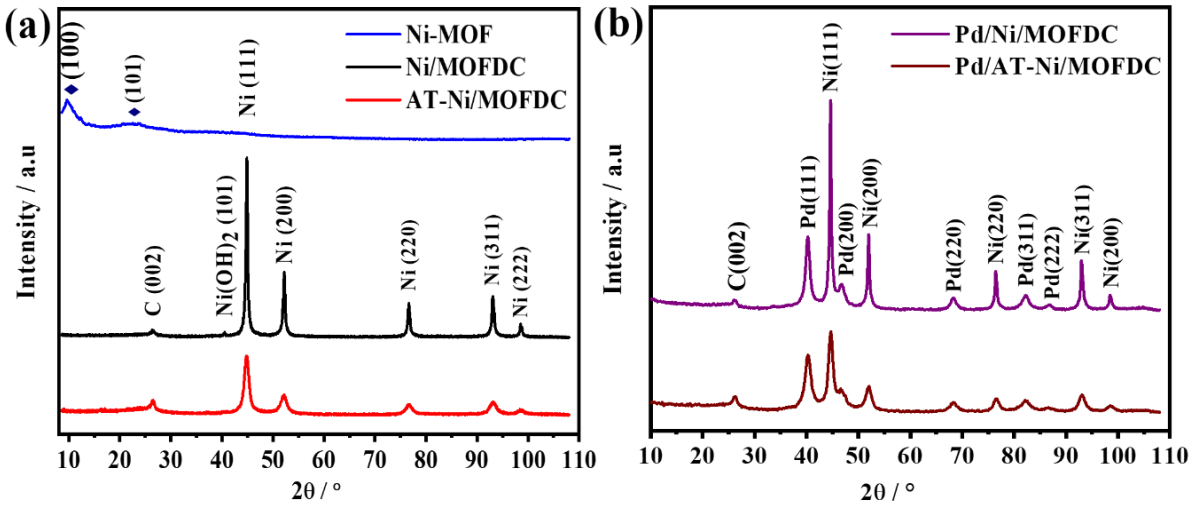

Figure 4.19: PXRD of (a) Ni-MOF, Ni/MOFDC and AT-Ni/MOFDC and (b) Pd/Ni-based electrocatalysts

Table 4.6: Lattice parameters of the Pd/Ni-based electrocatalysts at Pd(111)

Lattice parameters	Pd/Ni-based Electrocatalysts	
	Pd/Ni/MOFDC	Pd/AT-Ni/MOFDC
2θ / ^{o}	40.2567	43.5151
d / Å	2.6507	5.3037
τ / nm	7.94	2.57

4.2.32.4 X-Ray Photoelectron Spectroscopy (XPS)

Figure 4.20a and **4.20b** show the XPS of the Pd/Ni-based electrocatalysts that explain their surfaces' qualitative and quantitative elemental (Pd, Ni, C, O and very little N) compositions and chemical natures. The chemical environments of each constituent element are further investigated by deconvolution of their respective spectra. The deconvoluted Pd 3*d* (**Figures 4.20c** and **4.20d**) give doublet spectra splitting at binding energies of 335.6 eV (Pd $3d_{5/2}$) and 341.0 eV (Pd $3d_{3/2}$), which are mixed metallic Pd and PdO_x ($0 < x < 2$) shown in the inset lower additional spectra fitting [23]. Ni 2*p* deconvolution for the Pd/Ni/MOFDC (**Figure 4.20e**) was fitted to four distinct spectra at binding energies of 878.5 eV ($Ni(OH)_2$ $2p_{1/2}$ satellite), 872.8 eV (Ni $2p_{1/2}$), 860.7 eV ($Ni(OH)_2$ $2p_{3/2}$ satellite) and 855.1 eV (Ni $2p_{3/2}$), respectively [32]. Ni 2*p* deconvolution of the Pd/AT-Ni/MOFDC (**Figure 4.20f**) was also fitted to four distinct spectra at binding energies of 876.0 eV (Ni $2p_{1/2}$ shake-up satellite), 869.7 eV (Ni $2p_{1/2}$), 856.8 eV (Ni $2p_{3/2}$ shake-up satellite) and 853.2 eV (Ni $2p_{3/2}$) [33,34]. The local environments of the Ni 2*p* in the Pd/Ni-based electrocatalysts confirm that the Pd/Ni/MOFDC has additional $Ni(OH)_2$ ($2p_{1/2}$ and $2p_{3/2}$) satellites, while shifts of these spectra in the Pd/AT-Ni/MOFDC indicates that the $Ni(OH)_2$ satellites were removed, but remains only metallic Ni ($2p_{1/2}$ and $2p_{3/2}$) shake-up satellites. Moreover, slight shifts

of the Ni ($2p_{1/2}$ and $2p_{3/2}$) for the Pd/AT-Ni/MOFDC to lower binding energies confirms the formation of mainly metallic Ni nanoparticle, due to the induction of oxygen vacancies and inducing interaction between the Ni and C leading to increased electron density for the Ni relative to the Pd/Ni/MOFDC having additional $Ni(OH)_2$ satellites that would have caused the higher binding energies of the Ni ($2p_{1/2}$ and $2p_{3/2}$) with reduced electron density [35]. **Figure 4.20g** shows C 1*s* of the Pd/Ni/MOFDC deconvoluted into different spectra at binding energies of 287 (O=C-N), 285 (C-O), 284.6 (C sp^2/sp^3) [36] and 282.2 eV for metallic carbide (M-C) [37,38]. The metallic Ni nanoparticles are suspected to remain in the core of the carbon lattice after the carbonization of the Ni-MOF sacrificial template, thus preventing the exposure of the metallic Ni. Similar spectra fitting was obtained for C 1*s* deconvolution of the Pd/AT-Ni/MOFDC (**Figure 4.20h**), except the metallic carbide peak at 282.2 eV which became flat. This explains that the chemical etching does not only create some defects and strains in the Ni lattice and removal of the passive $Ni(OH)_2$, but also in the C lattice. Interestingly, the deconvoluted O 1*s* of the Pd/Ni/MOFDC (**Figure 4.20i**) shows two distinct spectra at 532.8 eV (surface oxygen, O_S) and 530.5 eV (lattice oxygen, O_L), significantly ascribed to the surface coverage of OH on the metals and metal-O bond in the sample. These results also agree with the formation of the $Ni/Ni(OH)_2$ interface. The deconvoluted O 1*s* of the Pd/AT-Ni/MOFDC (**Figure 4.20j**) shows only a single spectrum at 531.9 eV (oxygen vacancy, O_V) and a shoulder at 530.5 eV (O_L), but the surface coverage of OH was flat, confirming the removal of oxygen species ($Ni(OH)_2$) and induction of oxygen vacancies after the composite was being chemically etched before Pd deposition, which is an indication of absence of the $Ni/Ni(OH)_2$ interface [39]

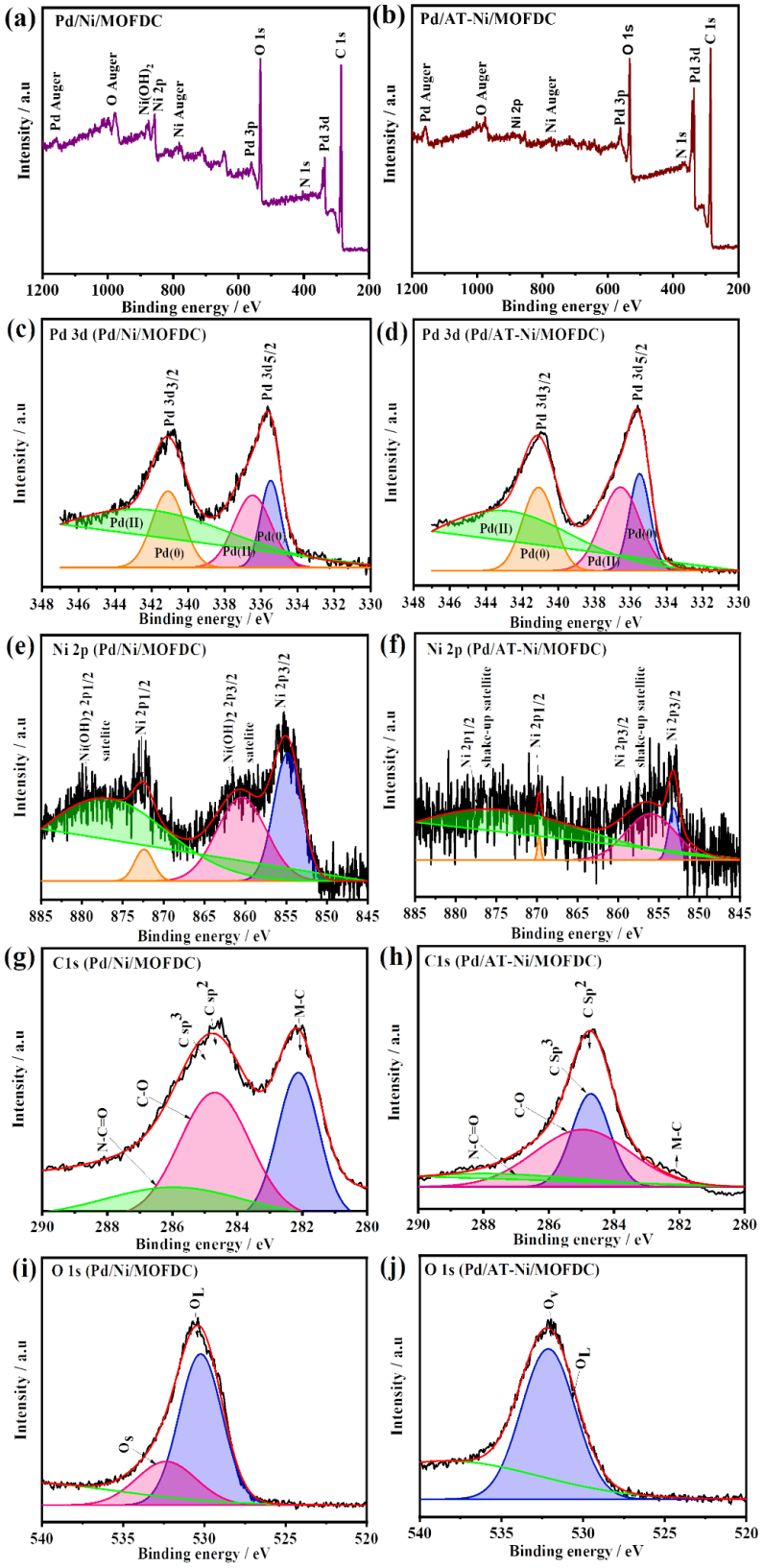

Figure 4.20: XPS of (a,b) wide survey of the Pd/Ni-based electrocatalysts, deconvolved spectra of (c,d) Pd 3*d*, (e,f) Ni 2*p*, (g,h) C 1*s* and (i,j) O 1*s*

The quantitative elemental composition of the electrocatalysts' surface, which was sampled at 6 different spots and averaged, as summarized in **Table 4.7**. It was observed that more amount of O and Ni are found in the Pd/Ni/MOFDC, attributable to the formation of the passive $Ni(OH)_2$. This passive $Ni(OH)_2$ layer covers or blocks a large portion of the nanostructured Pd in the Pd/Ni/MOFDC. Unlike in the Pd/AT-Ni/MOFDC with no passive $Ni(OH)_2$, it maximally deposited the nanostructured Pd with much more exposure. The percentage oxygen deficiency or vacancy in the Pd/AT-Ni/MOFDC was calculated to be *ca.* 13 %. The quantitative analysis conforms with the qualitative results.

Table 4.7: XPS Quantitative elemental composition of the Pd/Ni-based electrocatalysts

Elemental composition	Pd/Ni-based Electrocatalysts	
	Pd/Ni/MOFDC	Pd/AT-Ni/MOFDC
Pd / wt %	13.80 ± 0.84	26.29 ± 0.74
Ni / wt %	7.22 ± 0.79	2.67 ± 0.73
C / wt %	55.33 ± 1.03	51.16 ± 0.90
O / wt %	22.02 ± 0.73	19.16 ± 0.82
N / wt %	1.64 ± 0.71	0.51 ± 0.42

4.2.32.5 X-ray Absorption Near-Edge Spectroscopy (XANES) and Fourier-Transform Extended X-ray Absorption Fine Structure (FT-EXAFS)

The chemical nature of the elemental composition of the Pd/Ni-based electrocatalysts was further investigated using more sophisticated techniques like XANES and FT-EXAFS (**Figure 4.21**). **Figure 4.21a** shows the XANES at Ni K-edge of the

electrocatalysts where metallic Ni^0 and little amount of $Ni(OH)_2$ are present in the Pd/Ni/MOFDC, but only metallic Ni^0 is present in the Pd/AT-Ni/MOFDC with no traces of passive $Ni(OH)_2$. **Figure 4.21b** shows the XANES of PdNi interaction in the electrocatalysts revealing that both electrocatalysts contain metallic Pd^0 and little amount of amorphous PdO_x and agrees with the XPS analysis.

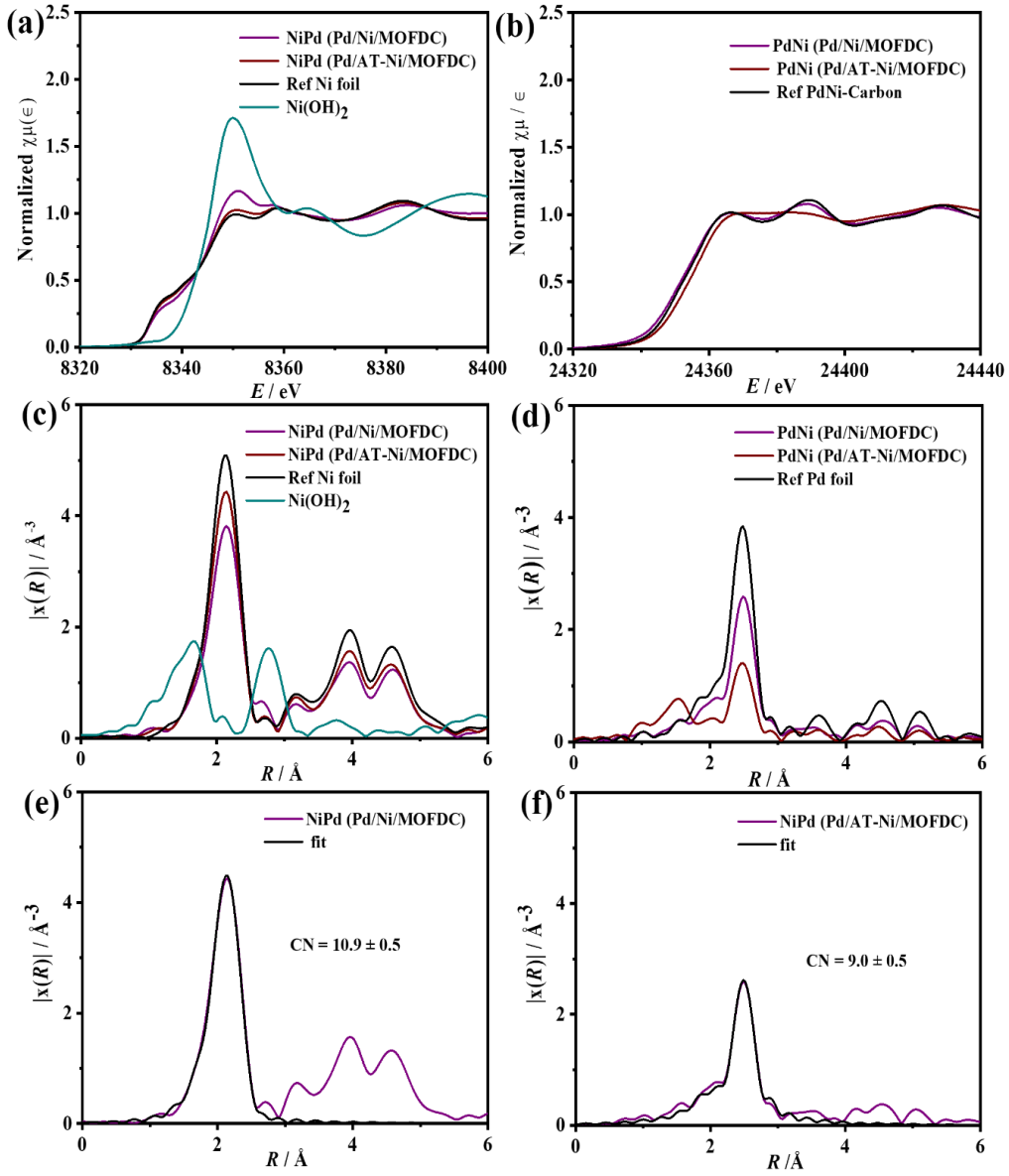

Figure 4.21: The XANES spectra of the Pd/Ni-based electrocatalysts collected at the (a) Ni K-edge, (b) Pd K-edge, the FT-EXAFS spectra of the Pd/Ni-electrocatalysts collected at the (c) Ni-K-edge, and Pd K-edge, the FT-EXAf+FS

spectra fitting of the (e) Ni K-edge and (f) Pd K-edge with the coordination number (*CN*) of the first shell Ni-Ni and Pd-Pd bonds given

Figures 4.21c and **4.21d** show the FT-EXAFS of the electrocatalysts revealing that the Pd and Ni nanoparticles do not form an alloy phase. Average bulk coordination numbers of the first shell Ni-Ni and Pd-Pd bonds of the Pd/Ni/MOFDC and Pd/AT-Ni/MOFDC are recorded as 10.9 ± 0.5 (**Figure 4.21e**) and 9.0 ± 0.5 nm (**Figure 4.21f**), corresponding to a mean particle size of >5 and ~3 nm, respectively. The results as a whole reveal that about half a portion of the nanostructured Pd surface in the Pd/Ni/MOFDC is covered by the passive ($Ni(OH)_2$), whilst the surface of the nanostructured Pd in the Pd/AT-Ni/MOFDC is maximally exposed and form a strong synergy with the more active metal Ni^0.

4.2.3.2.6 Scanning Electron Microscopy (SEM) and Energy Dispersive X-ray Spectroscopy (EDXS)

Figures 4.22a and **4.22b** show the SEM images of the Pd/Ni-based electrocatalysts' surfaces. The surfaces of the Pd/Ni-based electrocatalysts reveal flake-like morphology. Qualitative elemental analysis of the Pd/Ni-based electrocatalysts' surfaces is further revealed using the coupled EDX (**Figures 4.22c** and **4.22d**). The Pd/Ni/MOFDC shows the following elemental compositions: Pd, Ni, C, O, N and Au, while the Pd/AT-Ni/MOFDC contains the same elements, except O. The presence of O in the Pd/Ni/MOFDC could be traced to the passive $Ni(OH)_2$, which disappeared after being chemically etched of the composite of the Pd/AT-Ni/MOFDC. These results agree with the Raman (**Figure 4.18**), XPS (**Figure 4.20)** and XANES (**Figure 4.21**). The presence of Au absorption is due to the coating of the carbon tape, as the materials are charging.

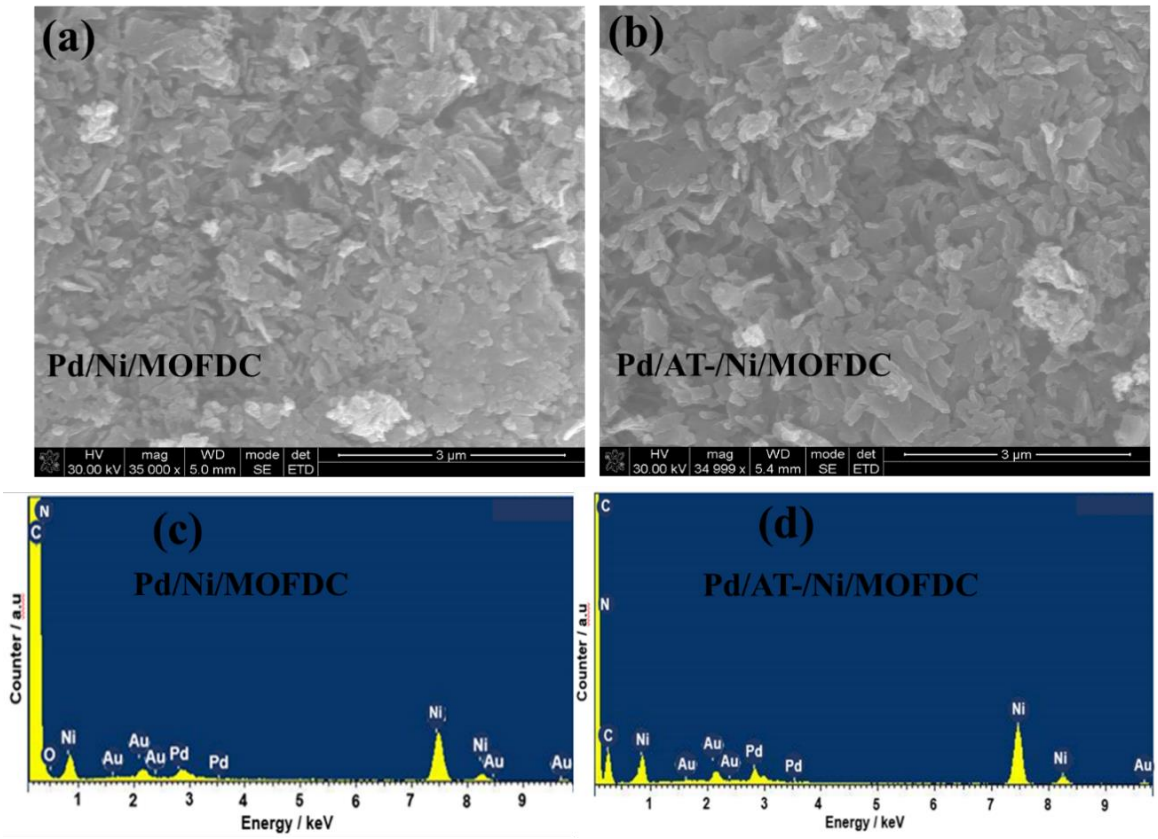

Figure 4.22: SEM images of (a) Pd/Ni/MOFDC, (b) Pd/AT-Ni/MOFDC, EDXS (c) Pd/Ni/MOFDC and (d) Pd/AT-Ni/MOFDC

4.2.3.2.7 Transmission Electron Microscopy (TEM)

Figure 4.23 shows the TEM micrographs of the as-prepared Ni-MOF, composites and Pd/Ni-based electrocatalysts. The as-prepared Ni-MOF (**Figure 4.23a)** reveal the interconnection of the Ni centre metal within frameworks. The Ni-based composites (**Figures 4.23b** and **4.23c)** show spherical Ni nanoparticles, which are closely packed in the Ni/MOFDC, but highly dispersed in the AT-Ni/MOFDC because of the chemical etching with average particle sizes of 13.7 ± 1.4 (**Figure 4.23f**) and 11.6 ± 1.3 nm (**Figure 4.23g**), respectively. The deposition of nanostructured Pd onto the composites (**Figures 4.23d** and **4.23e**), resulted in the distribution of a mixture of Pd and Ni nanoparticles, as the two elements do not alloy from the XANES and EXAFS analysis (**Figure 4.21**). The Pd/Ni nanoparticles in the Pd/Ni/MOFDC and Pd/AT-Ni/MOFDC

recorded average particle sizes of 10.1 ± 1.1 and 7.8 ± 0.9 nm (**Figures 4.23h** and **4.23i**), respectively. The reduced average nanoparticle sizes in the electrocatalysts may be trace to additional microwave irradiation.

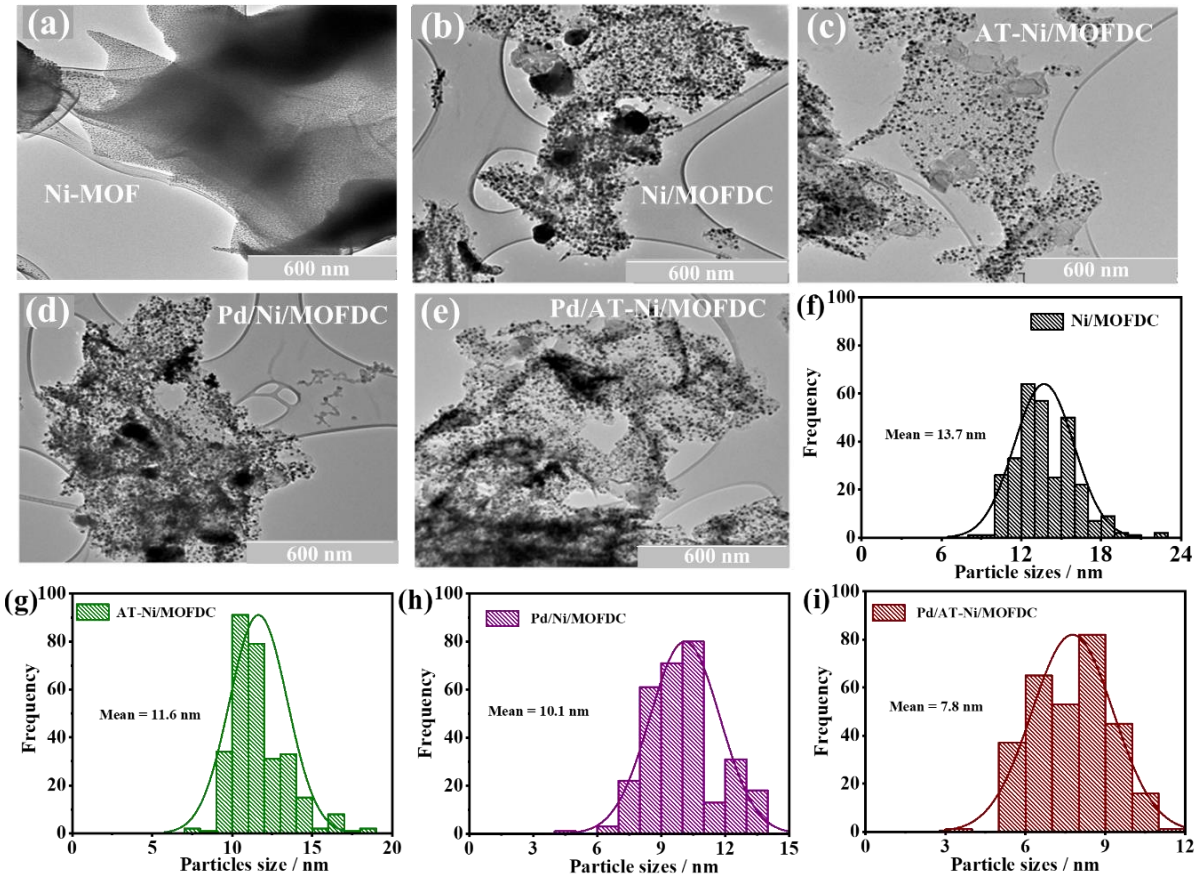

Figure 4.23: TEM micrographs (a) Ni-MOF, (b,c) Ni-based composites (d,e) Pd/Ni-based electrocatalysts, corresponding particle sizes of (f,g) Ni-based composites and (h,i) Pd/Ni-based electrocatalysts

4.2.3.2.8 Thermogravimetric Analysis (TGA)

The TGA profiles of the Ni-based composites and Pd/Ni-based electrocatalysts are shown in **Figure 4.24**. The composites and Pd/Ni-based electrocatalysts are thermally stable up to 200 ºC, where moist air adsorbed have been removed. Then, thermal oxidation of the metallic Ni in the composites was observed in the range (350 – 400 ºC) and thereafter from 500 ºC, a single transition of the $Ni(OH)_2$ to NiO was observed

for the Ni/MOFDC, while the Ni in the AT-Ni/MOFDC was alternating by oxidizing to NiO and reducing to metallic Ni [40,41]. The Pd/Ni-based electrocatalysts have more pronounced thermal decomposition between 400 – 600 ºC, may be traced to the combustion of the MOFDC and the PdO became reduced to metallic Pd at high temperature of 720 – 780 ºC [42,43].

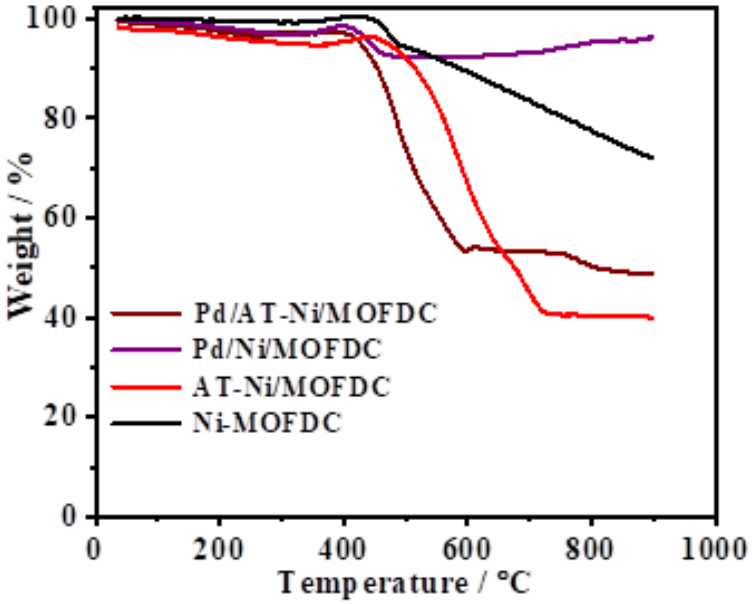

Figure 4.24: TGA profiles of the Ni-based composites and Pd/Ni-based electrocatalysts in air

4.2.3.2.9 Brunauer-Emmett-Teller (BET) Analysis

The surface area and porosity of the as-prepared Ni-MOF, Ni-based composites, and Pd/Ni-based electrocatalysts are investigated using the BET analysis, summarized in **Table 4.8**. The result reveals surface area (85.09 m^2 g^{-1}), pore volume (0.049 cm^3 g^{-1}), and pore size (7.17 nm) for the Ni-MOF sacrificial template. Carbonization of this template increase abruptly the surface area and pore volume for the Ni/MOFDC to 148.92 m^2 g^{-1}, 0.105 cm^3 g^{-1}, but decreased the pore size to 2.95 nm. Whereas chemical etching of the carbonized component further increases these physical properties to 153.05 m^2 g^{-1}, 0.124 cm^3 g^{-1}, and 3.48 nm for the AT-Ni/MOFDC.

Nanostructured Pd deposition on the composites decreased the surface area and pore volume for the Pd/Ni/MOFDC (105.88 m^2 g^{-1}, 0.095 cm^3 g^{-1}) and Pd/AT-Ni/MOFDC (66.89 m^2 g^{-1}, 0.075 cm^3 g^{-1}), but their pore sizes increase to 6.15 and 7.60 nm, respectively. The increased pore sizes of the Pd/Ni-based electrocatalysts may be ascribed to additional microwave irradiation.

Table 4.8: Brunauer-Emmett-Teller (BET) analysis of the as-prepared Ni-MOF, composites and Pd/Ni-based electrocatalysts

Samples	BET parameters		
	Pore size / nm	Pore volume / cm^3 g^{-1}	S_{BET} / m^2 g^{-1}
Ni-MOF	7.17	0.049	85.09
Ni/MOFDC	2.95	0.105	148.92
AT-Ni/MOFDC	3.48	0.124	153.05
Pd/Ni/MOFDC	6.15	0.095	105.88
Pd/AT-Ni/MOFDC	7.60	0.075	66.89

4.2.3.2.10 Ethanol Oxidation Reaction (EOR) Measurements

In this section, the Pd/Ni-based electrocatalysts were tested for half-cell reaction (EOR, **Figure 3.1**) using CV, LSV, CA and EIS.

4.2.3.2.10.1 Cyclic Voltammetry (CV)

The CV was used to verify the activities of Pd/Ni-based electrocatalysts in the supporting electrolyte and toward the EOR in alkaline conditions. Redox probe of the Pd/Ni-based electrocatalysts was first carried out in the supporting electrolyte (0.5 M KOH solution), shown in **Figure 4.225a**. Well-resolved voltammograms were

displayed with the following characteristics: (i) hydrogen adsorption/desorption occurring in the range of -0.6 and -1.0 V *vs.* AglAgCl,$(KCl)_{sat'd}$, which is consistent with the literature [25,26]; (ii) Pd oxidation and PdO reduction at around -0.23 and -0.36 V *vs.* AglAgCl,$(KCl)_{sat'd}$, respectively; and (iii) Ni oxidation and NiO reduction at 0.44 and 0.33 V *vs.* AglAgCl,$(KCl)_{sat'd}$, respectively. The ECSA of the Pd/Ni-based electrocatalysts were determined following **Equation 2.11** and recorded as 1264.4 ± 2.7 and 257.7 ± 0.5 $cm^2\ mg^{-1}$ for Pd/AT-Ni/MOFDC and Pd/Ni/MOFDC, respectively. The reduced ECSA of the Pd/Ni/MOFDC is traced to the coverage of the Pd's active sites by the passive $Ni(OH)_2$, evidence by the XPS and XANES analysis. The ECSA values of the Pd/AT-Ni/MOFDC relatively increased by a factor of *ca.* 5.5, due to strong synergy between the more active metallic Ni and nanostructured Pd toward facile diffusion of the OH^- ions of the supporting electrolyte. Then, EOR activities of the Pd/Ni-based electrocatalysts were probed on the addition of 0.5 M EtOH to the 0.5 M KOH supporting electrolyte (**Figure 4.25b**), where two distinct forward and reversed voltammograms were revealed, explained previously. The forward signature E_{onset} values of -0.7 and -0.63 V (*vs.* AglAgCl, $(KCl)_{sat'd}$) for Pd/AT-Ni/MOFDC and Pd/Ni/MOFDC, respectively. Also, the EOR activities of the Pd/Ni-based electrocatalyst are determined by considering the *j* values. The Pd/AT-Ni/MOFDC has 5.5 times increased *j* values compared to the Pd/Ni/MOFDC. These results show that the Pd/AT-Ni/MOFDC does not only require less energy but also increased activity for the EOR. These observations quite agree with the fact that the EOR activity for the Pd/Ni/MOFDC dwindled because the passive layer of $Ni(OH)_2$ covers almost half of the active sites of Pd catalyst, but it has slight tolerance to CO poisoning, as its j_f/j_r value relatively increased slightly. To further understand the interaction between the

electrodes and electrolyte, the EOR was cycled at different scan rates (**Figures 4.25c** and **4.25d**).

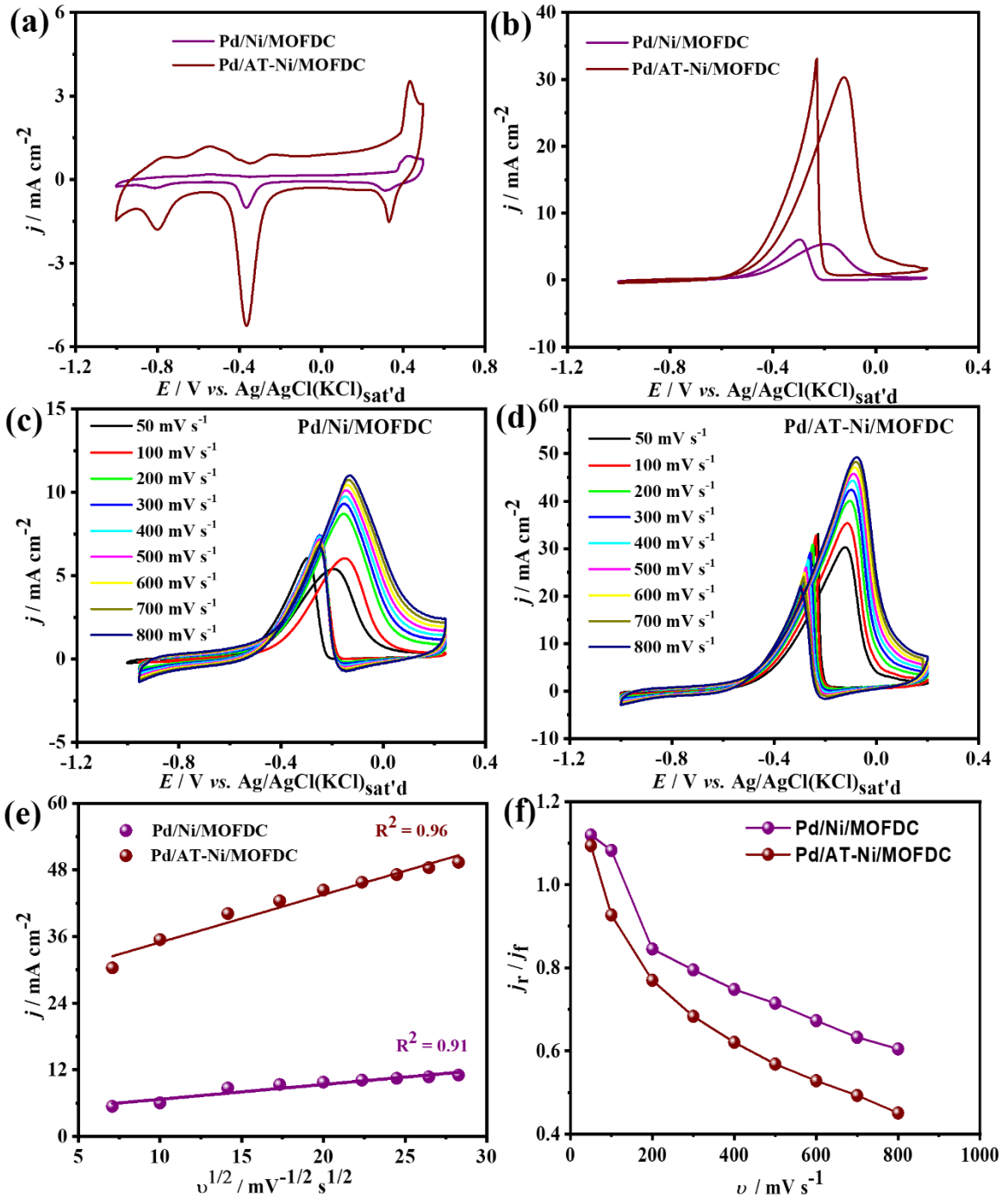

Figure 4.25: CV at 50mV s^{-1} in (a) 0.5 M KOH purged with N_2 gas (b) a mixture of 0.5 M KOH and 0.5 M EtOH solutions, scan rate studies of (c) Pd/Ni/MOFDC, (d) Pd/AT-Ni/MOFDC, (e) plots of j_f *vs.* $\upsilon^{1/2}$ and (f) plots of $1/j_f/j_r$ *vs.* υ of the Pd/Ni-based electrocatalysts in 0.5 M KOH/0.5 M EtOH solutions

As the scan rate increase, the forward signatures' *j* values increase concurrently, indicating that the chemisorbed CO got oxidized faster, as the scan rate increase. Then, the plot of the *j* values for the forward signatures was made against the square root of the scan rate (**Figure 4.25e**), showing a linearity behavior with least square coefficients (R^2 = 0.91 – 0.96) close to unity, signifies that the interaction between the electrodes and electrolyte is diffusion-controlled. However, the corresponding line exhibits nonzero intercepts. This result is an indication that reaction at modified working electrode−electrolyte interfaces could be at least in part diffusion controlled, although localized resistivity phenomena could also contribute. The tolerance of the electrocatalysts toward CO poisoning were further verified with the plots of j_r/j_f values against scan rates (**Figure 4.25f**). Although the Pd/Ni/MOFDC has reduced activity toward the EOR but has better tolerance for CO poisoning. The EOR performances of the Pd/SnO_2- and Pd/Ni-based electrocatalysts with literature in the three-electrode configuration are summarized in **Table 4.9**.

4.2.3.2.10.2 Linear Sweep Voltammetry (LSV)

Kinetic studies of the Pd/Ni-based electrocatalysts toward the EOR were investigated using LSV (**Figures 4.26a** and **4.26b**) at different EtOH concentrations and a very low scan rate (1.0 mV s^{-1}). It was observed that increase in the concentration of EtOH up to 1.75 M, increase the *j* values, while further increase in EtOH's concentration led to decreased *j* values. These results show that the electrodes were saturated and the OH^- ions present in the electrolyte have been used up, as the EOR is a function of the EtOH and OH^- ions concentrations to the first order.

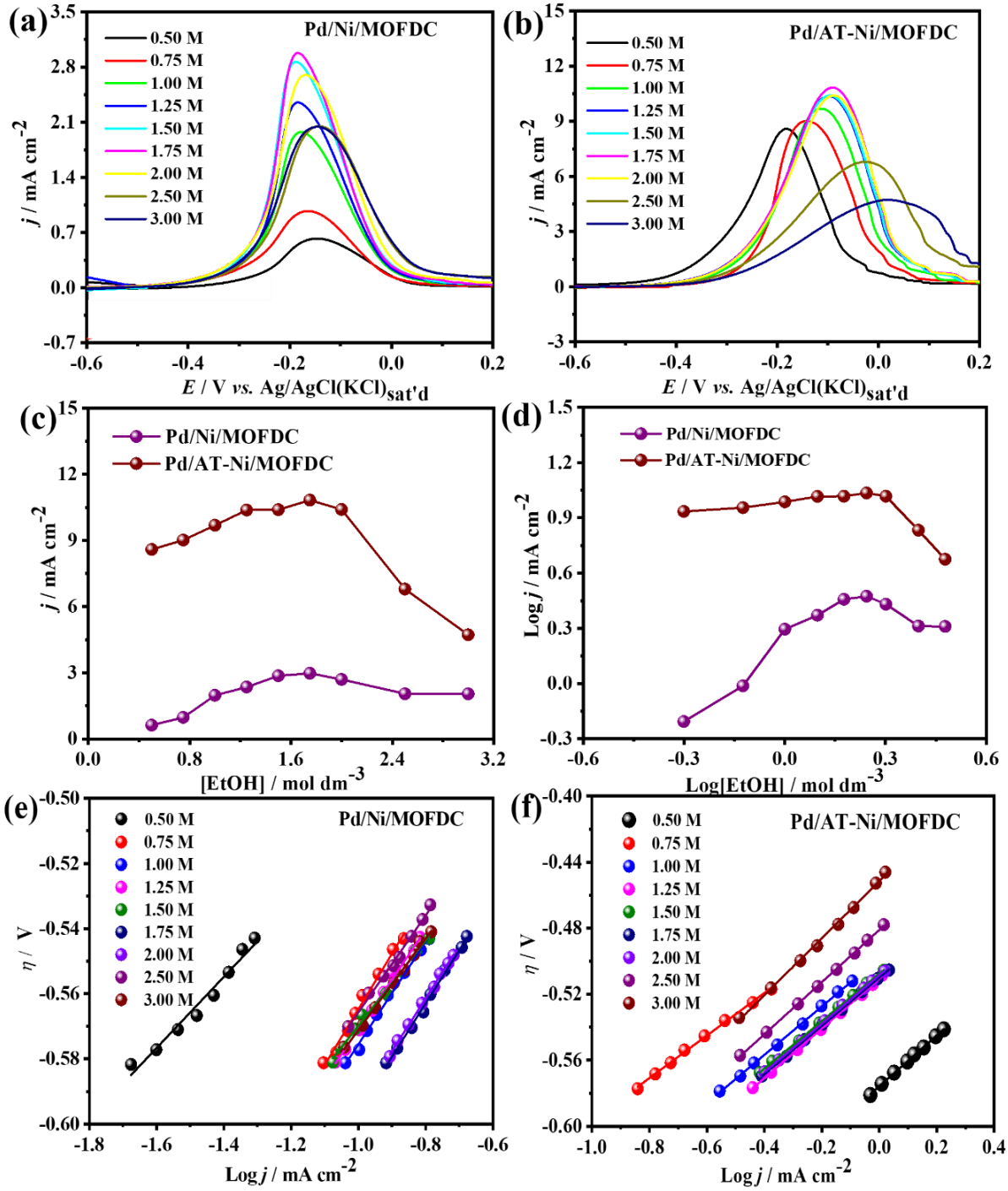

Figure 4.26: (a,b) LSV, (c) plots of *j vs.* [EtOH], (d) plots of Log *j vs.* Log [EtOH] and (e,f) Tafel plots of the Pd/Ni-based electrocatalysts in a mixture of 0.5 M KOH and 0.5 M EtOH solutions at 1.0 mV s^{-1}

Then, kinetic parameters for the Pd/Ni-based electrocatalysts were deduced from the LSV signature of each EtOH's concentration and aggregated, using the Tafel plots

(**Figures 4.26e** and **4.26f**). The aggregate b_a values of 112.0 ± 9.6 and 166.7 ± 8.0 mV dec^{-1} with corresponding α values of 0.65 and 0.47 were calculated for the Pd/AT-Ni/MOFDC and Pd/Ni/MOFDC, respectively. These results show the rate determining step of the EOR is when carbonyl group (CH_3CO) and OH^- ions combined to form CH_3COOH as by-product.

Table 4.9: Comparative EOR activities of the Pd/SnO_2- and Pd/Ni-based electrocatalysts for half-cell reaction (three-electrode system) with literature

Electrocatalysts	Electrolyte mixtures	ECSA / $cm^2\ mg^{-1}$	E_{onset} / V	j_f / mA cm^{-2}	j_f/j_b	Refs.
Pd/AT-Ni/MOFDC	0.5 M KOH /0.5 M EtOH	1264.4 ± 2.7	-0.70	30.4	0.90	[This work]
Pd/Ni/MOFDC	0.5 M KOH/ 0.5 M EtOH	257.7 ± 0.5	-0.63	5.5	0.92	[This work]
Pd/SnO_2/MOFDC	0.25 M KOH/ 0.25 M EtOH	962.2 ± 2.3	-0.65	7.3	0.80	[This work]
Pd/MOFDC	0.25 M KOH/ 0.25 M EtOH	263.4 ± 0.4	-0.58	3.2	0.77	[This work]
Pd/SnO_2/CB	0.25 M KOH/ 0.25M EtOH	806.6 ± 1.9	-0.62	3.0	0.82	[This work]

Pd/CB	0.25 M KOH/ 0.25M EtOH	235.3 ± 0.4	0.60	1.7	0.70	[This work]
$Pd_{59}Ni_{41}$/C	0.1 M KOH/ 0.5 M EtOH	n/a	-0.56	19.8	0.81	[44]
$Ni_{50}Pd_{50}$/Graphene	1.0 M KOH/ 0.5 M EtOH	770.0	-0.80	8.0	0.82	[45]
Pd-NiO/C	0.5 M KOH/ 1.0 M EtOH	1076.5	-0.59	31.1	1.11	[46]
FeCo@Fe@Pd/C	0.5 M KOH/ 0.5 M EtOH	246.0	-0.71	3.9	1.28	[47]
PdNi/CeO/C	1.0 M KOH/ 1.0 M EtOH	n/a	-0.40	5.3	1.4	[48]
Pd/Cu/Graphene	1.0 M KOH/ 1.0 M EtOH	202.2	-0.26	1.94	2.98	[49]
Pd_2Ni_1/C	1.0 M KOH/ 1.0 M EtOH	680.0	-0.76	17.61	0.79	[50]
$Pt_{23}Pd_{77}$/C	1.0M KOH/ 1.0 M EtOH	219.8	-0.70	11.16	0.94	[51]
$Au@Au_{0.20}Pd_{2.0}$ NPs	0.5 M KOH/ 0.5 M EtOH	1258.0	-0.65	9.5	0.90	[52]
$PdAu_3$/C	1.0 M KOH/ 1.0 M EtOH	-	-0.48	54.56	~1.1	[53]

4.2.3.2.10.3 Electrochemical Impedance Spectroscopy (EIS)

The interaction of the electrodes was further probed using the EIS. The Nyquist plots (**Figure 4.27a**) were made with the Voigt *EEC* model (**Figure 4.27b**) to determine the EIS parameters (**Table 4.10**). R_s value of *ca.* 21.0 Ω was recorded for the Pd/Ni-based electrocatalysts, indicating similar ionic conductivity of the electrocatalysts in the electrolyte for the three-electrode system. However, an extremely lower R_{ct} value of *ca.* 21.0 Ω was recorded for Pd/AT-Ni/MOFDC compared to that of Pd/Ni/MOFDC (305.0 Ω), explaining its excellent EOR kinetics obtained from the CV and LSV curves. Overall, the (R_s + R_{ct}) value of the Pd/AT-Ni/MOFDC (*ca.* 42.56 Ω) is relatively lower than the Pd/Ni/MOFDC (*ca.* 325.36 Ω) further confirms the faster EOR kinetic of the Pd/AT-Ni/MOFDC. Also, the reduced Warburg diffusion (Z_w) value of the Pd/AT-NI/MOFDC corroborates the rapid diffusion of the electrolyte on its active sites for facile EOR.

Figures 4.27b and **4.27c** show the Bode plots of the Pd/Ni-based electrocatalysts in a mixture of 0.5 M EtOH and 0.5 M KOH solution, where their resistive and capacitive behaviors were observed in the high-frequency and the low-frequency regions, respectively. The Pd/Ni-based electrocatalysts recorded phase angle of *ca.* 80º suggests that the adsorption process is coupled with the diffusion process occurring at the electrode-electrolyte interfaces. The plots of Log *Z* (Ω) *vs.* Log *f* (Hz) give slope values of -0.9926 ± 0.0413 and -0.8379 ± 0.05334 with R^2 values of 0.993 and 0.984 calculated at the linear high-frequency region for the Pd/Ni/MOFDC and Pd/AT-Ni/MOFDC, respectively. The deviation of the slope values from the ideal value (-1) is an indication that the charge storage capacity is not pure C_{dl} but *CPE*, which supports the Voigt *EEC* model employed for fitting [54].

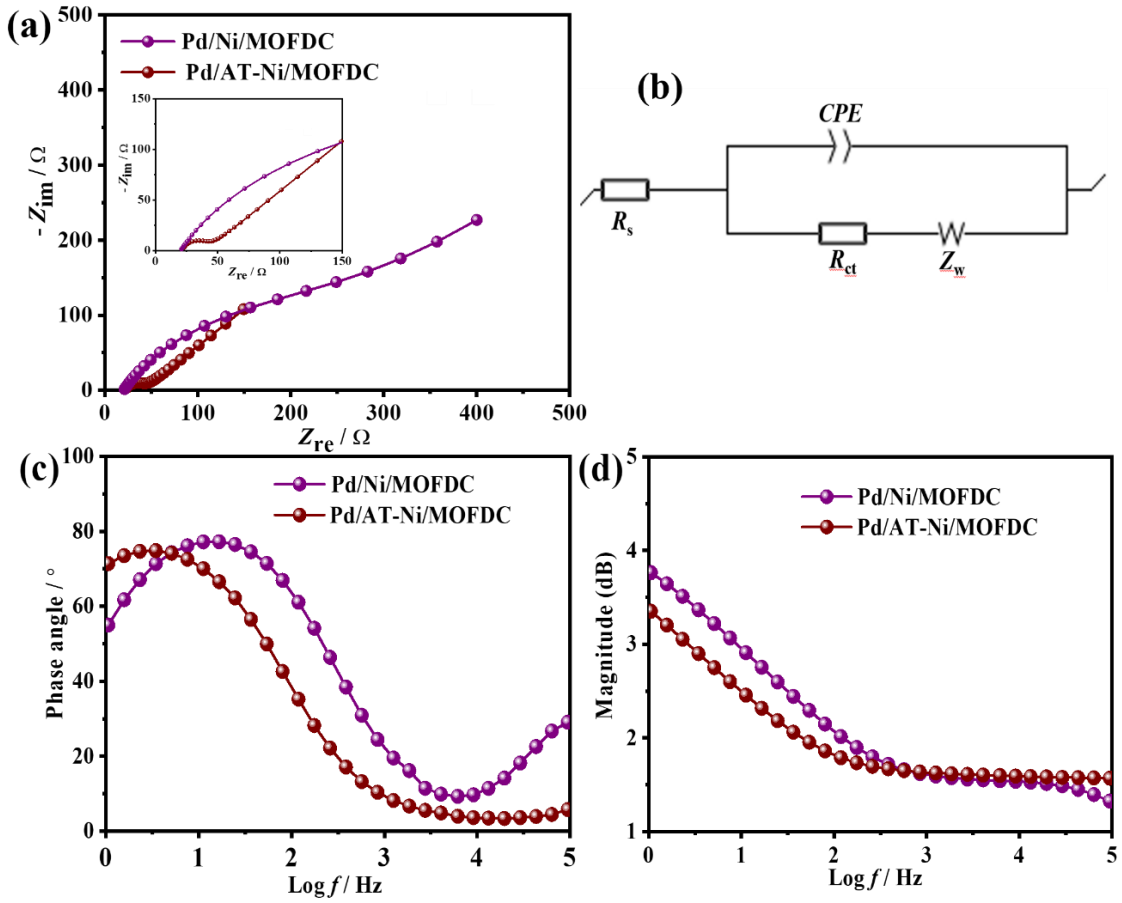

Figure 4.27: (a) Nyquist plots and (b,c) Bode plots of the Pd/Ni-based electrocatalysts for ethanol oxidation in a mixture of 0.5 M KOH and 0.5 M EtOH solutions at potential -0.3 V (*vs.* AglAgCl, $(KCl)_{sat'd}$)

Table 4.10: EIS parameters of the Pd/Ni-based electrocatalysts in a mixture of 0.5 M KOH and 0.5 M EtOH solutions at potential -0.3 V (*vs.* AglAgCl, $(KCl)_{sat'd}$)

EIS parameters	Pd/Ni-based Electrocatalysts	
	Pd/Ni/MOFDC	Pd/AT-Ni/MOFDC
R_s / Ω	20.26 ± 0.51	21.87 ± 1.34
R_{ct} / Ω	305.1 ± 3.81	20.69 ± 1.18
CPE / µF.s^(1-a)	63.19 ± 6.85	2.90 ± 0.29
a	0.69	0.87
Z_w / Ω $s^{-1/2}$	983.4 ± 20.19	516 ± 0.70

4.2.3.2.10.4 Chronoamperometry (CA)

Additional information on the stability of the Pd/Ni-based electrocatalysts for the *EOR* was obtained from the CA (**Figure 4.28**). The Pd/Ni-based electrocatalysts' *j* values begin to decline slowly from 5.8 to 1.01 mA cm^{-2} (Pd/AT-Ni/MOFDC), and 1.12 to 0.19 mA cm^{-2} (Pd/Ni/MOFDC). The decline in the *j* values of the Pd/Ni-based electrocatalysts is attributed to the adsorption of the CO species on their active sites, hence, increasing their resistance and reducing their EOR activities. The percentage retention of the electrocatalysts (*ca.* 17.0 %) for the EOR activities are traced to the accumulation of the incompletely oxidized CO species on the active sites of the Pd/Ni-based electrocatalysts to prevent additional oxidation.

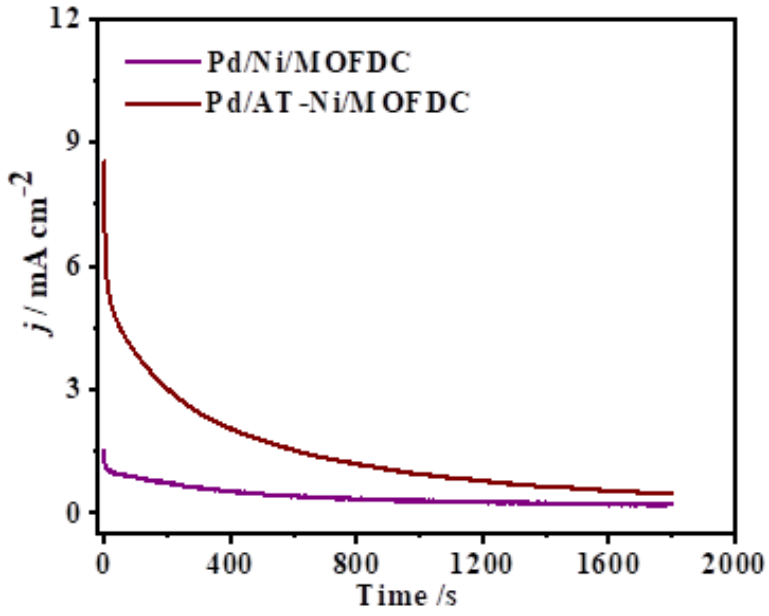

Figure 4.28: CA analysis of the Pd/Ni-based electrocatalysts for the EOR in a mixture of 0.5 M EtOH and 0.5 M KOH solutions at potential -0.3 V (*vs.* AglAgCl, $(KCl)_{sat'd}$)

4.2.3.2.11 Direct Ethanol micro-Fuel Cell (μ-DEFC) Measurements

A proof-of-concept of the μ-DEFC (set-up shown in **Figure 4.14**) was carried out using the micro-3D printed cell. Potential and power curves of the Pd/Ni-based

electrocatalysts (**Figure 4.29a**) recorded peak power density (P_m) of 26.49 and 11.91 mW cm^{-2} for the Pd/AT-Ni/MOFDC and Pd/Ni/MOFDC, respectively. Then, the Pd/Ni-based electrocatalysts were subjected to galvanostatic discharge (**Figure 4.29b**) at 40 mA cm^{-2} for 24 h, after which the Pd/AT-Ni/MOFDC has voltage retention of 0.58 V from the *OCV* (0.85 V), amounting to 68 % energy retention after 24 h, while the Pd/Ni/MOFDC crashed at 15 h discharging all its energy. Then, EIS with Nyquist plots (**Figure 4.29c**) was employed to further probe the Pd/Ni-based electrocatalysts at initial and after the galvanostatic discharge processes, which are modelled with the Voigt *EEC* (**Figure 4.29d**) and the obtained EIS parameters are summarized in **Table 4.11**. The R_b values of *ca.* 3.5 and 2.6 Ω for the Pd/AT-Ni/MOFDC at initial and after 24 h discharge are relatively lower than those of the Pd/Ni/MOFDC (*ca.* 3.5 and 3.1 Ω). These results show that bulk conductivity on the electrode-electrolytes interfaces became more rapid after the long discharge process with the Pd/AT-Ni/MOFDC displaying better conductivity. Also, the interfacial conductivity of the electrodes in the electrolyte at the high-frequency region could be deduced from the values of R_{int} values, which are inversely related. Signifying that lower the R_{int} values, the higher the interfacial conductivity of the electrode materials. The R_{int} values of the Pd/Ni/MOFDC at initial (*ca.* 13.5 Ω) and after discharge process (*ca.* 60.0 Ω) are higher compared to the Pd/AT-Ni/MOFDC with values of *ca.* 4.0 and 40.0 Ω, respectively confirming the relatively lower ohmic resistance of the Pd/AT-Ni/MOFDC in the μ-DEFC. The extremely lower R_{int} values of the Pd/AT-MOFDC justify its superior electronic conductivity at the initial and after the discharge process due to ohmic loss from the electrolytes' diffusion. The third resistance value observed is the charge transfer resistance (R_{ct}) due to electron transport at the low-frequency region. The Pd/AT-Ni/MOFDC also shows extremely lower R_{ct} at both initial and after discharge process.

Although, both electrocatalysts recorded increased series resistance (R_b + R_{int} + R_{ct}) values after the discharge process may be due to the poisoning by the CO species.

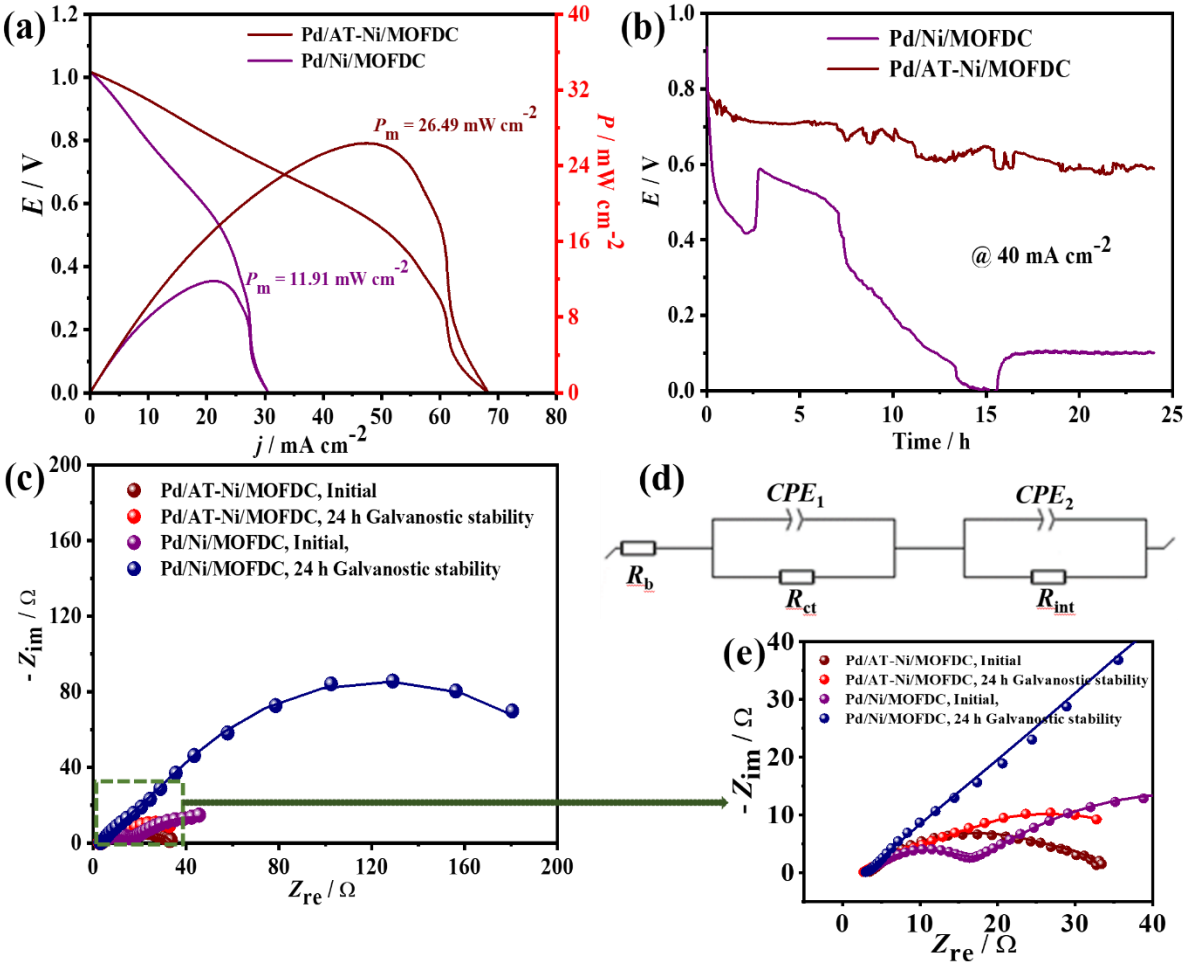

Figure 4.29: (a) potential and power curves, (b) galvanostatic discharge test at 40 mA cm^{-2} of the Pd/Ni-based electrocatalysts, and (c) EIS before and after stability test of the Pd/AT-Ni/MOFDC and Pd/Ni/MOFDC at OCVs 0.85 V and 0.64 V, respectively in a mixture of 2.0 M EtOH and 2.0 M KOH solution, (d) Voigt *EEC* used in modelling the Nyquist plots and (e) the expanded portion of the Nyquist plot.

However, the (R_b + R_{int} + R_{ct}) value of the Pd/AT-Ni/MOFDC at the initial and after discharge process for 24 h is relatively lower than those of the Pd/Ni/MOFDC, indicating better electron transport in the μ-DEFC and corroborate the results obtained

for the potential and power curves. Comparative electrocatalytic activities of the electrocatalysts for μ-DEFC with literature are summarized in **Table 4.12**.

Table 4.11: EIS parameters of the Pd/Ni-based electrocatalysts for the μ-DEFC in a mixture of 2.0 M EtOH and 2.0 M KOH solutions at *OCVs* of Pd/AT-Ni/MOFDC (0.85 V) and Pd/Ni/MOFDC (0.64 V)

EIS parameter	Pd/AT-Ni/MOFDC		Pd/Ni/MOFDC	
	Initial	After 24 h discharge	Initial	After 24 h discharge
R_b / Ω	3.49 ± 0.51	2.59 ± 1.00	3.38 ± 0.71	3.08 ± 0.41
R_{int} / Ω	3.59 ± 1.74	39.72 ± 1.00	13.4 ± 4.48	59.67 ± 4.70
CPE1 / mF.s^(1- *a*)	68.91 ± 4.84	20.15 ± 0.01	0.33 ± 0.07	5.24 ± 3.68
a_1	0.90	0.53	0.63	0.57
R_{ct} / Ω	26.66 ± 1.97	6.78 ± 0.01	55.61 ± 26.43	160.6 ± 26.22
CPE1 / mF.s^(1- *a*)	1.75 ± 0.24	104.40 ± 1.00	21.02 ± 5.88	4.61 ± 0.84
a_2	0.60	1.00	0.58	0.95

Table 4.12: Comparative performance of all the electrocatalysts for μ-DEFC tests showing operating conditions and power density with literature

Anode (An.)	An. support	Cathode (Cad.)	Cad. support	Operating cond./ Temperature	P_m / mW cm^{-2}	Refs.
Pd/AT-Ni/MOFDC	Ni foam	FeCo/C	C paper	2.0 M EtOH + 2.0 M KOH	26.49	[This work]
Pd/Ni/MOFDC	Ni foam	FeCo/C	C paper	2.0 M EtOH + 2.0 M KOH	11.91	[This work]
Pd/SnO_2/MOFDC	Ni foam	FeCo/C	C paper	2.0 M EtOH + 2.0 M KOH	19.73	[This work]
Pd/MOFDC	Ni foam	FeCo/C	C paper	2.0 M EtOH + 2.0 M KOH	11.06	[This work]
Pd/C	Ni foam	Hypermec	C cloth	1.0 M EtOH + 1.0 M KOH	26.04	[1]
PdNiO	C paper	Ag black	C paper	4.0 M EtOH + 4.0 M KOH	1.00	[6].
Pt-Ru	C paper	Pt	C paper	2.0 M EtOH + 2.0 M KOH	11.40	[55]
Pt-Pd	C paper	Pt/C	C paper	1.0 M EtOH + 0.5 M KOH, 40 ºC	30.00	[56]
PdNiSn	C paper	Pt/C	C paper	2.0 M EtOH + 6.0 M KOH	27.10	[57]

$Pd(DBA)_2$	C paper	Fe-Co Hypermec	C paper	5.0 wt% EtOH + 5.0 wt% KOH	31.00	[58]
PtRu black	C paper	MnO_2/C	C paper	2.0 M EtOH + 8.0 M KOH, 25 ºC	10.74	[59]
Pt-Au	C paper	Pt/C	C paper	1.0 M EtOH + 0.5 M KOH, 20 – 80 ºC	35.00	[60]
In_3Pd_2/C	C paper	Pt/C	C paper	1.0 M EtOH/ 1.0 M KOH	6.7	[61]
PdNPs-$SrFeO_{3-\delta}$NP-CH	C paper	PtNPs-CH	C paper	1.0 MeOH/ 2.0 M NaOH	14.52	[62]
Pd/Ni	C paper	Pt/C	C paper	2.0 M EtOH/ 6.0 M NaOH	19.8	[63]

4.3 Conclusions

Summary of the electrocatalysts' performances are presented in two distinct forms: (i) the Pd/SnO_2-based electrocatalysts; and (ii) Pd/Ni-based electrocatalysts. The Pd/SnO_2-based electrocatalysts (Pd/SnO_2/MOFDC and Pd/MOFDC), Pd/SnO_2/CB and Pd/CB were demonstrated for the EOR (half-cell reaction). The Pd/SnO_2/MOFDC displays increased *j* value by factors 2.3, 2.4, and 4.3 compared to the Pd/MOFDC, Pd/SnO_2/CB and Pd/CB, respectively. Also, the Pd/SnO_2/MOFDC has least ΔE value of 0.080 V relative to the Pd/MOFDC (0.089 V), Pd/SnO_2/CB (0.094 V) and Pd/CB (0.118 V). These results amongst others confirmed the superior EOR activities on the

Pd/SnO_2/MOFDC for the half-cell reaction. A proof-of-concept was verified with only the Pd/SnO_2/MOFDC and Pd/MOFDC with the aid of a micro-3D printed cell for the alkaline µ-DEFC. The Pd/SnO_2/MOFDC has a relatively higher P_m value of 19.73 mW cm^{-2} than that of the Pd/MOFDC (11.06 mW cm^{-2}). The electrocatalysts containing SnO_2 equally has better stability when subjected to a discharge test for 24 h, which was supported with decreased series resistances at initial and after the discharge test. In the second scenario, the Pd/Ni-based electrocatalysts (Pd/Ni/MOFDC and Pd/AT-Ni/MOFDC) for the EOR (half-cell- reaction) and alkaline µ-DEFC (full cell). The Pd/AT-Ni/MOFDC has improved EOR activities in terms of: (i) increased *j* and ECSA values by factors of *ca.* 5.5; (ii) lower E_{onset} and ΔE; and (iii) reduced series resistance compared to the Pd/Ni/MOFDC. These electrocatalysts were verified for real-life applications with the aid of a micro-3D printed cell for the alkaline µ-DEFC. The Pd/AT-Ni/MOFDC also shows superior performances with characteristics: (i) higher P_m of 26.49 mW cm^{-2} compared to 11.91 mW cm^{-2} (Pd/Ni/MOFDC); (ii) relatively high stability after 24 h discharge test with 68 % energy retention; and (iii) lower series resistances at initial and after the discharge test. The excellent performances of the electrocatalysts open an avenue to explore the use of MOF sacrificial templates for making excellent supports for highly efficient and efficient Pd electrocatalysts for the viable fabrication of reduced-cost direct ethanol fuel cell.

4.4 References

[1] J. Huang, A. Faghri, *Journal of Fuel Cell Science and Technology*, **11**,5(2014): 051007.

[2] L. An, T. S. Zhao, *Energy and Environmental Science*, **4**,6(2011): 2213–2217.

[3] E. Antolini, E. R. Gonzalez, *Journal of Power Sources*, **195**,11(2010): 3431–3450.

[4] N. Shaari, S. K. Kamarudin, S. Basri, L. K. Shyuan, M. S. Masdar, D. Nordin, *Journal of Applied Polymer Science,* **135**,37(2018): 46666.

[5] S. P. S. Badwal, S. Giddey, A. Kulkarni, J. Goel, S. Basu, *Applied Energy*, **145**(2015): 80–103.

[6] R. W. Verjulio, F. Alcaide, G. Alvarez, N. Sabate, N. Torres-Herrero, J. P. Esquivel, J. Santander, *Journal of Micromechanics and Microengineering*, **23**,11(2013): 115006.

[7] K. I. Ozoemena, *RSC Advances*, **6**(2016): 89523.

[8] E. Antolini, *Journal of Power Sources*, **170**,1(2007): 1–12.

[9] L. Wang, A. Lavacchi, M. Bevilacqua, M. Bellini, P. Fornasiero, J. Filippi, M. Innocenti, A. Marchionni, H. Miller, F. Vizza, *ChemCatChem*, **7**,14(2015): 2214–2221.

[10] H. Meng, D. Zeng, F. Xie, *Catalysts*, **5**,3(2015): 1221–1274.

[11] A. K. Ipadeola, B. Rasmita, S. C. Ray, K. I. Ozoemena, *Electrocatalysis,* **10**,4(2019): 366–380.

[12] H. Choi, J. Park, B. Kim, *Journal of Physical Chemistry B*, **109**,10(2005): 4333–4340.

[13] L. Hou, Z. Chen, Z. Zhao, X. Sun, J. Zhang, C. Yuan, *ACS Applied Energy Materials,* **2**(2019): 548–557.

[14] Y. Liu, Z. Sun, Y. Lin, K. Tan, J. Sun, L. Liang, L. Hou, C. Yuan, *Angewandte Chimie International Edition*, **59**(2020): 2473–2482.

[15] C. Mattevi, G. Eda, S. Agnoli, S. Miller, K. A. Mkhoyan, O. Celik, D. Mastrogiovanni, G. Granozzi, E. Garfunkel, M. Chhowalla, *Advance Functional Materials*, **19**,16(2009): 2577–2583.

[16] G. A. Zickler, B. Smarsly,N. Gierlinger, H. Peterlik, O. Paris, *Carbon*, **44**,15(2006): 3239–3246.

[17] L. W. Aguiar, C. T. Pereira-da-Silva, H. H. Carline-de-Lima, M. P. Moises, A. W. Rinaldi, *AIMS Materials Science*, **5**,3(2018): 467–478.

[18] H. Li, L. Chi, C. Yang, L. Zhang, F. Yue, and J. Wang, *Journal of Materials Research*. **31**,19(2016): 3069–3077.

[19] J. Chen, B. Wiley, J. McLellan, Y. Xiong, Z. Y. Li, Y. Xia, *Nano Letters,***5**,10(2005): 2058–2062.

[20] G. Yang, Y. Chen, Y. Zhou, Y. Tang, T. Lu, *Electrochemistry Communication*, **12**,3(2010): 492–495.

[21] C. Wen, Y. Wei, D. Tang, B. Sa, T. Zhang, C. Chen, *Scientific Reports*, **7**(2017): 4907.

[22] K. M. Hassan, A. A. Hathoot, R. Maher, M. Abdek Azzem, *RSC Advances*, **8**(2018): 15417–15426.

[23] A. E. Fahim, R. M. Abdel-Hameed, N. K. Allam, *New Journal of Chemistry*, **42**,8(2018): 6144–6160.

[24] R. S. Nicholson, I. Shain, *Analytical Chemistry*, **36**,4(1964): 706–723.

[25] Q. Cui, S. Chao, Z. Bai, H. Yan, K. Wang, L. Yang, *Electrochimica Acta*, **132**(2014): 31–36.

[26] J. Cai, Y. Zeng, Y. Guo, *Journal of Power Sources*, **270**(2014): 257–261.

[27] J. Pillay, K. I. Ozoemena, *Electrochimica Acta*, **54**,22(2009): 5053–5059.

[28] K. I. Ozoemena, N. S. Mathebula, J. Pillay, G. Toschi, J. A. Verschoor, *Physical Chemistry Chemical Physics*, **12**,2(2010): 345–357.

[29] Y. Ge, H. Adler, A. Theertham, L. L. Kesmodel, S. L. Tait, *Langmuir*, **26**,21(2010), 16325–16329.

[30] H. Zhang, R. Xiao, M. Song, D. Shen, J. Liu, *Journal of Thermal Analysis and Calorimetry,* **115**,2(2014),1921–1927.

[31] P. Du, Y. Dong, C. Liu, W. Wei, Dong Liu, P. Liu, *Journal of Colloid and Interface Science*, **518**(2018): 57–68.

[32] H. Jiang, Y. Guo, T. Wang, P. L. Zhu, S. Yu, Y. Yu, X. Z. Fu, R. Sun, C. P. Wong, *RSC Adv*ance, **5**,17(2015): 12931–12936.

[33] A. M. Hengne, A. K. Samal, L. R. Enakonda, M. Harb, L. E. Gevers, D. H. Anjum, M. N. Hedhili, Y. Saih, K. W. Huang, J. M. Basset, *ACS Omega*, **3**,4(2018): 3688–3701.

[34] J. B. Wu, Z. G. Li, X. H. Huang, Y. Lin, *Journal of Power Sources*, **224**(2013): 1–5.

[35] J. Wang, Q. Zhao, H. Hou, Y. Wu, W. Yu, X. Ji, L. Shao, *RSC Advance*, **7**(2017): 14152–14158.

[36] A. Li, H. Song, Z. Blan, L. Shi, X. Chen, J. Zhou, *Journal of Material Chemistry A*, **5**,12(2017): 5934–5942.

[37] D. G. Georgiev, R. J. Baird, G. Newaz, G. Auner, R. Witte, H. Herfurth, *Applied Surface Science*, **236**(2004): 71–76.

[38] M. C. Li, L. Kang, *Journal of Energy Chemistry*, **26**,4(2017): 750–756.

[39] K. M. Wong, Y. Fang, A. Devaux, L. Wen, J. Huang, L. D. Cola, Y. Lei, *Nanoscale*, **3**(2011): 4830–4839.

[40] M. Ahmadi, R. Younesi, T. Vegge, M. J. F. Guinel, *Materials Resources Express*, **1**,2(2014): 25501.

[41] C. S. Carney, R. E. Chinn, N. Dołan, M. C. Gao, *Journal of Alloys Compound*, **644**(2015): 968–974.

[42] P. H. Jen, Y. H. Hsu, S. D. Lin, *Catalysis Today*,**123**,1-4(2007): 133–141.

[43] Y. Holade, C. Morais, S. Arrii-Clacens, K. Servat, T. W. Napporn, K. B. Kokoh, *Electrocatalysis*,**4**,3(2013): 167–178.

[44] K. Lee, S. W. Kang, S. U. Lee, K. H. Park, Y. W. Lee, S. W. Han, *ACS Applied Material Interfaces,* **4**,8(2012): 4208–4214.

[45] M. S. Ahmed, S. Jeon, *ACS Catalysis,***4**,6(2014): 1830–2837.

[46] R. M. AbdelHammed, *Journal of Colloid and Interface Science*,**505**(2017): 230–240.

[47] O. O. Fashedemi, K. I. Ozoemena, *Electrochimica Acta,***128**(2014): 279–286.

[48] Y. C. Wei, C. W. Liu, W. D. Kang, C. M. Lai, L. D. Tsai, K. W. Wang, *Journal of Electroanalytical Chemistry*,**660**,1(2011): 64–70.

[49] Q. Dong, Y. Zhao, X. Han, Y. Wang M. Li, Y. Li, *Internal Journal of Hydrogen Energy*,**39**,27(2014): 14669–14679.

[50] Z. Zhang, L. Xin, K. Sun, W. Li, *International Journal of Hydrogen Energy***,36**,20(2011): 12686–12697.

[51] Q. Zhang, T. Chen, R. Jiang, F. Jiang, *RSC Advances*, **10**(2020): 10134–10143.

[52] C. Bi, Y. Song, H. He, C. Wu, W. Du, L. Huang, H. Moehwald, H. Xia, *Journal of Material Chemistry A*, **6**(2018): 7675–7685.

[53] S. Shen, Y. Guo, L. Luo, F. Li, L. Li, G. Wei, J. Yin, C. Ke, J. Zhang, *Journal of Physical Chemistry C*, **122**(2018): 1604–1611.

[54] N. W. Maxakato, C. J. Arendse, K. I. Ozoemena, *Electrochemistry Communication*, **11**,3(2009): 534–537.

[55] Z. Zakaria, S. K. Kamarudin, S. N. Timmiati, *Nanoscale Research Letters*, **14**,1(2019): 28.

[56] A. Dutta, M. Biswas, J. Datta, *Electrochemistry Communication*, **20**(2012): 56–59.

[57] L. P. R. Moraes, B. R. Matos, C. Radtke, E. I. Santiago, F. C. Fonseca, S. C. Amico, C. F. Malfatti, *International Journal of Hydrogen Energy*, **41**,15(2016): 6457–6468.

[58] M. Zhiani, S. Majidi, H. Rostami, M. M. Taghiabadi, *International Journal of Hydrogen Energy*, **40**,1(2015): 568–576.

[59] C. C. Yang, Y. J. Lee, S. J. Chiu, K. T. Lee, W. C. Chien, C. T. Lin, C. A. Huang, *Journal of Applied Electrochemistry*, **38**(2008): 1329–1337.

[60] A. Dutta, A. Mondal, J. Datta, *Journal of Power Sources,* **283(**2015): 104–114.

[61] Y. J. Chen, Y. R. Chen, C. H. Chiang, K. L. Tung, T. K. Yeh, H. Y. Tuan, *Nanoscale*, **11**(2019): 3336–3343.

[62] Y. Zahra, N. Meissan, M. R. Mahsa, A. Bahman, *Iran Journal of Chemistry and Chemical Engineering*, **36**(2017): 21–37.

[63] L. P. R. Moraes, B. R. Matos, C, Radtke, E. I. Santiago, F. C. Fonseca, S. C. Amico, C. F. Malfatti, *International Journal of Hydrogen Energy*, **41**(2016): 6457–6468.

CHAPTER 5

Electrochemical Probing of Pd/M Nanocatalysts on MOF-Derived Carbons and Fuel Cell-Based Breath Alcohol Sensor

5.1 Introduction

Alcohol is one of the common volatile organic compounds (VOCs) present in human blood that cause different health challenges when its limit of intake is exceeded [1,2]. The VOCs occur in the form of breath alcohol concentration (BAC) and can easily be detected in a human breath because breath samples are non-incursive using a well-known sensing device, called breathalyzer [3,4]. It can also be used in clinical analyses, food and beverage industries, agricultural and environmental analysis [5,6]. The breathalyzer provides an opportunity to measure the BAC in suspects' exhale and compare the amount of gaseous EtOH to the standard EtOH concentration in blood, whose volume ratio is 1:2100 [7]. It is well known that the breathalyzer adopts the operational modes of the fuel cells (explained in Chapter 2, sub-section 2.3.2). It is otherwise known as the FCBrAS with characteristic low-cost, portability, accurate, fast, sensitivity, selectivity and low limit of detection, unlike other less portable and more costly sensors systems like solid-state sensing [8], infrared spectroscopy [9], biosensors [10], gas chromatography [11], multi-sensors arrays (includes semiconductors and infrared devices) [12–15] and colorimetry [16]. For drivers in developed countries, it is an offense to drive vehicles when the BAC is above the

critical value: 80 mg of EtOH per 100 mL of blood or 0.08 g/dL or 0.08 %, while new drivers are not allowed to have any alcohol in their system [4]. The portability of the FCBrAS makes it easy for the law enforcement agencies to screen and electrochemically detect the BAC of drivers and employees on the roadsides and at workplaces, respectively. Although the FCBrAS has a long history dates back as the 1970s, it still utilizes the old technology (high loading of Pt at the electrodes) [17]. Despite the advances in nanotechnology for fuel cell technologies to reducing their cost of fabrication, the FCBrAS has got little or no attention to utilizing nanotechnology to reduce its fabrication cost and improve the performance.

Amongst the recent approaches of nanotechnology for fuel cell technology that is also applicable in the FCBrAS is the use of Pd-based electrocatalysts in alkaline media [18–20]. The deviation from the conventional PEMFCs that utilize acidic conditions is due to the ease of the electrodes and membranes to corrosion and low utilization. Recent findings have proved that alkaline environments are less prone to corrosion with Pd-based electrocatalysts performing excellently and surpassing the state-of-the-art Pt electrocatalysts. This informed the choice of Pd-based electrocatalysts in this work. Hence, two batches of Pd-based electrocatalysts: (i) Pd/SnO_2-based electrocatalysts (Pd/SnO_2/MOFDC and Pd/MOFDC): and (ii) Pd/Ni-based electrocatalysts (Pd/Ni/MOFDC and Pd/AT-Ni/MOFDC) are thoroughly probed electrochemically with redox-active Ferri/ferrocyanides solution and the most active electrocatalyst is tested for the FCBrAS in alkaline condition.

5.2 Results and discussion

The physical characterization of the electrocatalysts has been explained in Chapter 4. In this chapter, electrochemical behaviors of the electrocatalysts (Pd/MOFDC, Pd/SnO_2/MOFDC, Pd/Ni/MOFDC and Pd/AT-Ni/MOFDC) are investigated in redox-active 3.0 mM $Fe(CN)_6^{4-}/Fe(CN)_6^{3-}$ solution containing 0.1 M potassium chloride (KCl) using CV and EIS techniques. Then, the best performing electrocatalyst is tested for FCBrAS in an alkaline electrolyte, as well as show the experimental set-up employed.

5.2.1 Fuel Cell-Based Breath Alcohol Sensing Set-up

The gas sensing set-up was carried out following previously established method [21] with modifications, as schematically illustrated in **Figure 5.1** and briefly explained: A 3-neck round bottom flask containing stirrer bar was used as breath simulator and labelled as: (i) where N_2 gas was passed into solution as a carrier gas; (ii) where supporting electrolyte (0.5 M KOH solution), stirrer bar and different ethanol solutions were added; and (iii) where EtOH vapor and dry air were passed out to the sensor chamber to mimic exhale breath for sensing measurements. Then, the 3-neck round bottom flask was placed in a water bath and temperature raised to 34 ºC using heating mantle and thermometer to monitor the temperature. The carrier gas (N_2) is pumped through (i), stirrer bar agitating the solution in (ii), then mixture EtOH vapor and dry air were passed out of the sensor chamber. The sensing chamber consists of GCE-modified Pd/AT-Ni/MOFDC (WE and anode) and Pt rod (CE and cathode) were placed at the bottom and top, respectively and a tiny hole on the other side for the air outlet. Before each measurement, the electrode was wet with H_2O. The electrocatalyst ink preparation was made following the procedure described in sub-section 3.5.1.

However, 20 µL of the prepared ink was deposited on the cleaned GCE to afford electrocatalyst loading of 0.0039 mg_{Pd}.

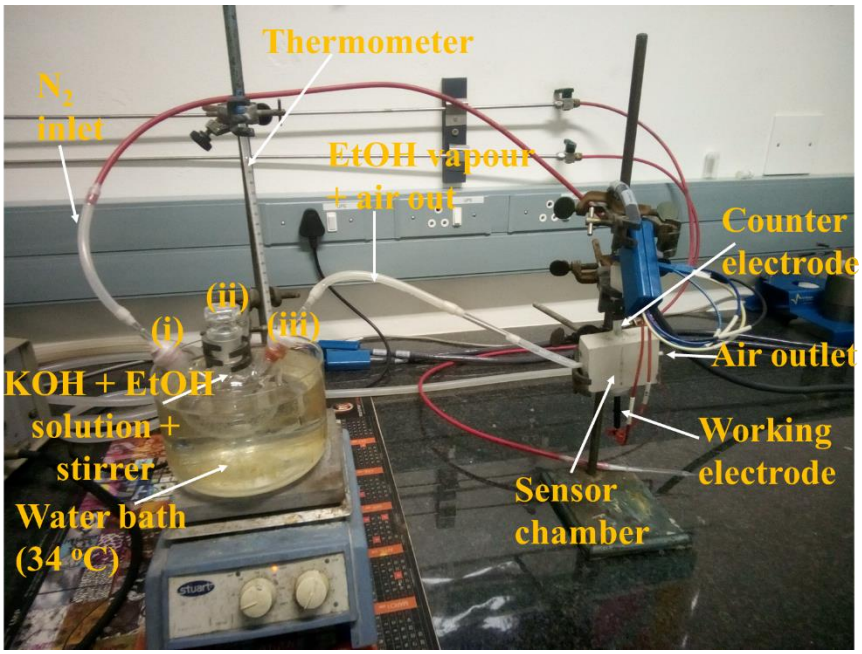

Figure 5.1: Fuel cell-based breath ethanol sensor set-up for data collection

5.2.2 Electrochemical probing of the Electrocatalysts with Ferri/ferrocyanide Solution

Figure 5.2 shows the CVs of the electrocatalysts in 3.0 mM $Fe(CN)_6^{4-}/Fe(CN)_6^{3-}$ containing 0.1 M KCl solution, as a redox probe. **Figure 5.2a** compares the CVs of bare GCE (3 mm, 0.0707 cm^{-2}) and electrocatalysts in the redox-couple at 50 mV s^{-1}, run at the potential window of -0.3 to 0.8 V *vs.* AgIAgCl, $(KCl)_{sat'd}$. The surface behavior of the bare GCE and electrocatalysts in the redox probe are explained in terms of the anode-cathode peak to peak separation (ΔE_{pp}, **Equation 2.13**) and half-wave potential ($E_{1/2}$, **Equation 2.12b**). The ΔE_{pp} values of 631.8, 443.2, 310.8, 427.2 and 127.8 mV *vs.* AgIAgCl, $(KCl)_{sat'd}$ with corresponding $E_{1/2}$ values of 315.9, 221.6, 155.4, 213.4, and 63.9 mV *vs.* AgIAgCl, $(KCl)_{sat'd}$ are recorded in the redox probe at 50 mV s^{-1} for

the bare GCE, Pd/MOFDC, Pd/SnO_2/MOFDC, Pd/Ni/MOFDC and Pd/AT-Ni/MOFDC, respectively.

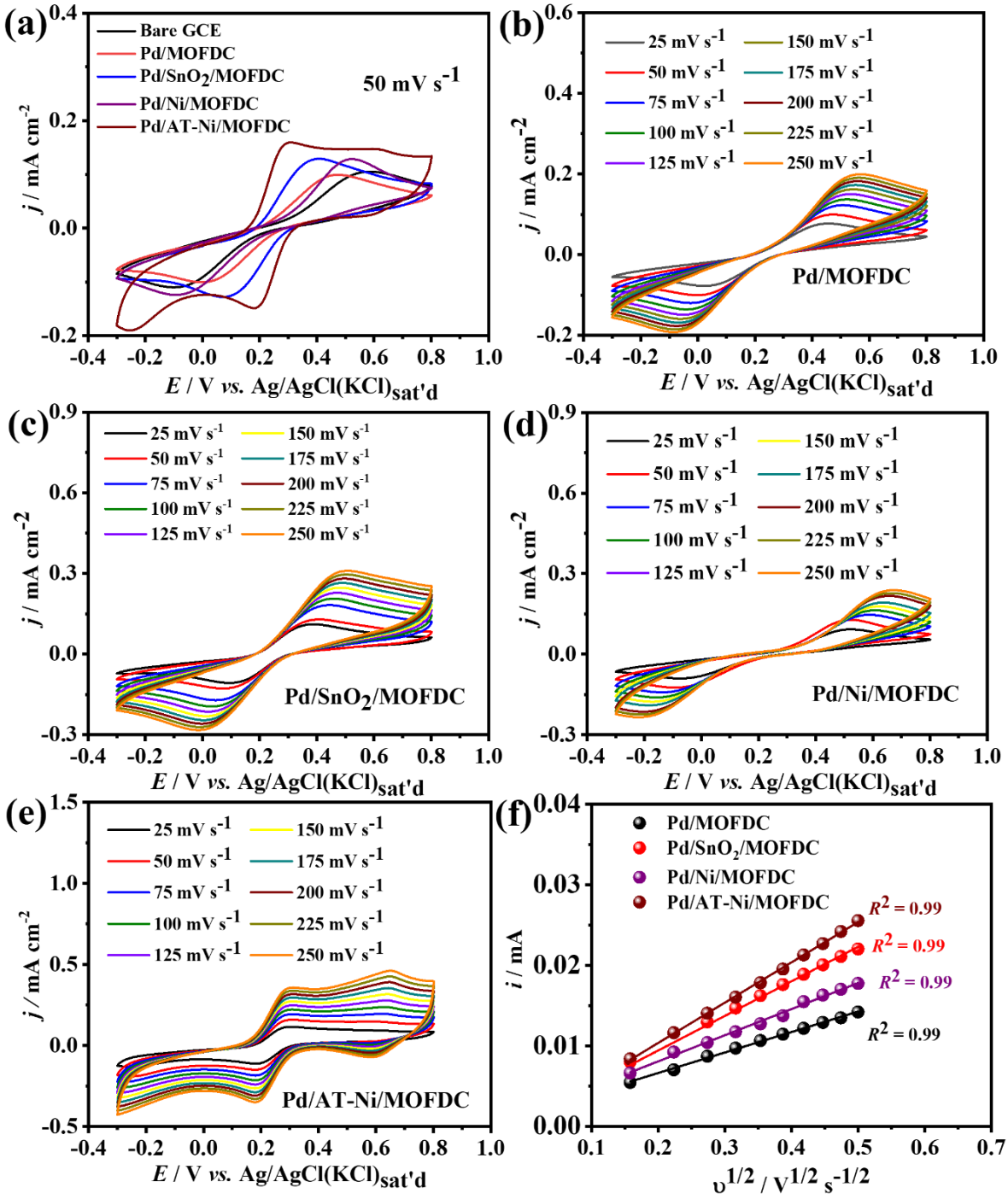

Figure 5.2 CVs of the bare GCE and electrocatalysts at (a) 50 mV s^{-1}, (b–e) different scan rates (25 – 250 mV s^{-1}) and (f) Randle-Sevcik's plots in 3.0 mM $Fe(CN)_6^{4-}$ /$Fe(CN)_6^{3-}$ containing 0.1 M KCl solution and 298 K

These results reveal that electron transport of the redox probe is most facile on the modified electrode with the Pd/AT-Ni/MOFDC, followed by the Pd/SnO_2/MOFDC, then Pd/Ni/MOFDC and Pd/MOFDC, while the least is the bare GCE, according to the sequential order of Pd/AT-Ni/MOFDC < Pd/SnO_2/MOFDC < Pd/Ni/MOFDC < Pd/MOFDC < bare GCE. The ΔE_{pp} values of the bare GCE and electrodes show irreversible redox couple, ascribable to the $Fe(CN)_6^{4-}/Fe(CN)_6^{3-}$ redox couple [22]. However, the $E_{1/2}$ value of the bare GCE, Pd/MOFDC, Pd/SnO_2/MOFDC and Pd/Ni/MOFDC indicate low mass transport than the Pd/AT-Ni/MOFDC with highest mass transport of the $Fe(CN)_6^{4-}/Fe(CN)_6^{3-}$ ions because of it lowest value of *ca.* 60 mV.

The ratio of anodic (i_{pa}) and cathode (i_{pc}) peak currents of the electrodes in the redox probe is approximately unity, which confirms the transfer of the charges on the electrocatalysts in the redox probe. Then, the study of the electrocatalysts in the redox probe is interrogated at different scan rates (25 – 250 mV s^{-1}), shown in **Figures 5.2a – 5.2e**. It was observed that as the scan rates increase the ΔE_{pp} and $E_{1/2}$ values of the electrocatalysts increase with high deviation from the reversibility of the redox couple but increasing current (*i*) response. The increasing *i* values at high scan rate are traced to faster potential sweep resulting in a high concentration gradient at the electrode [23]. Deducing the active surface area (*A*) of the electrocatalysts in the redox probe, the scan rate studied are modelled to Randle-Sevcik equation (plots of i_p *vs.* $\upsilon^{1/2}$, **Equation 5.1**) [24,25].

$$i_p = 2.69 \times 10^5 n^{3/2} A D^{1/2} C \upsilon^{1/2} \quad (5.1)$$

where i_p, n, A, D, C and υ are the peak current (amps), number of electrons transferred in the redox couple (n = 1), diffusion coefficient (7.20 x10^{-6} cm^2 s^{-1}), concentration (3.0 x10^{-6} mol cm^{-3}) and scan rates (V s^{-1}), respectively.

Figure 5.2f shows the Randle-Sevcik plots of the bare GCE and electrocatalysts in the redox probe. The R^2 of 0.99 is recorded for all the electrodes is an indication of the diffusion-controlled process of the redox probe onto the surface coverage of the electrodes. However, the non-zero intercepts indicate that reaction at modified working electrode−electrolyte interfaces could be at least in part diffusion controlled, although localized resistivity phenomena could also contribute. Then, slope values of 0.0254, 0.0429, 0.0324 and 0.0500 are extracted from the plots to calculate the electrodes' surface area (A) of 11.7, 19.8, 15.0 and 23.1 x 10^{-3} cm^2 for the Pd/MOFDC, Pd/SnO_2/MOFDC, Pd/Ni/MOFDC and Pd/AT-Ni/MOFDC, respectively. Hence, the order of A values for the electrocatalysts is Pd/AT-Ni/MOFDC > Pd/SnO_2/MOFDC > Pd/Ni/MOFDC > Pd/MOFDC, which agrees with the ΔE_{pp} and $E_{1/2}$ values.

The EIS is employed to further investigate the charge transfer and kinetics of the redox probe on the bare GCE and electrocatalysts to provide information on the electrodes/ electrolyte interfaces [26–28]. Nyquist plots of the bare GCE and electrocatalysts in the redox probe are shown in **Figure 5.3a**. The Voigt *EEC* (**Figure 5.3b**) used to model the experimental data consists of solution resistance (R_s), charge transfer resistance (R_{ct}, kinetic control domain), inhomogeneous capacitive behavior or *CPE* replaces the ideal capacitor (C_{dl}) and Warburg impedance (Z_w, mass transport or diffusion control domain). The *EEC* shows satisfactory fitting with the experimental data with the EIS parameters summarized in **Table 5.1**. All the electrocatalysts and bare GCE have the

same R_s value, an indication of the same ionic conductivity in the redox probe. The R_{ct} of the electrodes are in sequential order of Pd/AT-Ni/MOFDC < Pd/SnO_2/MOFDC < Pd/Ni/MOFDC < Pd/MOFDC < bare GCE, whose magnitudes are manifested in their heterogeneous rate constant (k^0) values of 1.57, 1.42, 1.35, 1.28, 1.24 x10^{-2} cm s^{-1}, respectively, following **Equation 5.2** [29,30]. Hence, the redox couple is fast on the Pd/AT-Ni/MOFDC. The observation agrees with the CV results.

$$k^0 = \frac{RT}{n^2F^2AR_{ct}C} \qquad (5.2)$$

where n, A, C, k^0, R, T and F are the number of electrons transferred (1), experimentally determined area of the electrode, heterogeneous rate constant, the concentration of the redox probe, the universal gas constant, absolute temperature (298 K) and Faraday constant, respectively.

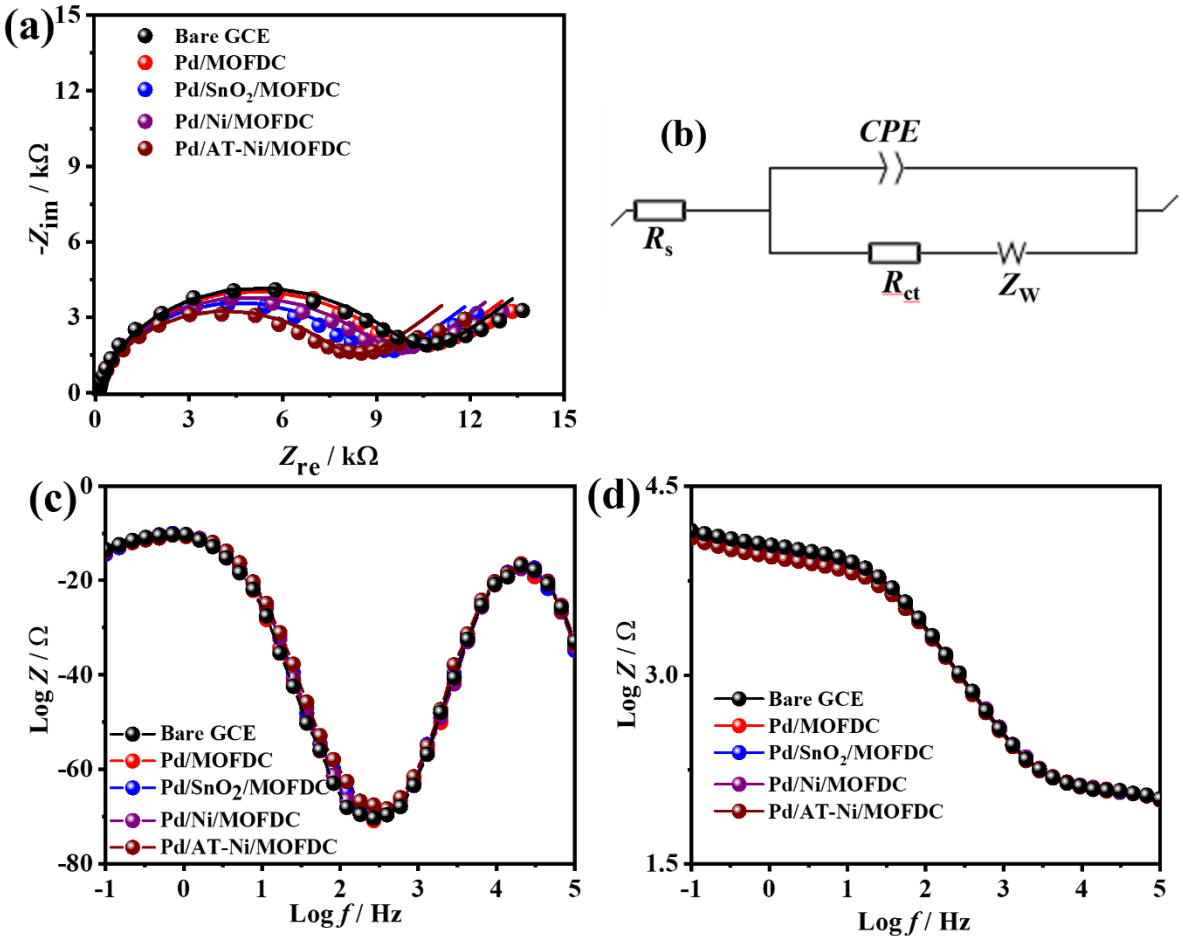

Figure 5.3 (a) Nyquist plots, (b) Voigt *EEC* and (c,d) Bode plots of the electrocatalysts in 3.0 mM $Fe(CN)_6^{4-}/Fe(CN)_6^{3-}$ containing 0.1 M KCl solution, as redox probe at their respective $E_{1/2}$

Table 5.1: EIS parameters of the electrocatalysts in $Fe(CN)_6^{4-}/Fe(CN)_6^{3-}$ containing 0.1 M KCl solution at respective $E_{1/2}$ values with deviation in parenthesis

	R_s / Ω	R_{ct} / Ω	*CPE* / μF.s^(*a*-1)	*a*	Z_w / Ω.s$^{-1/2}$	k^0 / 10^{-2} cm s^{-1}
Bare GCE	105.60	9746.00	1.37	0.88	2857	1.24
	(0.29)	(0.99)	(0.00)		(0.89)	
Pd/MOFDC	105.40	9493.00	1.39	0.88	2796	1.28
	(0.29)	(0.99)	(0.00)		(0.88)	
Pd/SnO_2/MOFDC	105.00	8504.00	1.50	0.87	2625	1.42
	(0.29)	(1.01)	(0.00)		(0.86)	
Pd/Ni/MOFDC	105.30	8999.00	1.44	0.87	2757	1.35
	(0.33)	(1.01)	(0.00)		(0.87)	
Pd/AT-Ni/MOFDC	105.20	7703.00	1.55	0.87	2673	1.57
	(0.30)	(1.02)	(0.00)		(0.84)	

Based on the power law of the impedance of *CPE* (Z_{CPE}), the *CPE* values of the electrodes are relatively close in magnitudes and *a* value that describes the deviation from C_{dl} are between 0.5 and 1.0, reveals the pseudocapacitive behavior of the electrodes in the redox probe [31–33]. Also, the Z_w values of the electrode are in the order Pd/AT-Ni/MOFDC < Pd/SnO_2/MOFDC < Pd/Ni/MOFDC < Pd/MOFDC < bare GCE. This explains that the mass transport or diffusion of the redox probe onto the surfaces of the electrode is high on the Pd/AT-Ni/MOFDC and least on the bare GCE.

Additional cogent information about the electrical properties of the electrocatalysts in the redox probe at the electrode/electrolyte interface is further explained by the Bode plots. **Figure 5.3c** shows the plots of phase angles *vs.* Log *f* with symmetric peak attributable to the relaxation process of the electrode/electrolyte interface. The broadness of the symmetric peak shows the roughness or irregular surface properties of the electrodes in the redox probe. Phase angle ranges of 70 – 80º are recorded for the electrodes confirm the inhomogeneity of the surface of the electrodes, explaining their non-ideal capacitive properties in the redox probe and less than the phase angle (90º) for ideal capacitor [34]. The plots of Log *Z vs.* Log *f* (**Figure 5.3d**) for the bare GCE, Pd/MOFDC, Pd/SnO_2/MOFDC, Pd/Ni/MOFDC and Pd/AT-Ni/MOFDC gave slopes with R^2 (in parenthesis) values of -0.5481 ± 0.0312 (0.9993), -0.4987 ± 0.0283 (0.9993), -0.4903 ± 0.0301 (0.9971), -0.4971± 0.0342 (0.9910) and -0.4103± 0.0332 (0.9996), respectively. The deviation of the slope values from the ideal value (-1.0) for C_{dl} confirms the pseudocapacitive properties of the electrodes in the redox probe and the use of *CPE* in the Voigt *EEC* [35]. Overall, The Pd/AT-Ni/MOFDC exhibits the highest activity with increased surface area in the redox probe. Hence, the Pd/AT-Ni/MOFDC is employed as an electrode for the FCBrAS application.

5.2.3 Investigating Pd/AT-Ni/MOFDC Electrocatalyst for Fuel Cell-Based Breath Alcohol Sensor (FCBrAS)

The Pd/AT-Ni/MOFDC being the most active electrocatalyst for EOR and µ-DEFC in previous Chapter, and $[Fe(CN)_6]^{4-}$/$[Fe(CN)_6]^{3-}$ redox probe is further tested for FCBrAS within the range of EtOH acceptable limit (0.00, 0.03, 0.06, 0.08, 0.12, 0.15, 0.18 and 0.20 %), corresponding to (0.00, 6.51, 13.02, 17.36. 26.06, 32.56, 39.07, and 43.41 mM) in alkaline condition (0.5 M KOH) using CA at potential of 0.03 V *vs.* AglAgCl,

$(KCl)_{sat'd}$. The FCBrAS was carried out with the set-up (**Figure 3.5**), where the sensing chamber consists of GCE-modified Pd/AT-Ni/MOFDC (calculated Pd loading = 0.0039 mg_{Pd}) as working electrode and anode, and Pt rod as counter electrode and cathode. Recall from sub-section 5.2.1, that high purity N_2 was used as a carrier gas to transport moist air and EtOH vapor to the sensing chamber. At the initial experiment, 0.5 M KOH electrolyte (serves as blank without any trace of EtOH) was in the breath simulator (3-neck stoppered round bottom flask with stirrer bar for agitation) and after each run, the sensing chamber is flushed with moist air from deionized water to avoid interferences in subsequent runs. Then, CA was performed on the sensing chamber connected to the Potentiostat for the blank with the current response (i_0) and calculated amounts of EtOH are subsequently added with current responses (i).

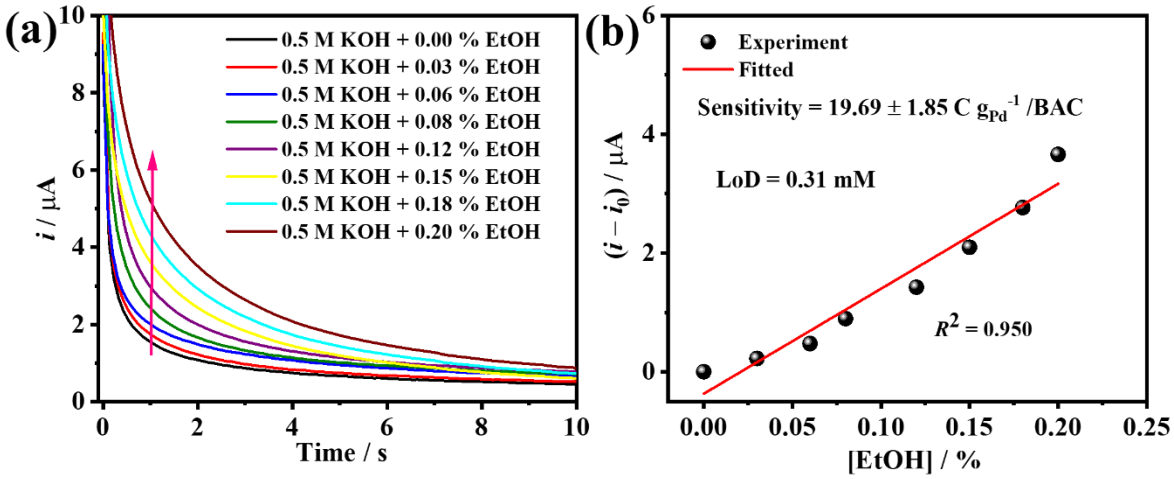

Figure 5.3 (a) current-time curves of the Pd/AT-Ni/MOFDC (anode)//Pt rod (cathode) and (b) a plot of (i – i_0) *vs.* EtOH vapour concentrations for FCBrAS in 0.5 M KOH at 0.03 V

Figure 5.3a shows the current–time (i–t) curves of the Pd/AT-Ni/MOFDC toward FCBrAS at very low EtOH concentrations (0.00 – 0.20 %) for 10 s. It is interesting to observe that between 0 – 3 s, there is an increasing current response of the Pd/AT-Ni/MOFDC toward the FCBrAS, as the EtOH concentration increases. Then, as peak

current responses of the i-t curves are taken at 1s, where there are significant and noticeable current changes. However, the current response of the blank is deducted from the current response of each EtOH concentration (i.e., $i - i_0$). Then, plots of the ($i - i_0$) *vs.* [EtOH] was made and presented in **Figure 5.3b**, where R^2, sensitivity, limit of detection (*LoD* from **Equation 5.3**) and limit of quantification (*LoQ* from **Equation 5.4**) values of 0.950, 19.69 ± 1.85 C g_{Pd}^{-1}/BAC (98.40 ± 9.24 mA g^{-1}), 0.28 ± 0.01 mM (0.0013% of BAC) and 0.94 ± 0.13 mM (0.004%), respectively are calculated for the sensing of EtOH vapor by the Pd/AT-Ni/MOFDC. The value of R^2 shows a good linearity response of the Pd/AT-Ni/MOFDC toward EtOH gas sensing. The sensitivity of the Pd/AT-Ni/MOFDC toward EtOH gas sensing are compared with literature, as summarized in **Table 5.2**. Although, the limit of detection is still lower than the real breath alcohol levels.

The *LoD* (0.0013 %) obtained in this work is way below the BAC acceptable limit of 0.08% for business driving.

$$LoD = \frac{3.0\delta}{m} \tag{5.3}$$

$$LoQ = \frac{10.0\delta}{m} \tag{5.4}$$

where δ, m, *LoD* and *LoQ* are the standard deviation of the plot, the slope of the fitted curve, limit of detection and limit of quantification of the electrocatalyst toward EtOH gas sensing, respectively [36].

Table 5.2: Comparison of sensitivity of the Pd/AT-Ni/MOFDC toward EtOH gas sensing with literature

Materials	Sensitivity	Refs
10% Pt/C	11.44 C g^{-1}_{Pt}/BAC (85.10 mA g^{-1})	[21]
20% Pt/C	18.06 C g^{-1}_{Pt}/BAC (141.10 mA g^{-1})	[21]
30% Pt/C	18.96 C g^{-1}_{Pt}/BAC (165.44 mA g^{-1})	[21]
40 % Pt/C	23.53 C g^{-1}_{Pt}/BAC (225.47 mA g^{-1})	[21]
E_{20}BrAS	24.25 C g^{-1}_{Pt}/BAC (n/a)	[4]
JM20BrAS	32.60 C g^{-1}_{Pt}/BAC (n/a)	[4]
Commercial BrAS	1.3 C g^{-1}_{Pt}/BAC (n/a)	[37]
Pt/C	57.5 C g^{-1}_{Pt}/BAC (n/a)	[37]
Pt-Mn/C-Sc-HT	86.8 C g^{-1}_{Pt}/BAC (n/a)	[37]
Pt-Sn/C	109.0 C g^{-1}_{Pt}/BAC (n/a)	[37]
Pd/AT-Ni/MOFDC	19.7 ± 1.9 C g^{-1}_{Pd}/BAC (98.40 ± 9.24 mA g^{-1})	[This work]

5.3 Conclusion

The electrochemical properties of the electrocatalysts (Pd/MOFDC, Pd/SnO_2/MOFDC, Pd/Ni/MOFDC and Pd/AT-Ni/MOFDC) are investigated in $Fe(CN)_6^{4-}$/$Fe(CN)_6^{3-}$ solution using CV and EIS techniques. These techniques are employed to deduce the behavior of the electrocatalysts in the redox probe which are associated with the ΔE_{pp}, $E_{1/2}$, A, R_{ct} and k^0, amongst other key parameters. The Pd/AT-Ni/MOFDC exhibits the best activity in the redox probe concerning these key parameters, as well as demonstrated the best activities toward the EOR and µ-DEFC in alkaline conditions. Hence, it is used for the FCBrAS in alkaline conditions. The performance of the Pd/AT-Ni/MOFDC toward the FCBrAS is satisfactory with the sensitivity of 19.69 ± 1.85 C

g_{Pd}^{-1}/BAC (98.40 ± 9.24 mA g^{-1}), *LoD* of 0.31 ± 0.01 mM, *LoQ* of 0.94 ± 0.13 mM and R^2 of 0.95. Although the values are slightly below recent reports in the literature, there is a need for optimization of the experimental procedure to meet and surpass the performances of state-of-the-art electrode materials.

5.4 References

[1] P. D. Thungon, A. Kakoti, L. Ngashangva, P. Goswami, *Biosensors and Bioelectronics*, **97**(2017): 83–99.

[2] K. I. Ozoemena, S. Musa, R. Modise, A. K. Ipadeola, L. Gaolatlhe, S. Peteni, G. Kabongo, *Current Opinion in Electrochemistry*, **10**(2108):82–87.

[3] R. G. Gullberg, *Forensic Science International*, **131**(2003): 30–35.

[4] M. R. Rahman, J. T. S. Allan, M. Z. Ghavidel, I. E. Prest, F. S. Saleh, E. B. Easton, *Sensors and Actuators B: Chemical,* **228**(2016): 448–457.

[5] A. M. Azevedo, D. M. F. Prazeres, J. M. S. Cabral, I. P. Fonseca, *Biosensors and Bioelectronics*, **21**,2(2005): 235–24.

[6] H. Zhao, J. Shen, J. Zhang, H. Wang, D. P. Wilkinson, C. E. Gu, *Journal of Power Sources*, **159**(2006): 626–636.

[7] P. Millet, A. Michas, R. Durand, *Journal of Applied Electrochemistry*, **26**(1996): 933–937.

[8] M. Mason, K. M. Dubowsbi, *Journal of Forensic Science*, **21**(1976): 9–41.

[9] B. Goldberger, Y. Caplan, *Journal of Forensic Science*, **31**(1986): 16–19.

[10] J. K. Park, H. J. Yee, K. S. Lee, W. Y. Lee, M. C. Shin, T. H. Kim, S. R. Kim, *Analytica Chimica Acta*, **390**,1-3(1999): 83–91.

[11] T. Kamel, T. Tsuda, Y. Mibu, S. Kitagawa, H. Wada, K. Naitoh, K. Nakashima, *Analytica Chimica Acta*, **365**,1-3(1998): 259–266.

[12] Y. V. Kaneti, Q. M. Zakaria, Z Zhang, C. Chen, J. Yue, M. Liu, X. Jiang, A. Yu, *Journal of Materials Chemistry A*, **2**,33(2014): 13283–13292.

[13] C. Wang, D. Cai, B. Liu, H. Li, D. Wang, Y. Liu, L. Wang, Y. Wang, Q. Li, T. Wang, *Journal of Materials Chemistry A*, **2**,27(2014): 10623–10628.

[14] R. Ab Kadir, W. Zhang, Y. Wang, J. Z. Ou, W. Wlodarski, A. P. O'Mullane, *Journal of Materials Chemistry A,* **3**,15(2015): 7994–8001.

[15] L. Zhang, Z. Gao, C. Liu, Y. Zhang, Z. Tu, X. Yang, F. Yang, Z. Wen, L. Zhu, R. Liu, Y. Li, L. Cui, *Journal of Materials Chemistry A*, **3**,6(2015): 2794–2801.

[16] M. B. Williams, H. D. Reese, *Analytical Chemistry,* **22**(1950): 1556–1561.

[17] B. Krotoszynski, G. Gabriel, H. O'Neill, M. Claudlo, *Journal of Chromatographic Science*, **15**(1977): 239–244.

[18] K. I. Ozoemena, *RSC Advances*, **6**(2016): 89523–89550.

[19] C. Wen, Y. Wei, D. Tang, B. Sa, T. Zhang, C. Chen, *Scientific Reports,* **7**(2017): 4907.

[20] A. K. Ipadeola, R. Barik, S. C. Ray, K. I. Ozoemena, *Electrocatalysis*, **10**(2019): 366–380.

[21] A. Modjatahedi, A. Amirfazli, S. Farhad, *Sensors Actuators B Chemical*, **234**(2016): 70–79.

[22] K. I. Ozoemena, T. Nyokong, *Electrochimica Acta*, **51**(2006): 2669–2677.

[23] N. Elgrishi, K. J. Rountree, B. D. McCarthy, E. S. Rountree, T. T. Eisenhart, J. L. Dempsey, *Journal of Chemical Education*, **95**(2018): 197–206.

[24] L. Bai, R. Yuan, Y. Yuan, Y. Wang, S. Xie, C*hemical Communication*, **48**(2012): 10972–10974.

[25] K. Ngamhua, S. Eloul, K. Tshulik, R. G. Compton, *Journal of Solid State Electrochemistry*, **18**(2014): 3251–3257.

[26] G. Nurk, H. Kasuk, K. Lust, A. Janes, E. Lust, *Journal of Electroanalytical Chemistry*, **553**(2003): 1–19.

[27] T. Pajkossy, *Solid State Ionics*, **176**,25-28(2005): 1997–2003.

[28] D. D. MacDonald, *Electrochimica Acta*, **51**(2006): 1376–1388.

[29] E. Sabatini, I. Rubinstein, *Journal of Physical Chemistry*, **91**(1987): 6669–6669.

[30] A. J. Bard, L. R. Faulkner, *John Wiley,* (2004), Chapter 4: 1376.

[31] J. Pillay, K. I. Ozoemena, *Electrochimica Acta*, **54**(2009): 5053–5050.

[32] A. T. Chidembo, K. I. Ozoemena, B. O. Agboola, V. Gupta, G. G. Wildgoose, R.G. Compton, *Energy and Environmental Science*, **3**(2010): 228–236.

[33] K. I. Ozoemena, N. S. Mathebula, J. Pillay, G. Toschi, J. A. Verschoor, *Physical Chemistry Chemical Physics*, **12**(2010): 345–357.

[34] J. Sun, Y. Liu, *Nanomaterials*, **9**,7(2019): 923.

[35] B. O. Agboola, K. I. Ozoemena, *Physical Chemistry Chemical Physics*, **10**(2008): 2399–2408.

[36] E. Oleneva, M. Khaydukova, J. Ashina, I. Yaroshenko, I. Jahatspanian, A. Legin, D. Kirsanov, *Sensors*, **19**,6(2019): 1359.

[37] M. Z. Ghavidel, M. R. Rahman, E. B. Easton, *Sensors and Actuators B: Chemical*, **273**(2018): 574–584.

CHAPTER 6

Investigating Alkaline Water-Splitting Reactions using Pd/M Electrocatalysts on MOF-Derived Carbons

6.1 Introduction

Over the decades, H_2 has been identified as an exceptionally good fuel to actualize environmentally friendly, renewable and sustainable energy, due to the extremely high energy demands globally. However, the major change is the production and storage of the fuel (H_2). Amongst the numerous methods for H_2 production, electrochemical water-splitting or electrolysis has emerged as one of the most important, efficient and effective strategies because the process is highly clean and alleviates the discharge of GHGs that could have negatively affected the climate [1]. The electrolysis occurs via two complementary processes: (i) HER; and (ii) OER. The former is the most significant parameter of concern, as it is a process that produces highly purity H_2 fuel employed for varieties of applications, especially fuel cells, while the latter leads to O_2 production and it is less important because of the abundant of O_2 in the air [2]. Moreover, both reactions are being driven by highly efficient electrocatalysts. Hence, more emphasis is laid on the study of HER.

Industrial state-of-the-art water electrolysis occurs in alkaline media with a very long history of over 50 years, as acid water electrolyzer is still at the infancy to date, owing

to partly corrosion of electrocatalysts and its low utilization or very short lifespan in acid conditions. The H_2O-splitting has previously been represented in simple terms (**Equation 2.7** and **2.8**) for the OER and HER, respectively. The HER can be achieved by following two out of the three sub-equations, depending on its value of Tafel slope, as presented in **Equations 6.1** – **6.3** [3]. Pt-based electrocatalysts are often used to produce H_2 in alkaline conditions because the HER requires multiple-steps reactions requiring high energy to cleave H-O-H bonds before the H is chemisorbed (MH_{ads}) and subsequent desorption of the intermediate (H_{ads}) [4]. The rds of the reactions is the Volmer, which involves cleavage of the H-O-H bond and adsorption of the H on the active sites of the electrocatalysts, while subsequent desorption of the H_{ads} can follow either Tafel or Heyrovsky [1].

$$M + H_2O + e^- \rightarrow MH_{ads} + OH^- \quad (\text{Volmer, } b_c = \frac{2.3RT}{\propto F} \text{ of } ca. \text{ 118.2 mV dec}^{-1}) \qquad (6.1)$$

$$MH_{ads} + MH_{ads} \rightarrow H_2 + 2M \qquad (\text{Tafel, } b_c = \frac{2.3RT}{2F} \text{ of } ca. \text{ 29.6 mV dec}^{-1}) \qquad (6.2)$$

$$MH_{ads} + H_2O + e^- \rightarrow M + H_2 + OH^- \quad (\text{Heyrovsky, } b_c = \frac{2.3RT}{(1+\propto)F} \text{ of } ca. \text{ 39.4 mV dec}^{-1}) \qquad (6.3)$$

The binding energy of Pd (E_{ads} = 0.48 eV) to H_2 is close to that of Pt (E_{ads} = 0.43 eV) according density functional theory (DFT) [5], with a high tendency to exhibit superior HER activities [6]. Also, Pd electrocatalysts have been reported to display superior electrocatalytic performance than Pt in alkaline conditions [7]. This informed our interest to study the alkaline water-splitting on Pd/M (M = SnO_2 or Ni) supported on MOF-derived carbons electrocatalysts. The electrocatalysts are divided into two parts and their HER and OER performances are separately presented and elucidated in this chapter.

6.2 Results and Discussion

The electrochemical performances of the electrocatalysts toward HER and OER are discussed based on the classes of the electrocatalysts: (i) Pd/SnO_2-based electrocatalysts (Pd/SnO_2/MOFDC, Pd/MOFDC) and compared with Pd/CB; and (ii) Pd/Ni-based electrocatalysts (Pd/Ni/MOFDC and Pd/AT-Ni/MOFDC).

6.2.1 Pd/SnO_2-based Electrocatalysts for Alkaline Water Electrolysis (AWE)

In this section, comparative performances of the Pd/SnO_2/MOFDC, Pd/MOFDC and Pd/CB electrocatalysts toward HER and OER are presented and discussed.

6.2.1.1 Hydrogen Evolution Reaction (HER)

HER Polarization curves of the Pd/SnO_2/MOFDC, Pd/MOFDC, Pd/CB and bare GCE toward HER in N_2-deaerated 0.1 M KOH electrolyte at a scan rate of 5 mV s^{-1} and 1600 rpm are presented in **Figure 6.1a**. The results reveal that Pd/MOFDC has the highest HER activity, followed by Pd/CB, while the Pd/SnO_2/MOFDC displays the lowest HER activity. This is a clear indication that the addition of SnO_2 to the Pd/MOFDC led to diminishing its activity for HER in this condition. This observation may be traced to the fact that strong oxophilic property of the SnO_2 is detrimental to the HER activity. The detrimental effect of the SnO_2 addition may be explained on its ability to donate oxygen-containing species to the chemisorbed hydrogen (H_{ads}) leading to H_2O formation, instead of the desorption of the H_{ads} for H_2 production. **Figure 6.1b** shows the HER polarization curves of the Pd/MOFDC and Pd/CB at different rotation speeds, except 1600 rpm, while those of the Pd/SnO_2/MOFDC (**Figure 6.1c**). It was observed that the HER activities of the Pd/MOFDC and Pd/CB electrocatalysts increase, as the rotation speeds increase, but remain the same at all

rotations for the Pd/SnO_2/MOFDC. Hence, subsequent HER experiments will be based on the comparative performances between Pd/MOFDC and Pd/CB because of the negative consequences of SnO_2 addition to the Pd/MOFDC. Conventional Tafel formulae are employed to probe HER kinetic parameters of the electrocatalysts, following **Equations 2.23** – **2.25**, previously explained in chapter 2.

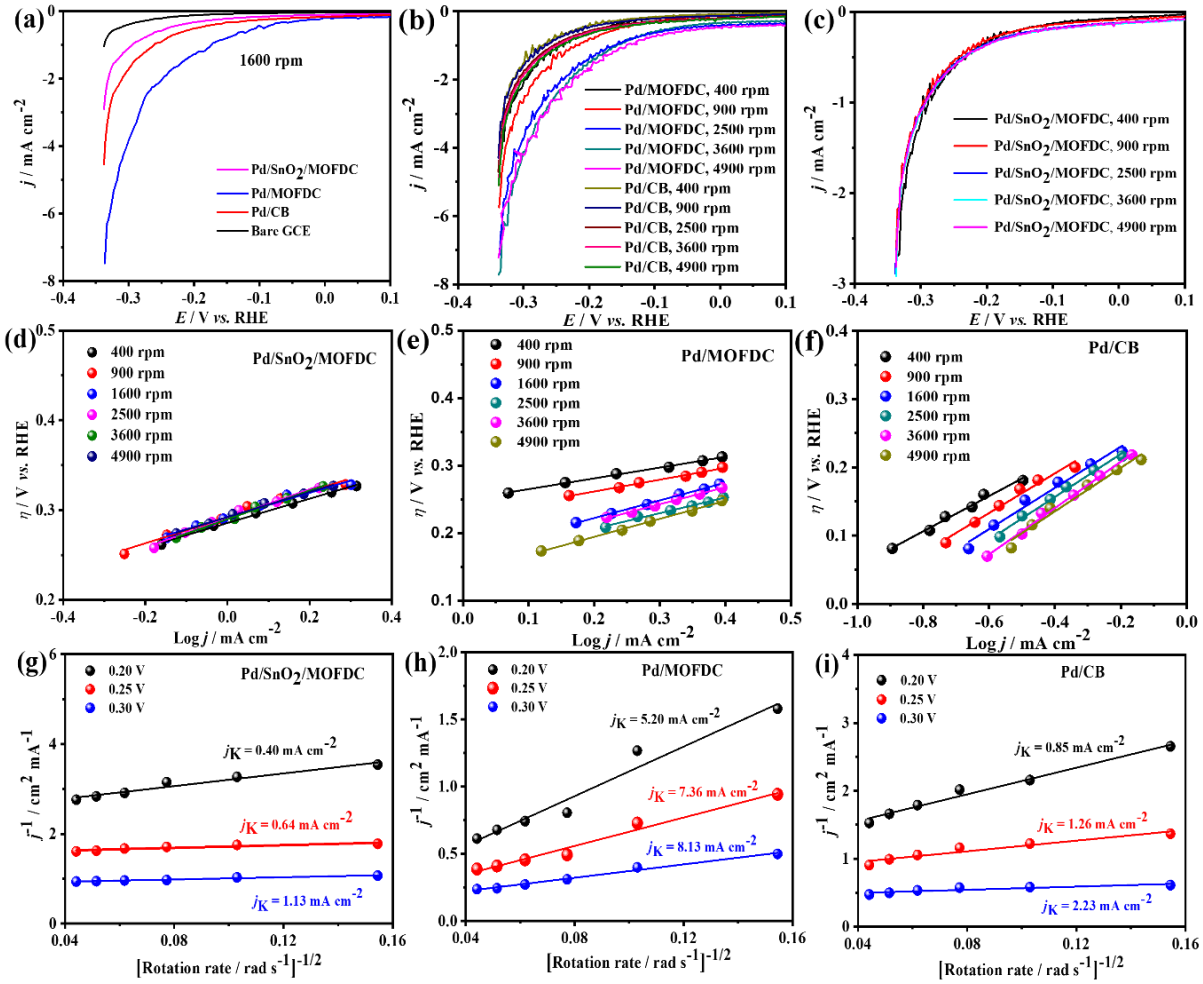

Figure 6.1: HER polarization curves of Bare GCE and the Pd/SnO_2-based electrocatalysts at (a) 1600 rpm, (b–c) different rotations, (d–f) corresponding HER Tafel plots and (g–i) Koutecky-Levich plots of the electrocatalysts in N_2-deaerated 0.1 M KOH solution at 5 mV s^{-1} and 298 K

Equation 2.24 was adopted for the HER Tafel plots for all the electrocatalysts by plotting graphs of η against logarithm (j_c), shown in **Figures 6.1c – 6.1f**. Comparative

kinetic parameters of the Pd/SnO_2-based electrocatalysts toward HER at all rotation speeds in terms of E_{onset}, $j_{o,s}$ and Tafel slopes (b_c) are summarized in **Table 6.1**. As revealed at 1600 rpm, the Pd/MOFDC has the highest $j_{o,s}$ value of 0.2226, which increased by factors of *ca.* 2 and 35 times relative to Pd/CB and Pd/SnO_2/MOFDC and at all other rotation speeds. Also, E_{onset} values of 35.2, 56.7 and 80.5 mV *vs.* RHE are recorded for the Pd/MOFDC, Pd/CB and Pd/SnO_2/MOFDC, respectively, indicating the ease of H_{ads} recombination after desorption from the electrocatalysts' active sites follows similar order. These results agree with previous observations that facile desorption of H_{ads} occurs on the electrocatalysts without SnO_2 addition to producing H_2. However, the SnO_2 containing electrocatalyst rather donate oxygen species to some of the desorbed H_{ads}, thereby reducing the recombination of the intermediate hydrogen to H_2, but rather produces H_2O as a side reaction product.

The $j_{o,s}$ values of the electrocatalysts only explain mass transfer characteristics. However, kinetic currents (j_K) of the electrocatalysts were separated from the mass transfer kinetic and are obtained by modelling the polarization curves at different rotation speeds to the Koutecky-Levich formulae (**Equations 2.19** and **2.20**), where plots of the inverse of current density (j^{-1}) against the inverse square root of rotation speeds ($\omega^{-1/2}$) to give straight lines. The j_K value is extrapolated from the intercept ($1/j_K$), which has a direct relationship with k^0, given in **Equation 2.21**. The Koutecky-Levich plots of the electrocatalysts at different overpotentials (η = 0.20, 0.25, 0.30 V *vs.* RHE) are presented in **Figures 6.1g – 6.1i**.

Table 6.1: Kinetic parameters of the Pd/SnO_2-based electrocatalysts for HER in N_2-deaerated 0.1 M KOH solution at different rotation, 298 K and 5 mV s^{-1}

Kinetic parameters	Pd/SnO_2-based Electrocatalysts		
	Pd/SnO_2/MOFDC	Pd/MOFDC	Pd/CB
@400 rpm,			
b_c / mV dec^{-1}	135.2	159.3	258.0
$j_{o,s}$ / mA cm^{-2}	0.0077	0.1272	0.0614
α_c	0.44	0.37	0.23
@900 rpm,			
b_c / mV dec^{-1}	144.4	175.1	290.1
$j_{o,s}$ / mA cm^{-2}	0.0095	0.1506	0.0875
α_c	0.41	0.34	0.20
@1600 rpm,			
b_c / mV dec^{-1}	135.2	261.1	301.9
$j_{o,s}$ / mA cm^{-2}	0.0064	0.2226	0.1089
α_c	0.44	0.23	0.20
@2500 rpm,			
b_c / mV dec^{-1}	162.2	231.5	314.5
$j_{o,s}$ / mA cm^{-2}	0.0161	0.2030	0.1264
α_c	0.36	0.26	0.19
@3600 rpm,			
b_c / mV dec^{-1}	160.1	252.9	339.4
$j_{o,s}$ / mA cm^{-2}	0.0155	0.2185	0.1537
α_c	0.37	0.23	0.17

@4900 rpm,			
b_c / mV dec^{-1}	139.6	266.3	318.7
$j_{o,s}$ / mA cm^{-2}	0.0081	0.2943	0.1495
α_c	0.42	0.22	0.19

At the varied η values, the j_K values of (0.40, 0.64 and 1.13 mA cm^{-2}), (5.20, 7.36 and 8.13 mA cm^{-2}), and (0.85, 1.26 and 2.23 mA cm^{-2}) were recorded for the Pd/SnO_2/MOFDC, Pd/MOFDC and Pd/CB, and their mean k^0 values were deduced as 3.75 x 10^{-5}, 3.57 x 10^{-4}, and 7.53 x 10^{-5} cm s^{-1}, respectively. These results elucidate that facile HER in terms of kinetic current occurs on the Pd/MOFDC, followed by the Pd/CB and the most sluggish HER kinetic occurs on the Pd/SnO_2/MOFDC. A similar observation was recorded for the mass transfer characteristic with respect to $j_{o,s}$ at all rotation speeds.

Further investigation for the ease of the Pd/SnO_2-based electrocatalysts toward the HER was carried out with temperature-dependent studies in N_2-deaerated 0.1 M KOH solution at 1600rpm, 5 mV s^{-1} and different temperature (298, 308, 318 and 328 K), as shown in **Figure 6.2**. **Figures 6.2a** and **6.2b** show the HER polarization curves of the Pd/SnO_2-based electrocatalyst at varying temperature. It was observed that increasing temperature of the reaction, increase their HER activities. The HER Tafel plots of the electrocatalysts are displayed in **Figures 6.2c – 6.2e**, employed to determine their $j_{o,s}$ values, which increase with increasing temperature. The temperature-dependent HER parameters of the Pd/SnO_2-based electrocatalysts in the reaction conditions (1600 rpm, 5 mV s^{-1} and varying temperature) are summarized in **Table 6.2**.

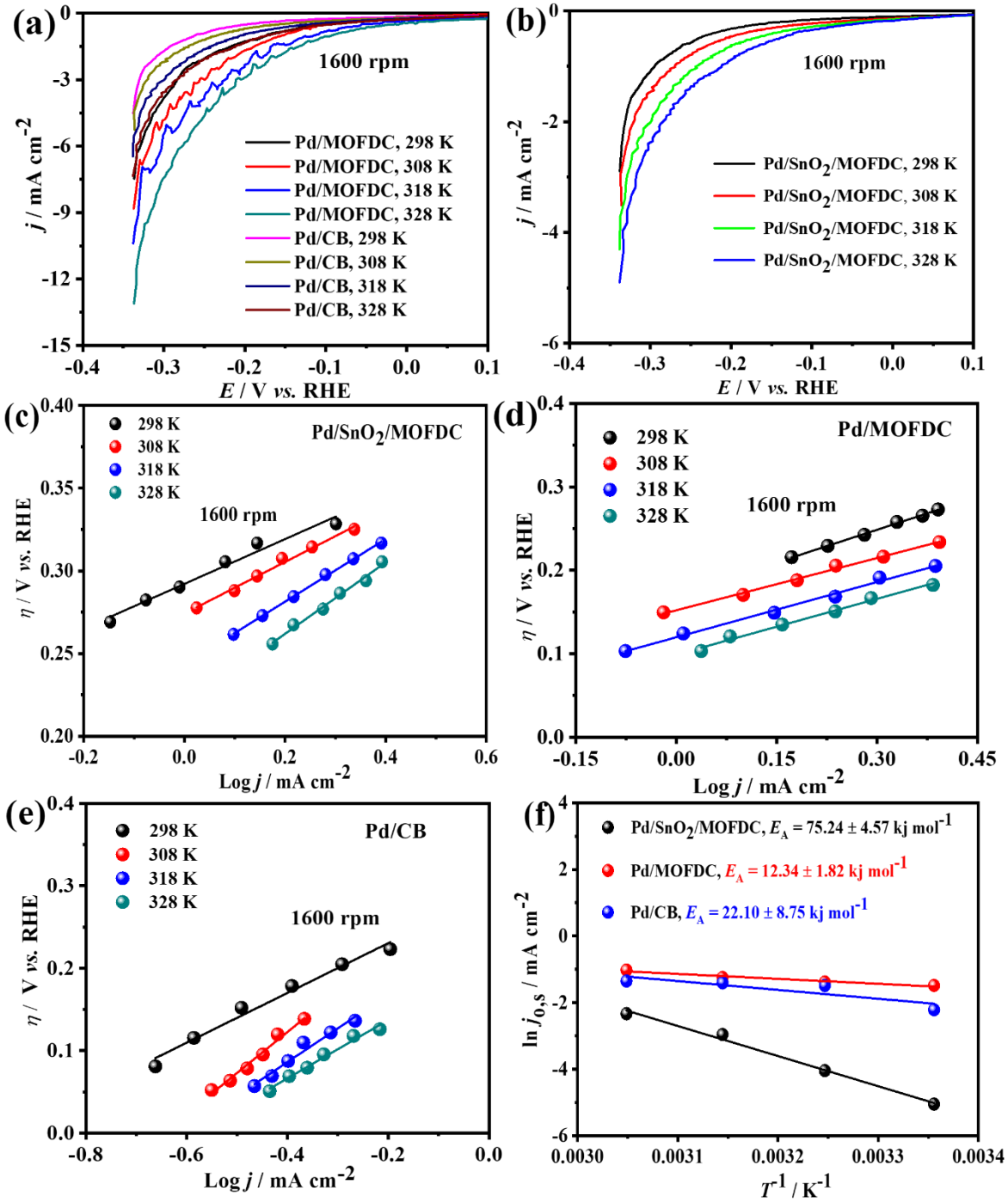

Figure 6.2: (a,b) HER polarization curves, (c–e) corresponding HER Tafel plots and (f) Arrhenius plots of the Pd/SnO_2-based electrocatalysts in N_2-deaerated 0.1 M KOH solution at 1600 rpm, 5 mV s^{-1} and different temperature.

Table 6.2: Temperature-dependence kinetic parameters of HER in N_2-deaerated 0.1 M KOH solution on the Pd/SnO_2-based electrocatalysts at 1600 rpm, 5 mV s^{-1} and different temperature

Kinetic Parameters	Pd/SnO_2-based Electrocatalysts		
	Pd/SnO_2/MOFDC	Pd/MOFDC	Pd/CB
@298 K			
b_c / mV dec^{-1}	135.2	261.1	301.9
$j_{o,s}$ / mA cm^{-2}	0.0064	0.2226	0.1089
α_c	0.44	0.23	0.20
@308 K			
b_c / mV dec^{-1}	156.0	205.1	496.5
$j_{o,s}$ / mA cm^{-2}	0.0175	0.2513	0.2255
α_c	0.40	0.30	0.12
@318 K			
b_c / mV dec^{-1}	189.4	220.9	409.8
$j_{o,s}$ / mA cm^{-2}	0.0518	0.2871	0.2455
α_c	0.33	0.29	0.15
@328 K			
b_c / mV dec^{-1}	215.9	222.9	353.5
$j_{o,s}$ / mA cm^{-2}	0.0970	0.3597	0.2585
α_c	0.30	0.29	0.27

The varying temperature of the Pd/SnO_2-based electrocatalysts, concurrently increase the $j_{o,s}$ values, with the highest values recorded for the Pd/MOFDC and the least for the Pd/SnO_2/MOFDC at all the temperature values studied in this work. The increasing

values of $j_{o,s}$ with increasing temperature was modelled to the Arrhenius equation **(Equation 6.4**), where plots of the natural logarithm of exchange current densities (ln $j_{o,s}$) were made against the inverse of the absolute temperature (T^{-1}) and the slopes ($-\frac{E_A}{R}$) extrapolated are used to deduced activation energy (E_A), which is the minimum amount of energy required for the electrocatalysts to drive HER.

$$\text{Arrhenius equation: } \ln j_{o,s} = -\frac{E_A}{R}T^{-1} \quad (6.4)$$

Figure 6.2f shows the Arrhenius plots of the Pd/SnO_2-based electrocatalysts toward the HER activities. The E_A values of 12.34 ± 1.82, 22.10 ± 8.95 and 75.24 ± 4.57 kJ mol^{-1} are measured for the Pd/MOFDC, Pd/SnO_2/MOFDC and Pd/CB, respectively. Least E_A value of the Pd/MOFDC toward HER shows that low energy is required for electrochemical water-splitting due to reduced hydride phase formation for quick H_2 production [8], confirming its ease of H adsorption and H_{ads} desorption for H_2 production, amongst other electrocatalysts. Interestingly, the E_A value of the Pd/MOFDC is less than that previously reported for Pt/C (*ca.* 18.0 kJ mol^{-1}) [8]. These results align with the DFT study that proved that binding energy of H onto active sites of Pd electrocatalyst is lower with carbon support with increased electron density [9,10]. This observation explains improved HER activity on the Pd/MOFDC than the Pd/CB.

For the mechanism of the HER, the magnitude of the b_c is the key parameter to deduce if the HER follows Volmer-Heyrovsky or Volmer-Tafel processes, as given in **Equations 6.1 – 6.3**. The b_c values obtained are in the range of 135 and 266 mV dec^{-1} for all the electrocatalysts, which are values higher than the theoretical values for Volmer, Heyrovsky and Tafel processes. The high b_c values of the electrocatalysts toward HER suggest that Volmer–Heyrovsky may predominate, as it involves

continuous breaking of H-O-H bond, adsorption of H (MH_{ads}) and subsequent desorption of the H_{ads} [11]. This assumption agrees with the free energy diagram study of HER in alkaline electrolytes [12]. However, the high b_c values are due to high hydrogen adsorption on the active sites of polycrystalline Pd electrocatalysts, as supplementary reaction step, which have previously been reported for Pd-based electrocatalysts in literature [13,14].

6.2.1.2 Oxygen Evolution Reaction (OER)

6.2.1.2.1 OER Polarization Curves

As a matter of interest and curiosity, activities of the Pd/SnO_2-based electrocatalysts toward the OER were performed. **Figure 6.3a** shows the OER polarization curves of the Pd/SnO_2-based electrocatalysts and bared GCE electrode at 1600 rpm, 5 mV s^{-1} and 298 K. As seen from the curve, the Pd/SnO_2/MOFDC has the highest *j* value of 20.8 mA cm^{-2} compared to the Pd/MOFDC (18.40 mA cm^{-2}) and Pd/CB (14.68 mA cm^{-2}), with their respective *onset η* values of *ca.* 1.25, 1.29 and 1.49 V *vs.* RHE. This result shows that the Pd/SnO_2/MOFDC does not only have increase OER activity but also the least energy for the OER, amongst the electrocatalysts compared. Noteworthily, the E_{onset} of the Pd/SnO_2-based electrocatalysts is higher than the thermoneutral potential of H_2O (1.23 V *vs.* RHE). The electrocatalyst (Pd/SnO_2/MOFDC) with the closest potential for splitting H_2O more easily than others [15,16]. The onset *η* of the Pd/SnO_2/MOFDC recorded is lower than the previously reported value for Pd-based electrocatalyst toward OER [17]. This makes the addition SnO_2 to the Pd/MOFDC be beneficial for OER. Also, overpotential (η_{10}) of the Pd/SnO_2-based electrocatalysts for OER at a benchmark of *j* = 10 mA cm^{-2} are 1.81, 1.83 and 1.86 V *vs.* RHE, with Tafel slopes (b_a) of *ca.* 34.0, 66.0 and 88.0 mV dec^{-1} are calculated for the

Pd/SnO_2/MOFDC, Pd/MOFDC and Pd/CB, respectively. Low b_a value is related to excellent OER activity [16,18]. Thus, the Pd/SnO_2/MOFDC has the highest OER activity, followed by the Pd/MOFDC and the least is the Pd/CB.

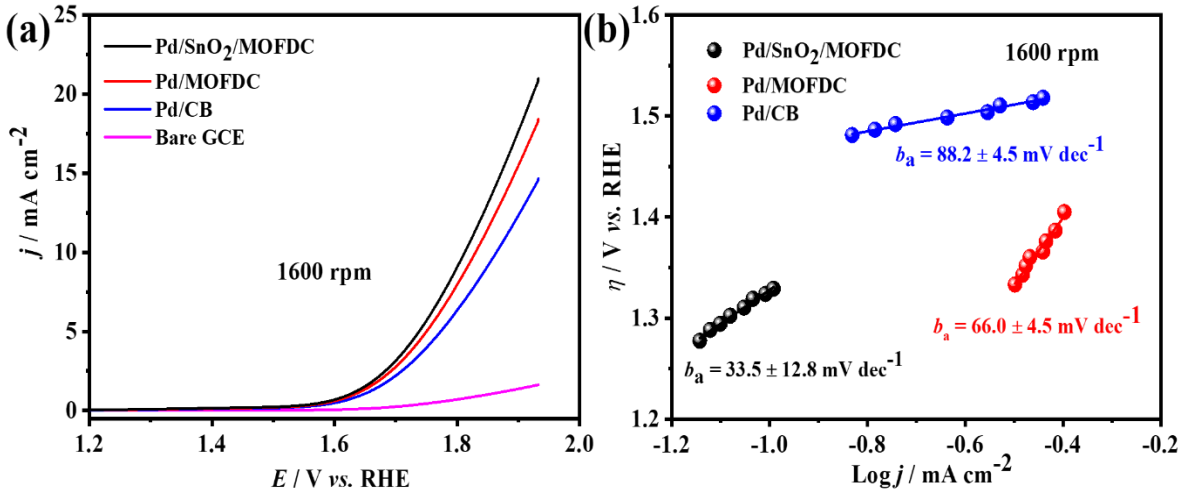

Figure 6.3: (a) OER polarization curves and (b) OER Tafel plots of the Pd/SnO_2-based electrocatalysts in N_2-deaerated 0.1 M KOH at 1600 rpm, 5 mV s^{-1} and 298K

6.2.1.2.2 Electrochemical Impedance Spectroscopy (OER)

The OER activities on the Pd/SnO_2-based electrocatalysts are further investigated with the EIS. Nyquist plots of the Pd/SnO_2-based electrocatalysts with Voigt *EEC* (inset) are presented in **Figure 6.4**. The inset Voigt *EEC* was the model employed to extract EIS parameters of the Pd/SnO_2-based electrocatalysts toward the OER, summarized in **Table 6.3**. Solution resistance (R_s), charge transfer resistance (R_{ct}) and internal resistance (R_{int}) are parameters that give the clue of how ions interact with the electrocatalysts, electron transports and Ohmic (*IR*) loss, respectively. The R_s value of *ca.* 54.0 Ω was recorded for all the Pd/SnO_2-based electrocatalysts, showing that the electrocatalysts exhibit similar ionic conductivity.

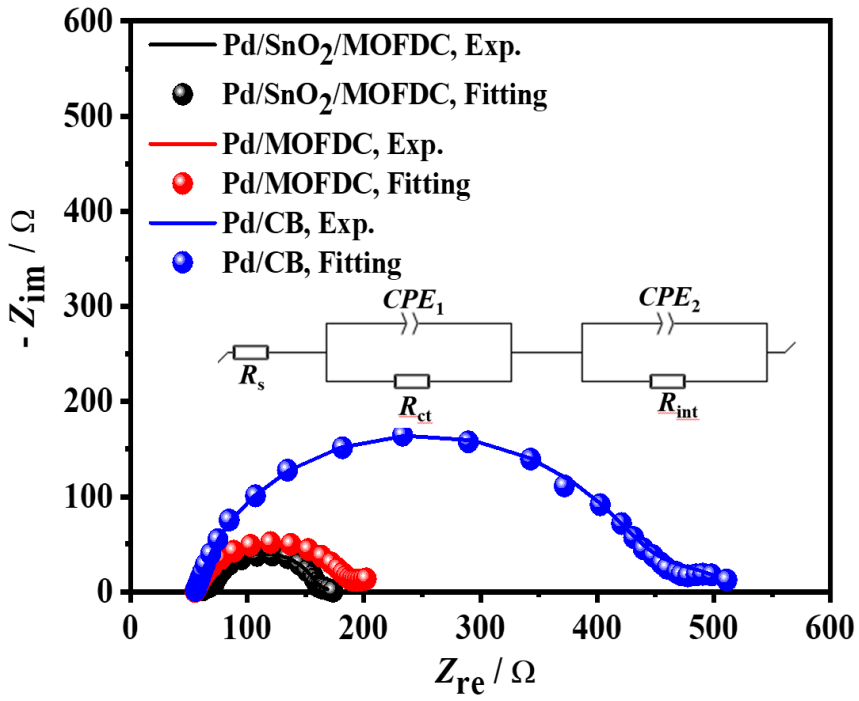

Figure 6.4: Nyquist plots for OER of the Pd/SnO_2-based electrocatalysts at 1.7 V *vs.* RHE at 1600 rpm and 298 K

Table 6.3: EIS parameters of the Pd/SnO_2-based electrocatalysts for OER in the alkaline electrolyte at 1.7 V (*vs.* RHE), 1600 pm, 5 mV s^{-1} and 298 K

EIS Parameters	Pd/SnO_2-based Electrocatalysts		
	Pd/SnO_2/MOFDC	Pd/MOFDC	Pd/CB
R_s / Ω	53.69 ± 0.68	54.73 ± 0.61	54.80 ± 0.58
R_{int} / Ω	49.25 ± 1.15	121.60 ± 4.37	349.60 ± 14.54
CPE_1 / µF s^(1-a)	3443.00 ± 492.6	105.90 ± 0.01	55.97 ± 3.77
a_1	0.76	0.86	0.92
R_{ct} / Ω	69.18 ± 21.45	27.91 ± 2.16	124.30 ± 17.32
CPE_2 / µF s^(1-a)	34.34 ± 14.22	39.84 ± 6.11	7.334 ± 2.19
a_2	1	0.57	0.54

The Pd/SnO_2/MOFDC, Pd/MOFDC and Pd/CB recorded R_{ct} values of *ca.* 49.0, 122.0 and 350.0 Ω, respectively. These results show that the Pd/SnO_2/MOFDC has the highest electron transport during the OER, followed by the Pd/MOFDC and the least is the Pd/CB. The Pd/SnO_2/MOFDC also possesses the least *iR* drop, amongst the Pd/SnO_2-based electrocatalysts compared. The overall resistance of the electrocatalyst toward the OER could be evaluated by taking a series of resistance (R_s + R_{int} + R_{ct}). The (R_s + R_{int} + R_{ct}) values of *ca.* 172.0, 204.0 and 528.7 Ω were measured for the Pd/SnO_2/MOFDC, Pd/MOFDC and Pd/CB, respectively. The least (R_s + R_{int} + R_{ct}) value of the Pd/SnO_2/MOFDC makes it the best performing electrocatalyst toward OER, amongst the Pd/SnO_2-based electrocatalysts, which agree with the polarization curves and Tafel plots.

6.2.2 Pd/Ni-based Electrocatalysts for the Alkaline Water Electrolysis (AWE)

Comparative performances of the Pd/Ni/MOFDC and Pd/AT-Ni/MOFDC electrocatalysts toward HER and OER are illustrated and explained in this section.

6.2.2.1 Hydrogen Evolution Reaction (HER)

The study of the HER on the Pd/Ni/MOFDC and Pd/AT-Ni/MOFDC electrocatalysts was carried out by recording their polarization curves at 1600 rpm (**Figure 6.5a**) and other rotation speeds (**Figure 6.5b**) in 0.1 M KOH solution at 298 K and 5 mV s^{-1}. Increasing the rotation speeds increase the *j* values of the Pd/Ni-based electrocatalysts. However, the Pd/Ni/MOFDC displays earlier *onset η* and higher *j* values than the Pd/AT-Ni/MOFDC at all rotation speeds, which is an indication of increased HER activity. Affirming this assumption, the polarization curves of the Pd/Ni-

based electrocatalysts are modelled to the Tafel formula (**Equation 6.2**) and the Tafel plots are presented in **Figures 6.5c** and **6.5d**.

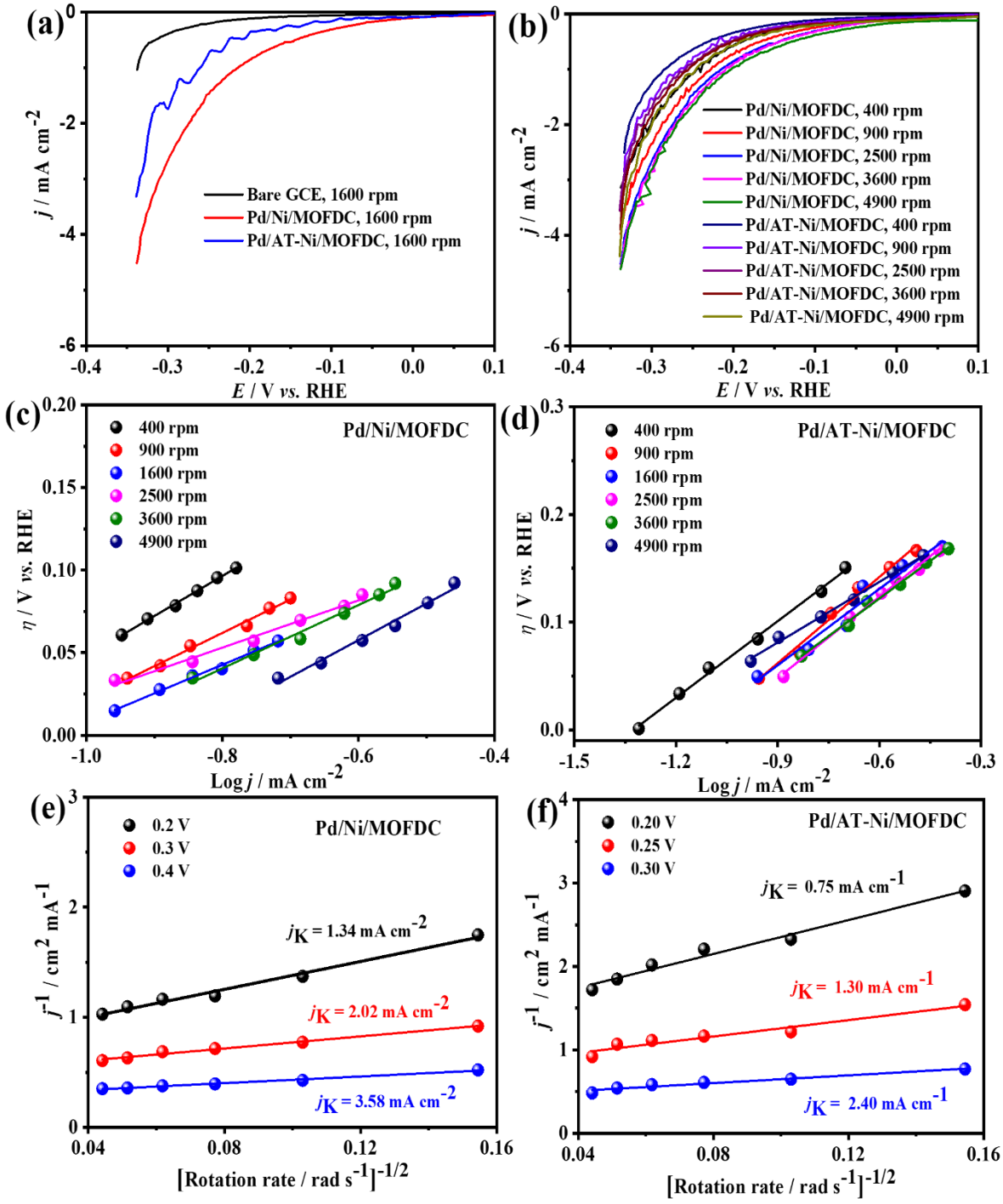

Figure 6.5: HER polarization curves of Bare GCE and the Pd/Ni-based electrocatalysts at (a) 1600 rpm, (b) other rotation speeds, (c,d) corresponding HER Tafel plots and (e,f) Koutecky Levich plots in N_2-deaerated 0.1 M KOH solution at 5 mV s^{-1} and 298 K

Table 6.4: Kinetic parameters of the Pd/Ni-based electrocatalysts for HER in H_2-saturated 0.1 M KOH solution, in term of $j_{o,s}$, b_c and α_c at different rotation speeds and 5 mV s^{-1}

Kinetic parameters	Pd/Ni-based Electrocatalysts	
	Pd/Ni/MOFDC	Pd/AT-Ni/MOFDC
@400 rpm		
b_c / mV dec^{-1}	242.0	239.0
$j_{o,s}$ / mA cm^{-2}	0.0633	0.0476
α_c	0.34	0.25
@900 rpm		
b_c / mV dec^{-1}	201.0	266.0
$j_{o,s}$ / mA cm^{-2}	0.0777	0.0732
α_c	0.39	0.22
@1600 rpm		
b_c / mV dec^{-1}	173.0	187.0
$j_{o,s}$ / mA cm^{-2}	0.1079	0.0757
α_c	0.38	0.25
@2500 rpm		
b_c / mV dec^{-1}	142.0	236.0
$j_{o,s}$ / mA cm^{-2}	0.1121	0.0794
α_c	0.41	0.24
@3600 rpm		
b_c / mV dec^{-1}	190.0	251.0
$j_{o,s}$ / mA cm^{-2}	0.1186	0.0810
α_c	0.40	0.25

@4900 rpm		
b_c / mV dec^{-1}	221.0	323.0
$j_{o,s}$ / mA cm^{-2}	0.1381	0.0857
α_c	0.47	0.32

The Tafel plots were employed to extract kinetic parameters of the Pd/Ni-based electrocatalysts toward HER. As seen in **Table 6.4**, where the kinetic parameters are summarized, the Pd/Ni/MOFDC has relatively increased $j_{o,s}$ values compared to those of the Pd/AT-Ni/MOFDC at all rotation speeds. The better HER kinetic on the Pd/Ni/MOFDC may be traced to the strong synergy between the nanostructured Ni/Ni(OH)$_2$ and Pd, which is beneficial for facile H-O-H cleavages, H adsorption and subsequent H_{ads} desorption for facile H_2 production [19]. The beneficial effects of Ni(OH)$_2$ have previously been reported for Pt/Ni(OH)$_2$ electrocatalysts toward HER in alkaline conditions, where the Ni(OH)$_2$ serves as the active site for H-O-H cleavage, while the adsorption of H and subsequent H_{ads} desorption to form H_2 was brought about by Pt [20]. Other researchers independently found out that incorporation of Ni(OH)$_2$ into the lattice of Pt, enhance the Pt activities toward HER in alkaline conditions [21–23].

The b_c values (> 120 mV dec^{-1}) of the Pd/Ni-based electrocatalysts toward HER, suggest that the adsorption of H onto the active sites of the electrocatalysts follows the Volmer (rds), while subsequent desorption of the H_{ads} may follow the Heyrovsky [24,25]. The higher b_a values of the Pd/Ni-based electrocatalysts than the theoretical values (29.4 – 118.2 mV dec^{-1}) is ascribed to the surface coverage of hydrogen onto polycrystalline Pd/Ni electrocatalysts [13,14]. Following **Equation 2.19**, the Koutecky-

Levich plots of the Pd/Ni-based electrocatalysts at different overpotentials (η = 0.20, 0.25, 0.30 V *vs.* RHE) are presented in **Figures 6.5e** and **6.5f**. At the varied η values, the j_K values of (1.34, 2.02 and 3.58 mA cm^{-2}), and (0.75, 1.30 and 2.40 mA cm^{-2}) were recorded for the Pd/Ni/MOFDC and Pd/AT-Ni/MOFDC, whereas their mean k^0 values deduced as 1.19 x 10^{-4} and 7.69 x 10^{-5} cm s^{-1}, respectively. These results reveal that the HER is more facile in terms of kinetic current on the Pd/Ni/MOFDC, due to the synergy between the Ni/Ni(OH)$_2$ interface and Pd, but the HER is more sluggish on the Pd/AT-Ni/MOFDC. A similar observation was recorded for the mass transfer characteristic with respect to $j_{o,s}$ at all rotation speeds.

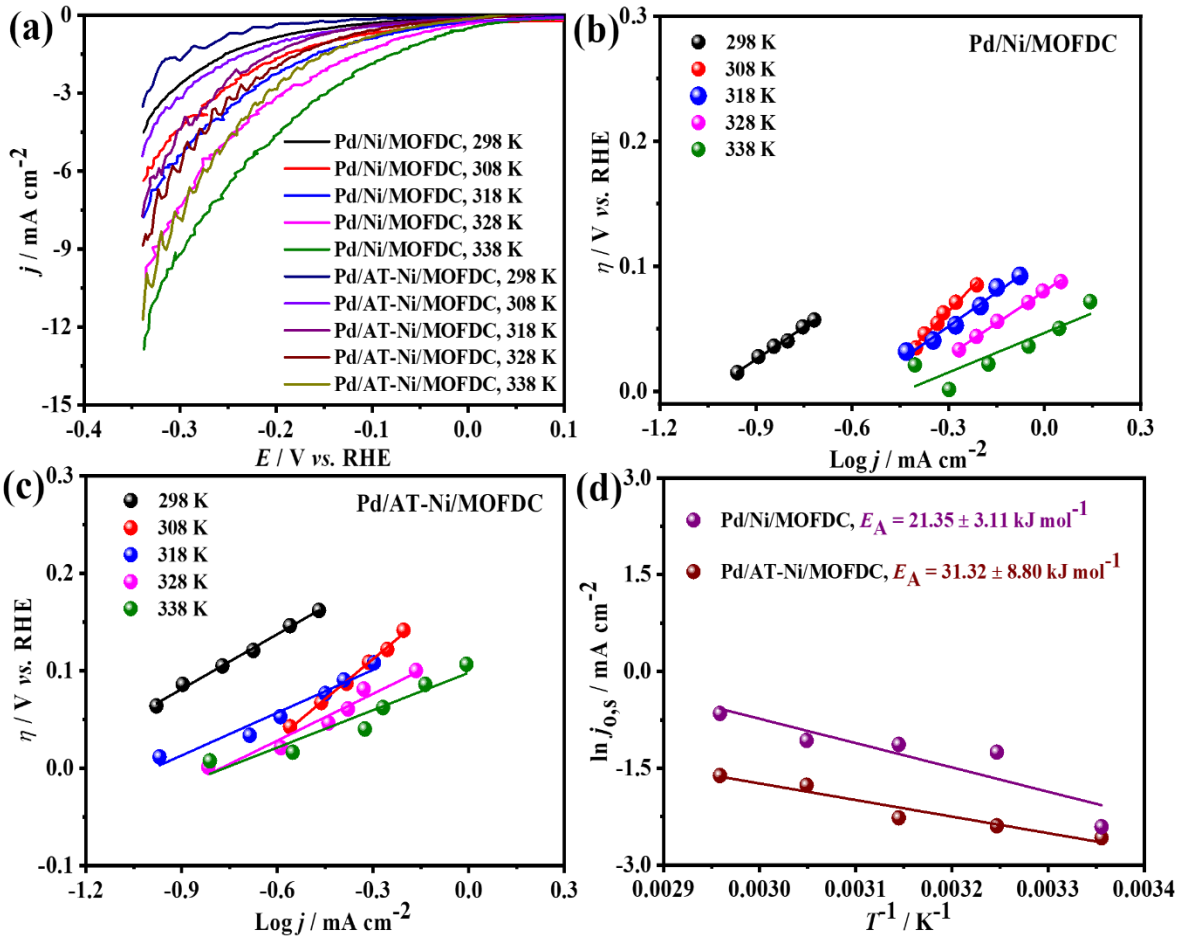

Figure 6.6: (a) HER polarization curves, (b,c) corresponding Tafel plots (d) Arrhenius plots of the Pd/Ni-based electrocatalysts in N$_2$-deaerated 0.1 M KOH solution at 1600 rpm, 5 mV s^{-1} and different temperature.

Table 6.5: Temperature-dependence kinetic parameters of HER in 0.1 M KOH solution on the Pd/Ni-based electrocatalysts at 1600 rpm, 5 mV s^{-1} and varied temperature

Kinetic parameters	Pd/Ni-based Electrocatalysts	
	Pd/Ni/MOFDC	Pd/AT-Ni/MOFDC
@298 K		
b_c / mV dec^{-1}	173.0	187.0
$j_{o,s}$ / mA cm^{-2}	0.1079	0.0757
α_c	0.38	0.25
@308 K		
b_c / mV dec^{-1}	261.0	313.0
$j_{o,s}$ / mA cm^{-2}	0.2857	0.0912
α_c	0.23	0.22
@318 K		
b_c / mV dec^{-1}	181.0	146.0
$j_{o,s}$ / mA cm^{-2}	0.3221	0.1032
α_c	0.34	0.43
@328 K		
b_c / mV dec^{-1}	172.0	163.0
$j_{o,s}$ / mA cm^{-2}	0.3427	0.1711
α_c	0.35	0.41
@338 K		
b_c / mV dec^{-1}	162.0	144.0
$j_{o,s}$ / mA cm^{-2}	0.5201	0.1989
α_c	0.58	0.53

A temperature-dependent study is a tool employed to determine the E_A of the Pd/Ni-based electrocatalysts toward HER. **Figure 6.6a** shows the polarization curves of the Pd/Ni-based electrocatalysts at 1600 rpm, 5 mV s^{-1} and varied temperature (298 – 338 K). Increasing the temperature of the reaction concurrently increase the *j* values with earlier onset potential observed at high temperature. However, high *j* values were observed for the Pd/Ni/MOFDC at all temperature studied in this work. These results agree with the previous observation that strong synergy between Ni/$Ni(OH)_2$ interface and nanostructured Pd is favorable for continuous H-O-H cleavage and fast H_{ads} recombination. Then, the polarization curves were fitted to Tafel plots (**Figure 6.6b** and **6.6c**) to determine the kinetic parameters for the temperature-dependent study, summarized in **Table 6.5**. The $j_{o,s}$ values also increase with increasing temperature. The trend of increasing $j_{o,s}$ values, as the temperature increase is further modelled to the Arrhenius formula (**Equation 6.4**). **Figure 6.6d** shows the Arrhenius plots of the Pd/Ni-based electrocatalysts, where E_A values of *ca.* 21 and 31 kJ mol^{-1} were calculated for Pd/Ni/MOFDC and Pd/AT-Ni/MOFDC, respectively. The lower E_A value of the Pd/Ni/MOFDC explains that reduced energy is required for the alkaline HER compared to the Pd/AT-Ni/MOFDC. Also, the E_A values of the electrocatalysts are less than or lower than those previously reported for PdSiW (30.0 kJ mol^{-1}) [26], Pt/WC (33.0 kJ mol^{-1}) [27], Pd-modified zeolite (39.0 kJ mol^{-1}) [28], Pt-rare earth electrocatalysts (39.0–60.0 kJ mol^{-1}) [29]. The HER activities on the Pd/Ni-based electrocatalysts depend largely on the H adsorption strength on their active sites and subsequent H_{ads} desorption bond strength values giving optimum HER performances [30]. Thus, the lower E_A value of the Pd/Ni/MOFDC is due to the synergy between the Ni/$Ni(OH)_2$ interface and nanostructured Pd. Comparative HER activities of the

Pd/SnO_2- and Pd/Ni-based electrocatalysts with the literature of Pd electrocatalysts with carbon-containing supports are summarized in **Table 6.6**.

Table 6.6: Comparison of all the electrochemical HER activity of the electrocatalysts with literature in alkaline media at 1600 rpm and 5 mV s^{-1} in terms of *onset* η, b_c, $j_{o,s}$ and $j_{o,m}$

Electrocatalysts	Solutions	*Onset* η / mV(*vs.* RHE)	b_c / mV dec^{-1}	$j_{o,s}$ / mA cm^{-2}	Refs
Pd/Ni/MOFDC	0.1 M KOH	73.0	173	0.0899	This work
Pd/AT-Ni/MOFDC	0.1 M KOH	96	183	0.0757	This work
Pd/SnO_2/MOFDC	0.1 M KOH	80.5	135	0.064	This work
Pd/MOFDC	0.1 M KOH	35.2	261	0.2226	This work
Pd/CB	0.1 M KOH	56.7	302	0.1089	This work
Pd/C-500 ºC	0.1 M KOH	60.0	148	0.1220	[31]
f-MWCNTs/Pd/TiO_2	0.1 M KOH	<100.0	130	0.0600	[32]
PdNiMo film	0.1 M KOH	85.0	227	n/a	[33]
rGO-$Au_{48}Pd_{52}$	0.1 M KOH	80.0	149	0.1300	[34]
Pd-CN_x	0.5 M KOH	≈ 89.0	150	0.2450	[35]
Pd	1.0 M KOH	n/a	210	0.1259	[36]
Pd-$FeOx(OH_2)_{2-2x}$	0.1 M KOH	50	135	0.1700	[37]
Pd/zeolite-C	8.0 M KOH	237	167	0.0383	[38]

6.2.2.2 Oxygen Evolution reaction (OER)

6.2.2.2.1 OER Polarization Curves

OER polarization curves of the Pd/Ni-based electrocatalysts at 1600 rpm, 5 mV s^{-1} and 298 K are shown in **Figure 6.7a**. The Pd/Ni/MOFDC was observed to show oxidation peaks in the range of 1.34 – 1.52 and at 1.54 V *vs.* RHE, which are ascribed to the contributions of the $Ni/Ni(OH)_2$ interface and Pd, respectively. The $Ni/Ni(OH)_2$ in the Pd/Ni/MOFDC drew the *onset η* of the OER to a lower value compared to the Pd/AT-Ni/MOFDC without the $Ni/Ni(OH)_2$, as it has been removed by chemical etching. Thus, the *onset η* values of 1.34 and 1.59 V *vs.* RHE were recorded for the Pd/Ni/MOFDC and Pd/AT-Ni/MOFDC, respectively. The result shows that OER is more facile on the Pd/Ni/MOFDC than the Pd/AT-Ni/MOFDC, due to the synergistic effect of the nanostructured $Ni/Ni(OH)_2$ and Pd. The synergy between the metals in electrocatalysts have previously been reported and proved to be beneficial with respect to their OER activity and stability during electrolysis [39–42].

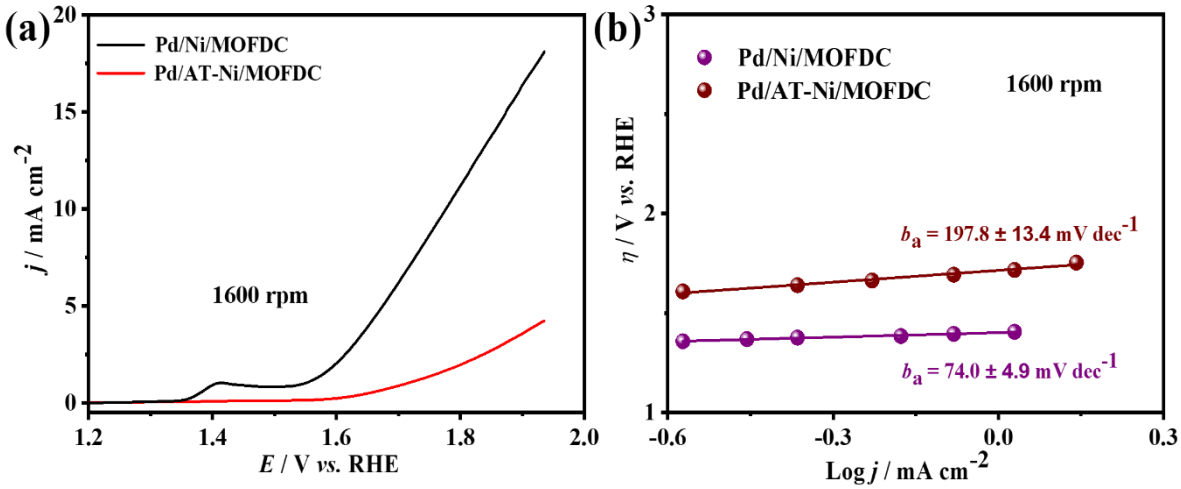

Figure 6.7: (a) OER polarization curves and (b) OER Tafel plots of the Pd/Ni-based electrocatalysts at 1600 rpm and 298 K

The activity of the OER is explained in terms of *j* values. Optimum *j* values of 18.06 and 4.14 mA cm^{-2} were observed for the Pd/Ni/MOFDC and Pd/AT-Ni/MOFDC,

respectively, which are higher than the value previously reported for Pd/MnO_2/C toward OER in alkaline condition [43]. The relatively increased *j* value of the Pd/Ni/MOFDC by a factor of 4.5 indicates high OER activity due to the synergy between the nanostructured Ni/$Ni(OH)_2$ and Pd [44]. Then, the OER polarization curves were fitted to Tafel plots, shown in **Figure 6.6b**. The b_a values of *ca.* 74 and 197 mV dec^{-1} were calculated for the Pd/Ni/MOFDC and Pd/AT-Ni/MOFDC, respectively. The lower b_a value of the Pd/Ni/MOFDC is an indication of fast water dissociation for OER [45–47]. Thus, the enhanced OER activity was confirmed for the Pd/Ni/MOFDC.

6.2.2.2.2 Electrochemical Impedance Spectroscopy (OER)

The EIS was employed to further prove the performances of the Pd/Ni-based electrocatalysts toward OER in 0.1 M KOH solution at 1600 rpm, 5 mV s^{-1} and 298 K. Nyquist plots of the Pd/Ni-based electrocatalysts (**Figure 6.8**) were modelled with Voigt *EEC* (inset) to extract the EIS parameters summarized in **Table 6.7**. Solution resistance (R_s) values of *ca.* 56.0 and 58.0 Ω were recorded for the Pd/Ni/MOFDC and Pd/AT-Ni/MOFDC, respectively. The lower R_b of the Pd/Ni/MOFDC explains its improved conductivity during the OER. The interfacial resistance (R_{int}) explains the conductivity due to the ohmic drop at the electrode's layers during the OER. The Pd/Ni/MOFDC and Pd/AT-Ni/MOFDC have R_{int} values of *ca.* 42 and 754 Ω, respectively. This result shows that the Pd/Ni/MOFDC also extremely improved conductivity at the electrode layer during the OER. The third resistance parameter is the charge transfer resistance (R_{ct}) that explains the electron transport between the electrodes and electrolyte. An extremely lower R_{ct} value was recorded for the Pd/Ni/MOFDC during the OER. Overall, lower series resistance (R_s + R_{int} + R_{ct}) was

recorded for the Pd/Ni/MOFDC compared to the Pd/AT-Ni/MOFDC toward the OER, confirms it excellent catalytic performance as bifunctional material for electrochemical water splitting.

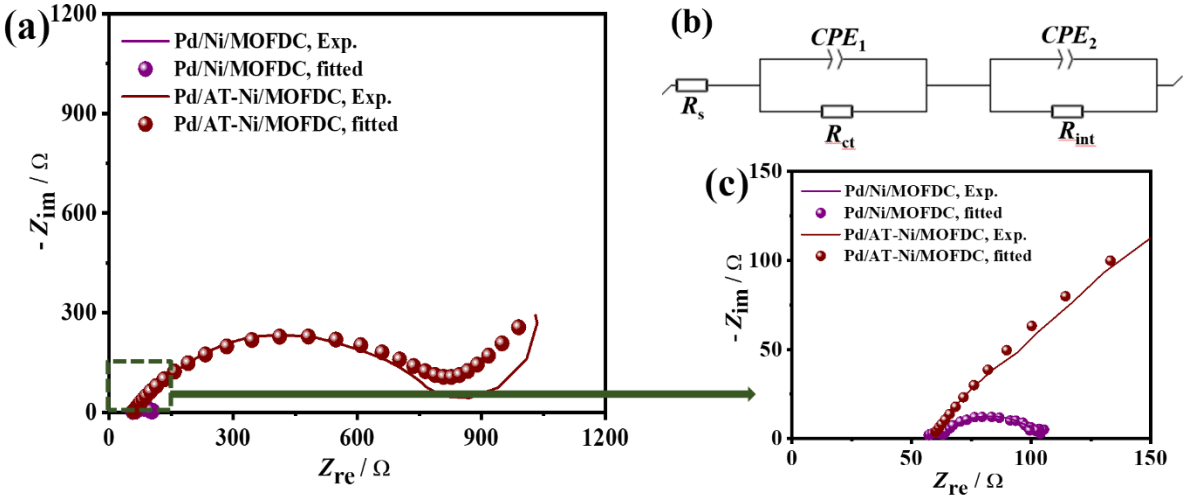

Figure 6.8: (a) Nyquist plots and (b) Voigt *EEC* model for OER of the Pd/Ni-based electrocatalysts at 1.7 V *vs.* RHE at 1600 rpm and 298 K

Table 6.7: EIS parameters of the Pd/Ni-based electrocatalysts for OER in the alkaline electrolyte at 1.7 V *vs.* RHE, 1600 pm, 5 mV s^{-1} and 298 K

EIS parameters	Pd/Ni-based Electrocatalysts	
	Pd/Ni/MOFDC	Pd/AT-Ni/MOFDC
R_s / Ω	56.49 ± 2.35	57.98 ± 0.44
R_{int} / Ω	42.30 ± 2.67	753.90 ± 8.18
CPE_1 / µF s^(1-a)	734.50 ± 133.60	131.70 ± 2.44
a_1	0.68	0.68
R_{ct} / Ω	5.35 ± 1.25	257.84 ± 8.14
CPE_2 / µF s^(1-a)	2.25 ± 1.78	1911.00 ± 16.76
a_2	0.97	0.59

6.3 Conclusions

The conclusions were sub-sectioned into two parts for the electrochemical alkaline water electrolyzer because of the distinct electrocatalysts discussed above. The study of AWE reactions (HER and OER) was successfully carried out on the Pd/SnO_2-based electrocatalysts (Pd/SnO_2/MOFDC and Pd/MOFDC) and compared with the Pd/CB. Comparative HER studies on these electrocatalysts reveal that enhanced HER kinetic and energies on the Pd/MOFDC compared to Pd/SnO_2/MOFDC and Pd/CB) at all reaction conditions in terms of $j_{o,s}$, j_K, $j_{o,m}$ and reduced E_A. The relatively improved HER activity on the Pd/MOFDC to the Pd/CB is traced to increased electron density and very little amount of Co nanoparticles residue of chemical etching, which is beneficial for H_{ads} recombination, following Heyrovsky process after the initial H-O-H cleavage (Volmer). However, the addition of SnO_2 to Pd/MOFDC suppresses the HER activity because the SnO_2 donates OH_{ads} to the H_{ads} to form H_2O rather than facile H_{ads} desorption to form H_2. OER studies of these electrocatalysts were investigated at a single rotation speed (1600 rpm). The oxophilic property and spill-over effect of the Sn and SnO_2 of the Pd/SnO_2/MOFDC is advantageous for O_2 production. Thus, the Pd/SnO_2/MOFDC has superior OER kinetics and energy with respect to high peak j, low b_a and least η, followed by the Pd/MOFDC and the least performed is the Pd/CB. In the second scenario, the study of HER and OER was investigated on the Pd/Ni-based electrocatalysts (Pd/Ni/MOFDC and Pd/AT-Ni/MOFDC). Comparative HER performance on these electrocatalysts reveals that the synergy between Ni/$Ni(OH)_2$ and Pd in the Pd/Ni/MOFDC relatively improves its kinetics and energies to the Pd/AT-Ni/MOFDC, with respect to enhanced $j_{o,s}$, $j_{o,m}$ and decreased E_A values. Thus, the Ni/$Ni(OH)_2$ interface presence in Pd/Ni/MOFDC aided quick continuous cleavage of H-O-H bond and desorption of the H_{ads} from the active sides of Pd for fast H_2

production. The b_c values for the electrocatalysts suggested that the mechanism of the HER follows the Volmer-Heyrovsky process. OER studies of the Pd/Ni-based electrocatalysts were also investigated at 1600 rpm only. The Pd/Ni/MOFDC displays superior OER activity in terms of low η, b_a but high j compared to the Pd/AT-Ni/MOFDC. The enhanced OER performance of the Pd/Ni/MOFDC shows that the synergistic effect of $Ni/Ni(OH)_2$ and Pd is not only advantageous for HER but also OER. Thus, the Pd/Ni/MOFDC is a bifunctional electrocatalyst for electrochemical water-splitting.

6.4 References

[1] A. K. Ipadeola, K. I. Ozoemena, *RSC Advances*, **10**,29(2020): 17359–17368.

[2] D. G. Narehood, S. Kishore, H. Goto, J. H. Adair, J. A. Nelson, H. R. Gutierrez, P. C. Eklund, *International Journal Hydrogen Energy,* **34**,2*(*2009): 952–960.

[3] K. Zeng, D. Zhang, *Progress in Energy Combustion Science,* **36**(2010): 307–326.

[4] J. R. Varcoe, P. Atanassov, D. R. Dekel, A. M. Herring, M. A. Hickner, P. A. Kohl, A. R. Kucernak, W. E. Mustain, K. Nijmeijer, K. Scott, T. Xu and L. Zhuang, *Energy and Environmental Science,* **7**,10(2014): 3135–3191.

[5] I. A. Pasti, N. M. Gavrilov, S. V. Mentus, *Advances in Physical Chemistry,* **2011**(2011): 41.

[6] M. M. Jaksic, *International Journal of Hydrogen Energy,* **26**,6(2001): 559–578.

[7] K. I. Ozoemena, *RSC Advances,* **6**,92(2016): 89523–89550.

[8] J. Durst, C. Simon, F. Hasche, H. A. Gasteiger, *Journal of the Electrochemical Society,* **162**,1(2015): F190–F203.

[9] M. Johansson, E. Skulason, G. Nielsen, S. Murphy, R. M. Nielson, I. Chorkendorff, *Surface Science*, **604**,7-8(2010): 718–729.

[10] K. S. Joya, M. A. Ehsan, N. U. A. Babar, M. Sohail, Z. H. Yamani, *Journal of Material Chemistry A*, **7**,15(2019): 9137–9144.

[11] S. John St., R.W. Atkinson, R.R. Unocic, T.A. Zawodzinski, A. B. Papandrew, *Journal Physical Chemistry C*, **119**,24(2015): 13481–13487.

[12] J. Hu, C. Zhang, L. Jiang, H. Lin, Y. An, D. Zhou, M. K. H. Leung, S. Yang, *Joule*, **1**,2(2017): 383–393.

[13] Y. Pluntke, I. A. Kibler, *Electrocatalysis*, **2**(2011): 192.

[14] A. Safavi, S. H. Kazemi, H. Kazemi, *Fuels*, **118**(2014): 156–162.

[15] Y. Cheng, S. P. Jiang, *Progress in Natural Science: Materials International*, **25**,6(2015): 545 –553.

[16] S. Xiong, P. Li, Z. Jin, T. Gao, Y. Wang, Y. Guo, D. Xiao, *Electrochimica Acta*, **222**(2016): 999–1006.

[17] X. Liu, J. Dong, B. You, Y. Sun, *RSC Advances*, **6**,77(2016): 73336–73342.

[18] Y. Shao, M. Zheng, M. Cai, L. He, C. Xu, *Electrochimica Acta*, **257**(2017): 1–8.

[19] M. Chhetri, S. Sultan, C. N. R. Rao, *Proceedings of the National Academy of Sciences*, **114**,34,(2017): 8986–8990.

[20] R. Subbaraman, D Tripkovic, D Strmcnik, K. C. Chang, M. Uchimura, A. P. Paulikas, V. Stamenkovic, N. M. Markovic, *Science*, **334**,6060(2011): 1256–1260.

[21] H. Yin, S. Zhao, K. Zhao, A. Muqsit, H. Tang, L. Chang, H. Zhao, Y. Gao, Z. Tang, *Nature Communication*, **6**(2015): 6430.

[22] L. Wang, C. Lin, D. Huang, J. Chen, L. Jiang, M. Wang, L. Chi, L. Shi, J. Jin, *ACS Catalysis*, **5**,6(2015): 3801–3806.

[23] L. Wang, Y. Zhu, Z. Zeng, C. Lin, M. Giroux, L. Jiang, Y. Han, J. Greeley, C. Wang, J. Jin, *Nano Energy*, **31**(2017): 456–461.

[24] Y. Li, P. Hasin, Y. Wu, *Advanced Materials,* **22**,17(2010): 1926–1929.

[25] S. Chen, S. Qiao, *ACS Nano,* **7**,11(2013):10190–10196.

[26] O. Savadogo, K. Amuzgar, D. I. Piron, *International Journal of Hydrogen Energy*, **15**,11(1990): 783–788.

[27] Y. Liu, W. E. Mustain, *International Journal of Hydrogen Energy,* **37**,11(2012): 8929–8938.

[28] M. Vasic, M. Cebela, I. Pasti, L. Amaral, R. Hercigonja, D. M. F. Santos, B. Sljikic, *Electrochimica Acta*, **259**(2018): 882–892.

[29] D. M. F. Santos, C. A. C. Sequeira, D. Maccio, A. Saccone, J. I. Fiqueredo, *International Journal of Hydrogen Energy*, **38**,8(2013): 3137–3145.

[30] J. Greeley, T. F. Jaramillo, J. Bonde, I. Chorkendorff, J. K. Norskov, *Nature Materials,* **5**,11(2006): 909–913.

[31] J. Durst, A. Siebel, C. Simon, F. Hasche, J. Herranz and H. A. Gasteiger, *Energy and Environmental Science,* **7**,7(2014): 2255–2260.

[32] G. Valenti, A. Boni, M. Melchionna, M. Cargnello, L. Nasi, G. Bertoni, R. J. Gorte, M. Marcaccio, S. Rapino, M. Bonchio, P. Fornasiero, M. Prato and F. Paolucci, *Nature Communication*, **7**(2016): 13549.

[33] J. Tang, X. Zhao, Y. Zuo, P. Ju and Y. Tang, *Electrochimica Acta*, **174**(2015): 1041–1049.

[34] J. A. S. B. Cardoso, L. Amaral, Ö. Metin, D. S. P. Cardoso, M. Sevim, T. Sener, C. A. C. Sequeira and D. M. F. Santos, *International Journal of Hydrogen Energy*, **42**,7(2017): 3916–3925.

[35] T. Bhowmik, M, K. Kundu and S. Barman, *ACS Catalysis*, **6**,3(2016): 1929–1941.

[36] W. Sheng, M. Myint, J. G. Chen and Y. Yan, *Energy and Environmental Science*, **6**,5(2013): 1509–1512.

[37] H. Liao, C. Wei, J. Wang, A. Fisher, T. Sritharan, Z. Feng and Z. J. Xu, *Advanced Energy Materials*, **7**,21(2017): 1701129.

[38] M. Vasic, M. Cebela, I. Pasti, L. Amaral, R. Hercigonja, D. M. F. Santos, B. Sljikic, Electrochimica Acta, **259**(2018): 882–892.

[39] R. Forgie, G. Bugosh , K. C. Neyerlin, Z. Liu, P. Strasser, *Electrochemical and Solid State Letters*, **13**,4(2010): B36–B39.

[40] A. Marshall, B. Borresen, G. Hagen, M. Tsypkin, R. Tunold, *Electrochimica Acta*, **51**,15(2006): 3161–3167.

[41] S. Fierro, T. Nagel, H. Baltruschat, C. Comninellis, *Electrochemistry Communication,* **9**,8(2007): 1969–1974.

[42] J. P. Singh, X. G. Zhang, H. L. Li, A. Singh, R. N. Singh, *International Journal Electrochemical Science,* **3**,4(2008): 416–426.

[43] Z. Y. Li, Z. L. Liu, J. C. Liang, C. W. Xu, X. Lu, *Journal of Material Chemistry A*, **2**,43(2014): 18236–18240.

[44] Y. Rao, Y. Wang, H. Ning, P. Li, M. Wu, *ACS Applied Material Interfaces,* **8**,49(2016): 33601–33607.

[45] T. Zhang, S. A. Liao, L. X. Dai, J. W. Yu, W. Zhu, Y. W. Zhang, *Sci. China Mater.,* **61**(2018): 926–938.

[46] Y. Li, P. Hasin, Y. Wu, *Advanced Materials,***22**,17(2010): 1926–1929.

[47] S. Chen, S. Qiao, *ACS Nano,* **7**,11(2013):10190–10196.

CHAPTER 7

Demonstrating novel Pd/M Electrocatalysts on MOF-Derived Carbons for Alkaline Hydrogen Oxidation and Oxygen Reduction Reactions

7.1 Introduction

Global renewable energy demands are major concerns with tremendous efforts to replace fossil fuel technology. Given this disposition, the hydrogen economy is an important strategy for future sustainable energy technology because H_2 fuel is clean, commercially produced in high purity from H_2O as explained in previous chapter, has high specific energy (141.86 MJ kg^{-1}) and an energy carrier in FCs [1–3]. Unlike the conventional PEMFCs operating in acidic conditions, the AMFCs operate in alkaline conditions and are recently attracting extremely good interest, due to its intriguing attributes: increase cathodic reaction (ORR) kinetics [4]; mitigation of Pt catalyst corrosion [5]; reduction in H_2O management that may cause flooding; and the possibility of using reduced loading non-Pt electrocatalysts [6,7]. However, the anodic reaction (HOR) is the major challenge of the AMFCs because of the low dissolution of protons in alkaline conditions or high pH and deceased HOR activity, requiring high overpotential [8,9]. Previous research has proved that kinetics of the HOR is relatively lower to an order of two magnitudes in the AMFCs to that of the PEMFCs [10], even with a high loading of commonly used Pt electrocatalyst [11]. Pd-based electrocatalysts have been reported recently to have high activity for the AMFCs and

its more abundant than the Pt-based electrocatalyst, informed its choice in this work. As a strategy to reduce the cost of AMFCs fabrication, nanostructured Pd is often supported on carbon materials. Novel porous carbon support was derived from MOFs. The MOFs were explored as sacrificial templates because of their inherent characteristics, explained in Chapter 2. Moreover, co-metal catalysts (M = SnO_2, Ni) addition to the nanostructured Pd has been reported to improve the electrocatalytic performances and stability.

This chapter reports the electrochemical performance of nanostructured Pd/M (M = SnO_2, Ni) on MOF-derived carbons electrocatalysts toward alkaline HOR and ORR. Although non-precious electrocatalysts like FeCo/C, NCFe-950 are excellent for driving the ORR in the AMFCs [12,13], the study was investigated out of curiosity. Hence, more attention is given to the alkaline HOR and its comprehensive mechanism has been proposed in **Equations 7.1 – 7.3** [14]. The HOR is dependent on two importance descriptors: H binding energy or H adsorption as given in either **Equations 7.1** or **7.2** and promotional effect of oxygen-containing species (oxophilic or spill-over properties) of the co-metal catalysts to adsorb OH_{ads} and donate it to the M-H_{ads} to quickly remove the H_{ads} from the active site of the Pd electrocatalysts, as shown in **Equation 7.3**, which is often assumed to be the rds of the HOR [15,16].

$$H_2 + 2M \rightarrow MH_{ads} + MH_{ads} \quad \text{(Tafel, } b_a = \frac{2.3RT}{2F} = 29.6 \text{ mV dec}^{-1}\text{)} \quad (7.1)$$

$$H_2 + OH^- + M \rightarrow MH_{ads} + H_2O + e^- \quad \text{(Heyrovsky, } b_a = \frac{2.3RT}{2F} = 39.4 \text{ mV dec}^{-1}\text{)} \quad (7.2)$$

$$MH_{ads} + OH^- \rightarrow H_2O + M + e^- \quad \text{(Volmer, } b_a = \frac{2.3RT}{2F} = 118.2 \text{ mV dec}^{-1}\text{)} \quad (7.3)$$

Where M is an active site of the electrocatalysts to chemisorb hydrogen intermediate (H_{ads}), the co-metal catalyst with hydroxides promotional effects (oxophilic property and spill-over for metal and metal oxide, respectively).

7.2 Results and discussion

The results discussed are based on the electrocatalysts' classification: (i) Pd/SnO_2-based electrocatalysts (Pd/SnO_2/MOFDC and Pd/MOFDC); and (ii) Pd/Ni-based electrocatalysts (Pd/Ni/MOFDC and Pd/AT-Ni/MOFDC) for alkaline HOR and ORR separately.

7.2.1 Pd/SnO_2-based Electrocatalysts for Hydrogen Oxidation (HOR) and Oxygen Reduction Reactions (ORR)

Investigation of alkaline HOR and ORR performances on the Pd/MOFDC and Pd/SnO_2/MOFDC are discussed in this session.

7.2.1.1 Hydrogen Oxidation Reaction (HOR)

7.2.1.1.1 HOR Polarization Curves

HOR polarization curves of the Pd/MOFDC and Pd/SnO_2/MOFDC in H_2-saturated 0.1 M KOH solution using the RDE at 1600 rpm and other rotation speeds (400 – 4900 rpm) are shown in **Figures 7.1a – 7.1c**. Explaining the inherent activity of the electrocatalysts toward the HOR, the current (*i*) is generally normalized by the mass of estimated Pd loading, resulting in the mass current densities (j_m). The HOR started evolving at the positive potential shortly after 0.0 V *vs.* RHE with the corresponding j_m at 1600 rpm and other rotation speeds because of ohmic (*iR*) drops. The j_m values of the Pd/SnO_2/MOFDC towards the HOR at all reaction conditions increased averagely by *ca.* 4.0 factors relative to those of the Pd/MOFDC, due to the OH promotional

effects of Sn (oxophilic) and SnO_2 (spill-over) to quickly desorb the H_{ads} from the active sites of the Pd, as shown in the Volmer (rds, **Equation 7.3**).

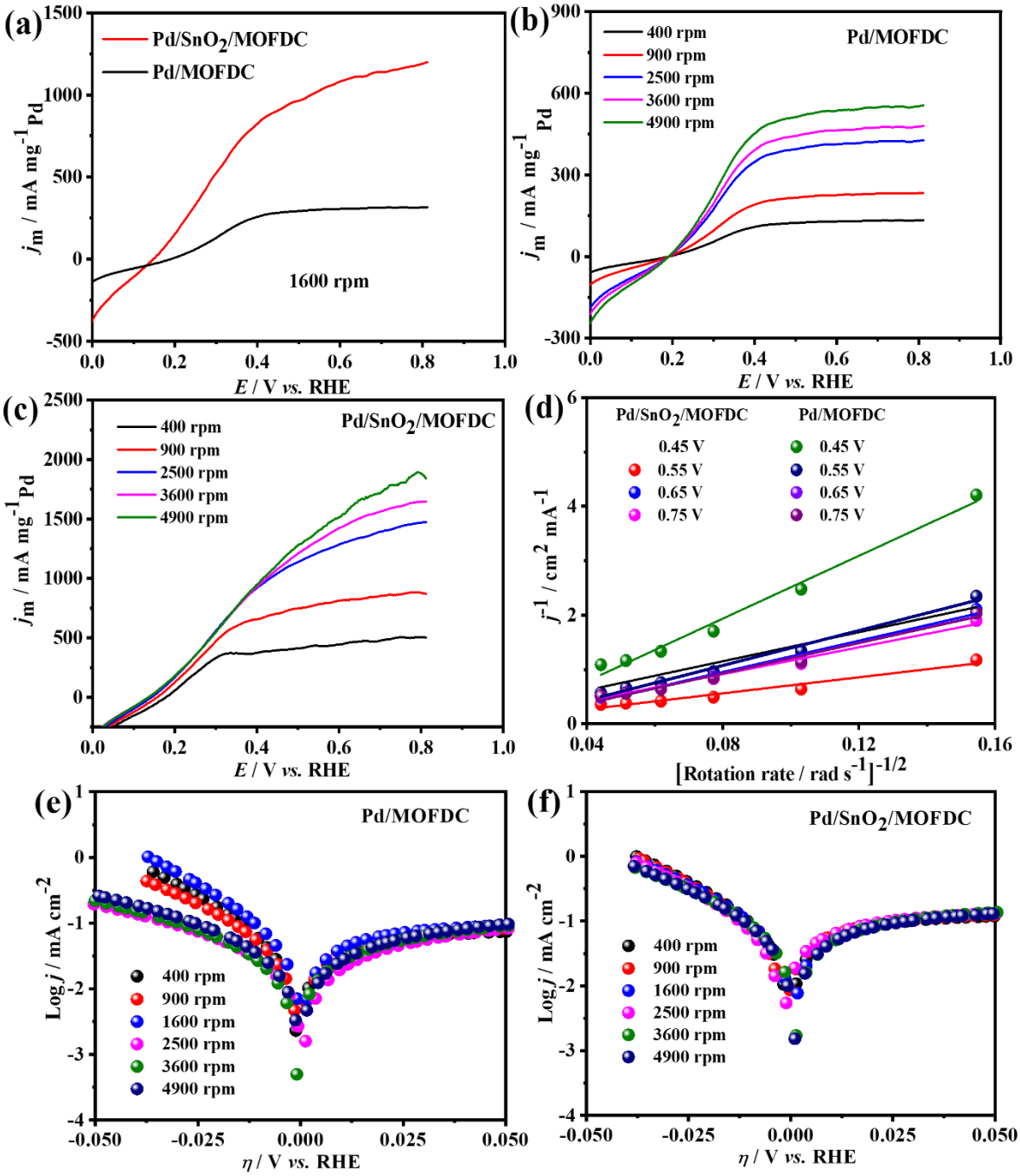

Figure 7.1: HOR polarization curves at (a) 1600 rpm, (b,c) other rotation speeds, (d) Koutecky-Levich plots at different overpotential (η = 0.45, 0.55, 0.65, and 0.75 V *vs.* RHE) and (e, f) Butler-Volmer plots of the Pd/SnO_2-based electrocatalysts in H_2-saturated 0.1 M KOH solution at 5 mV s^{-1} and 298 K

Table 7.1: Kinetic parameters of the Pd/SnO_2-based electrocatalysts for HOR in H_2-saturated 0.1 M KOH solution, in terms of the $j_{o,s}$, $j_{o,m}$ and b_a at different rotation speeds and 5 mV s^{-1}.

Kinetic parameters	Pd/SnO_2-based Electrocatalysts	
	Pd/SnO_2/MOFDC	Pd/MOFDC
@400 rpm		
b_a / mV dec^{-1}	55.43 ± 6.21	76.38 ± 8.00
$j_{o,s}$ / mA cm^{-2}	0.109	0.059
$j_{o,m}$ / mA mg^{-1}	104.68	15.65
@900 rpm		
b_a / mV dec^{-1}	52.85 ± 6.65	78.90 ± 8.49
$j_{o,s}$ / mA cm^{-2}	0.112	0.071
$j_{o,m}$ / mA mg^{-1}	107.67	18.61
@1600 rpm		
β_a / mV dec^{-1}	58.72 ± 9.67	72.53 ± 6.76
$j_{o,s}$ / mA cm^{-2}	0.119	0.078
$j_{o,m}$ / mA mg^{-1}	114.68	20.62
@2500 rpm		
b_a / mV dec^{-1}	70.62 ± 4.65	75.95 ± 4.89
$j_{o,s}$ / mA cm^{-2}	0.1126	0.085
$j_{o,m}$ / mA mg^{-1}	108.34	22.43
@3600 rpm		
b_a / mV dec^{-1}	50.36 ± 6.80	85.29 ± 7.01

$j_{o,s}$ / mA cm^{-2}	0.122	0.089
$j_{o,m}$ / mA mg^{-1}	117.04	23.48
@4900 rpm		
b_a / mV dec^{-1}	55.05 ± 6.21	81.78 ± 5.09
$j_{o,s}$ / mA cm^{-2}	0.110	0.086
$j_{o,m}$ / mA mg^{-1}	105.66	22.79

As the rotation speeds increase from 400 to 4900 rpm, the j_m values increase concurrently for the electrocatalysts, due to enhanced mass transport properties. There is also a contribution of a mixed kinetic-diffusion controlled process for the HOR [17]. The diffusion-limited current density (j_{lim} = 1.5 mA cm$^{-2}{}_{disk}$) is separated and determined by modelling the polarization curves at different rotation speeds to the conventional Koutecky-Levich formulae (**Equations 2.19** and **2.20)**, where the total current density (j) is resolved into two components: (i) kinetic process ($1/j_K$); and (ii) diffusion ($1/j_D$) process.

Koutecky-Levich plot (**Figure 7.1d**) of the electrocatalysts involves a plot of inverse of current density (j^{-1} / cm^2 mA^{-1}) against inverse square root of rotation speed ($\omega^{-1/2}$ / (rad s^{-1})$^{-1/2}$) at different overpotentials (η = 0.45, 0.55, 0.65 and 0.75 V *vs.* RHE). The kinetic current (j_K) values of (2.7, 4.7, 5.4 and 5.4 mA cm$^{-2}{}_{disk}$) and (7.3, 14.4, 5.1 and 12.1 mA cm$^{-2}{}_{disk}$) are calculated from the intercept ($1/j_K$) at the η values studied for the Pd/MOFDC and Pd/SnO_2/MOFDC, respectively. The j_K values obtained are employed to determine the HOR heterogeneous rate constant (k^0) with mean values of 2.36 ± 0.09 x 10^{-4} and 5.04 ± 0.12 x 10^{-4} cm s^{-1} for the Pd/MOFDC and Pd/SnO_2/MOFDC, respectively. While the slopes are used to calculate the diffusivity (D) of H_2 gas onto

the electrocatalysts during the HOR, as given in **Equation 2.22**. The Pd/MOFDC and Pd/SnO_2/MOFDC records the average *D* values of 2.77 ± 0.15 x 10^{-5} and 5.14 ± 0.24 x 10^{-5} cm^2 s^{-1}, respectively. These results show the rate at which H_2 gas is chemisorbed and desorbed from the active sites of Pd in the Pd/SnO_2/MOFDC is doubled that of the Pd/MOFDC. This observation is ascribed to the oxophilic and spill-over natures of Sn and SnO_2, respectively, as well as electronic properties which help to hasten the removal of the H_{ads} from the electronically modified Pd for strong H_2 adsorption and subsequently weaken the Pd-H_{ads} for quicker H_2 oxidation [18].

The mass transfer kinetics of the HOR is understood in term of the $j_{o,s}$ and $j_{o,m}$ values by modelling the polarization curves to renowned Butler-Volmer formula. The Butler-Volmer plots of the electrocatalysts are shown in **Figures 7.1e** and **7.1f**, where the $j_{o,s}$ values of the Pd/SnO_2-based electrocatalysts were extrapolated and determined. The $j_{o,s}$ values were normalized to the ECSA of the electrocatalysts to obtain equivalent $j_{o,m}$. The $j_{o,m}$ value of the Pd/SnO_2/MOFDC (114.68 mA mg^{-1}_{Pd}) at 1600 rpm is *ca.* 5.5 times more than the Pd/MOFDC (20.62 mA mg^{-1}_{Pd}), due to the oxophilic property of Sn, spill-over effect of SnO_2, as well as electronic property of modified Pd. The mass transfer kinetic parameters obtained at all rotation speeds for the Pd/SnO_2/MOFDC are higher than those of the Pd/MOFDC, summarized in **Table 7.1**. These results reveal that the Pd/SnO_2/MOFDC possesses increased $j_{o,s,}$ and $j_{o,m}$ by factors of *ca.* 2 and 5.5, respectively at all rotation speeds compared to the Pd/MOFDC. These observations are the same as those obtained for the kinetic and diffusion processes.

The anodic Tafel slope (b_a) is the major parameter for deducing favorable pathways for the HOR. The b_a values of the Pd/MOFDC and Pd/SnO_2/MOFDC at 1600 rpm are 72.53 ± 6.76 and 58.72 ± 9.67 mV dec^{-1}, with α values of 0.32 and 0.39, respectively.

The lower b_a values of the Pd/SnO_2-based electrocatalysts may be ascribed to the high Pd polycrystalline surface coverage for HOR and quicker desorption of the H_{ads}. This observation agrees with the previous report for Pd surface coverage dependent Tafel slopes [9]. The mechanism of HOR on noble metal electrocatalysts with Tafel slopes within the values obtained in this study has been reported to favor the Heyrovsky-Volmer process, with the Volmer being the rds [19], while the Tafel-Volmer process predominates when the Tafel slope is extremely low [20,21]. Therefore, the HOR mechanism of the electrocatalysts is suggested to follow the Heyrovsky-Volmer process.

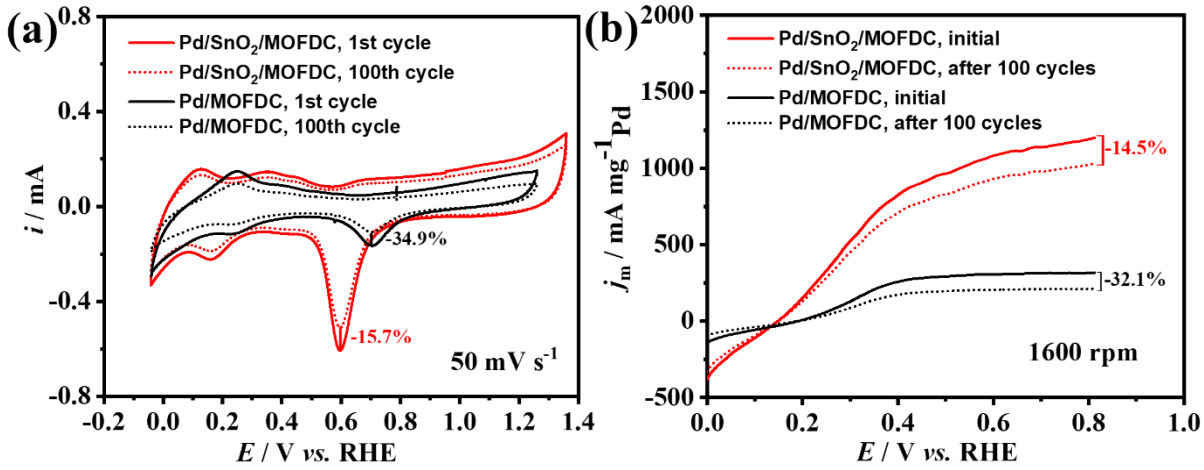

Figure 7.2: (a) CV at 1st and 100th cycles and (b) HOR polarization curves at 1600 rpm, 298 K, initial and after 100th cycles of the Pd/SnO_2-based electrocatalysts

Th stability of the Pd/MOFDC and Pd/SnO_2/MOFDC was investigated with cyclic voltammograms (**Figure 7.2a**) ran for 100 cycles. The CV revealed well-resolved signatures with prominent peaks like hydrogen adsorption/desorption (-0.05 – 0.3 V *vs.* RHE) and PdO reduction peak (0.5 – 0.8 V *vs.* RHE). The PdO reduction peak has been employed to deduce the ECSA in Chapter 4 and it increased by a factor of 3.7 for the Pd/SnO_2/MOFDC compared to the Pd/MOFDC. Besides, the peak also shifts

to more negative potential for the Pd/SnO_2/MOFDC, which is an indication that it requires relatively less energy. When the electrocatalysts were cycled for 100 times, degradation was observed with decreased 34.9 and 15.7% for the Pd/MOFDC and Pd/SnO_2/MOFDC, respectively. Then, HOR polarization curves of the electrocatalysts are shown in **Figure 7.2b**, where HOR activities of the Pd/MOFDC and Pd/SnO_2/MOFDC reduced after 100 cycles by 14.5 and 32.1%, respectively. The lower % degradation observed for the Pd/SnO_2/MOFDC reveals that the addition of SnO_2 does not only improve the HOR kinetics, but also stabilizes the electrocatalyst.

Temperature-dependent HOR polarization curves of the Pd/SnO_2-based electrocatalysts are shown in **Figures 7.3a** and **7.3b**, whose kinetic parameters are extracted from the Butler-Volmer plots (**Figures 7.3c – 7.3e**) and the values summarized in **Table 7.2**. Arrhenius plots (**Figure 7.3f**) of the Pd/SnO_2-based electrocatalysts, where a plot of the ln $j_{o,s}$ to the T^{-1} give straight lines. The E_A values of the electrocatalysts are calculated from the slope ($\frac{-E_A}{R}$). The slope values obtained for the Pd/MOFDC and Pd/SnO_2/MOFDC are -4744.34 ± 699.75 and -1725.65 ± 163.74, resulting in E_A values of 39.44 ± 5.82 and 14.37 ± 1.36 kJ mol^{-1}, respectively. These results show that the Pd/SnO_2/MOFDC requires very much lower energy to catalyze the HOR in H_2-saturated 0.1 M KOH solution relative to the Pd/MOFDC, due to the facile desorption of the H_{ads} from the active sites of the Pd by the Sn and SnO_2. The E_A value of the Pd/SnO_2/MOFDC is also lower than those previously reported for the HOR on Pt/C (29.5 ± 4.0 kJ mol^{-1}) [11], Pd/C (38.9 ± 3.0 kJ mol^{-1}) [22] and Ir/C (32.9 ± 1.5 kJ mol^{-1}) [23]. However, high energy is required for the Pd/MOFDC to drive the HOR kinetics in the reaction conditions, further explains its lower $j_{o,s}$ and $j_{o,m}$ values. While the Pd/SnO_2/MOFDC possesses high $j_{o,s}$ and $j_{o,m}$ values, but lower E_A because

of the timely desorption of the H_{ads} by the SnO_2 from the active sites of Pd. This observation agrees with the correlation between E_A, $j_{o,s}$ and $j_{o,m}$ values [24].

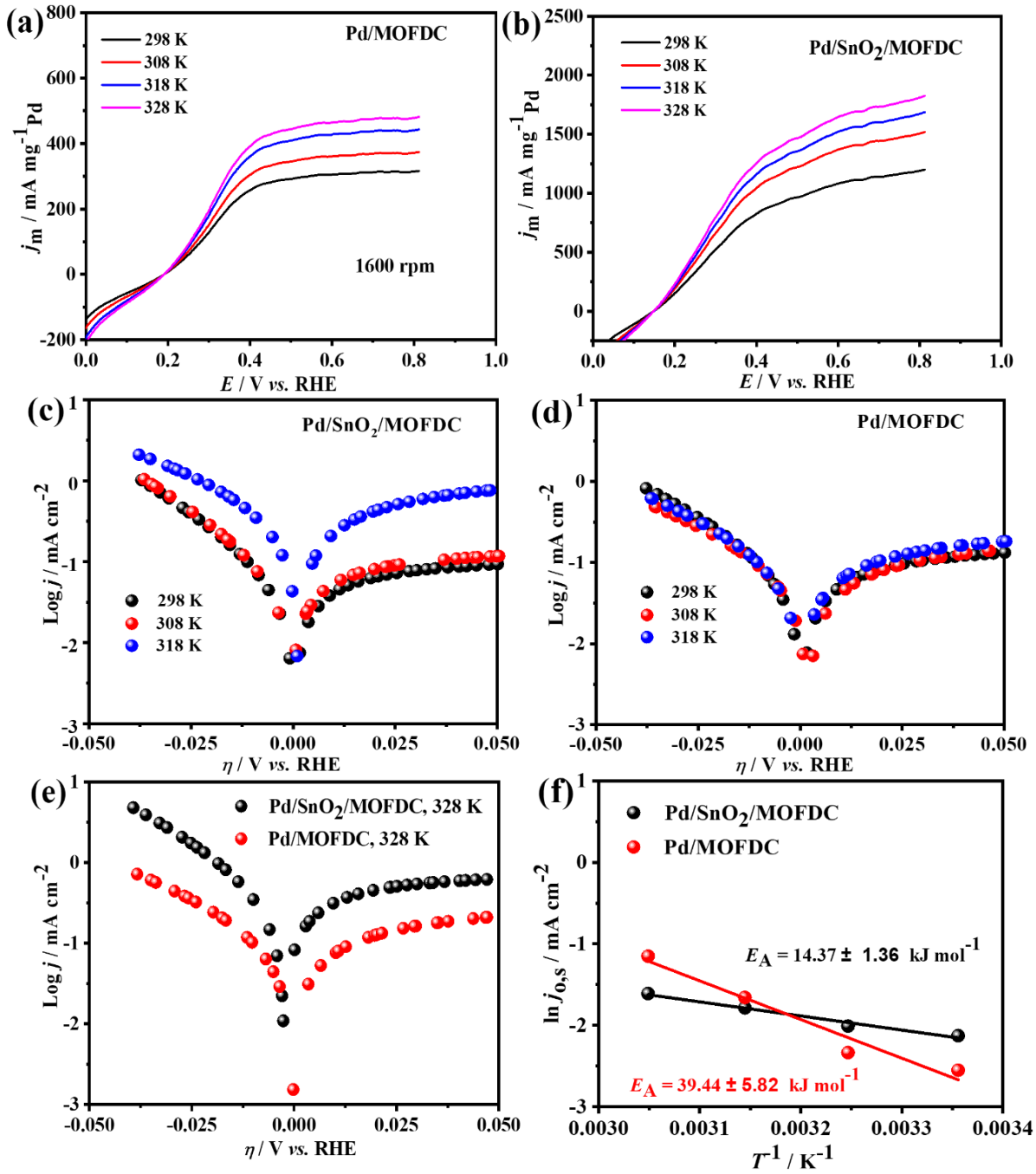

Figure 7.3: (a,b) HOR polarization curves, (c–e) Butler-Volmer plots and (f) Arrhenius plots of the Pd/SnO_2-based electrocatalysts in H_2-saturated 0.1 M KOH at 1600 rpm, 5 mV s^{-1} and varying temperature

Table 7.2: Kinetic parameters of the Pd/SnO_2-based electrocatalysts for HOR in H_2-saturated 0.1 M KOH solution, in terms of the $j_{o,s}$, $j_{o,m}$ and b_a at 1600 rpm, 5 mV s^{-1} and varying temperature (298, 308, 318, 328 K).

Kinetic parameters	Pd/SnO_2-based Electrocatalysts	
	Pd/SnO_2/MOFDC	Pd/MOFDC
@298 K		
b_a / mV dec^{-1}	58.72 ± 9.67	72.53 ± 6.76
$j_{o,s}$ / mA cm^{-2}	0.119	0.078
$j_{o,m}$ / mA mg^{-1}	114.68	20.62
@308 K		
b_a / mV dec^{-1}	75.23 ± 6.11	89.34 ± 5.90
$j_{o,s}$ / mA cm^{-2}	0.134	0.097
$j_{o,m}$ / mA mg^{-1}	129.00	25.50
@318 K		
b_a / mV dec^{-1}	82.04 ± 6.59	102.84 ±
$j_{o,s}$ / mA cm^{-2}	0.168	2.59
$j_{o,m}$ / mA mg^{-1}	161.32	0.191
		50.19
@328 K		
b_a / mV dec^{-1}	84.90 ± 6.88	98.89 ± 4.19
$j_{o,s}$ / mA cm^{-2}	0.200	0.316
$j_{o,m}$ / mA mg^{-1}	192.19	83.29

7.2.1.1.2 Chronoamperometry (HOR)

To ascertain the stability of the electrocatalysts toward alkaline HOR, CA (**Figure 7.4**) was carried at 0.4 V *vs.* RHE for 1200 s. The results further confirm the improved stability on addition of SnO_2 in the Pd/SnO_2/MOFDC compared to the Pd/MOFDC.

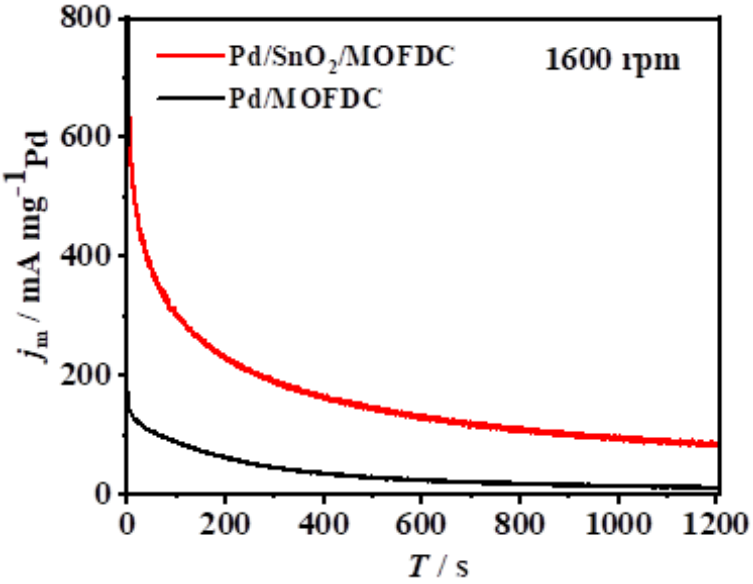

Figure 7.4: CA at 0.3 V *vs.* RHE of the Pd/SnO_2-based electrocatalysts in H_2-saturated 0.1 M KOH solution at 298 K and 5 mV s^{-1}

7.2.1.1.3 Electrochemical Impedance Spectroscopy (HOR)

The Pd/SnO_2 interfacial electrochemistry for the alkaline HOR kinetics as a result of OH promoting effect of the co-metal catalysts is further investigated with the EIS. **Figure 7.5a** shows the Nyquist plots of the electrocatalysts toward the alkaline HOR with the Voigt *EEC* model (**Figure 7.5b**). The EIS parameters extracted consist of R_s, R_{int}, R_{ct} and *CPE*, explained previously and the values are summarized in **Table 7.3**. The R_s value of *ca.* 55 Ω is recorded for the electrodes indicate the same conductivity in the supporting electrolyte. The R_{ct} values of *ca.* 172 and 252 Ω are recorded for the Pd/SnO_2/MOFDC and Pd/MOFDC, respectively.

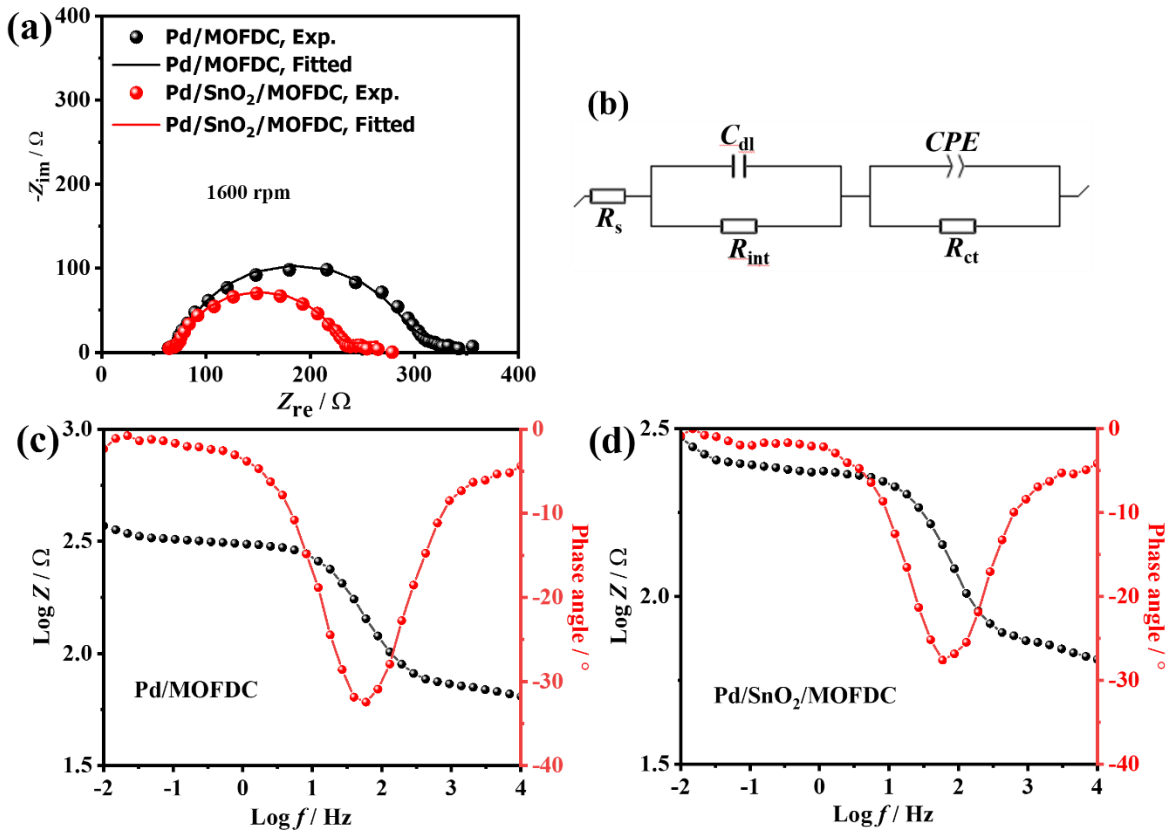

Figure 7.5: (a) Nyquist plots, (b) Voigt *EEC* model and (c,d) Bode plots of the Pd/SnO_2-based electrocatalysts in H_2-saturated 0.1 M KOH at 1600 rpm, 298 K and 0.3 V *vs.* RHE

The lower R_{ct} value of the Pd/SnO_2/MOFDC reveals its improved HOR kinetics. Also, the R_{int} value for the Pd/SnO_2/MOFDC (43 Ω) is lower than that of Pd/MOFDC (48 Ω) shows the facile H desorption than the latter. According to the *CPE* impedimetric power law, the a = 0.53 and 0.56 are close to ideal Z_w with a = 0.5. This result suggests a diffusive process at the interface of electrodes and electrolytes. Bode plots (**Figures 7.5c** and **7.5d**) were further employed to probe the electrodes with the logarithm of series resistance values of 2.96 and 2.48 for the Pd/MOFDC and Pd/SnO_2/MOFDC, as well as phase angles of 32.23 and 27.88º, respectively. The lower overall resistance of the Pd/SnO_2/MOFDC confirms the interfacial behavior between the Pd and SnO_2 for enhanced HOR kinetics.

Table 7.3: EIS parameters of the Pd/SnO_2-based electrocatalysts toward HOR in alkaline condition at 1600 rpm, 298 K and 0.3 V *vs.* RHE

EIS parameters	Pd/SnO_2-based Electrocatalysts	
	Pd/MOFDC	Pd/SnO_2/MOFDC
R_s / Ω	55.38 ± 1.90	55.09 ± 6.77
R_{ct} / Ω	252.26 ± 2.14	172.40 ± 1.28
C_{dl} / µF	33.26 ± 0.76	31.33 ± 0.95
R_{int} / Ω	48.43 ± 4.75	43.25 ± 3.79
CPE / mF.s($^{a-1}$)	4.28 ± 0.19	7.75 ± 0.68
n	0.53	0.56

7.2.1.2 Oxygen Reduction Reaction (ORR)

7.2.1.2.1 ORR Polarization Curves

RDE and RRDE experiments were employed to probe the ORR kinetic of the Pd/SnO_2-based electrocatalysts. **Figures 7.6a** and **7.6b** show the ORR polarization curves of the Pd/SnO_2-based electrocatalysts in O_2-saturated 0.1 M KOH solution at 10 mV s^{-1} and varied rotation speeds. The two renowned regions of kinetic and diffusion regions were observed, where the *j* values increase concurrently with increasing rotation speeds. However, at all rotation speeds, the Pd/MOFDC electrocatalyst displayed high *j* values in the diffusion region. The polarization curves of the electrocatalysts were then modelled to Koutecky-Levich formulae (**Equations 2.19** and **2.20**) to obtain to the j_K, k^0 and the number of electrons during the ORR.

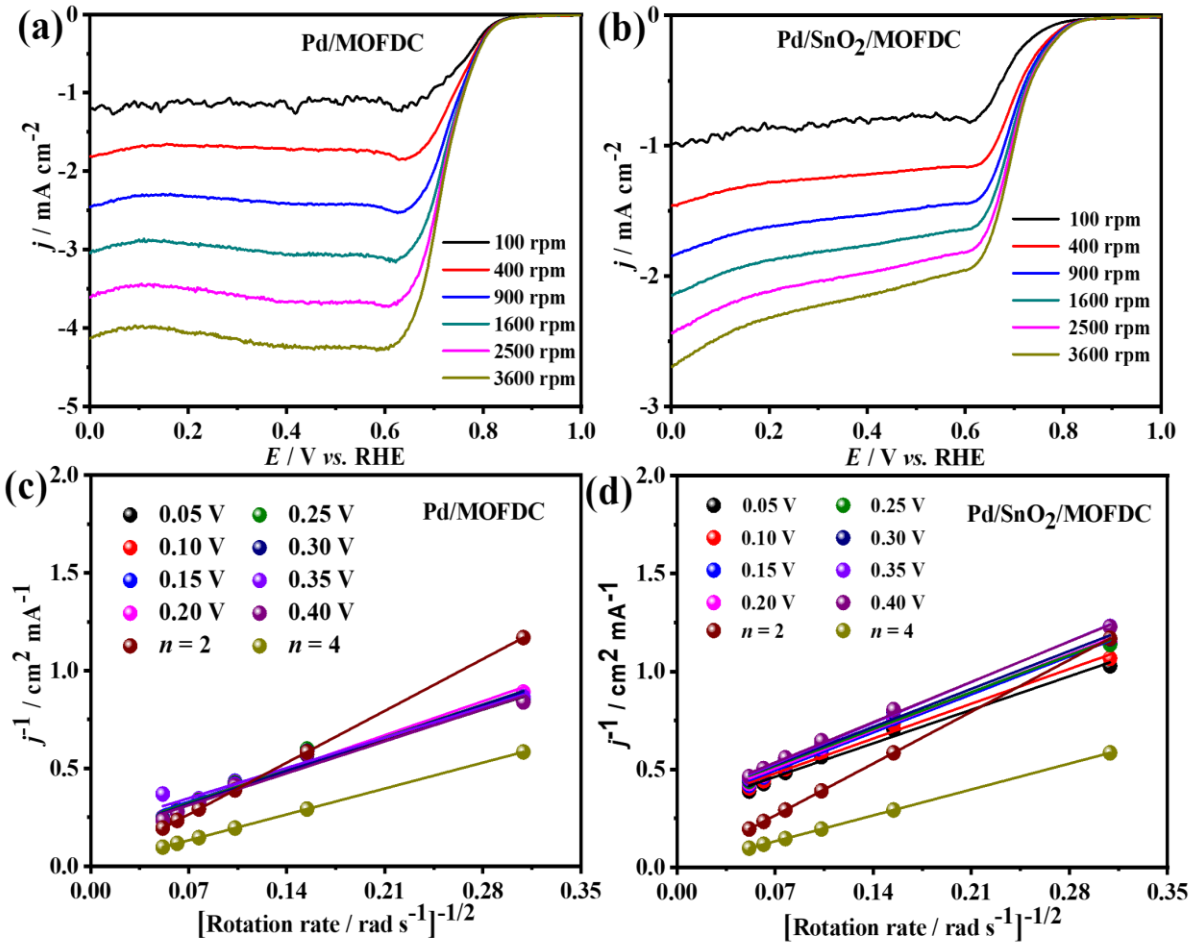

Figure 7.6: (a,b) ORR polarization curves and (c,d), Koutecky-Levich plots at varied η values of the Pd/SnO_2-based electrocatalysts in O_2-saturated 0.1 M KOH solution at 10 mV s^{-1} and different rotation speeds

Figures 7.6c and **7.6d** show the Koutecky-Levich plots of the Pd/SnO_2-based electrocatalysts at varied η = 0.05 – 0.40 V (*vs.* RHE) and limiting current density (j_{lim} = 4.5 mA cm^{-2}), as well as theoretical plots when the number of electrons (n = 2 or 4). The j_K values ranges of 5.18 – 6.72 mA cm^{-2} and 3.03 – 3.44 mA cm^{-2} are recorded for the Pd/MOFDC and Pd/SnO_2/MOFDC, respectively. The *n* values calculated for the Pd/MOFDC and Pd/SnO_2/MOFDC are 3.53 and 2.77, respectively. These results suggest that $4e^-$ pathway predominates during the ORR for the Pd/MOFDC with no oxidation of H_2O_2, while the Pd/SnO_2/MOFDC drives the ORR through mixed

processes (i.e., $2e^-$ and $4e^-$ pathways). This observation was supported by the theoretical model. The amount of the H_2O_2 produced in the $2e^-$ pathway of the Pd/SnO_2/MOFDC will be deduced using the RRDE experiment. The values of *n* calculated are between 2 or 4 may be traced to the possible errors involved during the extrapolation of the kinetic and diffusion parameters in the Koutecky-Levich diagnosis [25]. These assumptions are latter confirmed using the RRDE experiments for modelling the ORR mechanism. Using the *n* values in the relationship between the j_K and k^0 (**Equation 2.22**), mean k^0 values of 2.00 x 10^{-4} and 1.04 x 10^{-4} cm s^{-1} are calculated for the Pd/MOFDC and Pd/SnO_2/MOFDC, respectively. The lower k^0 value of the Pd/SnO_2/MOFDC toward the ORR further confirms its reduced ORR performance, due to the conflicting effect of the SnO_2 nanoparticles.

Figure 7.7 shows comparative RDE and RRDE polarization curves of the Pd/SnO_2-based electrocatalysts in O_2-saturated 0.1 M KOH solution at 1600 rpm and 10 mV s^{-1}. In **Figure 7.7a**, the E_{onset} values of 90 and 85 mV *vs.* RHE were recorded for the Pd/MOFDC and Pd/SnO_2/MOFDC, respectively. The more positive E_{onset} for the Pd/MOFDC shows that the ORR is more facile requiring less energy compared to the Pd/SnO_2/MOFDC. The result corroborates the increased mass transfer (*j*) and kinetic (j_K and k^0) parameters of the Pd/MOFDC obtained previously indicating improved ORR activity, relative to the Pd/SnO_2/MOFDC. The mechanism of the Pd/SnO_2-based electrocatalysts for the ORR was further verified with the RRDE, which was carried out at 10 mV s^{-1} and 1600 rpm, shown in **Figure 7.7b**. The RRDE consists of two distinct electrodes: (i) ring polarized at 1.2 V *vs.* RHE; and (ii) disk embedded together is used for oxidation peroxide species (O_2^{2-}, positive current response) and ORR (negative current response), respectively. As seen, the O_2^{2-} oxidation peak at the ring

for the Pd/MOFDC occurs at j = 0 mA cm^{-2}, indicating no production of H_2O_2 (i.e., 4e- pathway is favorable), while O_2^{2-} oxidation peak occurs at more significant j values for the Pd/SnO_2/MOFDC, showing that little amount of H_2O_2 was produced and the ORR tours the mixed 2e$^-$ and 4e$^-$ pathways. The amount of the H_2O_2 produced is calculated following **Equations 7.4** and **7.5** [26]:

$$\% H_2O_2 = \frac{200\frac{j_r}{N}}{j_d + \frac{j_r}{N}} \quad (7.4)$$

$$n = \frac{4j_d}{j_d + \frac{j_r}{N}} \quad (7.5)$$

where j_r and j_d are the ring and disk current densities, respectively and N is the theoretical collection efficiency (0.249)

The percentages of H_2O_2 produced during the ORR for the Pd/SnO_2-based electrocatalysts at varied potentials (0.05 – 0.4 V *vs.* RHE) are presented in **Figure 7.7c**. The Pd/MOFDC and Pd/SnO_2/MOFDC recorded 0.00 and 0.10 % of H_2O_2 produced, respectively. The null amount H_2O_2 produced during the ORR for the Pd/MOFDC shows that the 4e$^-$ pathway is most favorable, while the little amount of H_2O_2 produced for Pd/SnO_2/MOFDC suggests a mixed 2e$^-$ and 4e$^-$ pathways. Also, the n values from the RRDE experiments calculated for the Pd/MOFDC and Pd/SnO_2/MOFDC are 3.9999 and 3.9976, respectively. The RRDE model confirms that the ORR on the Pd/SnO_2-based electrocatalysts follows the 4e$^-$ pathway. The n values obtained for the RRDE experiments are higher than those recorded for the Koutecky-Levich diagnosis. Tafel plots of the Pd/SnO_2-based electrocatalysts toward the ORR is shown in **Figure 7.7d**, where the b_c is deduced. It is well known that the lower the b_c value, the high the ORR kinetics [27–29]. The b_c values of *ca.* 70 and 90

mV dec^{-1} are calculated for the Pd/MOFDC and Pd/SnO_2/MOFDC, respectively. Hence, improved ORR kinetic is recorded for the Pd/MOFDC. These results further corroborate previous observations for the RDE and RRDE experiments that the Pd/MOFDC is a better electrocatalyst for the ORR compared to the Pd/SnO_2/MOFDC.

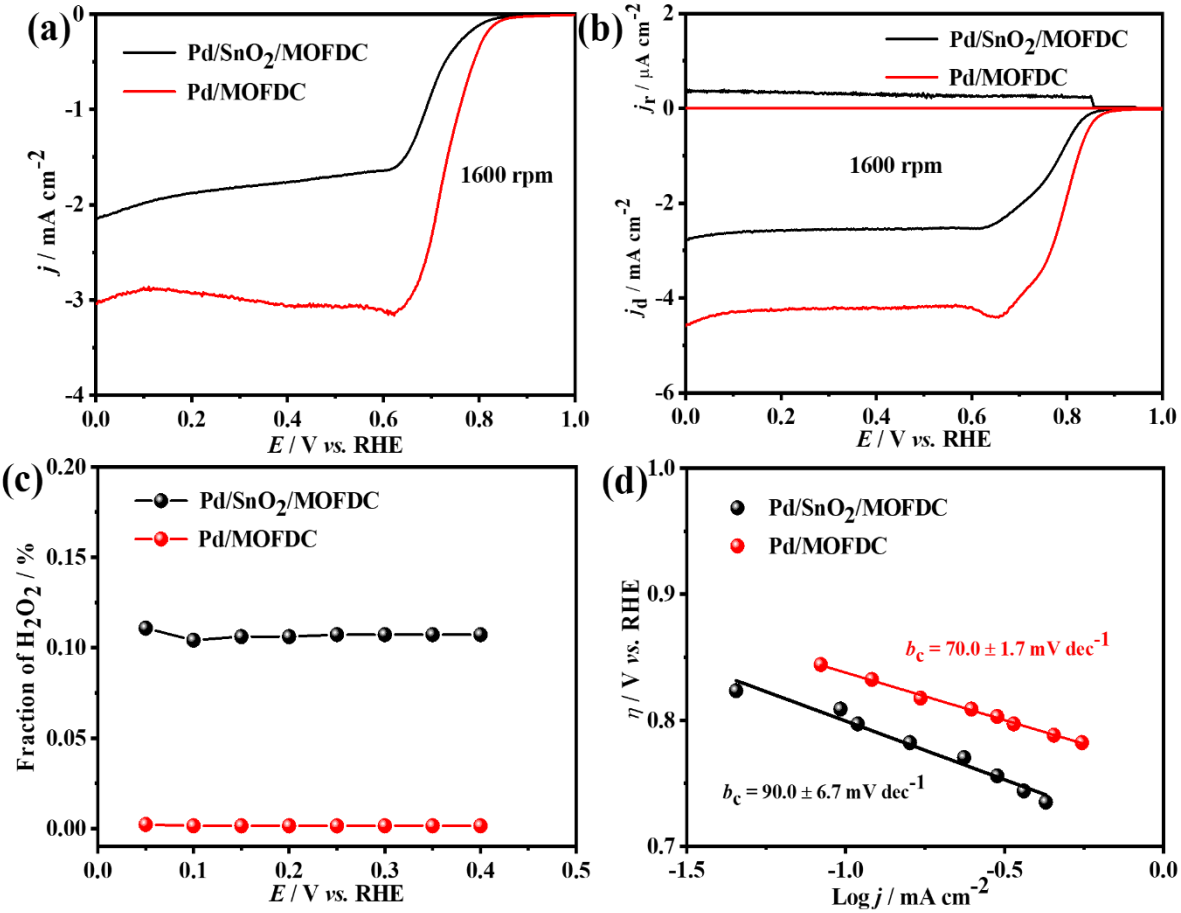

Figure 7.7: Comparative (a) RDE and (b) RRDE polarization curves, (c) a percentage of peroxides (H_2O_2) produced and (d) Tafel plots of the Pd/SnO_2-based electrocatalysts in O_2-saturated 0.1 M KOH solution at 10 mV s^{-1} and 1600 rpm

7.2.1.2.2 Electrochemical Impedance Spectroscopy (ORR)

The EIS was further employed to deduce the electron transport kinetics of the Pd/SnO_2-based electrocatalysts during the ORR. Nyquist plots of the Pd/SnO_2-based electrocatalysts toward the ORR are shown in **Figure 7.8** at $E_{1/2}$ = 0.635 V *vs.* RHE with the Voigt *EEC* model (inset) and the parameters are summarized in **Table 7.4**. R_s

values of *ca.* 66 and 71 Ω are obtained for the Pd/MOFDC and Pd/SnO_2/MOFDC, respectively. The lower R_s value of the Pd/MOFDC shows that it has increased ionic conductivity during the ORR. R_{ct} values of *ca.* 2.5 and 3.6 kΩ were recorded for the Pd/MOFDC and Pd/SnO_2/MOFDC, respectively. Lower value of the R_{ct} has been correlated to increased ORR activity [30]. Thus, the Pd/MOFDC has higher kinetic for the ORR than the Pd/SnO_2/MOFDC, attributable to the increased charge transport for beneficial ORR kinetics [31].

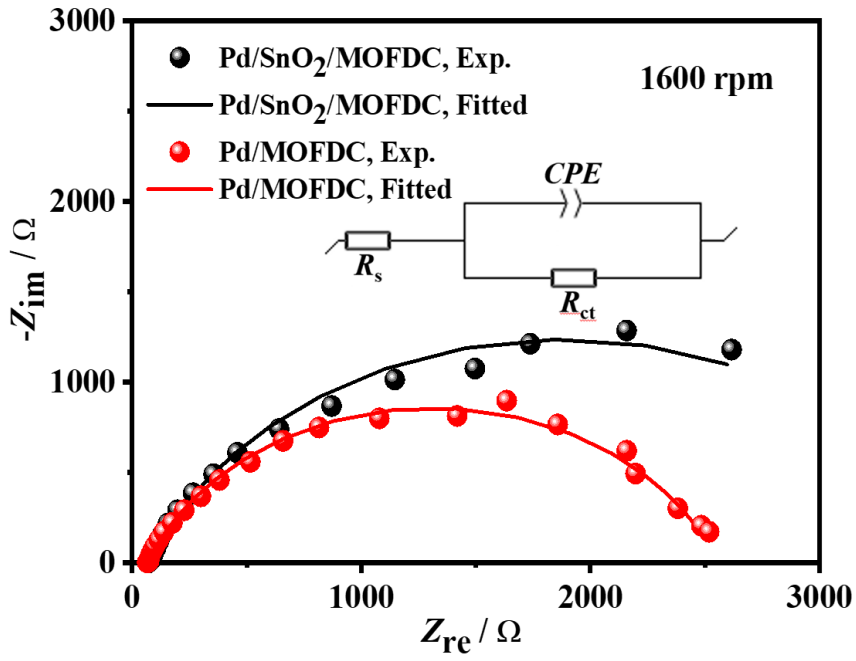

Figure 7.8: Nyquist of the Pd/SnO_2-based electrocatalysts in O_2-saturated 0.1 M KOH solution at 1600 rpm, 10 mV s^{-1} and η = 0.635 V *vs.* RHE

Table 7.4: Nyquist plots of the Pd/SnO_2-based electrocatalysts in O_2-saturated 0.1 M KOH solution at 1600 rpm, 10 mV s^{-1} and 0.635 V *vs.* RHE

EIS parameters	Pd/SnO_2-based electrocatalysts	
	Pd/MOFDC	Pd/SnO_2/MOFDC
R_s / Ω	66.27 ± 0.27	71.41 ± 0.24
*R*ct / kΩ	2.49 ± 0.00	3.62 ± 0.00
CPE / mF s^(1-*a*)	0.20 ± 0.00	0.12 ± 0.00
a	0.77	0.76

7.2.2 Pd/Ni-based Electrocatalysts for Hydrogen Oxidation (HOR) and Oxygen Reduction Reactions (ORR)

The performances of the Pd/Ni-based electrocatalysts toward alkaline HOR and ORR are presented and discussed in this session.

7.2.2.1 Hydrogen Oxidation Reaction (HOR)

7.2.2.1.1 HOR Polarization Curves

Figures 7.9a – 7.9c show the HOR polarization curves of the Pd/Ni-based electrocatalysts at 1600 rpm and other rotation speeds. The j_m values of the Pd/Ni-based electrocatalysts increase with increasing rotation speeds. However, high j_m values were observed for the Pd/AT-Ni/MOFDC than those of Pd/Ni/MOFDC at all rotation speeds, due to the oxophilic properties of the Ni nanoparticles to quickly remove H_{ads} on the active sites of Pd in the Pd/AT-Ni/MOFDC. Whereas the presence of Ni/$Ni(OH)_2$ interface in the Pd/Ni/MOFDC covering a large portion of the Pd's active sites, has less tendency to remove the H_{ads}. The E_{onset} of the electrocatalysts towards the alkaline HOR began after of 0.0 V *vs.* RHE due to iR drops, but its kinetics is

relatively fast on the Pd/AT-Ni/MOFDC to the Pd/Ni/MOFDC. The increased HOR activity on the Pd/AT-Ni/MOFDC is traced to its more exposed active sites of the nanostructured Pd and synergetic effect with more active Ni nanoparticles.

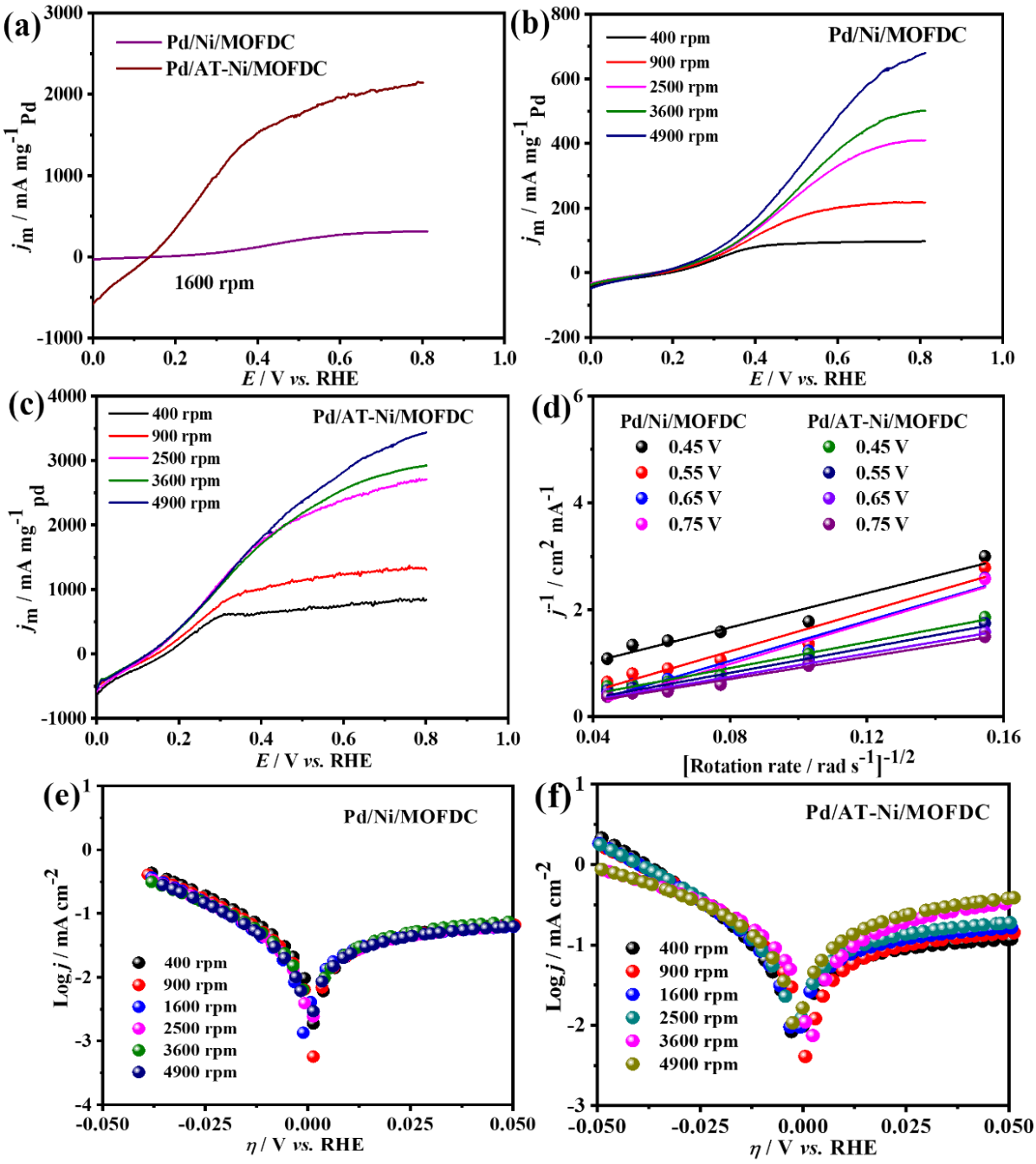

Figure 7.9: HOR polarization curves (a) 1600 rpm, (b,c) other rotation speeds, (d) Koutecky-Levich plots and (e,f) Butler-Volmer plots of the Pd/Ni-based electrocatalysts in H_2-saturated 0.1 M KOH solution at 5 mV s^{-1} and varied rotation speeds

The HOR activities of the Pd/Ni-based electrocatalysts was separated into kinetics- and diffusion-controlled process, using the well-known Koutecky-Levich formula. The Koutecky-Levich plots of the Pd/Ni-based electrocatalysts are shown in **Figure 7.9d**, at four distinct η = 0.45, 0.55, 0.65 and 0.75 V *vs.* RHE, at j_{lim} = 2.65 mA cm^{-2}. The j_K and *D* of the Pd/Ni-based electrocatalysts are extracted from the intercept and slope of the plots, respectively. At these η values, the j_K values of 2.60, 3.70, 2.19 and 1.81 mA cm^{-2} are recorded for the Pd/Ni/MOFDC, while those of the Pd/AT-Ni/MOFDC are 15.87, 8.47, 8.26 and 7.87 mA cm^{-2}. The j_K values of the Pd/Ni-based electrocatalysts were employed to deduce their k^0 value. The mean k^0 values of 1.33 ± 0.03 x 10^{-4} and 5.24 ± 0.14 x 10^{-4} cm s^{-1} are recorded for the Pd/Ni/MOFDC and Pd/AT-Ni/MOFDC, respectively. Also, the Pd/Ni/MOFDC and Pd/AT-Ni/MOFDC display *D* values of 2.40 ± 0.13 x 10^{-5} and 4.89 ± 0.19 x 10^{-5} cm^2 s^{-1}, respectively. These results show that the alkaline HOR kinetics and H_2 diffusivity are faster on the Pd/AT-Ni/MOFDC than on the Pd/Ni/MOFDC. The polarization curves were then modelled to the Butler-Volmer formula. **Figures 7.9e** and **7.9f** show the Butler-Volmer plots of the Pd/Ni-based electrocatalysts, where their mass transfer kinetic parameters such as the $j_{o,s}$, $j_{o,m}$ and b_a at all rotation speeds are determined and summarized in **Table 7.5**. It was observed that the Pd/AT-Ni/MOFDC also displays relatively increased $j_{o,s,}$ and $j_{o,m}$ values to those of the Pd/Ni/MOFDC at all rotation speeds. This observation further proved its improved HOR performance.

The significance of b_a values is to explain the mechanism of the alkaline HOR. Report on the HOR mechanism that predominates either Tafel-Volmer or Heyrovsky-Volmer process with b_a values of *ca.* 30 and range 37 – 112 mV dec^{-1}, respectively [19]. Hence, the former mechanism is favorable for the alkaline HOR on the Pd/AT-

Ni/MOFDC (b_a of *ca.* 30 mV dec^{-1}), while the latter mechanism predominates for the Pd/Ni/MOFDC toward the alkaline HOR (b_a = 52 - 142 mV dec^{-1}).

Table 7.5: Kinetic parameters of the Pd/Ni-based electrocatalysts for HOR in H_2-saturated 0.1 M KOH solution, in terms of the $j_{o,s}$, $j_{o,m}$ and b_a at 5 mV s^{-1} and varied rotation speeds

Kinetic parameters	Pd/Ni-based Electrocatalysts	
	Pd/Ni/MOFDC	Pd/AT-Ni/MOFDC
@400 rpm		
b_a / mV dec^{-1}	52.42 ± 7.33	27.6 ± 2.95
$j_{o,s}$ / mA cm^{-2}	0.0596	0.0883
$j_{o,m}$ / mA mg^{-1}	15.37	111.65
@900 rpm		
b_a / mV dec^{-1}	77.28 ± 9.25	28.44 ± 4.43
$j_{o,s}$ / mA cm^{-2}	0.0599	0.1150
$j_{o,m}$ / mA mg^{-1}	15.44	145.41
@1600 rpm		
b_a / mV dec^{-1}	88.45 ± 7.90	29.96 ± 3.78
$j_{o,s}$ / mA cm^{-2}	0.0608	0.1217
$j_{o,m}$ / mA mg^{-1}	15.67	153.88
@2500 rpm		
b_a / mV dec^{-1}	142.30 ± 1.95	33.92 ± 4.54
$j_{o,s}$ / mA cm^{-2}	0.0619	0.1371
$j_{o,m}$ / mA mg^{-1}	15.95	173.35

@3600 rpm		
b_a / mV dec^{-1}	119.90 ± 8.25	39.59 ± 4.67
$j_{o,s}$ / mA cm^{-2}	0.0626	0.1429
$j_{o,m}$ / mA mg^{-1}	16.13	180.68
@4900 rpm		
b_a / mV dec^{-1}	109.78 ± 7.18	42.93 ± 4.8
$j_{o,s}$ / mA cm^{-2}	0.0700	0.1509
$j_{o,m}$ / mA mg^{-1}	18.04	190.80

Stability of the Pd/Ni-based electrocatalysts was verified with CV (**Figure 7.10a**), where the materials were cycled 100 times. The ECSA previously determined from integration of the PdO reduction signature reduced after the 100th cycle by 13.6 and 10.8% for Pd/Ni/MOFDC and Pd/AT-Ni/MOFDC, respectively. Then, HOR polarization curves (**Figure 7.10b**) for the electrocatalysts reveal that the HOR kinetics on the Pd/Ni/MOFDC decreases by 11.7%, while that of the Pd/AT-Ni/MOFDC degrades by 9.4% after 100 cycles. The lower % loss of the Pd/AT-Ni/MOFDC toward the alkaline HOR indicate slightly better stability compared to the Pd/Ni/MOFDC.

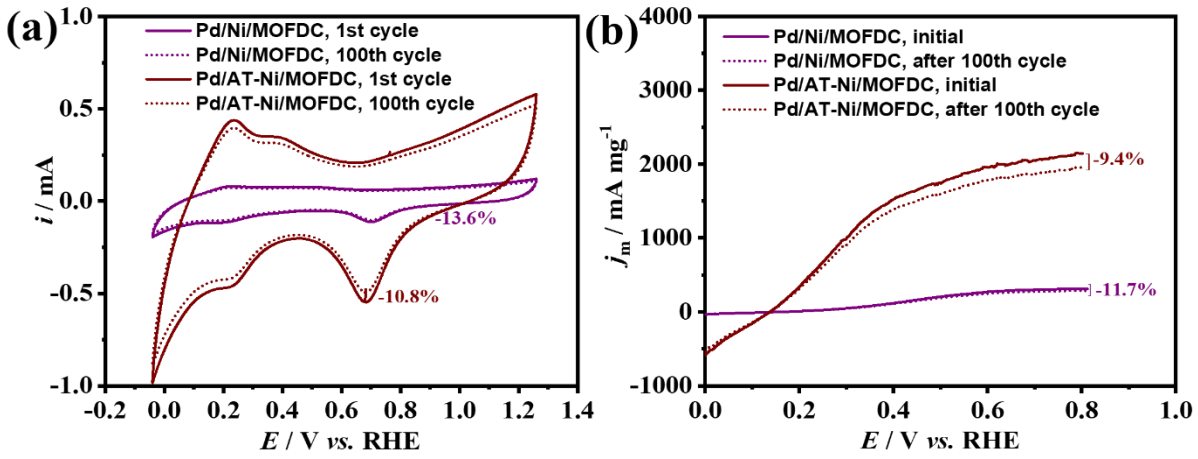

Figure 7.10: (a) CV at 1st and 100th cycles and (b) HOR polarization curves at 1600 rpm, initial and after 100th cycles of the Pd/Ni-based electrocatalysts

To further understand the behavior of the Pd/Ni-based electrocatalysts, temperature-dependent study toward alkaline HOR was carried out at 1600 rpm, 5 mV s^{-1} and varied temperature (298 – 328 K). Resulting polarization curves of the Pd/Ni-based electrocatalysts toward the alkaline HOR at different temperature are shown in **Figures 7.11a** and **7.11b**. Increasing the temperature of the experimental set-up, led to increasing the j_m values of the Pd/Ni-based electrocatalysts. Then, the polarization curves were fitted to the Butler-Volmer plots (**Figures 7.11c – 7.11e)** to extract the mass transfer kinetic parameters at varied temperature. It was observed that increasing the temperatures of the set-up, positively tilt the intercept between the anodic and cathodic regions, which is an indication of increasing $j_{o,s}$ values at high temperature. The minimum amount of energies (E_A) for the alkaline HOR activities by the Pd/Ni-based electrocatalysts was determined by modelling the extracted $j_{o,s}$ values from the fitted Butler-Volmer plots at respective temperature to the Arrhenius formula. **Figure 7.11f** shows the Arrhenius plots of Pd/Ni-based electrocatalysts (plots of ln $j_{o,s}$ vs. T^{-1}), where the E_A value was deduced from the slopes. The E_A values of 15.14 ± 2.40 and 45.02 ± 3.36 kJ were calculated for the Pd/AT-Ni/MOFDC and Pd/Ni/MOFDC, respectively. The reduced E_A value of the Pd/AT-Ni/MOFDC toward the alkaline HOR further confirms the fast removal of H_{ads} from the active sites of Pd by the more active Ni in the treated composite, an indication that the Volmer is a fast process, while the slow process is the Tafel (i.e., rds). The extremely large E_A value of the Pd/Ni/MOFDC may be ascribed to continuous water cleavages in the Heyrovsky step by the Ni/$Ni(OH)_2$ interface, which may be the slow the HOR.

+

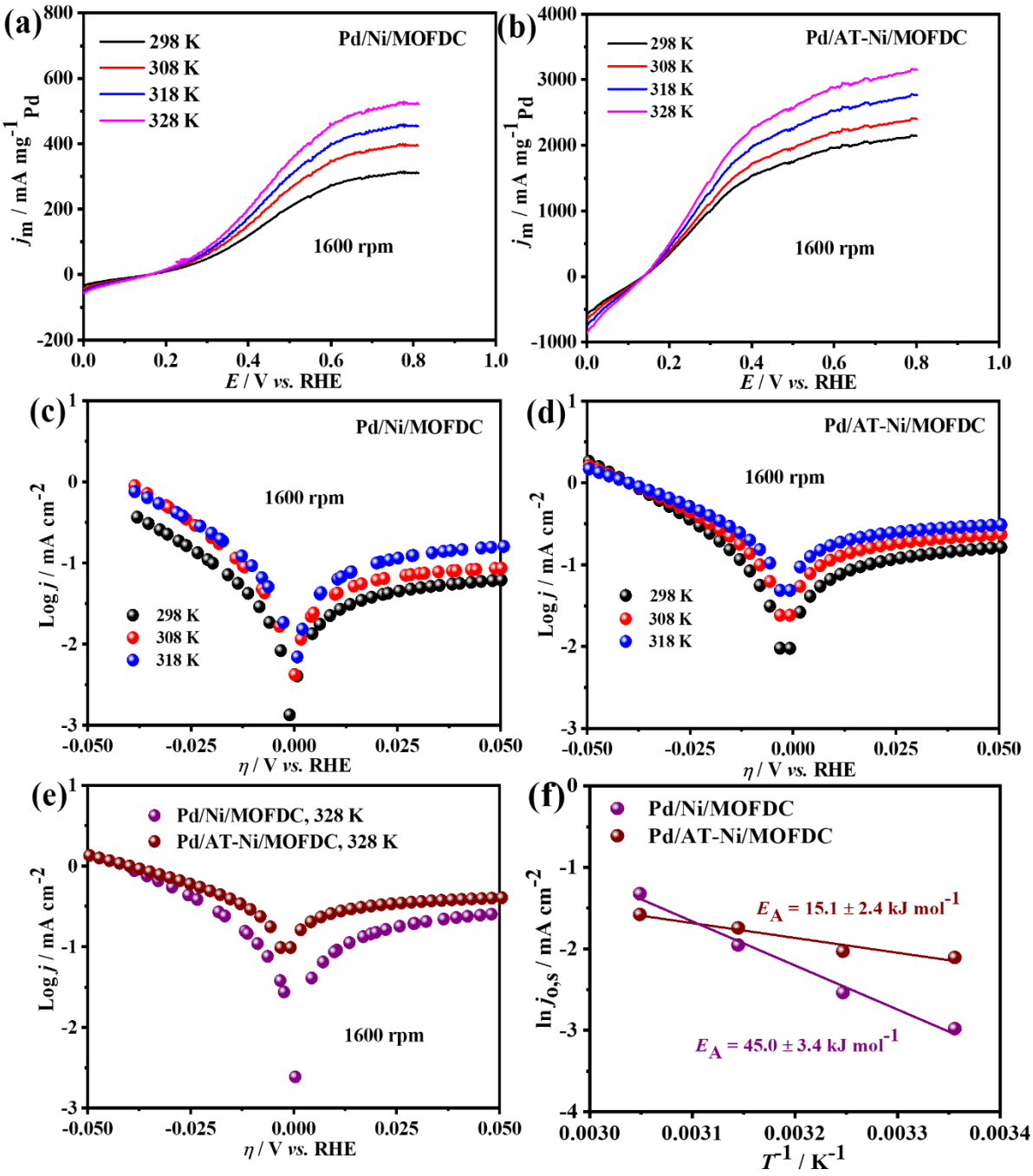

Figure 7.11: (a,b) HOR polarization curves, (c–e) Butler-Volmer plots and (f) Arrhenius plots of the Pd/Ni-based electrocatalysts in H_2-saturated 0.1 M KOH at 5 mV s^{-1} and varied temperature

7.2.2.1.2 Chronoamperometry (HOR)

The stability of the Pd/Ni-based electrocatalysts towards alkaline HOR was further confirmed with CA (**Figure 7.12**) at 1600 rpm, 298 K and 5 mV s^{-1} for 1200 rpm. The

Pd/AT-Ni/MOFDC equally shows better HOR activity retention than the Pd/Ni/MOFDC at the steady-state condition, agreeing with the CV and HOR polarization curves explained previously.

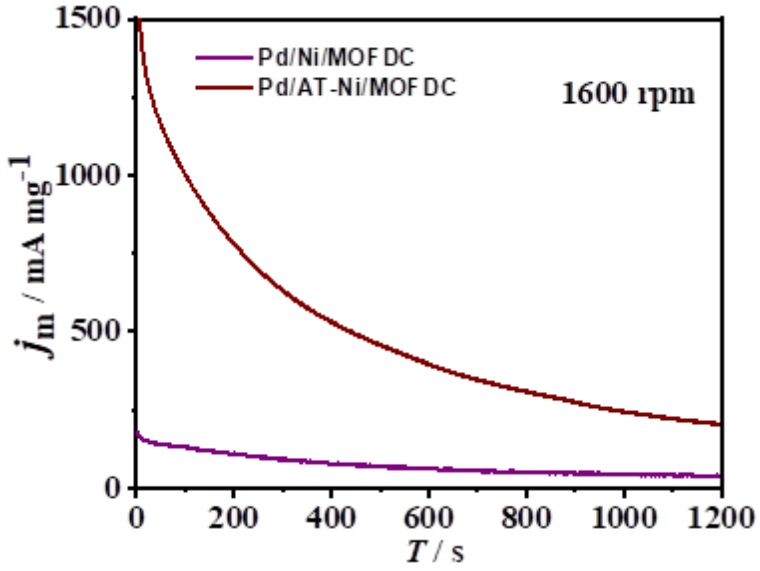

Figure 7.12: CA at 0.3 V *vs.* RHE of the Pd/Ni-based electrocatalysts in H_2-saturated 0.1 M KOH solution at 298 K and 5 mV s^{-1}

7.2.2.1.3 Electrochemical Impedance Spectroscopy (HOR)

The Pd/Ni interfacial electrochemistry for the alkaline HOR kinetics as a result of OH promoting effect of the co-metal catalysts is further investigated with the EIS. **Figure 7.13a** shows the Nyquist plots of the electrocatalysts toward the alkaline HOR with the Voigt *EEC* model (**Figure 7.13b**). The EIS parameters extracted consist of R_s, R_{int}, R_{ct} and *CPE*, explained previously and the values are summarized in **Table 7.6**. The R_s values of *ca.* 55 and 45 Ω are recorded for the Pd/Ni/MOFDC and Pd/AT-Ni/MOFDC, respectively indicating high ionic conductivity in the latter electrode. The R_{ct} values of *ca.* 115 and 207 Ω are recorded for the Pd/AT-Ni/MOFDC and Pd/Ni/MOFDC, respectively. The lower R_{ct} value of the Pd/AT-Ni/MOFDC reveals its improved HOR kinetics. Also, the R_{int} value for the Pd/AT-Ni/MOFDC (38 Ω) is lower than that of

Pd/Ni/MOFDC (45 Ω), shows the facile H desorption. According to the *CPE* impedimetric power law, the a = 0.53 and 0.54 are close to ideal Z_w with a = 0.5. This result suggests a diffusive process at the interface of electrodes and electrolytes. Bode plots (**Figures 7.13c** and **7.13d**) were further employed to probe the electrodes with the logarithm of series resistance values of 2.52 and 2.35 for the Pd/NIMOFDC and Pd/AT-Ni/MOFDC, as well as phase angles of 33.43 and 24.90º, respectively. The lower overall resistance of the Pd/AT-Ni/MOFDC confirms the interfacial behavior between the Pd and more active Ni for enhanced HOR kinetics. This is as a result of the passivation of the Ni/Ni(OH)$_2$ covering a large portion of the Pd.

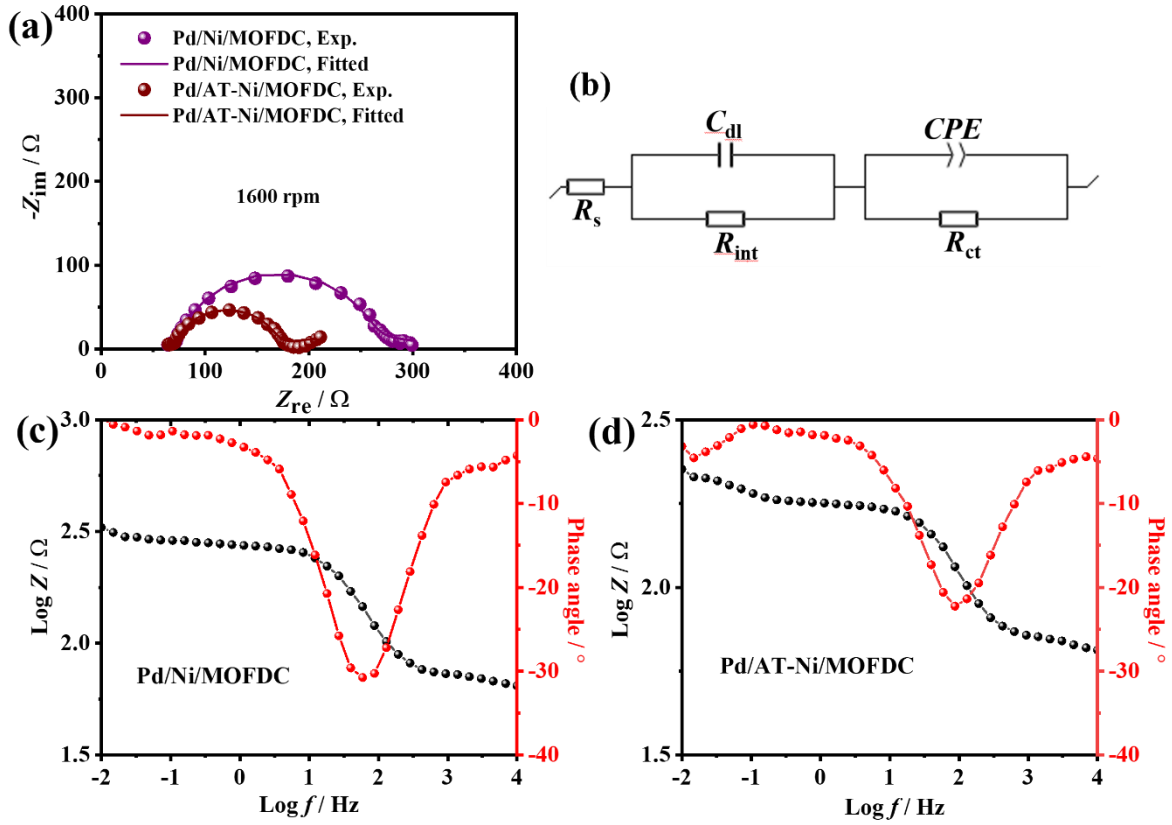

Figure 7.13: (a) Nyquist plots, (b) Voigt *EEC* model and (c,d) Bode plots of the Pd/Ni-based electrocatalysts in H_2-saturated 0.1 M KOH at 1600 rpm, 298 K and 0.3 V *vs.* RHE

Table 7.6: EIS parameters of the Pd/Ni-based electrocatalysts in H_2-saturated 0.1 M KOH at 1600 rpm, 298 K and 0.3 V *vs.* RHE

EIS parameters	Pd/Ni-based electrocatalysts	
	Pd/Ni/MOFDC	Pd/AT-Ni/MOFDC
R_s / Ω	55.37 ± 2.38	44.88 ± 8.12
R_{ct} / Ω	206.84 ± 1.92	114.54 ± 2.20
C_{dl} / µF	31.47 ± 0.80	31.11 ± 1.71
R_{int} / Ω	45.43 ± 4.75	38.58 ± 3.79
CPE / mF.s($^{a-1}$)	5.37 ± 0.17	14.30 ± 0.00
a	0.53	0.54

7.2.2.2 Oxygen Reduction Reaction (ORR)

7.2.2.2.1 ORR Polarization Curves

Figures 7.14a and **7.14b** show the ORR polarization curves of the Pd/Ni-based electrocatalysts in O_2-saturated 0.1 M KOH solution at 10 mV s^{-1} and varied rotation speeds. The *j* values increase with increasing rotation speeds for the Pd/Ni-based electrocatalysts. Although, relatively increased *j* values were observed for the Pd/AT-Ni/MOFDC at all rotation speeds to those of the Pd/Ni/MOFDC. The polarization curves of the electrocatalysts were then modelled to Koutecky-Levich formulae (**Equations 2.19** and **2.20**) to obtain to the j_K, k^0 and *n* values in the kinetic-diffusion regions. **Figures 7.14c** and **7.14d** show the Koutecky-Levich plots of the Pd/Ni-based electrocatalysts at varied η = 0.05 – 0.40 V (*vs.* RHE) and the j_{lim} = 3.0 mA cm^{-2}, as well as theoretical plots when *n* = 2 or 4. The j_K values ranges of 2.97 – 3.30 mA cm^{-2} and 17.91 – 35.88 mA cm^{-2} are recorded for the Pd/Ni/MOFDC and Pd/AT-Ni/MOFDC, respectively. The *n* values calculated for the Pd/MOFDC and Pd/SnO_2/MOFDC are

2.62 and 1.3, respectively. These results show that the ORR is fast on the Pd/AT-Ni/MOFDC following $2e^-$ pathway, whereas slow ORR was observed on the Pd/Ni/MOFDC with mixed pathways (i.e., $2e^-$ and $4e^-$ pathways). These observations are further confirmed using RRDE experiments. Using the *n* values in the relationship between the j_K and k^0 (**Equation 2.22**), mean k^0 values of 1.21 x 10^{-4} and 17.23 x 10^{-4} cm s^{-1} are calculated for the Pd/Ni/MOFDC and Pd/AT-Ni/MOFDC, respectively. The lower k^0 of the ORR at the Pd/Ni/MOFDC further confirms its reduced ORR kinetics, due to the negative effect of the $Ni/Ni(OH)_2$ interface.

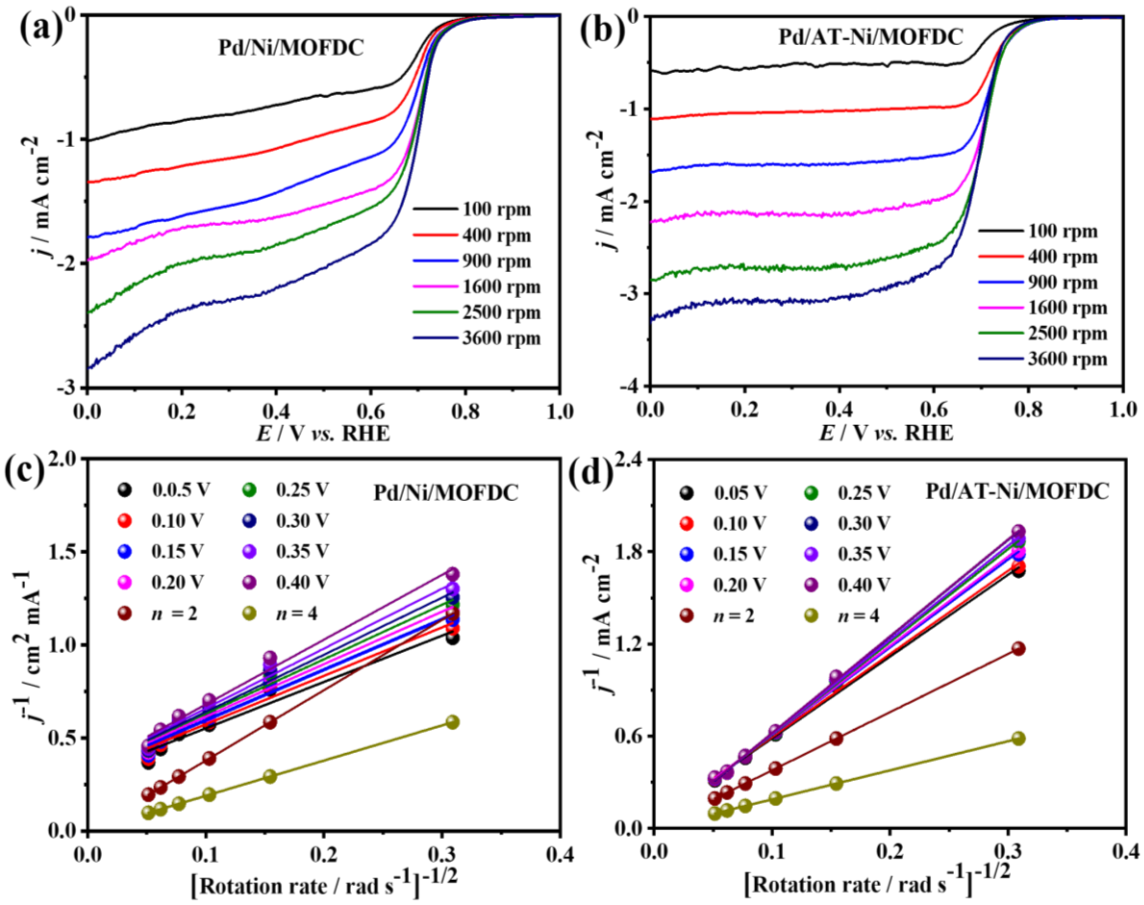

Figure 7.14: (a,b) ORR polarization curves and (c,d), Koutecky-Levich plots at varied η values of the Pd/Ni-based electrocatalysts in O_2-saturated 0.1 M KOH solution at 10 mV s^{-1} and varied rotation speeds

Figure 7.15 shows comparative RDE and RRDE polarization curves of the Pd/Ni-based electrocatalysts in O_2-saturated 0.1 M KOH solution at 1600 rpm and 10 mV s^{-1}. In **Figure 7.15a**, E_{onset} values of 90 and 93 mV *vs.* RHE were recorded for the Pd/Ni/MOFDC and Pd/AT-Ni/MOFDC, respectively. The more positive E_{onset} at the Pd/AT-Ni/MOFDC shows that the ORR is more facile requiring less energy compared to the Pd/Ni/MOFDC. The result corroborates the increased mass transfer (j) and kinetic (j_K, k^0) parameters of the Pd/AT-Ni/MOFDC obtained previously indicating improved ORR activity, relative to the Pd/Ni/MOFDC. **Figure 7.15b** shows the RRDE of the Pd/Ni-based electrocatalysts toward the ORR. The Pd/Ni-based electrocatalysts produce a significant amount of H_2O_2. The Pd/Ni/MOFDC produces a smaller amount of the H_2O_2 (*ca.* 2.3 %) because its ORR mechanism follows mixed 2 and $4e^-$-pathways, whereas the ORR on the Pd/AT-Ni/MOFDC follows only the $2e^-$-pathway with a high amount of H_2O_2 produced (*ca.* 11.0 %), as shown in **Figure 7.15c**. The Tafel plots of the Pd/Ni-based electrocatalysts are shown in **Figure 7.15d**, with b_c values of 85 and 70 mV dec^{-1} recorded for the Pd/Ni/MOFDC and Pd/AT-Ni/MOFDC, respectively. This result agrees with the previous assumption that the ORR is more facile on the Pd/AT-Ni/MOFDC, although follows the $2e^-$-pathway.

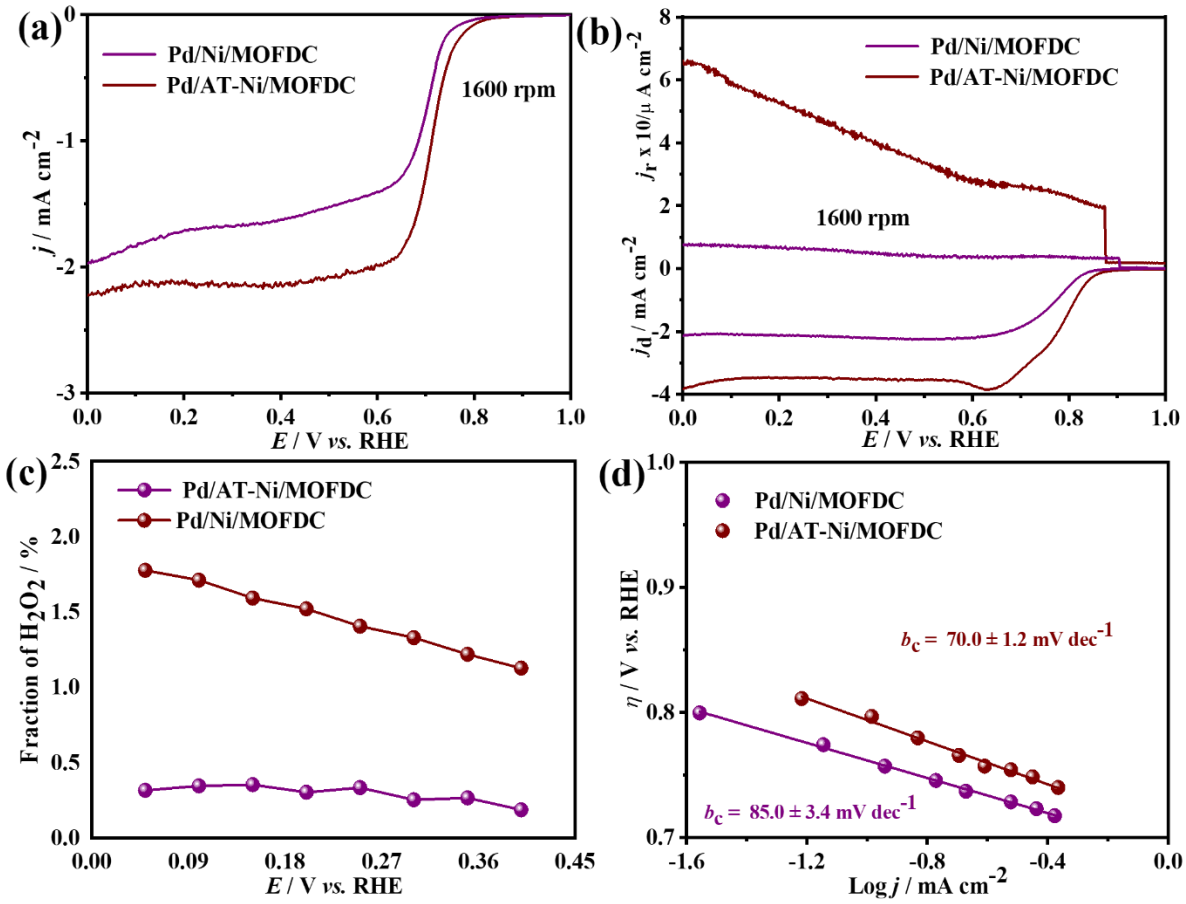

Figure 7.15: Comparative (a) RDE and (b) RRDE polarization curves, (c) a percentage of peroxides (H_2O_2) produced and (d) Tafel plots of the Pd/Ni-based electrocatalysts in O_2-saturated 0.1 M KOH solution at 10 mV s^{-1} and 1600 rpm

7.2.2.2.2 Electrochemical Impedance Spectroscopy (ORR)

Figure 7.16 shows the Nyquist plots of the Pd/Ni-based electrocatalysts toward the ORR at $E_{1/2}$ = 0.635 V *vs.* RHE and the Voigt *EEC* model (**inset**) employed to obtain the EIS parameters (**Table 7.7**). R_s values of *ca.* 62 and 53 Ω are obtained for the Pd/NiMOFDC and Pd/AT-Ni/MOFDC, respectively. The lower R_s value of the Pd/AT-Ni/MOFDC shows its increased ionic conductivity during the ORR. R_{ct} values of *ca.* 9.9 and 1.7 kΩ was recorded for the Pd/Ni/MOFDC and Pd/AT-Ni/MOFDC, respectively. The lower R_{ct} value on the Pd/AT-Ni/MOFDC toward the ORR shows relatively increased ORR activity. Hence, the Pd/AT-Ni/MOFDC has higher kinetic for

the ORR than the Pd/Ni/MOFDC, ascribable to the strong synergy between the more active metal Ni and nanostructured Pd beneficial to the ORR

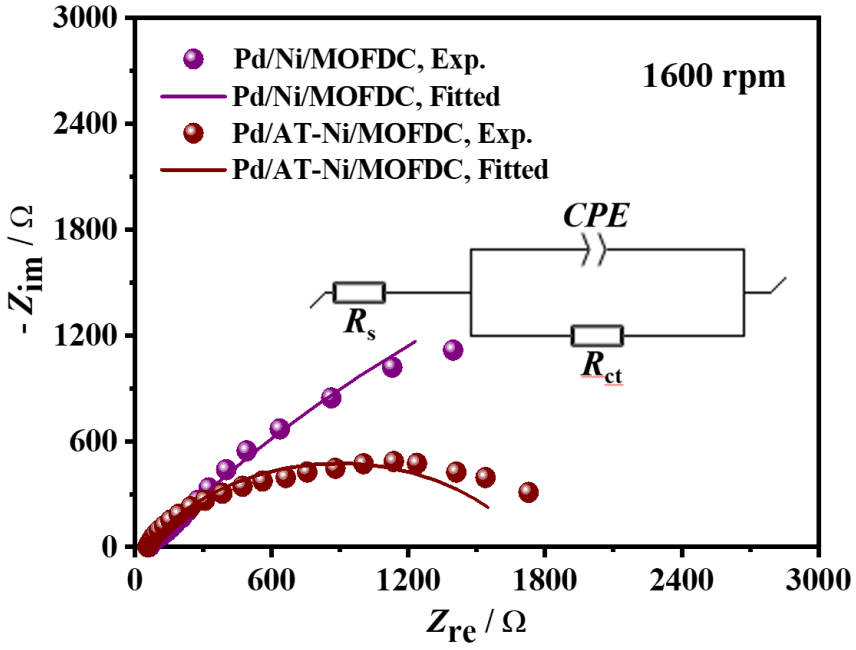

Figure 7.16: Nyquist of the Pd/Ni-based electrocatalysts in O_2-saturated 0.1 M KOH solution at 1600 rpm, 10 mV s^{-1} and η = 0.635 V vs RHE

Table 7.7: Nyquist plots of the Pd/Ni-based electrocatalysts in O_2-saturated 0.1 M KOH solution at 1600 rpm, 10 mV s^{-1} and 0.635 V *vs.* RHE

EIS parameters	Pd/Ni-based electrocatalysts	
	Pd/Ni/MOFDC	Pd/AT-Ni/MOFDC
R_s / Ω	62.23 ± 0.27	53.12 ± 0.28
R_{ct} / kΩ	9.85 ± 0.25	1.68 ± 0.00
CPE / mF. s^(1-a)	0.71 ± 0.00	0.16 ± 0.00
a	0.58	0.65

7.3 Conclusions

The Pd/SnO_2-based electrocatalysts were tested for HOR and ORR kinetics in alkaline conditions. The strong synergy between Pd and SnO_2 nanoparticles in the Pd/SnO_2/MOFDC electrocatalyst contributed to its improved HOR performance in terms of averagely doubled j_K, k^0, D, and $j_{o,s}$, whereas its mass $j_{o,m}$ value increased by a factor of *ca.* 5.5 compared to the Pd/MOFDC. A weakening of the M-H_{ads} by OH promotional effect of Sn and SnO_2 in the Pd/SnO_2/MOFDC justifies its improved HOR, relative to the Pd/MOFDC. The b_a values of the electrocatalysts for the HOR suggests that the Heyrovsky-Volmer process predominates. Also, the lower E_A value of the Pd/SnO_2/MOFDC to the Pd/MOFDC further explains its facile HOR kinetics. Thus, the increased HOR activity and lower energy of the Pd/SnO_2/MOFDC makes it an excellent anodic electrocatalyst material for the development of AMFCs. However, the Pd/MOFDC exhibits superior ORR activity with respect to its increased j, j_K and k^0, but lower b_c and series resistance (R_s + R_{ct}) values, relative to the Pd/SnO_2/MOFDC. The RRDE model supersedes the Kouteckly-Levich diagnosis indicates the 4e^- pathway is favourable for the Pd/SnO_2-based electrocatalyst toward the ORR. In the other scenario, where the Pd/Ni-based electrocatalysts were demonstrated for alkaline HOR and ORR kinetics. The Pd/AT-Ni/MOFDC delivers improved alkaline HOR performance with respect to high j_K, k^0, D, $j_{o,s}$ and $j_{o,m}$ compared to the Pd/Ni/MOFDC. The b_a values of the Pd/Ni-based electrocatalysts indicate that the mechanism of the alkaline HOR on the Pd/Ni/MOFDC and Pd/AT-Ni/MOFDC follow Heyrovsky-Volmer and Tafel-Volmer processes, respectively. The Pd/AT-Ni/MOFDC equally exhibits relatively higher ORR activity with respect to its increased j, j_K and k^0, but lower b_c, R_s, and R_{ct} values to those of the Pd/Ni/MOFDC. The Kouteckly-Levich diagnosis and RRDE experiments indicate the ORR follows mixed-pathways (i.e., 2 and 4e^-) and only

2e$^-$-pathway on the Pd/Ni/MOFDC and Pd/AT-Ni/MOFDC, respectively. Hence, the bifunctional behavior of the Pd/AT-Ni/MOFDC for the alkaline HOR and ORR.

7.4 References

[1] K. Wong, S. Dia, *Journal of Energy Resource* Technology, **139**,1(2017): 014001.

[2] M. Zhou, H. I. Wang, S. Guo, *Chemical Society Review,* **45**,5(2016): 1273–1307.

[3] H. Zhang, M. Jin, Y. Xia, *Chemical Society Review,* **41**,24(2012): 8035–8049.

[4] J. S. Spendelow, A. Wieckowski, *Physical Chemistry Chemical Physics,* **9**,21(2007): 2654–2675.

[5] D. Tang, J. Pan. S. Lu, L. Zhuang, J. Lu, *Science China Chemistry,* **53**(2010): 357–364.

[6] C. Yang, B. Huang, L. Xiao, Z. Ren, Z. Liu, J. Lu, L. Zhuang, *Chemical Communication,* **49**,94(2013): 11023–11025.

[7] J. Suntivich, H. A. Gasteiger, N. Yabuuchi, H. Nakanishi, J. B. Goodenough, Y. Shao-Horn, *Nature Chemistry,* **3**,7(2011): 546–550.

[8] T. E. Sutto, *Inorganic Chemistry,* **53**,9(2014): 4570–4578.

[9] S. Henning, J. Herranz, H. A. Gasteiger, *Journal Electrochemistry Society,* **162**,1(2015): F178–F189.

[10] J. Durst, A. Siebel, C. Simon, F. Hasche, J. Herranz, H. A. Gasteiger, *Energy and Environmental Science,* **7**,7(2014): 2255–2260.

[11] W. Sheng, H. A. Gasteiger, Y. Shao-Horn, *Journal of Electrochemical Society,* **157**,11(2010): B1529–B1536.

[12] L. An, N. Jiang, B. Li, S. Hua, Y. Fu, J. Liu, W. Hao, D. Xia, Z. Sun, *Journal of Material Chemistry A.,* **6**,14(2018): 5962–5970.

[13] Y. Zhan, F. Xie, H. Zhang, Z. Lin, J. Huang, W. Zhang, X. Sun, Y. Zhang, J. Chen, H. Meng, *Journal of the Electrochemical Society*¸**165**,15(2018): J3008.

[14] E. S. Davydova, S. Mukerjee, F. Jaouen, D. R. Dekel, *ACS Catalysis,* **8**(2018): 6665–6690.

[15] T. Bhowmik, M. K. Kundu, S. Barman, *ACS Catalysis,* **6**,3(2016): 1929–1941.

[16] S. Lu, Z. Zhuang, *Journal American Chemical Society,* **139**(2017): 5156–5163.

[17] N. M. Markovic, S. T. Sarraf, H. A. Gasteiger, P. N. Ross, *Journal of the Chemical Society, Faraday Transaction,* **92**,20(1996): 3719–3725.

[18] K. Elbert, J. Hu, Z. Ma, Y. Zhang, G. Chen, W. An, P. Liu, H. S. Isaac, R. R. Adzic, J. X. Wang, *ACS Catalysis*, **5**,11(2015): 6764–6772.

[19] N. M. Markovic, B. N. Grgur, and P. N. Ross, *Journal Physical Chemistry B*, **101**,27(1997): 5405–5413.

[20] S. John St., R. W. Atkinson, R.R. Unocic, T. A. Zawodzinski, A. B. Papandrew, *Journal Physical Chemistry C*, **119**,24(2015): 13481–13487.

[21] P. M. Quaino, M. R. Gennero de Chialvo, A. C. Chialvo, *Electrochimica Acta.,* **52**,25(2007), 7396–7403.

[22] J. Zheng, S. Zhou, S. Gu, B. Xu, Y. Yan, *Journal of Electrochemical Society,* **163**,6(2016), F499–F506.

[23] W. Sheng, Z. Zhuang, M. Gao, J. Zheng, J. G. Chen, Y. Yan, *Nature Communication,* **6**(2015): 5848.

[24] J. Durst, C. Simon, F. Hasché, H. A. Gasteiger, *Journal of Electrochemical Society*, **162**,1(2015): F190–F203.

[25] F. J. Vidal-Iglesias, J. Solla-Gullon, V. Montiel, A. Aldaz, *Electrochemical Communications*, **15**,1(2012): 42–45.

[26] S. Sfaelou, X. Zhuang, P. Lianos, *RSC Advances*, **5**(2015): 27953–27963.

[27] M. H. Seo, S. M. Choi, H. J. Kim, W. B. Kim, *Electrochemistry Communication*, **13**,2(2011): 182–185.

[28] G. Hu, F. Nitze, T. Sharifi, H. R. Barzegar, T. Wagberg, *Journal of Material Chemistry*, **22**,17(2012): 8541–8548.

[29] C. Zhu, S. Guo, S. Dong, *Chemistry-A European Journal*, **19**,3(2013): 1104–1111.

[30] C. Adamo, X. Ke, H. Q. Wang, H. L. Xin, T. Heeg, M. E. Hawley, W. Zander, J. Schubert, P. Schiffer, D. A. Muller, L. Maritato, D. G. Schlom, *Applied Physics Letters*, **95**(2009): 112504.

[31] M. Korotin, S. Ezhov, I. Solovyev, V. Anisimov, D. Khomskii, G. Sawatzky, *Physical Review B*, **54**,8(1996): 5309–5316.

CHAPTER 8

General Conclusions and Future Works

8.1 Introduction

The overall conclusions of all the results acquired in this work and recommendation for future works are highlighted in this chapter.

8.2 Conclusions

8.2.1 Study of Nanostructured Pd/M Electrocatalysts on MOF-Derived Carbons for Direct Ethanol Micro-Fuel Cell

- The possibility of using the MOFs sacrificial templates for the synthesis of novel MOF-derived carbon supports for nanostructured Pd electrocatalysts using microwave-assisted methods, as well as the influence of co-metal catalysts (M = SnO_2 or Ni) were studied for the EOR in alkaline media and µ-DEFC.
- Systematic addition of co-metals catalysts (M = SnO_2, Ni) to Pd electrocatalysts supported on different MOFs-derived carbons demonstrated for the EOR and µ-DEFC were grouped into two: (a) Pd/SnO_2-based (Pd/MOFDC and Pd/SnO_2/MOFDC) using ligand having a 2-aromatic ring and 4-COOH group, and (b) Pd/Ni-based (Pd/Ni/MOFDC (with Ni-rich composite) and Pd/AT-Ni/MOFDC (with Ni-deficient composite)) using ligand having a 1-aromatic ring and 3-COOH group.
- The addition of the M (SnO_2 or Ni) to the electrocatalysts improves their performances toward the EOR and µ-DEFC. However, the cleaning of Ni-rich

component before the dispersion of nanostructured Pd as in Pd/AT-Ni/MOFDC is most beneficial amongst other electrocatalysts. Hence, the Pd/AT-Ni/MOFDC is the most active material for EOR and μ-DEFC.

8.2.2 Electrochemical Probing of Pd/M Nanocatalysts Supported MOF-Derived Carbons and Testing the Best Material for Fuel Cell-Based Breath Alcohol Sensor

- Ferri/ferrocyanide solution was employed as a redox probe to investigate the electrochemical behavior of the electrocatalysts (Pd/MOFDC, Pd/SnO_2/MOFDC, Pd/Ni/MOFDC and Pd/AT-Ni/MOFDC).
- The Pd/AT-Ni/MOFDC exhibits the best electrocatalytic performance in terms of mass transport and electron transfer kinetics.
- The excellent performance of the Pd/AT-Ni/MOFDC in the redox probe and for EOR and μ-DEFC informed its choice to be tested for FCBrAS at extremely low concentrations of EtOH within the acceptable limit. The preliminary results show that the material is promising for its application in real-life alcohol sensor.

8.2.3 Investigation of Alkaline Water-Splitting Reactions using Pd/M Electrocatalysts on MOFDC-Derived Carbons

- The electrocatalysts (Pd/MOFDC, Pd/SnO_2/MOFDC, Pd/Ni/MOFDC and Pd/AT-Ni/MOFDC) were demonstrated for electrochemical water-splitting (i.e., the HER and OER) with more emphasis on the HER.
- The addition of SnO_2 in the Pd/SnO_2-based electrocatalysts was detrimental to the HER activity, as the Pd/MOFDC performs better. However, the Pd/SnO_2/MOFDC displays better OER activity than the Pd/MOFDC.

- For the Pd/Ni-based electrocatalysts, the Pd/Ni/MOFDC display superior HER and OER activities, due to the presence of Ni/Ni(OH)$_2$ interface confirmed to be active toward water electrolysis.

8.2.4 Demonstrating novel Pd/M Electrocatalysts on MOF-Derived Carbons for Alkaline Hydrogen Oxidation and Oxygen Reduction Reactions

- Alkaline HOR and ORR were interrogated on the novel electrocatalysts (Pd/MOFDC, Pd/SnO$_2$/MOFDC, Pd/Ni/MOFDC and Pd/AT-Ni/MOFDC).
- The addition of the M (SnO$_2$ or Ni) to the Pd electrocatalysts on the MOFs-derived carbons enhances their performances toward the alkaline HOR. However, further cleaning of the Ni/MOFDC with acid as in the Pd/AT-Ni/MOFDC further augmented the alkaline HOR activity and stability with the best performance among other electrocatalysts tested in this work.
- For the alkaline ORR, the presence of SnO$_2$ in the Pd/SnO$_2$-based electrocatalysts does not show any beneficial effect rather it suppresses the ORR activity of the Pd/MOFDC. Also, the cleaning of the Ni/MOFDC composite in the Pd/AT-Ni/MOFDC is advantageous for ORR activity. Although, the Pd/MOFDC exhibits the best mass transport properties amongst the electrocatalyst but has the same ORR kinetic with the Pd/AT-Ni/MOFDC.

8.3 Future works

This study opens an avenue for exploring MOFs sacrificial templates for making novel carbons and/or composites supports for Pd-based electrocatalysts for energy conversion applications: alkaline direct ethanol fuel cell, fuel cell-based breath alcohol sensor, alkaline water electrolyzer and alkaline membrane fuel cell in liquid electrolytes. The following recommendations should be considered in the future:

- MOFs sacrificial templates with ligands containing two or more functional groups will be prepared, as this may enhance the surface area of the supports and electrocatalysts.
- Other synthesis methods like sol-gel can also be explored for making the MOFs sacrificial templates and electrocatalysts to manipulate the construction of precursor materials and final products.
- Experimental conditions for the synthesis of the MOFs, composites and electrocatalysts can be varied to further fine-tune the physicochemical properties of the electrocatalysts for beneficial performance in energy conversion devices.
- The experimental set-ups for fuel cell-based breath alcohol sensor will be properly designed and carried out for days for optimal performance and reproducibility.
- Fabrication of the best electrocatalyst in a breathalyzer for real-life application.
- The electrocatalysts were tested for the electrochemical energy conversion applications in liquid alkaline electrolytes in this work. For the sake of safety and portability, the electrocatalysts can be tested in solid-state alkaline electrolytes.
- The use of spray pyrolysis to deposit catalysts slurries on substrates (nickel foam and Toray carbon paper) for the μ-DEFC testing.
- The best performing electrocatalysts (Pd/AT-Ni/MOFDC) will be tested for alkaline membrane fuel cell (full cell).